Studies of QCD-related Aspects of Event Evolution at e^+e^- Colliders

Dissertation
zur Erlangung des Doktorgrades
des Fachbereichs Physik
der Universität Hamburg

vorgelegt von
Kristian Harder
aus Lübeck

Hamburg
2002

Gutachter der Dissertation	:	Prof. Dr. A. Wagner Prof. Dr. B. Naroska
Gutachter der Disputation	:	Prof. Dr. A. Wagner Prof. Dr. W. Schmidt-Parzefall
Datum der Disputation	:	24. Juni 2002
Dekan des Fachbereichs Physik und Vorsitzender des Promotionsausschusses	:	Prof. Dr. F.-W. Büßer

Abstract

Using data collected at the Z resonance with the OPAL detector at LEP in the years 1992–2000, the fragmentation of b quarks into hadrons is investigated. Several models are compared to data, and a model-independent measurement of the mean scaled energy of weakly decaying B hadrons is performed, resulting to

$$\langle x_{\mathrm{E}} \rangle = 0.7194 \pm 0.0016(stat)^{+0.0035}_{-0.0038}(syst) \ .$$

This is the most precise measurement of this quantity so far.

With the OPAL data taken in the years 1992–1995, a search for a radial excitation of the $\mathrm{D}^{*\pm}$ meson is performed, the existence of which is predicted by Heavy Quark Effective Theory. No narrow resonance is found, and a production rate limit of

$$f(\mathrm{Z} \to \mathrm{D}^{*\prime\pm}(2629)) \times Br(\mathrm{D}^{*\prime+} \to \mathrm{D}^{*+}\pi^+\pi^-) < 3.1 \times 10^{-3} \quad (95\%\ \mathrm{C.L.})$$

is obtained.

Studies to gain realistic expectations about the physics capabilities of next generation particle physics detectors are presented. Realistic track reconstruction software has been created and adapted for the TESLA project detector. The track reconstruction performance is evaluated, and the expected improvement for the OPAL analyses presented in this thesis is demonstrated for critical parts of the analyses.

Zusammenfassung

Mit Daten, die mit dem OPAL-Detektor bei LEP in den Jahren 1992–2000 auf der Z-Resonanz aufgezeichnet wurden, wird die Fragmentation von b-Quarks in Hadronen untersucht. Mehrere Modelle werden mit Daten verglichen, und eine modellunabhängige Messung der mittleren skalierten Energie schwach zerfallender B-Hadronen wird durchgeführt, mit dem Ergebnis

$$\langle x_{\mathrm{E}} \rangle = 0.7194 \pm 0.0016(stat)^{+0.0035}_{-0.0038}(syst) \ .$$

Dies ist die zur Zeit präziseste Messung dieser Größe.

Mit den OPAL-Daten der Jahre 1992–1995 wird eine Suche nach einer radialen Anregung des $\mathrm{D}^{*\pm}$-Mesons durchgeführt, deren Existenz im Rahmen der Effektiven Theorie Schwerer Quarks (HQET) vorhergesagt wird. Es wird keine schmale Resonanz gefunden, und ein oberer Grenzwert auf die Produktionsrate von

$$f(\mathrm{Z} \to \mathrm{D}^{*\prime\pm}(2629)) \times Br(\mathrm{D}^{*\prime+} \to \mathrm{D}^{*+}\pi^+\pi^-) < 3.1 \times 10^{-3} \quad (95\%\ \mathrm{C.L.})$$

wird bestimmt.

Studien zur Gewinnung realistischer Abschätzungen der physikalischen Möglichkeiten von Teilchenphysik-Detektoren der nächsten Generation werden präsentiert. Realistische Spurrekonstruktionsprogramme sind für den Detektor des TESLA-Projektes geschrieben und angepaßt worden. Die Leistung der Spurrekonstruktion wird untersucht, und die zu erwartenden Verbesserungen für die in dieser Arbeit präsentierten OPAL-Analysen werden anhand kritischer Teile der Analysen demonstriert.

While it may be difficult to find a man on the street who does not believe in the Lagrangian of Quantum Chromodynamics, $\mathcal{L}_{QCD}$, it is even more difficult to find one who knows what $\mathcal{L}_{QCD}$ really means.

T.D. Gottschalk, D.A. Morris,
Nucl. Phys. B288 (1987) 729.

Contents

1 Overview **3**

2 Theoretical Foundations **5**
2.1 A Brief History of Particles . . . 5
2.2 The Standard Model of Particle Physics . . . 6
2.2.1 Abelian Gauge Theories . . . 8
2.2.2 Non-Abelian Gauge Theories . . . 8
2.2.3 Renormalisability . . . 11
2.2.4 Perturbative and Non-Perturbative QCD . . . 14
2.3 e^+e^- Colliders as QCD Laboratories . . . 15
2.4 Fragmentation and Hadronisation . . . 17
2.4.1 Fragmentation . . . 18
2.4.2 Hadronisation Models . . . 21
2.4.3 Fragmentation Functions for the String Scheme . . . 28
2.4.4 General Thoughts on Hadronisation of Heavy Quarks . . . 29
2.4.5 Parametrisations of the Heavy Quark Fragmentation Function . . . 30
2.5 Excited Heavy Mesons . . . 35
2.6 Shortcomings and Possible Extensions of the Standard Model . . . 39

3 Experimental Setup **44**
3.1 The LEP Accelerator . . . 44
3.2 The OPAL Detector . . . 44
3.3 OPAL Dataset and Monte Carlo Samples . . . 49

4 Bottom Hadronisation at 90 GeV **52**
4.1 Event Selection and Monte Carlo Optimisation . . . 53
4.2 Selection and Reconstruction of B Hadrons . . . 54
4.2.1 Preselection of $Z \to b\overline{b}$ Events . . . 54
4.2.2 Reconstruction of B Hadron Energy and Direction . . . 54
4.3 Additional Monte Carlo Corrections . . . 59
4.4 Test of Hadronisation Models . . . 61
4.5 Model-independent Analysis . . . 67
4.5.1 Stabilisation of the Unfolding Solution . . . 68
4.5.2 Results of the Unfolding Analysis with RUN . . . 69
4.5.3 Results of the Unfolding Analysis with SVD-GURU . . . 69
4.6 Systematic Studies . . . 71
4.6.1 Systematic Uncertainties of the Model-dependent Fit . . . 71
4.6.2 Systematic Uncertainties of the Unfolding Analysis . . . 73

4.7 Discussion . . . 75

5 Excited D Mesons at OPAL **79**
5.1 Event Selection and Monte Carlo Optimisation . . . 80
5.2 Reconstruction of $D^{*\prime+}(2629)$ Candidates . . . 81
5.3 Selection Results . . . 84
5.4 Reconstruction of $D_J^{(*)0}$ Candidates . . . 85
5.5 Systematic Checks of the $D^{*\prime+}(2629)$ Reconstruction . . . 94
5.6 Calculation of $D^{*\prime+}(2629)$ Production Limits . . . 96
5.7 Discussion . . . 97

6 The TESLA Project **104**
6.1 The TESLA Accelerator . . . 105
6.2 The Physics Program . . . 107
6.3 TESLA Detector Design . . . 110
6.4 Tracking Detector Setup . . . 113
6.4.1 Detector Specifications . . . 114
6.4.2 Beam-related Background . . . 116

7 Track Reconstruction at a TESLA Detector **118**
7.1 The Full Reconstruction Package . . . 118
7.1.1 Global Steering . . . 119
7.1.2 Local Reconstruction Packages . . . 119
7.1.3 Kalman Filter Track Fit . . . 122
7.1.4 Global Track Search . . . 123
7.1.5 The Concept of Exclusions . . . 124
7.1.6 Event Ambiguity Processing . . . 124
7.2 Performance of the Proposed Detector . . . 125
7.2.1 Performance of the Local Pattern Recognition Packages . . . 125
7.2.2 Track Efficiencies and Fake Rates in $Z \to d\bar{d}$ Events at 500 GeV . . . 131
7.2.3 Track Efficiencies and Fake Rates in $Z \to \tau^+\tau^-$ 3-prong Events at 800 GeV 132
7.2.4 Hit Efficiencies and Fake Rates for the Different Detector Components . 132
7.2.5 Momentum, Vertex, and Direction Resolutions . . . 134
7.3 Summary . . . 137

8 Physics Capabilities of a TESLA Detector **138**
8.1 B Hadron Energy Reconstruction at TESLA . . . 138
8.1.1 Selection of B Decay Vertices . . . 139
8.1.2 Vertex Mass b Tag . . . 140
8.1.3 B Hadron Energy Reconstruction . . . 141
8.1.4 Discussion . . . 143
8.2 Excited D Mesons at TESLA . . . 145
8.2.1 Event and Track Selection . . . 145
8.2.2 Reconstruction of $D_J^{(*)0}$ Candidates . . . 146
8.2.3 Discussion . . . 147
8.3 Summary . . . 148

9 Conclusion **149**

Chapter 1

Overview

This thesis deals with reactions of presumably elementary particles that start from a very simple configuration and end up in a complicated system of many particles. An electron and a positron constitute the common initial state for the reactions investigated here. They are accelerated to high energy and towards each other by large particle accelerators. If electron and positron approach each other sufficiently close, they annihilate into an intermediate state, which itself decays into at least one particle and one anti-particle. In a large fraction of the cases, these other particles are quarks. These interact in such a strong fashion that they have never been observed as isolated particles so far, but instead use up a certain amount of their energy to tear out additional quark anti-quark pairs from the vacuum. The quarks then combine almost immediately to form hadrons. The hadron properties, above all its mass and lifetime, are defined not only by the type of quarks inside it, but also by the relative angular momentum and average distance of the quarks. These hadrons, or their decay products, can then be observed in a particle detector.

Many details beyond the very rough and qualitative picture given above are still far from being understood quantitatively. An overview of the status of physical theory of the evolution of an e^+e^- reaction ("event") to hadrons is given in Chapter 2. The experimental setup used for the measurements presented in this thesis is outlined in the subsequent chapter. Chapter 4 contains an investigation of the hadronisation process of b quarks — the process during which primary quarks form hadrons. The b ("bottom", "beauty") quark is the most interesting quark for such a study, because it can be identified easily due to its long lifetime and large mass, which also leads to specific properties of the b quark hadronisation. The measurement presented here is the most precise result on this topic at the time of completion of this thesis.

Chapter 5 deals with the composition of hadrons created either directly in the hadronisation process, or later during the decay of heavier hadrons. The spectrum of D mesons, which contain a c ("charm") quark and a light u ("up") or d ("down") anti-quark (or c anti-quark and u or d quark), is investigated. Two dominant production processes exist for these mesons: In events with primary charm quarks, D mesons are usually created during the hadronisation of the primary quarks. However, also events with primary b quarks contain a large amount of D mesons, because b quarks decay almost exclusively into c quarks. In both cases, a certain fraction of D mesons is created in states where quark and anti-quark have non-vanishing relative orbital angular momentum (orbital excitations), or the average relative distance of the quarks is larger than in the ground state (radial excitations). The former have been seen by several experiments already, but the reconstruction performance is poor for current generation experiments, as will be discussed in Chapter 5. The experimental results about the possible

existence of the latter turned out to be controversial; a search for a radial excitation in the D meson system is presented, the result of which differs significantly from an earlier analysis.

The interpretation of the results described in Chapters 4 and 5 suffers from limited ability to model the underlying physics in simulations or calculations. Another limiting factor is the performance of the particle detector, whose finite resolution smears out the measured quantities. The analysis of the D meson spectrum is furthermore limited by the insufficient number of reactions made available by the LEP particle accelerator. The thesis does therefore proceed with a look into next generation accelerator and detector technology. After a short description of the proposed linear e^+e^- accelerator TESLA and a suggested experimental apparatus, Chapter 7 describes the efforts that have been made to evaluate the performance of charged particle track reconstruction in the proposed device. Detailed simulations and realistic reconstruction algorithms are used to provide estimates of the expected performance. Because the technical quality of the reconstruction is in itself not very demonstrative, important parts of the analyses from Chapters 4 and 5 are applied to simulated TESLA data in Chapter 8.

The main motivation of the analysis part of this thesis is to add to the experimental results available to constrain phenomenological models and approximations for QCD-dominated processes. This includes both perturbative QCD, mainly the question to what extent it is applicable in the D meson system, and non-perturbative QCD, which is necessary to describe hadronisation of quarks. However, the investigation of b quark hadronisation is driven also by the prospect to improve many other heavy quark related analyses, a large fraction of which suffers from limited knowledge of the b hadron energy spectrum as important systematic uncertainty. It cannot be anticipated today what theoretical progress will be made in light of the current experimental precision, but in any case it is clear that there are many open questions remaining which can only be studied experimentally at higher energies and/or higher event rates, and this justifies detailed studies of scenarios for the near future, like the simulation studies for the TESLA linear collider project, which are presented in this thesis.

Chapter 2

Theoretical Foundations

This chapter starts with a brief overview on the Standard Model of particle physics. First the currently known elementary particles are introduced, as well as the interactions observed among them. Special emphasis will then be given to the description of the fundamental strong interaction. The basic concepts of quantum chromodynamics (QCD) are developed, including illustrative comparisons with quantum electrodynamics (QED) as a simpler field theory. Topics of direct relation to the analyses presented in this thesis will constitute the following sections. These include a short discussion of e^+e^- annihilation reactions, and the aspects of the strong interaction that govern the transition of quarks into hadrons and the mass spectrum of hadrons created during this process. The chapter will close with a review of current ideas why physics beyond the Standard Model is expected, and how it might look like. Although this chapter is intended to deal with the theoretical foundation of the work presented in this thesis, a few important experimental results will be mentioned to illustrate recent developments.

2.1 A Brief History of Particles

The concept of elementary particles was introduced in ancient Greek philosophy by Leucippos and Democritos about 2400 years ago, who assumed that matter is not infinitely divisible, but that there is a smallest, indivisible part ("atomos"). This concept remained philosophical, until in the 19th century first experimental results on atoms were brought forward by Clausius, Maxwell, and Boltzmann, who were able to estimate the size of an atom. However, atoms remained "atomos" until 1910, when Rutherford showed in scattering experiments of helium nuclei on gold foils that almost the complete mass of an atom is concentrated in a tiny positively charged nucleus at the centre of it, with the remaining volume being almost empty, but negatively charged. Not much later, protons and later also neutrons were identified as constituents of the nucleus ("nucleons"), and electrons, which had already been discovered as particles in 1897 by Thomson, were found to form the shell. With the experimental techniques developed alongside the discoveries in the evolving nuclear physics, many additional particles were found in cosmic rays, and later in accelerator experiments. It was quickly realized that some of the newly discovered particles were to be classified as anti-particles to known particles, i.e. particles which have identical mass, but opposite charge (and all other additive quantum numbers to be discovered later of opposite sign). However, still an ever growing number of seemingly independent particle species was collected, loosely classified as leptons ("light"), and hadrons, which again were subdivided into baryons ("heavy") and mesons ("intermediate" mass).

Our current idea of elementary particles began to show up in 1964, when Gell-Mann and

Zweig were able to classify hadrons into symmetry groups which represent all possible combinations of two or three constituent particles [1]. This was initially seen as a mathematical concept, not as a next step in substructure, but deep inelastic scattering experiments of electrons with nucleons soon convinced physicists that hadrons were indeed composite. Measurements of the intrinsic angular momentum of the constituents, or spin, of 1/2, identified them as the "quarks" proposed by Gell-Mann and Zweig. Three quarks, u ("up") d ("down"), and s ("strange") were sufficient to describe the complete spectrum of hadrons known at that time. During later accelerator-based experiments, additional quarks (also called quark flavours), c ("charm") and b ("bottom" or "beauty"), were identified. The latest addition is the t ("top") quark, discovered 1995 by the CDF and D0 experiments at the Fermi National Accelerator Laboratory close to Chicago, US. Mesons are explained in this model as consisting of one quark and one anti-quark. Baryons are identified as states with three quarks or three anti-quarks.

The number of different lepton species is smaller than the number of hadrons, and in fact no evidence for a lepton structure has been found so far. Three charged leptons have been known for decades: The electron, muon (discovered in cosmic rays, and originally falsely identified as meson), and tau. Each charged lepton has a neutral counterpart, the neutrino, which is very difficult to investigate because it interacts only very weakly with matter. Even the experimental verification that there are three different species was very difficult. The existence of a light neutral particle was postulated by Pauli in 1931 to fix a seeming energy and momentum non-conservation in radioactive β-decays. A suitable theory, along with the name "neutrino", was then contributed by Fermi. The partner neutrinos for electrons (ν_{e}) and muons (ν_μ) were found around 1960; different reactions of the respective neutrino species with matter lead to the conclusion that these were indeed different particles. No direct evidence for a third neutrino (ν_τ) was obtained until the year 2000, when the DONUT experiment at the Fermi National Accelerator Laboratory was able to prove its existence.

Neutrinos are much lighter than all other elementary particles; until recently, it was generally assumed that their mass is zero. This has changed. Strong indirect evidence for non-zero neutrino masses has come from the Super-Kamiokande experiment in Japan and the SNO experiment in Canada, where oscillations between different neutrino types have been verified to a large degree of certainty. These oscillations can only occur for neutrinos with finite mass. Unfortunately, direct neutrino mass measurements have not yet achieved the necessary resolution to resolve small enough masses, and the results from oscillation measurements can only be expressed in terms of mass differences, not absolute masses.

2.2 The Standard Model of Particle Physics

A complete list of elementary particles according to current knowledge is shown in Table 2.1. All particles have a spin of 1/2. According to quantum mechanics particles with half-integer spin have common specific properties, and therefore these particles are called fermions.

At low energy scales, the mutual interaction of fermions can be described by four different forces. In decreasing order of strength, these are the strong interaction, the electro-magnetic interaction, the weak interaction, and gravity. Gravity is too weak to be studied on length scales of elementary particles with current precision. It is described well at large scales by General Relativity, but this theory is expected to break down at small distances. Attempts to find a quantised description of gravity have not been successful so far; possibly the most promising ansatz is lurking behind the horizon of string/brane theory. The weak and electro-magnetic interaction have been identified as low-energy representations of a single, the electroweak, in-

quarks				leptons			
charge $+\frac{2}{3}$		charge $-\frac{1}{3}$		charge -1		charge 0	
u	1.5..5 MeV/c^2	d	3..9 MeV/c^2	e^-	0.511 MeV/c^2	ν_e	0..3 eV/c^2
c	1.15..1.35 GeV/c^2	s	60..170 MeV/c^2	μ^-	106 MeV/c^2	ν_μ	0..0.19 MeV/c^2
t	174.3 ± 5.1 GeV/c^2	b	4.0..4.4 GeV/c^2	τ^-	1.78 GeV/c^2	ν_τ	0..18.2 MeV/c^2

Table 2.1: *Overview of elementary fermions (spin 1/2) and their masses [2]. Antiparticles are not shown; they have same mass and spin, but opposite charge. Most significant difference between quarks and leptons is that the former interact strongly, the latter do not. The strong interaction of quarks leads to their confinement in hadrons. Quark masses can therefore not be measured directly, but have to be estimated from their influence on hadron masses. The values quoted in the table are renormalised masses according to the so-called $\overline{MS}$ scheme. Especially the masses of light quarks can thus only be determined with a large uncertainty. Neutrino masses have not yet been measured, but indirect evidence for non-vanishing masses exists.*

interaction	exchange boson	spin	mass
strong	8 gluons (g)	1	0
electromagnetic	γ	1	0
weak	$W^\pm$	1	80.4 GeV/c^2
	Z	1	91.2 GeV/c^2
gravity	graviton?	2	0

Table 2.2: *Overview of elementary bosons with spin and masses [2]. No quantum theory of gravity exists yet, and the respective exchange particle is hypothetical. All other bosons are well established.*

teraction. Both electroweak and strong force are described by renormalisable, gauge-invariant quantum field theories, which constitute today's Standard Model of Particle Physics.

In the picture of quantum field theories, forces are mediated by the exchange of field quanta. These field quanta have integer spin, and do thus belong to the quantum mechanical class of bosons. Table 2.2 provides a list of these so-called gauge bosons. Massless bosons correspond to infinite range of the force, i.e. the field strength decreases with $1/r^2$. The massive exchange bosons of the weak interaction lead to an exponentially falling field strength and thus the limited range of the weak interaction. The strong interaction does not appear on large scales despite its massless gauge bosons due to the fact that all particles carrying "color", the charge of the strong interaction, are confined to color-neutral hadrons. The strong force is therefore shielded at distance scales of the order of a nucleon radius. The following subsections will outline the specific properties of the quantum field theories comprising the Standard Model, and the mentioned properties will be discussed in detail. A more complete overview over the formalism of the Standard Model is given in Ref. [3].

2.2.1 Abelian Gauge Theories

In quantum theory, a particle is represented by a complex wave function ψ, whose squared absolute value[1] $\overline{\psi}\psi$ is interpreted as probability density of the wave function to manifest as a particle in a certain region in spacetime. The phase of ψ is not observable, and thus one requires that Physics be independent of the choice of this phase. The Lagrangian of a free fermion is[2]

$$\mathcal{L} = \overline{\psi}(i\gamma^\mu\partial_\mu - m)\psi = \overline{\psi}(i\not{\partial} - m)\psi \tag{2.1}$$

In this formula, m is the mass of the fermion, ∂_μ is a derivative operator, and γ^μ are the Dirac matrices. A global phase shift ϕ_0 corresponds to a multiplication of ψ with $e^{i\phi_0}$, which cancels in the calculation of $\mathcal{L}$. But the Lagrangian is not invariant under the more general case of phases shifted differently in different space-time points, $\psi' = e^{i\phi(x)}\psi$:

$$\begin{aligned} \mathcal{L}' &= \overline{\psi'}(i\not{\partial} - m)\psi' = \overline{\psi}(i\not{\partial} - m)\psi + \overline{\psi}i\gamma^\mu(i\partial_\mu\phi(x))\psi = \overline{\psi}(i\not{\partial} - m)\psi - \overline{\psi}(\not{\partial}\phi(x))\psi \quad (2.2)\\ &\neq \mathcal{L} \end{aligned}$$

However, if there is a field with vector potential A_μ, a *local gauge transformation* of A_μ can be applied simultaneously. In analogy to the wave function, the vector potential itself is not an observable, and the field strength tensor $F_{\mu\nu} = \partial_\mu A_\nu - \partial_\nu A_\mu$ does not change if the derivative of any scalar $\phi(x)$ is added to A. In the presence of a vector field, the derivative ∂_μ has to be replaced by the covariant derivative $D_\mu = \partial_\mu - iqA_\mu$, where q is the particle's charge with respect to the vector field. With simultaneous transformation of $\psi' = e^{i\phi(x)}\psi$ and $A'_\mu = A_\mu + \frac{1}{q}\partial_\mu\phi(x)$, the Lagrangian thus results to

$$\begin{aligned} \mathcal{L}' &= \overline{\psi'}(i\not{D}' - m)\psi' && (2.3)\\ &= \overline{\psi'}(i\not{\partial} - m)\psi' + q\overline{\psi'}\not{A}'(x)\psi' && (2.4)\\ &= \overline{\psi}(i\not{\partial} - m)\psi - \overline{\psi}(\not{\partial}\phi(x))\psi + q\overline{\psi'}\not{A}'(x)\psi' && (2.5)\\ &= \overline{\psi}(i\not{\partial} - m)\psi - \overline{\psi}(\not{\partial}\phi(x))\psi + q\overline{\psi'}\not{A}(x)\psi' + \overline{\psi'}(\not{\partial}\phi(x))\psi' && (2.6)\\ &= \overline{\psi}(i\not{\partial} - m)\psi - \overline{\psi}(\not{\partial}\phi(x))\psi + q\overline{\psi}\not{A}(x)\psi + \overline{\psi}(\not{\partial}\phi(x))\psi && (2.7)\\ &= \overline{\psi}(i\not{\partial} - m)\psi + q\overline{\psi}\not{A}(x)\psi && (2.8)\\ &= \overline{\psi}(i\not{D} - m)\psi && (2.9)\\ &= \mathcal{L} && (2.10) \end{aligned}$$

If more than one local phase transformation of the kind $\psi' = e^{i\phi(x)}\psi$ is applied, the transformations commute because of the scalar character of $\phi(x)$. This makes the description of a field with the properties described above an Abelian gauge theory. The infinite set of $e^{i\phi(x)}$ transformations forms the unitary symmetry group U(1). The formalism described in this subsection applies to the electro-magnetic field; it provides the basis of quantum electrodynamics (QED).

2.2.2 Non-Abelian Gauge Theories

Abelian gauge theories feature an invariant Lagrangian under transformations of the form $e^{i\phi(x)}$, as shown in the last subsection. Invariance of the Lagrangian can be achieved for more general transformations [4], although at the cost of losing the Abelian nature of the theory.

---

[1] $\overline{\psi}$ is the complex conjugate of ψ.

[2] Here the Einstein sum convention is used.

The transformation of a wave function $\psi' = U(x)\psi$ with a unitary matrix $U(x)$, $U^\dagger U = 1$, leads to a Lagrangian of

$$\mathcal{L} = \overline{\psi'}(i\partial\!\!\!/ - m)\psi' = \psi U^\dagger(i\partial\!\!\!/ - m)U\psi = \psi(i\partial\!\!\!/ - m)\psi + i\psi U^\dagger(\partial\!\!\!/ U)\psi \ , \tag{2.11}$$

which again is different from the Lagrangian before the transformation. This can again be resolved by a local gauge transformation of a vector field B. In a similar way as in the Abelian case, ∂_μ is replaced by the covariant derivative $D_\mu = \partial_\mu - igB_\mu(x)$, with g being the charge ($\approx$ coupling constant) of the particle with respect to the vector field B. A gauge transformation of B_μ to $B'_\mu = UB_\mu U^\dagger - \frac{i}{g}(\partial_\mu U)U^\dagger$ will then lead to an invariant Lagrangian:

$$\begin{aligned}
\mathcal{L}' &= \overline{\psi'}(iD\!\!\!/' - m)\psi' && (2.12)\\
&= \overline{\psi'}(i\partial\!\!\!/ - m)\psi' + g\overline{\psi'}B\!\!\!/'(x)\psi' && (2.13)\\
&= \overline{\psi}(i\partial\!\!\!/ - m)\psi + i\overline{\psi}U^\dagger(\partial\!\!\!/ U)\psi + g\overline{\psi'}B\!\!\!/'(x)\psi' && (2.14)\\
&= \overline{\psi}(i\partial\!\!\!/ - m)\psi + i\overline{\psi}U^\dagger(\partial\!\!\!/ U)\psi + g\overline{\psi}B\!\!\!/(x)\psi - i\overline{\psi}U^\dagger(\partial\!\!\!/ U)\psi && (2.15)\\
&= \overline{\psi}(i\partial\!\!\!/ - m)\psi + g\overline{\psi}B\!\!\!/(x)\psi && (2.16)\\
&= \overline{\psi}(iD\!\!\!/ - m)\psi && (2.17)\\
&= \mathcal{L} && (2.18)
\end{aligned}$$

A major property of non-Abelian gauge theories, which in fact is the main reason why the analyses presented in this thesis had to be performed, is the self-interaction of the field quanta. The field strength tensor $F_{\mu\nu}$ can be calculated from

$$\begin{aligned}
-igF_{\mu\nu} &= [D_\mu, D_\nu] && (2.19)\\
&= (\partial_\mu - igB_\mu)(\partial_\nu - igB_\nu) - (\partial_\nu - igB_\nu)(\partial_\mu - igB_\mu) && (2.20)\\
&= +\partial_\mu\partial_\nu - ig\partial_\mu B_\nu - igB_\mu\partial_\nu - g^2 B_\mu B_\nu \\
&\quad -\partial_\nu\partial_\mu + ig\partial_\nu B_\mu + igB_\nu\partial_\mu + g^2 B_\nu B_\mu && (2.21)\\
&= +\partial_\mu\partial_\nu - ig(\partial_\mu B_\nu) - igB_\nu\partial_\mu - igB_\mu\partial_\nu - g^2 B_\mu B_\nu \\
&\quad -\partial_\mu\partial_\nu + ig(\partial_\nu B_\mu) + igB_\mu\partial_\nu + igB_\nu\partial_\mu + g^2 B_\nu B_\mu && (2.22)\\
&= -ig\left((\partial_\mu B_\nu) - (\partial_\nu B_\mu) - ig\left[B_\mu, B_\nu\right]\right) && (2.23)\\
\Longleftrightarrow \quad F_{\mu\nu} &= (\partial_\mu B_\nu) - (\partial_\nu B_\mu) - ig\left[B_\mu, B_\nu\right] \ , && (2.24)
\end{aligned}$$

which reduces to the term given in Subsection 2.2.1 only if B_μ and B_ν commute. The kinetic term in the Lagrangian,

$$\begin{aligned}
\mathcal{L}_{kin} &= -\frac{1}{4}F_{\mu\nu}F^{\mu\nu} && (2.25)\\
&= -\frac{1}{4}\left((\partial_\mu B_\nu) - (\partial_\nu B_\mu) - ig\left[B_\mu, B_\nu\right]\right)\left((\partial^\mu B^\nu) - (\partial^\nu B^\mu) - ig\left[B^\mu, B^\nu\right]\right) \ , && (2.26)
\end{aligned}$$

will therefore include terms in third and fourth order of B arising from the non-zero commutators. These terms correspond to three- and four-particle vertices with only gauge bosons attached, as shown in Figure 2.1.

The electroweak theory is based on a SU(2)×U(1)-based non-Abelian gauge theory, resulting in WWZ/WWγ (triple gauge couplings), WWZZ/WW$\gamma\gamma$, and WWWW (quartic gauge couplings) vertices. Figure 2.2 shows the impressive experimental result achieved at LEP in favour of the non-Abelian character of the electroweak gauge theory. In the case of quantum

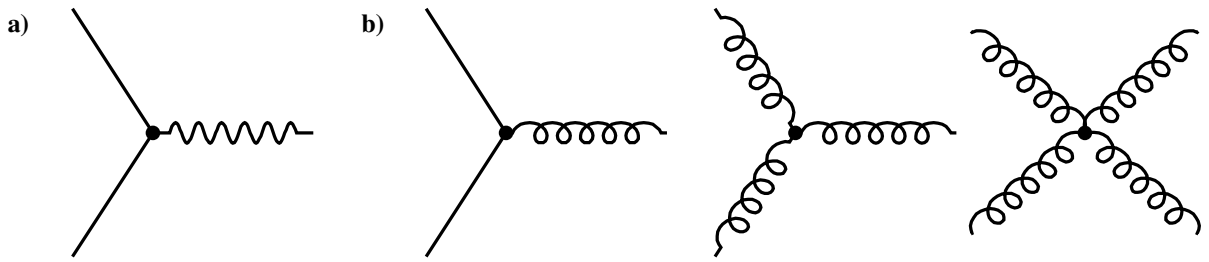

Figure 2.1: *Possible vertices a) in an Abelian gauge theory, and b) in a non-Abelian gauge theory.*

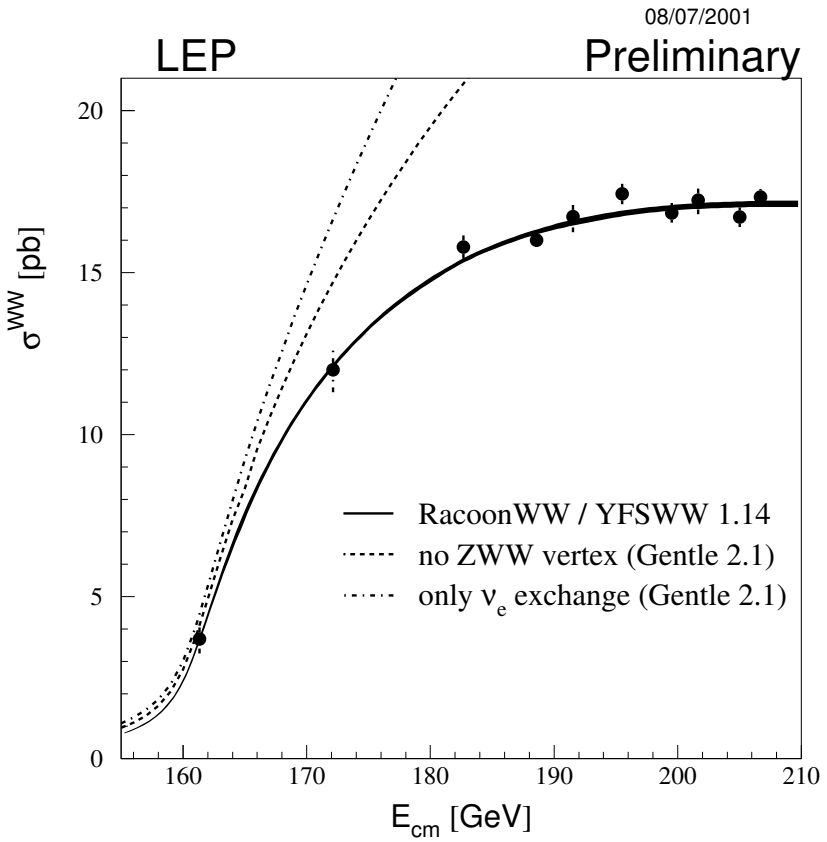

Figure 2.2: *Dependence of cross-section of* W *pair production on the centre-of-mass energy [5]. The self-interaction of the field quanta as predicted by the electroweak non-Abelian gauge theory is in excellent agreement with data, whereas models without self-interaction are clearly excluded.*

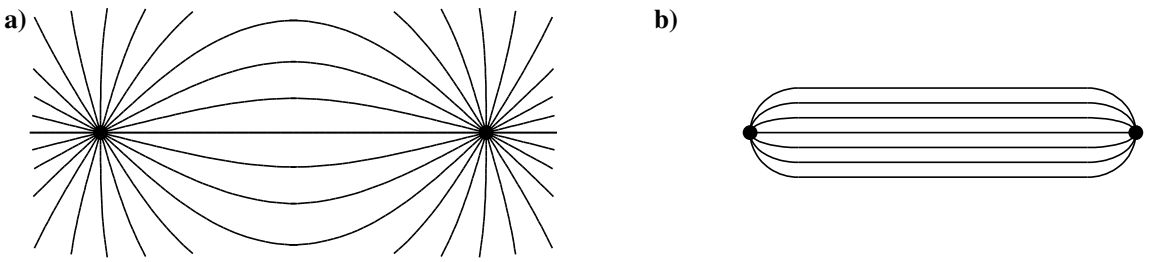

Figure 2.3: *a) Dipole field lines in an Abelian gauge theory with massless field quanta. The field strength of a charge decreases with $1/r^2$. Increasing the distance between two attractive (e.g. electric) charges leads to a decrease of the force exerted mutually on them; the potential energy approaches a finite value which represents the energy necessary to separate the two charges. b) Dipole field lines in QCD. Due to the self-interaction of the field lines, the force between the (colour) charges remains constant for large separation distances of the two charges. Therefore the potential energy in the field rises linearly with the distance, and a separation of the charges would require an infinite amount of energy. This effect is known as confinement.*

chromodynamics (based on a SU(3) gauge symmetry group), the self-interaction of gluons effectively leads to attractive interaction between the field lines spanned between two colour sources, e.g. quark and anti-quark (see Figure 2.3). The force along this "colour flux tube" between the quarks increases approximately linearly with the distance of the quarks. To separate the quarks would therefore require an infinite amount of energy. If the energy stored in the colour flux tube is larger than the mass of a quark pair, it is energetically more favourable to break the flux tube by creation of an intermediate quark anti-quark pair. This way, quarks are always confined to colourless objects. It should be noted that the relation between gluon self-interaction and confinement has not yet been proven mathematically. However, this picture provides a rough qualitative description of what happens during the hadronisation of quarks into jets, which will be discussed later in this chapter.

2.2.3 Renormalisability

An important requirement imposed on quantum field theories for the description of physical phenomena is that all observable quantities should remain finite at all energies and at all orders of the coupling constant. In practice, physical observables like charge and mass of interacting fermions are expressed as perturbation series in powers of the coupling constant, α_s in the case of QCD. It turns out that calculations to finite order diverge, because integrals over all possible momenta of virtual particles in internal loops like the ones shown in Figure 2.4 are generally not finite, unless the momentum integral is cut off at an arbitrary energy scale μ. As a simple example [6], the contribution of higher order can be parametrised depending on an energy scale Q^2 as

$$R_n = \sum_n a_n \left(\ln \frac{Q^2}{\mu^2} \right)^n , \tag{2.27}$$

which grows to infinity if calculated in finite order and $Q^2 \to \infty$. However, the full expansion is not necessarily infinite; in fact, if it were infinite, this would be a serious flaw in the theory. Taking for example $a_n = (-1)^n$, the sum of all orders in 2.27 is

$$R_\infty = \sum_{n=0}^{\infty} a_n \left(\ln \frac{Q^2}{\mu^2} \right)^n = \frac{1}{1 + \ln \frac{Q^2}{\mu^2}} , \tag{2.28}$$

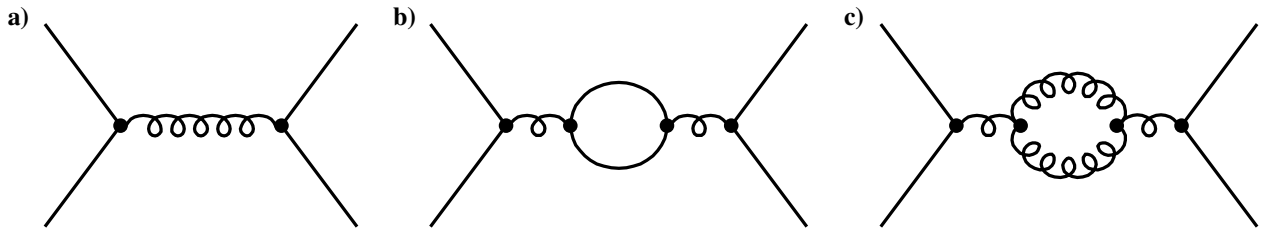

Figure 2.4: *a) Lowest order boson exchange diagram. b) Boson exchange with loop of virtual fermions. c) Boson exchange graph with loop of virtual bosons (non-Abelian gauge theories only).*

which remains finite even with $Q^2 \to \infty$.

All interactions described by the Standard Model can be freed from these divergences in finite order calculations by renormalisation. This renormalisation includes the cutoff of loop diagrams at μ, the replacement of the true, or "bare" coupling constant by an effective coupling, and the multiplication of the external fermion and boson wave functions with a new normalisation factor. This corresponds to incorporating part of the loop effects into the coupling constant, and removing the respective loops from the calculation. Renormalisation thus leads to a different perturbative description of observables, which avoids running into divergences in calculations of finite order.

Renormalisation introduces a formal dependence of renormalised observables $R(Q^2, \alpha)$ on the renormalisation scale μ. However, since the choice of μ is arbitrary, any dependence of the power expansion terms on μ must be cancelled by a corresponding dependence of the effective coupling constant on μ. For dimensional reasons, it must be possible to express the dependence of the observable on μ instead by a dependence on Q^2/μ^2. Then the requirement that the observable R must not depend on the arbitrarily chosen parameter μ translates into [7]

$$\mu^2 \frac{\mathrm{d}}{\mathrm{d}\mu^2} R(Q^2/\mu^2, \alpha(\mu^2)) = \left(\mu^2 \frac{\partial}{\partial \mu^2} + \mu^2 \frac{\partial \alpha}{\partial \mu^2} \frac{\partial}{\partial \alpha} \right) R = 0 \ . \tag{2.29}$$

The dependence of the effective coupling on the arbitrary energy scale μ is most naturally understood if μ^2 is chosen to be $\mu^2 = Q^2$. In this case, α depends directly and exclusively on the energy scale of the respective process:

$$Q^2 \frac{\partial \alpha(Q^2)}{\partial Q^2} =: \beta(\alpha(Q^2)) \tag{2.30}$$

The β function can be calculated in a perturbative expansion including higher order loop corrections. In the case of QCD (coupling constant α_s), calculations up to four-loop level have been performed [8], but for the following discussion the one-loop term will be used for simplicity. The energy dependence of the electro-magnetic coupling constant α_{EM} is much weaker, and α_{EM} is much smaller, and thus it will also only be given to one-loop order [9]:

$$\beta_{QCD}(\alpha_s(Q^2)) \approx \frac{2N_{flav} - 33}{12\pi} \alpha_s^2(Q^2) \tag{2.31}$$

$$\beta_{QED}(\alpha_{EM}(Q^2)) \approx \frac{4N_{chferm}}{12\pi} \alpha_{EM}^2(Q^2) \tag{2.32}$$

In the above formula for β_{QCD}, N_{flav} is the number of active quark flavours contributing to loops at the energy scale Q^2. Similarly, N_{chferm} is the number of contributing charged fermions

in QED loops. It is obvious that both expressions share a common term[3] associated with fermion loops, as shown in Figure 2.4b. The second term in β_{QCD} is related to gluon loops as in Figure 2.4c. This term is specific to non-Abelian gauge-invariant quantum field theories [10] and has very important consequences for the phenomenology of QCD. The fermionic loop term of the β function is always positive. Because the β function is the energy derivative of the coupling constant, the coupling constant necessarily increases with increasing energy if only fermion loops exist, like in QED. In QCD, the behaviour of the coupling constant depends on the relative size of the fermionic and bosonic terms, which have opposite sign. There is good reason to believe that even at large energies only six quark flavours occur in loops. The consequence of $N_{flav} \leq 6$ is $\beta_{QCD}(\alpha_s(Q^2)) < 0$, and thus the coupling constant of the strong interaction *decreases* with increasing energy.

The fermionic and bosonic terms of the β function can be exemplified in a simple picture: The creation of virtual particle loops corresponds to vacuum polarisation; pairs of temporary charged particle pairs screen the charge to be probed. This weakens the interaction, unless an experiment is performed at increasingly high energy, i.e. increasingly small distance. Approaching closer to the central charge, the screening gets weaker, and the interaction strengthens. On the other hand, boson loops in QCD dilute the colour charge of the central quark in space. This effect becomes more important as the probe distance to the central quark becomes of the order of the spatial extension of the colour charge dilution. Therefore this effect weakens the interaction with increasing energy. In the case of QCD, the latter effect dominates over the screening.

So far only statements about the derivative of $\alpha_s(Q^2)$ have been made. The functional form of the energy dependence of α_s in one-loop approximation can be calculated from the integral of Equations 2.30 and 2.31:

$$Q^2 \frac{\partial \alpha_s(Q^2)}{\partial Q^2} = \beta(\alpha_s(Q^2)) \approx \frac{2N_{flav} - 33}{12\pi} \alpha_s^2(Q^2) \tag{2.33}$$

This integral is solved by substituting $f(Q^2) = 1/\alpha_s(Q^2)$ with $\partial f / \partial \alpha_s = -1/f^2$. This gives

$$-\frac{1}{f^2(Q^2)} \frac{\partial f(Q^2)}{\partial Q^2} = \frac{2N_{flav} - 33}{12\pi} \frac{1}{Q^2} \frac{1}{f^2(Q^2)} \tag{2.34}$$

$$\iff \frac{\partial f(Q^2)}{\partial Q^2} = \frac{33 - 2N_{flav}}{12\pi} \frac{1}{Q^2} \tag{2.35}$$

$$\iff f(Q^2) - f(Q_0^2) = \frac{33 - 2N_{flav}}{12\pi} \left(\ln Q^2 - \ln Q_0^2 \right) \tag{2.36}$$

$$\iff f(Q^2) = f(Q_0^2) + \frac{33 - 2N_{flav}}{12\pi} \ln \frac{Q^2}{Q_0^2} \tag{2.37}$$

$$\iff \alpha_s(Q^2) = \frac{1}{1/\alpha_s(Q_0^2) + \frac{33-2N_{flav}}{12\pi} \ln \frac{Q^2}{Q_0^2}} \tag{2.38}$$

$$\iff \alpha_s(Q^2) = \frac{\alpha_s(Q_0^2)}{1 + \frac{33-2N_{flav}}{12\pi} \alpha_s(Q_0^2) \ln \frac{Q^2}{Q_0^2}} \, . \tag{2.39}$$

In these equations, Q_0^2 plays the role of an integration constant. QCD does therefore only predict the evolution of the coupling constant relative to the coupling at a fixed energy scale Q_0^2. This behaviour is clearly confirmed by experimental data (Figure 2.5).

[3]The factor of two difference between the fermionic terms arises from different trace normalisation of the

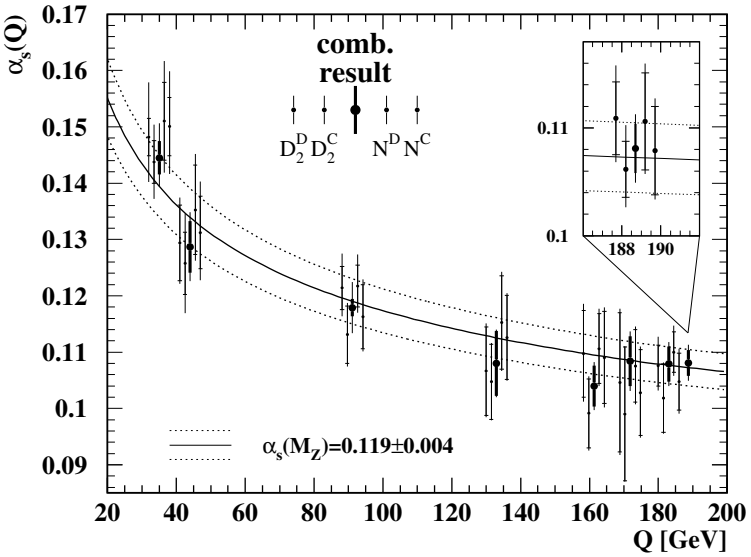

Figure 2.5: *Dependence of the strong coupling constant α_s on the centre-of-mass energy; the data shown in this plot are from the JADE and OPAL experiments [11]. Small points represent evaluations of α_s using different observables; large points with bold error bars are the combined values. The solid and dotted lines show the predicted evolution of α_s as obtained from a three-loop β function normalised to $\alpha_s(m_Z) = 0.119 \pm 0.004$.*

2.2.4 Perturbative and Non-Perturbative QCD

The renormalised (effective) QCD coupling constant $\alpha_s(Q^2)$ depends strongly on the energy scale. For values of N_{flav} as observed experimentally, it approaches zero for infinite momentum transfers. This leads to so-called "asymptotic freedom" at large energy scales, where the mutual QCD interaction of quarks can be neglected. This is approximately the case within hadrons, where quarks behave almost like free particles when probed by scattering with large momentum transfer. Furthermore, due to the comparatively small value of $\alpha_s(Q^2)$ at large Q^2, elementary processes can be calculated to a good approximation (≈10% precision) using the first few terms of a perturbative expansion of an observable R in powers of α_s.

For small Q^2, α_s increases strongly. A choice of the parameters $\alpha_s(m_Z)$ and N_{flav} as seen in current experiments leads to the prediction that α_s grows larger than 1 in the region 100 MeV to 1 GeV and diverges at even lower energies. At this scale the usual perturbative approach does not lead to useful approximations. The transition from perturbative to non-perturbative regime is usually emphasised in the functional form of $\alpha_s(Q^2)$ by replacing the arbitrary energy scale Q_0^2 by a scale Λ_{QCD}, where Λ_{QCD} is defined by

$$\Lambda_{QCD}^2 = \frac{Q_0^2}{e^{1/(\beta_0 \alpha_s(Q_0^2))}} \ , \quad \beta_0 = \frac{33 - 2N_{flav}}{12\pi} \ , \tag{2.40}$$

so that

$$\alpha_s(Q^2) = \frac{1}{\beta_0 \ln\left(Q^2/\Lambda_{QCD}^2\right)} \ . \tag{2.41}$$

This parametrisation of $\alpha_s(Q^2)$ is independent of any renormalisation scale; however, also the bare coupling has been removed. One can regard the QCD scale Λ_{QCD} as new fundamental parameter of QCD, which replaces the unrenormalised couplings. The value of Λ_{QCD} has been determined experimentally to ≈ 200 MeV [2].

fundamental symmetry group representation, which is 1/2 in the case of SU(N), and 1 for U(1) [9].

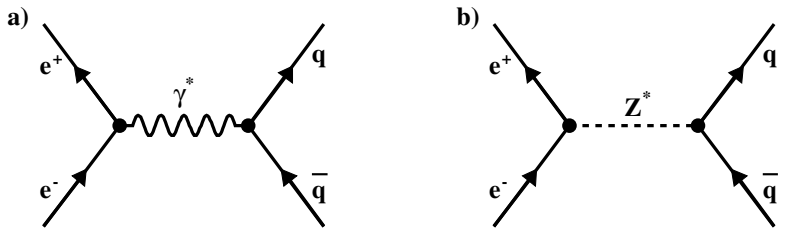

Figure 2.6: *Leading order electron positron reactions to quarks in* e^+e^- *colliding beam experiments. a) Annihilation to a virtual photon* (γ^*)*. b) Annihilation to a virtual* Z (Z*).

Processes that take place at an energy scale of or below Λ_{QCD} can not be calculated by perturbative expansion to powers of the strong coupling constant. This is the case for the transition of quarks into hadrons, discussed in Section 2.4. Predictions about properties of the hadronisation process have only been successfully made by either exploiting fundamental qualitative properties of the theory, like symmetries, or by applying phenomenological approaches not strictly related to the underlying fundamental QCD itself.

Another possibility to access the regime of large coupling constants is perturbative expansion to other small parameters of a specific problem. Section 2.5 outlines the description of mesons containing one heavy quark. In this case, an expansion is performed in the inverse mass of the heavy quark, starting from infinite mass ($1/m_{\mathrm{Q}} = 0$). QCD simplifies for infinitely heavy quarks due to additional symmetries.

A completely different, but nevertheless very successful approach to QCD in the non-perturbative regime is lattice gauge theory. If one approximates space-time as discrete, numerical evaluations of QCD processes can be performed by detailed simulation of all processes. This requires massive computing capacities which at the moment only allow calculations of processes with a small number of colour sources. Prime examples for lattice QCD calculations are semi-leptonic decays of light hadrons, mass calculations for light quarks, mass spectra of light hadrons. For a recent review see Ref. [12]. Lattice calculations of processes involving too many dynamic degrees of freedom, like the hadronisation of quarks, are far beyond the capabilities of current and mid-term future computers.

2.3 e^+e^- Colliders as QCD Laboratories

The previous sections have introduced the fundamental concepts of QCD. The following part departs temporarily from the purely theoretical discussion to describe the circumstances under which aspects of QCD are investigated in this thesis. Colliding e^+ and e^- beams provided by the LEP collider (see Chapter 3) and, in a simulation, by the TESLA collider (see Chapter 6) provide the basic experimental setup. Electron positron collisions at high energies provide an excellent laboratory for QCD studies, because the initial state is very well defined, and background is comparably low. The lowest order reactions of electrons and positrons with quarks in the final state are shown in Figure 2.6. The annihilation reaction into either a virtual photon γ^* or a virtual Z* with subsequent decay of the intermediate state into a fermion anti-fermion pair $f\overline{f}$ leads to the following total cross-section [2]:

$$\sigma(e^+e^- \to f\overline{f}) = N_c \frac{4\pi}{3} \frac{\alpha_{EM}^2}{s} \left[\underbrace{q_e^2 q_f^2}_{\gamma \text{ exchange}} + \underbrace{(v_e^2 + a_e^2)(v_f^2 + a_f^2)|\chi|^2}_{\text{Z exchange}} + \underbrace{2 q_e q_f v_e v_f Re(\chi)}_{\text{interference term}} \right] \quad (2.42)$$

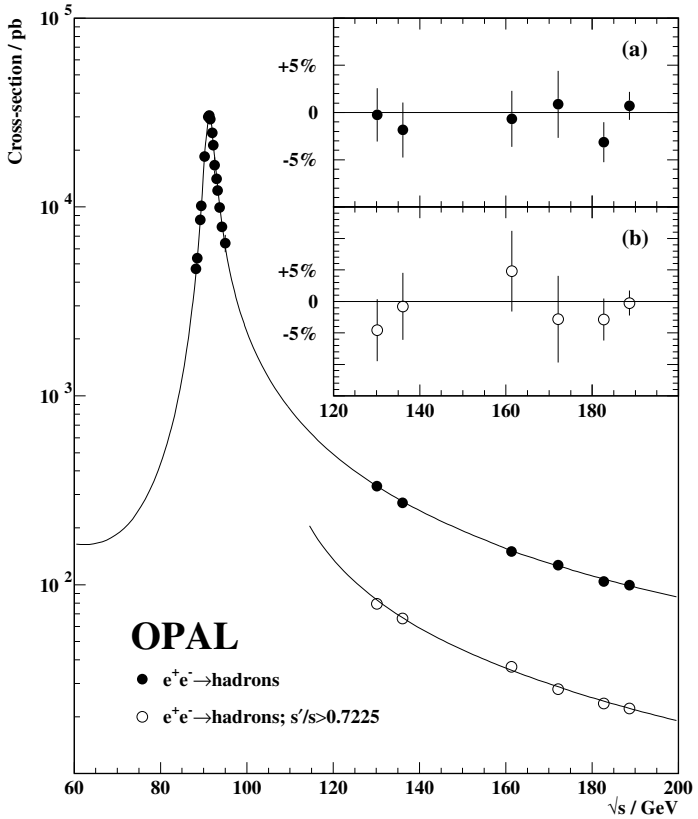

Figure 2.7: *Total hadronic cross-section in* e^+e^- *annihilation as measured by OPAL [13]. The lines indicate the matrix element prediction. The insets show the relative deviation of the high-energy cross-section measurements from the prediction. The open points represent a subset of the hadronic events, where at least a fraction of 72.25% of the centre-of-mass energy has been reconstructed in the detector. This selection removes a large fraction of events with initial state radiation.*

Here N_c is the number of different colours for the respective fermion (1 for leptons, 3 for quarks). s is the square of the centre-of-mass energy. q_e and q_f are the electric charges in units of e of electron and final state fermion, respectively. v_e and a_e (v_f and a_f) are the weak vector and axial vector couplings of the electron (final state fermion). χ is the Breit-Wigner parametrisation of the Z resonance:

$$\chi(s) = \frac{1}{4\sin^2\theta_W \cos^2\theta_W} \times \frac{s}{s - m_{\mathrm{Z}}^2 + i m_{\mathrm{Z}} \Gamma_{\mathrm{Z}}} \tag{2.43}$$

m_{Z} and Γ_{Z} are the mass and width of the Z boson, θ_W is the weak mixing angle. The sum over all quark flavours of the cross-sections of $\mathrm{q\overline{q}}$ production is called total hadronic cross-section. The energy dependence of the hadronic cross-section is depicted in Figure 2.7. At $\sqrt{s} \approx m_{\mathrm{Z}}$, the Z exchange dominates clearly over the γ exchange, with a cross-section ratio of about 1100. The interference term vanishes at m_{Z}. Therefore the cross-section shows a strong enhancement of several orders of magnitude around the Z mass, with a width of Γ_{Z}.

The symmetric shape of the Breit-Wigner-parametrisation of the Z resonance is distorted by the so-called initial state radiation: The processes shown in Figure 2.8 are suppressed by one additional order in α_{EM} with respect to the lowest-order diagrams of Figure 2.6. The effective

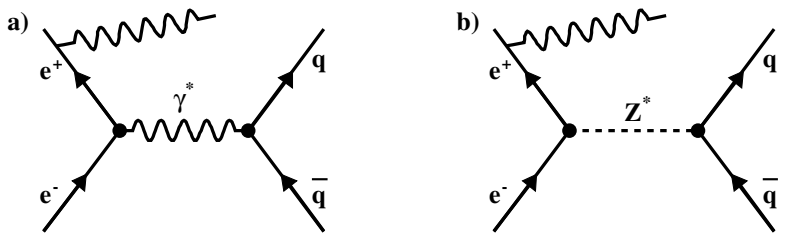

Figure 2.8: e^+e^- *annihilation reactions with a photon emitted by the initial state electron or positron. This lowers the effective centre-of-mass energy of the annihilation reaction to* Z^*/γ^* *and thus distorts the shape of the* Z *resonance.*

centre-of-mass energy of the annihilation reaction is lowered if a photon is radiated by the initial state electron or positron. Because of the strong energy dependence of the annihilation cross-section around the Z resonance, the cross-section for initial state radiation is strongly enhanced above the Z resonance, but suppressed on or just below m_Z. This has important consequences for the analysis presented in Chapter 4, which relies on a correct modelling of the correspondence of beam energy and effective centre-of-mass energy in simulated events.

The work presented in this thesis focuses around $e^+e^- \to Z/\gamma^* \to q\overline{q}$ reactions at a centre-of-mass energy of $\sqrt{s} \approx m_Z$, where the cross-section and thus the data sample is very large. The electroweak creation of $q\overline{q}$ pairs is well understood and can be modelled very precisely, due to the small ($\ll 1$) coupling constants of electroweak theory. Although of course the quarks in the final state also undergo processes of electro-magnetic and weak interaction, the next phases in the event evolution, fragmentation and hadronisation, are clearly governed by QCD. These processes will be subject to detailed discussion in the following sections.

2.4 Fragmentation and Hadronisation

Figure 2.9 summarises the different stages a hadronic e^+e^- event passes through. The first, or electroweak phase, contains the annihilation reaction itself. The emission of secondary gluons or quarks with high energy can be described perturbatively; this process is called fragmentation. Hadronisation, the transition from partons to hadrons, involves strong interaction at energy scales at or below Λ_{QCD}, where the perturbative approach is unusable, and mainly phenomenological descriptions are used. The last event phase sees the decay of the primary hadrons to stable particles. QCD plays an important role here as well by defining the hadron mass spectra and governing strong decays. Except in some special cases, these processes are also non-perturbative.

Except in the annihilation process itself, where it enters only via higher order corrections, QCD plays an important role in all phases. This section will begin with a short description of the fragmentation process of the primary quark anti-quark pair into a set of high energy partons, and will then focus on attempts to find an adequate description of the hadronisation of these partons. The idea that fragmentation and hadronisation can be treated separately is by no means trivial; it requires that the mathematical description of these two parts of the event evolution can be factorised. This is not proven, yet it turns out that the combination of separate descriptions of fragmentation and hadronisation reproduces experimental results quite well.

It has to be pointed out that the terms “fragmentation” and “hadronisation” are often

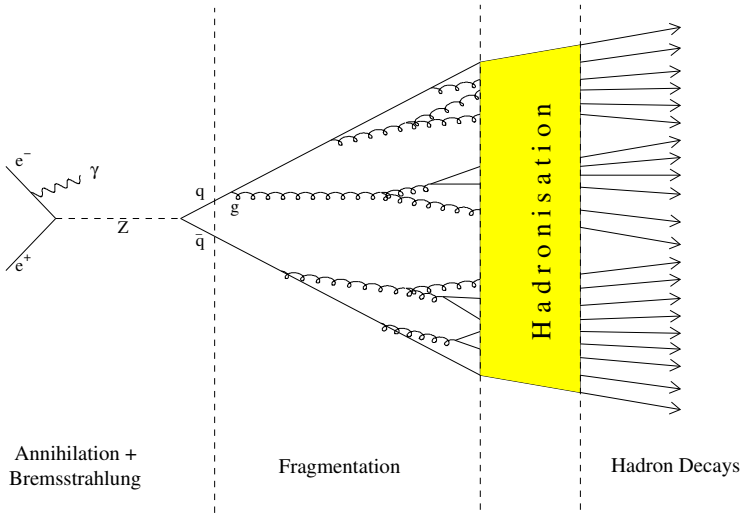

Figure 2.9: *Evolution of a hadronic* e^+e^- *annihilation event.*

commonly referred to as "fragmentation". This is e.g. reflected in the common choice of "fragmentation function" as designation for the parametrisation of the energy fraction retained by a primary quark during the *hadronisation* process. In this thesis, fragmentation and hadronisation will be distinguished; however, in order not to deviate too much from common notions, it will be made use of the slightly misleading term "fragmentation function".

2.4.1 Fragmentation

The emission of gluons of high energy can be calculated perturbatively. The lowest order cross-section for $e^+e^- \to q\overline{q}g$ for quarks with negligible mass $m_q \ll Q = \sqrt{s}$ is [14]

$$\frac{d\sigma}{dx_1 dx_2} = \sigma_0 \frac{2\alpha_s}{3\pi} \frac{x_1^2 + x_2^2}{(1-x_1)(1-x_2)} \ , \tag{2.44}$$

where x_1 and x_2 are the scaled momenta $x_i = p_i/\frac{1}{2}Q$, and σ_0 is the $e^+e^- \to q\overline{q}$ cross-section. This formula diverges for either $x_i \to 1$ $(i = 1, 2)$, and for gluons of vanishing energy. These divergences cancel in the full calculation due to corresponding divergences in the lowest order vertex and propagator correction processes. Physically a three-parton final state with $x_i \approx 1$ for at least one of the quarks is meaningless anyhow, since this corresponds to the gluon being almost collinear with one of the quarks. This final state can be described better by a two-parton final state, associating the gluon with the hadronisation process of its nearby quark. Also zero energy gluons lead to a better description as two parton final state.

The three-parton matrix element has been calculated up to two-loop level [15], and first order matrix elements are available for final states of up to 5 partons (see e.g. Ref. [16]). Monte Carlo generators exist that use QCD matrix elements to describe the fragmentation of quarks[4], but due to the limited number of partons in the final state and the limited precision due to low order α_s calculation, the ability of these generators to describe hadronic e^+e^- events at high energy is limited.

[4]The Jetset Monte Carlo generator [17] includes the option to use matrix elements for 2,3, and 4 parton events, but unless stated otherwise, Jetset will always be used as parton shower Monte Carlo for the purpose of this thesis.

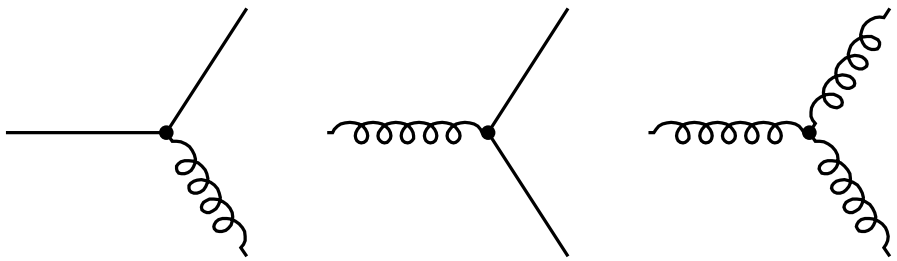

Figure 2.10: *Branching diagrams contributing to the leading logarithm approximation (LLA) of QCD. From left to right, gluon emission by a quark, gluon splitting into a* $q\overline{q}$ *pair, and gluon emission by a gluon are shown.*

A more successful description of hadronic events is achieved by parton shower approaches. Parton shower descriptions are based on a rearrangement of the usual perturbation expansion (see Equation 2.27) to

$$\sum_n a_n \left(\alpha_s \ln \frac{Q^2}{\Lambda^2_{QCD}}\right)^n + \alpha_s \sum_n b_n \left(\alpha_s \ln \frac{Q^2}{\Lambda^2_{QCD}}\right)^n + \ ... \tag{2.45}$$

The first sum dominates the asymptotic behaviour for large Q^2 if $\alpha_s(Q^2)$ is much smaller than one, and $\alpha_s(Q^2) \ln (Q^2/\Lambda^2_{QCD}) \approx 1$. The former requirement is evident from Equation 2.45; it makes sure the next-to-leading logarithm terms are sufficiently small. $\alpha_s \ll 1$ is fulfilled for sufficiently large energies, according to Equation 2.41. The second criterion is necessary to have a properly behaving perturbation series of leading logarithms. One can derive from Equation 2.41 that

$$\alpha_s(Q^2) \ln (Q^2/\Lambda^2_{QCD}) = \frac{1}{\beta_0} = \frac{12\pi}{33 - 2N_{flav}} \approx 1 \ . \tag{2.46}$$

The description of processes by only the first sum of Equation 2.45 is a good approximation under the above conditions; it is known as the leading logarithm approximation (LLA) [18]. The leading logarithm approximation corresponds to a selection of diagrams not according to the number of vertices, like a usual fixed order α_s calculation, but according to the topology of the subprocesses. Therefore it is well suited to describe e^+e^- annihilation final states with a large number of high energy partons. Gribov and Lipatov showed [18] that the leading logarithm approximation suppresses diagrams with internal loops, and that only simple branchings of one partons into two partons as in Figure 2.10 contribute leading logarithms. The combination of these branchings leads to tree-like diagrams like the one in Figure 2.11.

The LLA approach simplifies significantly the calculation and simulation of complex parton configurations. The creation of partons in this picture is viewed as succession of branching processes $q \to qg$, $g \to gg$, and $g \to q\overline{q}$, where interference between the individual branchings is neglected. This allows a simple iterative modelling of event evolution in parton shower Monte Carlo generators, where the appearance of branchings to partons of specific type and energy can be represented by classic probabilities. The branching probabilities are expected to fulfil some basic requirements. The probability should of course be proportional to $\alpha_s(Q^2)$. The remaining contributions to the branching probability should be scale-invariant, i.e. only depend on the type of the final state partons b and c in a process $a \to bc$, and on the fraction z $(1 - z)$ of the energy associated with parton b (c), $0 < z < 1$. This leads to the expression

$$Q^2 \frac{d^2\mathcal{P}_{a\to bc}}{dz dQ^2} = \frac{\alpha_s(Q^2)}{2\pi} P_{a\to bc}(z) \ . \tag{2.47}$$

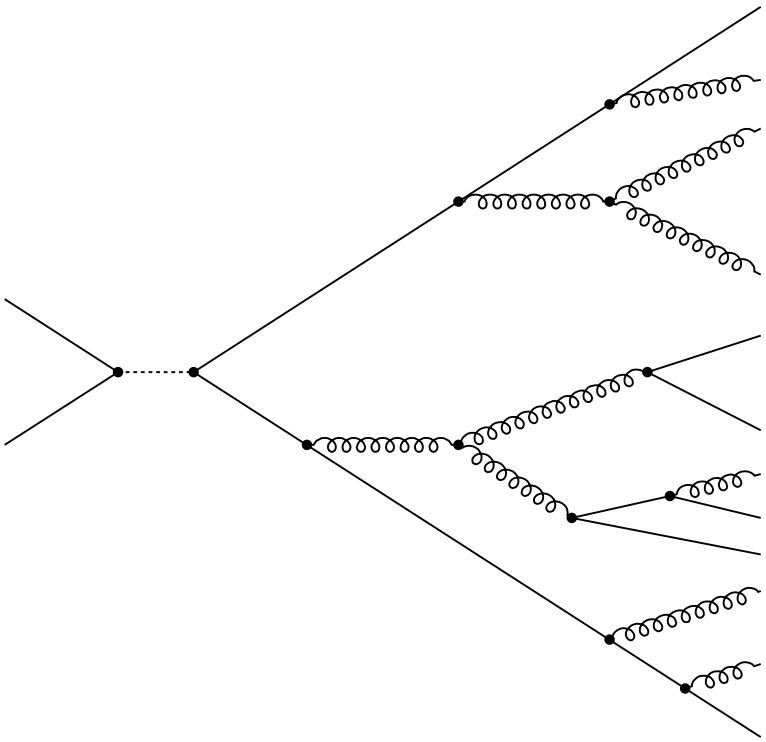

Figure 2.11: e^+e^- *annihilation event in leading logarithm approximation. A tree-like parton shower develops which is constructed exclusively of the elementary branchings in Figure 2.10.*

Here, $P_{a\to bc}(z)$ is the scale-independent parton splitting function for the process $a \to bc$. Integration of Equation 2.47 over the full z range leads to the Altarelli-Parisi type equation [19]

$$Q^2 \frac{d^2\mathcal{P}_{a\to bc}}{dQ^2} = \frac{\alpha_s(Q^2)}{2\pi} \int P_{a\to bc}(z)dz \ . \tag{2.48}$$

The resemblance of this equation to the differential equation for the running coupling constant α_s (Equation 2.30) is not accidental; the full derivation involves renormalisation group techniques.

Parton splitting functions are obtained as solutions to the above equation. The QED splitting function $P_{e\to e\gamma}(z)$ goes back to work by Weizsäcker and Williams [20]. For QCD, the so-called Altarelli-Parisi splitting kernels [19] in the spin-averaged, lowest order approximation are

$$P_{q\to qg} = \frac{4}{3}\left(\frac{1+z^2}{1-z}\right) \tag{2.49}$$

$$P_{g\to q\overline{q}} = \frac{1}{2}\left(z^2+(1-z)^2\right) \tag{2.50}$$

$$P_{g\to gg} = 6\left(\frac{1-z}{z}+\frac{z}{1-z}+z(1-z)\right) \tag{2.51}$$

As expected, the kernels for symmetric final states are invariant under exchange of z and $1-z$.

Parton shower Monte Carlo models are usually based on the probability that a given parton branches during a given decrease of the energy scale Q^2. This probability can be calculated by summing the splitting function for all possible final states and integrating over the Q^2 range in question. Splitting is then applied randomly according to these probabilities. The parton

shower model is only valid for large energy scales; once all partons have been tracked down to an energy Q_0 of the order of 1 GeV, still sufficiently larger than Λ_{QCD}, parton shower Monte Carlo generators usually stop the iterative shower evolution and proceed to non-perturbative hadronisation of the shower partons.

Parton shower models are very successful in modelling the distribution of secondary partons which are comparably soft and almost collinear to the primary partons, but their results for additional high energy partons with large transverse momentum (leading to three or more clearly disjunct jets) is not optimal. In practice, the rates and properties of events with a total of 2, 3, or 4 partons of very high energy are therefore matched to matrix element calculations for these configurations.

Further refinements to the simplest parton shower described in this section were introduced by taking interference between individual branching into account. It turned out that the impact of interference can be described easily as suppression of certain regions of phase space during branching, to the effect that the opening angle of a branching is always smaller than the one of the previous branching. This effect is taken into account in modern Monte Carlo generators like Jetset [17], Pythia [21], and Herwig [22].

2.4.2 Hadronisation Models

At an energy scale around Λ_{QCD}, the strong coupling constant $\alpha_s(Q^2)$ exceeds unity, and perturbation theory breaks down. The transition of partons to hadrons takes place at this energy scale, and therefore detailed descriptions of the hadronisation process that are based on first principles of QCD are not yet available. Three important classes of phenomenological models exist, which differ in how gluons created during fragmentation are treated, how (if at all) different partons interact during the hadronisation, and in the number, type, and momentum distribution of the created hadrons.

A common problem arising for all models is the production of baryons. The primary partons are confined to hadrons by creating additional $q\overline{q}$ pairs and combining the additionally created (anti-)quarks to mesons. The formation of baryons is a more complicated process for which currently two main scenarios exist. One approach is to create a certain amount of diquark anti-diquark pairs in the same manner as quark anti-quark pairs are created for the hadronisation procedure [23]. These can then combine with additional single quarks to form hadrons. The other approach, the so-called popcorn model [24], features a step-by-step baryon production: The creation of $q\overline{q}$ pairs with colour not matching to their neighbouring quarks keeps up a colour field in which additional $q\overline{q}$ pairs can emerge before mesons are formed. Diquark production is applicable to all hadronisation models described in the following; the popcorn model is mainly used in string models, which will be described later.

Independent Hadronisation

A simple approach to describe the creation of jets of hadrons from a primary or secondary parton created in the fragmentation process is the independent fragmentation picture [25, 26]. Although for reasons to be described later this model has mostly been removed from current Monte Carlo generators, it is well suited for a demonstration of the basic ideas about the hadronisation process.

Possible correlations between the hadronisation of the partons are neglected in this model; an independent hadronisation process is performed for each parton. An iterative procedure is applied: A $q\overline{q}$ quark pair is created in each step. One of the two new (anti-)quarks is combined

with the isolated parton to form a meson. The other (anti-)quark remains as isolated parton for the next step. Since this method does not work for gluons, these are usually split each into a $q\overline{q}$ pair before hadronisation. During each step of the hadronisation a fraction z of the light cone momentum of the isolated parton is assigned to the resulting hadron:

$$z = \frac{E_{hadron} + p_{z,hadron}}{E_{\mathrm{q}} + p_{z,\mathrm{q}}} \tag{2.52}$$

The choice of light cone variables is motivated by their Lorentz invariance, in contrast to e.g. a simple energy ratio. The remaining momentum fraction $(1-z)$ is left for further iterations. The actual fraction z assigned to the hadron is described by a probability distribution $f(z)$, which is assumed to be the same in each step. This assumption leads to important constraints on $f(z)$, due to the following argument: Be $F(z)dz$ the probability to find a hadron with momentum fraction between z and $z + dz$. The contribution to this probability from primary hadrons is directly obtained from the definition of $f(z)$ to be $f(z)dz$. A second contribution arises from the possibility that a hadron of momentum fraction z can occur as a secondary hadron created in the splitting of another hadron with larger momentum fraction $1 - \eta$, $\eta > z$. A primary hadron of momentum fraction between $1-\eta$ and $1-\eta+d\eta$ occurs with probability $f(1-\eta)d\eta$, and the probability for a hadron of momentum fraction z to appear in the remainder jet of it (which has a momentum fraction of η) is $F(z/\eta)dz/\eta$. The total probability to find a hadron with momentum fraction z is then obtained by an integration over all possible values of η, and a summation over the two contributions [26]:

$$F(z)dz = f(z)dz + \int_z^1 f(1-\eta)F(z/\eta)dzd\eta/\eta \tag{2.53}$$

$$\Longleftrightarrow \quad F(z) = f(z) + \int_z^1 f(1-\eta)F(z/\eta)d\eta/\eta \tag{2.54}$$

The most prominent assumption in this equation is scale invariance, i.e. the conjecture that the same probability distribution $f(z)$ applies for all steps of the hadronisation process, despite decreasing energy.

Both $f(z)$ and $F(z)$ are interesting functions; $F(z)$ describes the energy distribution of any hadrons created during the hadronisation process. In contrast to this, $f(z)$ describes the energy distribution only of hadrons containing the initial parton. Independent of specific models, both $f(z)$ and $F(z)$ are called fragmentation functions. It is interesting to note in this context that in Equation 2.54, $F(z) \approx f(z)$ for large z, or, in physical terms, if a hadron is found with very large z, it is most likely the one containing the initial parton. Since experimental observations indicate that only light quarks are created as secondary particles during hadronisation, $f(z)$ can be investigated separately from $F(z)$ in heavy quark hadronisation, where the primary hadron is easily distinguished from secondaries by its heavy quark content.

Field and Feynman have shown [26] that a simple solution to the integral equation 2.54 is found with the ansatz

$$f(z) = a(1-z)^b \quad (b \geq 0) \ . \tag{2.55}$$

The coefficient a is determined by the normalisation of the probability distribution $f(z)$:

$$\int_0^1 f(z)dz = \frac{a}{b+1} = 1 \quad \Longleftrightarrow \quad a = b + 1 \tag{2.56}$$

The integral equation can then be solved by looking at moments of $f(z)$ and $F(z)$ in z. One obtains

$$F(z) = f(z)/z \tag{2.57}$$

Field and Feynman favoured a modification of this solution, which has the property that $F(z) \to const \neq 0$ for $z \to 1$, not $F(z) \to 0$ for $z \to 1$ as it is the case in the parametrisation 2.55/2.57. They achieved this by adding a small constant:

$$f(z) = 1 - a + a(b+1)(1-z)^b \tag{2.58}$$

This function solves the integral equation 2.54 with $F(z)$ chosen adequately. Theoretical arguments in favour of a $F(z) \to const$ for $z \to 1$ scenario are explained in Ref. [27].

A complete determination of the kinematics of the hadronisation steps requires a choice of both longitudinal and transverse momentum of the participating particles. The longitudinal momentum is determined by $f(z)$ as above. Transverse momentum is assigned to the created $q\overline{q}$ pairs with a Gaussian distribution. The sum of the transverse momenta of quark and anti-quark is supposed to be zero. The transverse momentum of hadrons is obtained as the sum of the transverse momenta of its constituents. By choosing an adequately small average value of the transverse momentum, one obtains the characteristic jet structure of high energy hadronic events, where groups of hadrons with large longitudinal momentum, but small relative transverse momentum are observed. These jets are naturally explained as the remnant particles of the hadronisation process of a parton with large energy.

The independent fragmentation scheme has several intrinsic problems. It is hard to find an adequate termination of the iteration. If after creation of a hadron insufficient energy to form another hadron is left, the remaining isolated hadron is usually discarded. This means that energy, longitudinal momentum, charge, colour, and flavour are not strictly conserved in the hadronisation process. Jet correlations, as observed in data, are by construction not included in this scheme. The suppression of the creation of heavy $q\overline{q}$ pairs (charm, bottom) has to be put in manually. The requirement of scale invariance constraining $f(z)$ is only approximately true, especially close to the kinematic limit for further hadron production. Typical solutions to the integral equation 2.54, like the Field-Feynman fragmentation function (Equation 2.58), predict that the energy distribution of hadrons containing the primary quark should peak at $z = 0$. This and other properties of independent fragmentation have been clearly excluded by e^+e^- experimental data. Independent fragmentation does however still give reasonable approximations for hadron collider data. It is used in the Cojets [28] and Isajet [29] Monte Carlo generators, and is included as option in Jetset [17] and Pythia [21].

Cluster Hadronisation

The problems of energy, momentum, charge, colour, and flavour non-conservation in the independent hadronisation approach can be overcome if the partons are combined to massive, colourless clusters which then undergo hadronisation. This is physically well motivated by the so-called preconfinement property of perturbative parton showers [30]. The partons created in a perturbative shower according to the leading logarithm approximation have the interesting property that they tend to form colour-neutral sets of partons with similar momentum and small spatial separation. These sets have finite invariant masses of the order of the energy scale where the shower evolution was terminated. This mass spectrum does not depend on the initial event energy scale prior to fragmentation. It seems therefore reasonable to treat these states, or clusters, in analogy to hadronic resonances with averaged properties, i.e. isotropic decay,

predominantly two-body decays, and branching ratios as expected from phase-space and spin considerations only. This leads to a very simple transition from partons to hadrons without too many arbitrary assumptions and parameters.

Earlier statistical hadronisation descriptions (statistical bootstrap model [31], multiperipheral cluster model [32]) may in retrospect be seen as precursors to modern cluster hadronisation models. The first full-featured cluster hadronisation model, the CalTech scheme, was introduced by Gottschalk in 1984 [33]. It characterises clusters by a quark flavour, an anti-quark flavour, and a mass. Clusters can in principle be constructed from a quark, an anti-quark, and an arbitrary number of gluons. In practice, gluons are split into $\mathrm{q\overline{q}}$ pairs before cluster formation, and clusters are then formed from quarks only. Each cluster decays to two hadrons, where one flavour of each resulting hadron is determined from the intrinsic cluster (anti-)flavour, and the respective other flavour is created by addition of a $\mathrm{q\overline{q}}$ pair. Production of baryons is possible with creation of a diquark pair instead of a quark pair. Suppression of heavier flavours and diquarks is introduced automatically by the restricted phase space for such cluster decays. Very massive clusters (mass $> \mathcal{O}(1\ \mathrm{GeV}/c^2)$ for light quarks) can decay to one hadron and one sub-cluster, where the branching ratio to hadron and sub-cluster is set equal to the branching ratio to two hadrons with suitable quantum numbers. The decay to a sub-cluster increases the average particle multiplicity in a jet which would otherwise be too low in this model. All cluster decays, including decays to a sub-cluster, are assumed to be isotropic.

The most wide-spread cluster model was developed by Webber [34] and is implemented in the Herwig Monte Carlo generator [22]. It is in principle quite similar to the CalTech scheme, but uses an extended cluster decay scheme. Clusters of average mass decay to two hadrons as in the CalTech scheme. All clusters above a fission mass M_f are split into two sub-clusters, other than in the CalTech scheme, where one hadron and one sub-cluster are created[5].

The mechanism of heavy cluster splitting into lighter ones can not be adequately described by isotropic decays. Instead, the Herwig model borrows the mechanism from the string model described below. The two sub-clusters inherit a momentum fraction which, with increasing cluster mass, is increasingly dominated by the momentum of the quark of the original cluster that is transferred to the respective sub-cluster [22]:

$$p_{C1} = \left(1 - \frac{Q_0}{M_C}\right) p_{q1} + \frac{Q_0}{M_C} p_{q2} \tag{2.59}$$

$$p_{C2} = \left(1 - \frac{Q_0}{M_C}\right) p_{q2} + \frac{Q_0}{M_C} p_{q1} \tag{2.60}$$

Here, $C1$ ($C2$) is the sub-cluster containing (anti-)quark $q1$ ($q2$), M_C is the invariant mass of the original cluster, and Q_0 is the cutoff scale of the parton shower, i.e. a measure of the effective mass of the partons in the cluster.

Another exception to the two-hadron cluster decay rule applies for clusters with small invariant mass, which occasionally are too light to decay to two hadrons. These clusters are transformed into a single hadron. Momentum conservation is in this case enforced by transferring momentum to a neighbouring cluster of larger mass.

Comparison of earlier versions of this cluster model with data showed that the assumption of isotropic decay leads to a momentum spectrum of mesons with a heavy quark that is much too soft. A large fraction of heavy mesons is emitted against the cluster flight direction if isotropy

[5]Cluster splitting into two sub-clusters was also regarded as desirable option by Gottschalk, but was not permitted in the CalTech scheme simply due to computing power constraints.

is assumed, thus softening the spectrum. Therefore the default behaviour of current versions of the Herwig generator is to force the hadron containing a parton from the perturbative phase of the event to continue in the original flight direction of this parton, where this direction is optionally smeared by a Gaussian[6].

A good description of the longitudinal momentum distribution is thus only obtained by deviating from the very simple and elegant cluster picture in several respects. Still, the number of parameters of this model is small, and other properties that were put in manually in the independent fragmentation approach are intrinsic to the cluster model. This is true for the heavy flavour and baryon suppression during hadronisation, as explained above, and it is also evident in the mechanism to create a small, but non-zero transverse momentum of the hadrons created during hadronisation. In the cluster model, this arises naturally from the kinematics of a massive cluster decay.

String Hadronisation

A large class of models describes hadronisation involving colour flux tubes, or strings, each spanned between two quarks created during the perturbative event phase. Usually the motion of a string is described by classical, relativistic dynamics. The treatment of gluons seems more natural in the string picture than in the cluster or independent hadronisation schemes: Perturbative gluons are simply incorporated in the strings connecting two nearby quarks. They appear as a kink in the string. This complicates the dynamics, but does not lead to fundamentally different effects. Gluons will therefore be neglected in the following considerations.

It was already discussed earlier in this chapter (Subsection 2.2.2) that the force between two colour sources with large mutual distance is expected to be independent of the distance due to the self-interaction of gluons. The energy density, or string tension, κ is constant along the string, if the transverse extension of the string is assumed to be constant over its full length and much smaller than the longitudinal extension. A diameter of $\mathcal{O}(1\text{ fm})$ is estimated, and a tension of $\kappa \approx 1\text{ GeV/fm}$. As the quarks fly apart and the string is stretched, the energy stored in the string increases according to $E(d) \propto \kappa d$, where d is the distance of quark and anti-quark at the end of the string, or the length of the string. If a virtual $q\overline{q}$ pair fluctuates out of the vacuum somewhere along the string, and if this $q\overline{q}$ pair has the same colour as the endpoint quarks of the string, the colour field is locally compensated and the string breaks into two pieces. This procedure happens repeatedly until the remaining energy of the individual string segments is not sufficient to transform another virtual $q\overline{q}$ pair into a real one.

Because the string is assumed to be uniform along its length, the probability for a $q\overline{q}$ pair creation to occur on the string per unit length and per unit time is a constant P_0. To obtain the probability that the string breaks due to this pair creation, the history of the respective point has to be taken into account: The probability for a string break at a given point is proportional to the probability that no previous break occurred in its backward light cone. If there had been any previous break within the light cone, the considered space-time point would not be on the

[6] In terms of program parameters, which are often quoted in other publications on this topic, the direction enforcement corresponds to setting `cldir=1`. The default Herwig setup is `cldir=1` without any additional smearing of the direction. The Herwig setup used for the analysis in Chapter 4 deviates from this default behaviour in that directional smearing with a width of `clsmr=0.35` for all flavours is used for the Herwig 5.9 sample, and directional smearing with a width of `clsmr(1)=0.4` for udsc quarks only (`clsmr(2)=0.0` for b quarks) is used for the Herwig 6.2 sample. This is the standard OPAL tune of the respective Herwig versions [35].

string, since the endpoints of the newly created sub-strings move apart at the speed of light[7] (assuming massless endpoint quarks). The probability for no string break in the backward light cone is given by Wilson's area law [36]

$$\frac{d\mathcal{P}}{dA} = P_0 e^{-P_0 A} \ , \tag{2.61}$$

with A being the space-time area in the backward light cone. Essentially this area law states that evolution of long string pieces over long periods of time without decay is exponentially suppressed.

The area in the backward light-cone can be calculated in two-dimensional light-cone variables, in the centre-of-mass system of quark and anti-quark, with the string extended along the x axis:

$$A = \left| \left(\frac{\Delta t - \Delta x}{\sqrt{2}} \right) \left(\frac{\Delta t + \Delta x}{\sqrt{2}} \right) \right| = \frac{1}{2} \left| \Delta t^2 - \Delta x^2 \right| = \frac{1}{2\kappa^2} \left| p_x^2 - E^2 \right| = \frac{m_t^2}{2\kappa^2} \tag{2.62}$$

Thus the invariant transverse mass $m_t = \sqrt{m^2 + p_t^2}$ of a string piece is proportional to the area swept over by the backward light cone. Hence, the area law can be used to deduce the transverse mass distribution of sub-strings:

$$\frac{d\mathcal{P}}{dm_t^2} = \frac{d\mathcal{P}}{dA}\frac{dA}{dm_t^2} = P_0 e^{-P_0 A} \frac{1}{2\kappa^2} = b e^{-b m_t^2} \ , \quad b = P_0/2\kappa^2 \tag{2.63}$$

It has to be pointed out again that these results are only valid for massless quarks. Bowler [37] has performed a modification of this calculation which takes a non-zero mass of the endpoint quarks of a string into account. This is done by replacing the straight world line of the quarks by curved lines (see below for a discussion of the energy distribution of primary hadrons obtained with this modification).

The first string model was proposed by Artru and Mennessier in 1974 [38], based on the formalism reproduced above. The problem encountered in this model is that iterative application of string splitting by the area law leads to an infinite series of ever smaller sub-strings. To avoid this problem, Artru and Mennessier introduced a mass cut-off m_0, below which further string fission is prohibited. They end up with a finite set of hadronic states with a continuous mass spectrum, which strongly resemble the clusters described above. These cluster-like resonances decay into two usual on-shell hadrons.

The CalTech II string hadronisation scheme [39] suppresses string splitting to unphysically small mass sub-strings not by a strict cut-off at m_0, but by smoothly decreasing the probability for further string breaks. This probability is parametrised as

$$P_{break} = \begin{cases} 1 - e^{-P_0 (m - m_0)^2/\kappa^2} & m > m_0 \\ 0 & m \leq m_0 \end{cases} \tag{2.64}$$

If, with the above probability, a further string break is chosen, its space-time coordinates are found according to the area law. If no further string break takes place, the remaining sub-string decays à la cluster scheme to two hadrons. If the cut occurs close to one end of the string, one of the two sub-strings can have an invariant mass below the kinematic threshold $m_1 < m_0$ for production of two hadrons. These very light sub-strings are transformed into a single hadron.

[7] This has the immediate consequence that all string breaks are causally disconnected.

In general, this hadron will not be on-shell. The momentum is then corrected by moving the string break along the string until the decay into a single hadron is kinematically allowed. Gottschalk and Morris have shown that the extent to which the spring break point has to be moved is smaller than the transverse extension of the string [39], and that this procedure is therefore acceptable.

Hadron mass shell constraints and uniform splitting probability are irreconcilable, as evident from the above considerations. The Artru/Mennessier and CalTech II models rely on the uniform splitting probability and are thus forced to include cluster-like transitions from string fragments to hadrons. The probably most well-known and wide-spread string hadronisation model, invented by the Lund group [40] and realised in the Jetset [17] and Pythia [21] Monte Carlo event generators, gives up the concept of a necessarily constant $q\overline{q}$ pair creation probability over the full length of the string. Strings are broken exactly where necessary to ensure the creation of on-shell hadrons. Since all string breaks are causally disconnected, they can be treated in any possible order. The Lund scheme makes use of this property to establish a simple iterative algorithm: Hadronisation is started at the outer ends of the string, and the creation of hadrons is continued towards the inside until the invariant mass of the remaining string drops below a threshold value. This remainder is then split into two hadrons (again, in analogy to a cluster decay).

The creation of $q\overline{q}$ pairs along the string in the Lund model takes the quark masses into account[8]. This has important consequences: $q\overline{q}$ pairs are expected to be created locally, i.e. at one space point. However, in order to transfer a virtual $q\overline{q}$ pair into mass-shell particles, energy has to be taken from the string. For quarks of a mass m_{q}, and a transverse momentum p_t with respect to the string, the minimum required energy is $E_{min} = 2\sqrt{m_{\mathrm{q}}^2 + p_t^2} = 2m_t$. Here it is assumed that both members of the $q\overline{q}$ pair have a transverse momentum of same size, but opposite direction. Otherwise the string would acquire a transverse excitation, which is assumed not to happen. The required energy can only be obtained by a spatial separation of quark and anti-quark along the string of $\Delta x_{min} = E_{min}/\kappa = 2m_t/\kappa$. The string fission is thus suppressed by the probability for a tunnelling process of a locally created $q\overline{q}$ pair to spatially separated on-shell quarks. The suppression factor was found to be [41]

$$e^{-\frac{\pi}{\kappa}(m_{\mathrm{q}}^2+p_t^2)} = e^{-\frac{\pi}{\kappa}m_{\mathrm{q}}^2} \times e^{-\frac{\pi}{\kappa}p_t^2} \tag{2.65}$$

The first term provides for an automatic suppression of heavy quark production during string hadronisation. The ratio of flavour production rates is estimated to be $P_{\mathrm{u}} : P_{\mathrm{d}} : P_{\mathrm{s}} : P_{\mathrm{c}} = 1 : 1 : 0.3 : 10^{-11}$ using kinematical quark masses. The second term in the tunnelling probability corresponds to a suppression of large transverse momenta. Interestingly, the transverse momentum distribution is predicted to be independent of the quark flavour. A further prediction is that baryon production (requiring two quarks and two anti-quarks) is less likely than meson production, in accordance with observations.

Choice of flavour and transverse momentum for $q\overline{q}$ pairs are thus strictly regulated in the Lund string scheme. Hence, also the quark content and transverse momentum of hadrons is well constrained. Further quantum numbers, e.g. angular momentum, relative spin orientation, etc., are chosen based on rather general symmetry assumptions, or according to measured production

[8]Unfortunately it is not quite clear which quark masses should be used. The Lund model uses so-called kinematical masses for hard processes like quark pair creation, and constituent masses fitted to the hadron spectra to estimate masses of resonances that have not yet been found. Finally, the so-called current algebra masses are used as couplings to Higgs bosons or to fields of similar models.

ratios. What remains is the longitudinal hadron momentum with respect to the string axis. The choice of a longitudinal momentum is usually expressed in terms of the fraction of the string's light cone momentum to be taken by the hadron, i.e. the variable z introduced above. The probability distribution $f(z)$ of momentum fractions assigned to hadrons can be chosen arbitrarily. Each choice corresponds to a specific distribution of cut points on the string, which does not necessarily comply with Wilson's area law, or a constant breaking probability over the full string length. The most prominent parametrisations of $f(z)$ will be discussed later in this chapter.

A short summary of the Lund recipe amounts to the following: After the quark flavours for a hadron have been chosen, the next step is to select the remaining quantum numbers (e.g. spin, orbital angular momentum) for the hadron. Finally, the longitudinal momentum is determined with the fragmentation function. A modification of this approach is used in the UCLA scheme [42]. Here not only the choice of longitudinal momentum, but also the choice of the hadron species is determined by the fragmentation function. The fragmentation function in the Lund model is independently normalised for each hadron species that is selected for the next hadronisation step:

$$\int_0^1 f(z)dz = 1 \tag{2.66}$$

Since the hadron mass usually enters as parameter in the fragmentation function, there is in fact a different fragmentation function for each type of hadron, $f(z) \longrightarrow f_h(z)$. The UCLA ansatz is to combine the fragmentation functions for each hadron into a single, universal fragmentation function with a universal normalisation

$$\sum_h \int_0^1 f_h(z)dz = 1 \ . \tag{2.67}$$

The probability to select a certain hadron species is then equal to the normalisation of the respective $f_h(z)$. This normalisation depends on the hadron mass, thus automatically suppressing excited states due to their larger mass if $f(z)$ is chosen adequately[9]. Spin selection rules are represented by including the Clebsch-Gordon coefficients into the normalisation of $f_h(z)$. Main advantage of the UCLA model compared to Lund is the reduced number of parameters. The UCLA model is still in a phase of active development; so far it is only available in a modified version of Jetset.

2.4.3 Fragmentation Functions for the String Scheme

The string fragmentation scheme, as well as the independent fragmentation approach, requires a parametrisation $f(z)$ of the probability distribution of the light cone momentum fraction z transferred from a parton to a hadron. The Field-Feynman parametrisation discussed in the framework of the independent hadronisation scheme is but one example for such a parametrisation. In the following, similar parametrisations for the Lund string hadronisation scheme will be presented. Both independent and string hadronisation are performed iteratively, with the basic assumption of a scale invariant fragmentation function. The integral evolution equation 2.54 is therefore equally valid in the Lund string hadronisation picture.

[9]Basic choice for the UCLA scheme is the Lund symmetric fragmentation function discussed later.

In the first version of the Lund scheme [40] a solution of the evolution equation was derived from string dynamics under the assumption of massless quarks. A flat fragmentation function

$$f(z) = 1 \tag{2.68}$$

solves Equation 2.54 with an energy distribution of hadrons in a jet of

$$F(z) = 1/z \ . \tag{2.69}$$

With this parametrisation, the string model immediately provides a simple explanation for the "rapidity plateau" observed in hadronic jets[10]: The hadrons in a jet are approximately evenly distributed over the rapidity $y = -\ln z$. The density of hadrons in rapidity space is easily derived from the density in momentum space $F(z)$:

$$\left|\frac{dN_{had}}{dy}\right| = \left|-z\frac{dN_{had}}{dz}\right| = zF(z) = 1 \tag{2.70}$$

Similarly, for any energy distribution $F(z)$ with $1/z$ behaviour for $z \to 0$ it is expected that the hadron density along the rapidity axis is approximately constant close to $z = 0$, in accordance with experimental data.

In Ref. [43] it was argued that the limited extension of the colour field leads to a suppression of hadron production at large z by introducing a factor of $(1-z)$ into $f(z)$. This is a special case of the solution of the integral equation 2.54 discussed above, and it leads to a fragmentation function for light hadrons in a jet of

$$F(z) = \frac{1-z}{z} \ , \tag{2.71}$$

still exhibiting the $1/z$ behaviour at small z which is necessary to explain the observed rapidity distribution in a jet. This function delivered an adequate description of longitudinal momentum spectra in energy regimes where only uds quarks played a role. With the appearance of charm quarks on the scene, first indications arose that the energy distribution of hadrons containing a quark of large mass can not be explained with the above parametrisations [44].

2.4.4 General Thoughts on Hadronisation of Heavy Quarks

The hadronisation of heavy quarks (mass of at least several GeV) has some significantly different properties, the most important of which have been predicted by Bjorken [45] based on very general grounds. In practice, his ideas are applicable to the b and c quarks, although the quantitative agreement weakens for lower masses. The t quark is so heavy that its decay time scale is shorter than the hadronisation time scale — it decays already during the perturbative phase of the event, and therefore never hadronises.

Basic idea of Bjorken's arguments is to look at the system of one heavy and one light (anti-) quark in the rest frame of the heavy quark, analyse the properties of the light quark jet in this reference frame, and then transform back into the centre-of-mass system. Known properties of light quark jets that he infers are the energy dependence of the charged particle multiplicity in a jet, and the momentum spectrum of the jet particles.

[10] Refined calculations actually predict a dip in the central rapidity region. However, the mathematical background of this improved calculation is beyond the scope of this thesis.

In $e^+e^- \to q\overline{q}$ reactions at a centre-of-mass energy of $\sqrt{s}$, two jets with a total momentum of $\frac{1}{2}\sqrt{s}$ each are created (neglecting jet correlations). If one of the light quarks is replaced by a heavy quark Q with mass m_Q (which of course requires a different production process), still both quarks have a momentum of $\frac{1}{2}\sqrt{s}$ in the centre-of-mass frame of the system. For the following line of reasoning, the system is viewed in the rest frame of the heavy quark. From the Lorentz transformation of the energy component of the heavy quark[11], $E^{cms} = \gamma(E^{rest} - \beta p_\parallel^{rest})$, and thus $\frac{1}{2}\sqrt{s} = \gamma(m_Q - \beta \times 0)$. This gives $\gamma = \frac{1}{2}\sqrt{s}/m_Q$. The energy component of the momentum of the light quark in the heavy quark rest frame is therefore $E' = \gamma(E^{cms} - \beta p_\parallel^{cms})$. For a quark of negligible mass, $E^{cms} \approx p_\parallel^{cms}$, which leads to

$$E' = (\gamma + \beta\gamma)E^{cms} = \gamma\left(1 + \sqrt{1 - \frac{1}{\gamma^2}}\right)E^{cms} \; . \tag{2.72}$$

γ and E^{cms} are known; thus one obtains

$$E' = \frac{1}{2m_Q}\sqrt{s}\left(1 + \sqrt{1 - \frac{4m_Q^2}{s}}\right)\frac{1}{2}\sqrt{s} = \frac{s}{4m_Q}\left(1 + \sqrt{1 - \frac{4m_Q^2}{s}}\right) \; . \tag{2.73}$$

Bjorken assumed $m_Q \approx \frac{1}{2}\sqrt{s}$ and neglected the second term in parentheses. However, for the collider energies dealt with in this thesis, $m_Q \ll \frac{1}{2}\sqrt{s}$, and thus $E' \approx \frac{s}{2m_Q}$. Due to the semi-quantitative nature of the argument this will not lead to a different result than the one originally obtained by Bjorken.

The light quark moving away from the heavy quark will hadronise into a jet of properties that were well measured in e^+e^- annihilation below the threshold for heavy quark production. The inclusive momentum spectrum of charged particles in such a jet is adequately described by the momentum distribution described in Subsection 2.4.3, i.e. approximated by $dn_{ch}/dp \propto 1/p$ over a large region of momenta. The Lorentz transformation back into the centre-of-mass system reverses the direction of the particles at the lower end of the momentum spectrum with respect to the light quark direction: They form a jet associated to the heavy quark Q. The slowest particles in the heavy-quark rest frame will have largest momentum in the heavy quark flight direction in the centre-of-mass frame. The highest possible value is $\gamma m_q = \frac{1}{2}\sqrt{s}m_q/m_Q$, for a particle with zero momentum in the heavy-quark rest frame. This corresponds to a fraction of $m_q/m_Q \approx 1\ \mathrm{GeV}/m_Q$ of the initial momentum of the heavy quark; the average momentum will be even smaller. It can be assumed that the sum of the momenta of all light hadrons in the Q jet is still close to $1\ \mathrm{GeV}/m_Q$, leaving an average fraction of the available momentum of

$$\langle z \rangle \approx 1 - \frac{1\ \mathrm{GeV}}{m_Q} \tag{2.74}$$

for the hadron containing the heavy quark. The conclusion from this result is that the $f(z)$ parametrisations derived in Subsection 2.4.3 are not valid for the energy distribution of hadrons carrying a heavy quark. Dedicated heavy quark fragmentation functions are therefore necessary.

2.4.5 Parametrisations of the Heavy Quark Fragmentation Function

With the experimental capabilities of the LEP detectors and SLD in combination with detailed understanding of the spectrum and decay of heavy hadrons, it has meanwhile become possible

[11] For simplicity, the calculation of γ is shown for the inverse transformation from the heavy quark rest frame to the centre-of-mass system. The value of γ is identical for both directions of the transformation.

to verify not only the fact that the average momentum fraction of primary heavy hadrons peaks close to one, but one can also test functional forms which parametrise the z distribution. The fragmentation parametrisations which will be investigated in this thesis are presented in the following. Fragmentation functions derived from phenomenological ideas have been contributed by Peterson et al. [46], Collins and Spiller [47], and Kartvelishvili et al. [48]. Models that are built on more basic ideas of the string fragmentation process were suggested by Andersson et al. [49] and Bowler [37]. Most theoretic arguments are referring to heavy quark fragmentation into mesons. About 10% of all hadrons produced in the hadronisation process are baryons; they are neglected here.

In the general discussion of hadronisation models in this thesis, the fragmentation functions $f(z)$ and $F(z)$ have been distinguished. $F(z)$ describes the energy distribution of any hadron created in the hadronisation process; $f(z)$ parametrises the energy distribution of the primary hadron only. Since the production of heavy quarks during string/cluster splitting is almost completely suppressed, every hadron containing a heavy quark is most likely a primary hadron, or decay product of the primary hadron, which complicates the picture a bit. Anyhow, neglecting hadron decays for a while, the energy distribution of hadrons containing a heavy quark is described by the heavy quark fragmentation function $D_{\mathrm{Q}}(z) = f(z)$, where the change in nomenclature is introduced to stay conform with the common notation.

Peterson et al.

The most well known fragmentation parametrisation for heavy quarks is the one suggested 1983 by Peterson et al. [46]. It is based on the assumption that the amplitude T of the transition of a heavy quark Q into a heavy hadron $H = (Q\overline{q})$ plus a light quark q is mainly determined by the energy difference between initial and final state:

$$T \propto 1/\Delta E \tag{2.75}$$

The energy difference can be expressed as

$$\begin{aligned}
\Delta E &= E_H + E_{\mathrm{q}} - E_{\mathrm{Q}} && (2.76)\\
&= \sqrt{m_H^2 + (zP)^2} + \sqrt{m_{\mathrm{q}}^2 + ((1-z)P)^2} - \sqrt{m_{\mathrm{Q}}^2 + P^2} && (2.77)\\
&\approx \sqrt{m_{\mathrm{Q}}^2 + (zP)^2} + \sqrt{m_{\mathrm{q}}^2 + ((1-z)P)^2} - \sqrt{m_{\mathrm{Q}}^2 + P^2}\,, && (2.78)
\end{aligned}$$

where in the last step $m_H \approx m_{\mathrm{Q}}$ has been assumed. Here, P is the longitudinal momentum of the heavy quark, with respect to the string axis, prior to hadronisation. m_H, m_{Q}, and m_{q} are the transverse masses of the heavy hadron, the heavy quark, and the light quark, respectively. As above, the transverse mass is defined as the quadratic sum of rest mass and transverse momentum. After factoring zP, $(1-z)P$, or respectively P out of the square roots, they can be Taylor expanded following $\sqrt{1+x} \approx 1 + x/2$:

$$\begin{aligned}
\Delta E &\approx zP(1 + \frac{m_{\mathrm{Q}}^2}{2z^2P^2}) + (1-z)P(1 + \frac{m_{\mathrm{q}}^2}{2(1-z)^2P^2}) - P(1 + \frac{m_{\mathrm{Q}}^2}{2P^2}) && (2.79)\\
&= \frac{m_{\mathrm{Q}}^2}{2P}(\frac{1}{z} + \frac{m_{\mathrm{q}}^2/m_{\mathrm{Q}}^2}{1-z} - 1) && (2.80)\\
&\propto 1 - \frac{1}{z} - \frac{\varepsilon_{\mathrm{Q}}}{1-z} && (2.81)
\end{aligned}$$

The parameter $\varepsilon_{\mathrm{Q}} = m_{\mathrm{q}}^2/m_{\mathrm{Q}}^2$ cannot be calculated exactly, because the light quark mass put into the equation is a mere representation of the non-perturbative strong interaction scale. A realistic estimate for this scale is the constituent mass of light quarks in a ρ meson [46]. Using this value gives $\varepsilon_{\mathrm{b}} \approx (m_\rho/2)^2/(m_{\mathrm{B}^0})^2 \approx 50 \times 10^{-4}$ for the case of b quark fragmentation.

The actual fragmentation function is a probability distribution of hadrons carrying the momentum fraction z, and as such it is proportional to the square of the amplitude T, i.e. proportional to $1/(\Delta E)^2$. Together with a phase space factor of $1/z$ one obtains the following fragmentation function

$$D_{\mathrm{Q}}(z) = N\frac{1}{z}(1 - \frac{1}{z} - \frac{\varepsilon_{\mathrm{Q}}}{1-z})^{-2} \tag{2.82}$$

with a normalisation factor N.

Collins and Spiller

Collins and Spiller noted in 1985 that the Peterson parametrisation shows a behaviour $\propto (1-z)^2$ as z approaches unity [47]. This is in contradiction to the $(1-z)$ behaviour expected for mesons from dimensional counting arguments by Brodsky et al. [50]. For the same reason they stated that the Peterson parametrisation cannot fulfil the reciprocity relation [51] which connects exclusive heavy meson H structure functions F_H^Q to exclusive fragmentation functions $D_Q^H(z)$ at high z:

$$D_Q^H(z) \approx F_H^Q(z) \quad \text{for} \quad z \approx 1 \tag{2.83}$$

Although the exact derivation of reciprocity is beyond the scope of this thesis, it is easily made plausible with a qualitative argument by Field and Feynman [27]: For large z both cases deal with a quark dominating the whole configuration of a hadron, and a low energy remainder. This means that to a reasonable approximation, quark and hadron are identical. The functional form of the probability to observe such a configuration should not depend on whether the quark transforms into the hadron or whether the hadron transforms into the quark (the quark is extracted from the hadron).

Collins and Spiller have suggested a fragmentation parametrisation which takes care of reciprocity and dimensional counting. Their model is based on their own prediction of heavy meson structure functions, which is based on perturbative QCD calculations taking off-shell-mass effects into account [52]. The fragmentation parametrisation they obtain for heavy quarks is

$$D_{\mathrm{Q}}(z) = N(\frac{1-z}{z} + \frac{(2-z)\varepsilon_{\mathrm{Q}}}{1-z})(1+z^2)(1 - \frac{1}{z} - \frac{\varepsilon_{\mathrm{Q}}}{1-z})^{-2} \ . \tag{2.84}$$

In this formula, ε_{Q} is defined analogously as in the Peterson model. As indicated by the common terms in the Peterson and Collins/Spiller parametrisations, the latter is in effect a modification of the former: Peterson et al. assumed the transition matrix element to be constant, whereas Collins and Spiller introduced an explicit meson wave function into their calculation [53]. It has to be pointed out that the dimensional counting arguments providing the basis for the Collins/Spiller calculation were later disputed by other calculations [54], and it turned out that one might indeed expect a $(1-z)^2$ behaviour at large z.

Kartvelishvili et al.

A similar approach like the one by Collins and Spiller has been followed by Kartvelishvili et al. already in 1978 [48]. It also makes use of the reciprocity relation to derive a heavy quark fragmentation function from the corresponding heavy meson structure function: Kartvelishvili

et al. calculate the heavy valence quark distribution $F_H^{\mathrm{Q}}(x)$ in a heavy-light meson $H = (\mathrm{Q}\overline{\mathrm{q}})$ in analogy to the relativistic quark-parton model of nucleons by Kuti and Weisskopf [55]. They obtain

$$F_H^{\mathrm{Q}}(x) \propto x^{-\alpha_{\mathrm{Q}}(0)}(1-x)^{\gamma-\alpha_{\mathrm{q}}(0)} \ . \tag{2.85}$$

Here, $\alpha_{\mathrm{q}}(0)$ and $\alpha_{\mathrm{Q}}(0)$ are the Regge intercepts of quarkonia composed of the light or the heavy quark, respectively, and γ determines the sea quark normalisation [56]. The Regge intercept of a hadron spectrum is closely related to the respective quark masses. $\alpha_{\mathrm{q}}(0) = \alpha_{\mathrm{u}}(0) = \alpha_{\mathrm{d}}(0) = 0.5$ was obtained from ρ, ω, and other light quark resonances. $\alpha_{\mathrm{c}}(0)$ is close to -3, and $\alpha_{\mathrm{b}}(0)$ is approximately -9. (For a recent discussion of Regge trajectories and their correspondence to quark masses see e.g. Ref. [57].) The value of γ is obtained indirectly by fixing the exponent of $(1-x)^{\gamma-\alpha_{\mathrm{q}}(0)}$, which determines the behaviour of the structure function at $x \to 1$. The Drell-Yan-West relation [58] connects the large-Q^2 behaviour of the elastic form factor $F_A(Q^2)$ of a meson with the $x \to 1$ behaviour of the structure function. A power law $F_A(Q^2) \propto (1/Q^2)^k$ for $Q^2 \to \infty$ translates into the structure function decreasing with $(1-x)^{2k-1}$ at $x \to 1$. For pions, the form factor is known to vary precisely with $F_A(Q^2) \propto (1/Q^2)$, and therefore $\gamma - \alpha_{\mathrm{q}}(0)$ is fixed to one.

The next step in the determination of a fragmentation parametrisation is the application of the reciprocity relation. Strictly speaking, reciprocity is valid only in the region $z \to 1$, but since it is clear from Bjorken's argument that the z distribution of heavy hadrons is strongly peaked close to 1, Kartvelishvili et al. assume reciprocity to be valid for all z. Under these circumstances, one has

$$D_Q^H(z) = F_H^{\mathrm{Q}}(z) = N z^{-\alpha_{\mathrm{Q}}(0)}(1-z) \tag{2.86}$$

It is common practice to define $\alpha_{\mathrm{Q}} := -\alpha_{\mathrm{Q}}(0)$, giving the well-known form of the Kartvelishvili et al. fragmentation function:

$$D_Q^H(z) = F_H^{\mathrm{Q}}(z) = N z^{\alpha_{\mathrm{Q}}}(1-z) \tag{2.87}$$

Derived from the Regge intercept of bottomonia, Kartvelishvili et al. predict a value of $\alpha_{\mathrm{b}} \approx 9$ for b hadronisation.

Lund Symmetric

According to the string fragmentation model, hadrons are created iteratively at each end of the string. The z distribution determines the actual positions of breaks on the string. Andersson et al. have imposed the requirement that hadronisation from either (quark- or anti-quark-) end of the string should lead to the same distribution of string breaks. They have shown [49] that this symmetry condition, along with additional assumptions like no transverse string excitations and a constant string tension, is sufficient to constrain the functional form of the fragmentation function to

$$D_{\mathrm{Q}}(z) = N \frac{1}{z} z^{a_\alpha} \frac{(1-z)^{a_\beta}}{z} \exp(-\frac{b m_t^2}{z}) \ , \tag{2.88}$$

where m_t is the transverse mass of the meson created in the hadronisation process. b is a universal parameter. a_α and a_β are parameters for the quark flavour before and after the current hadronisation step. Usually one assumes $a_\alpha = a_\beta = a$ for all flavours. This assumption is not based on firm theoretical grounds, but on the fact that there are no experimental results contradicting it. It leads to a simplification of the fragmentation function to

$$D_{\mathrm{Q}}(z) = N \frac{1}{z}(1-z)^a \exp(-\frac{b m_t^2}{z}) \ . \tag{2.89}$$

It has been mentioned previously that dimensional counting arguments determine the behaviour of the fragmentation function for $z \to 1$. It turns out that the Lund symmetric function approaches $(1-z)^a$ in the large z region; it depends thus on the parameter choice whether this theoretically motivated boundary condition is fulfilled or not.

The parameters a and b do not only impact the energy spectrum of hadrons produced in the fragmentation spectrum, but also their rapidity distribution and the multiplicity of hadrons in a jet. These aspects will not be discussed further in this thesis, although they provide means for independent cross-checks of parameter fits to the hadron energy spectrum.

Bowler

Bowler [37] refers back to the original string model of Artru and Mennessier [38] and modifies the light cone area calculation to prove that the inclusion of quark masses at the endpoints of a string leads to the Lund symmetric function, corrected by an additional factor $z^{-bm_{\mathrm{Q}}^2}$, where m_{Q} is the transverse mass of the endpoint quark:

$$D_{\mathrm{Q}}(z) = N\frac{1}{z^{1+bm_{\mathrm{Q}}^2}}(1-z)^a \exp(-\frac{bm_t^2}{z}) \ . \tag{2.90}$$

For heavy quarks, the transverse mass of the heavy quark is approximately equal to the transverse mass of the heavy hadron, $m_{\mathrm{Q}} \approx m_t$:

$$D_{\mathrm{Q}}(z) = N\frac{1}{z^{1+bm_t^2}}(1-z)^a \exp(-\frac{bm_t^2}{z}) \ . \tag{2.91}$$

Because furthermore the transverse momentum of a heavy hadron obtained in the string fragmentation process is negligible compared to the mass, the product bm_t^2 has traditionally been used as one fit parameter. The analysis presented in Chapter 4 will also follow this convention.

Main modifications of the Bowler model with respect to the original Artru/Mennessier picture are the replacement of straight lines in space-time (massless particles) by hyperbolae (massive particles), modifying the area in the history of light-cones to be considered for string fission. An additional change is the replacement of the continuous mass spectrum of Artru/Mennessier string decays by a discrete spectrum. This is done by restricting possible string break points in space-time to discrete hyperbolae corresponding to different invariant masses. Only those space-time points in the light cone history of a possible string break are taken into account that coincide with one such hyperbola [59]. This leads to another modification of the area decay law. The advantage of this approach is that this way the uniform probability for string breaks is ensured despite the mass shell constraints, whereas the Lund symmetric approach had to give up uniformity.

The ansatz by Bowler is quite different from the symmetry constraint approach by the Lund group, and yet the results are remarkably similar. Although this might be surprising at first glance, it is not unexpected. Almost all conditions imposed by the Lund group are intrinsic to the basic Artru/Mennessier model. The Lund group starts from an iterative string fission ansatz and tries to ensure that during iteration the symmetries and properties of the basic model are accounted for. Bowler, on the other hand, starts from the basic model properties and arrives at a parametrisation which is also usable for iterative treatment of the string hadronisation.

An experimental test of most fragmentation and hadronisation models introduced in this section will be described in Chapter 4. There, the energy distribution of hadrons containing a b quark will be compared to the predictions made by the cluster model and the string model with the fragmentation functions discussed above.

2.5 Excited Heavy Mesons

The selection of quark flavours which are combined to form hadrons in Monte Carlo generators was described in Subsection 2.4.2. However, as both experiment and theory show, the flavour quantum numbers alone are not sufficient to identify a hadron. Each flavour combination leads to a full spectrum of resonances following from different relative spin orientation of the constituents, orbital angular momentum configuration, and radial excitations. The relative production rate of these individual states in Monte Carlo simulations is usually either tuned to production rates or branching ratio measurements, or obtained from phase space factors due to measured hadron masses. Simple symmetry considerations are often taken into account.

Two important production mechanisms have to be allowed for: A given resonance can be produced directly during hadronisation, but it can also occur as decay product of higher resonances. A possibility to calculate the hadronisation production rates and decay branching ratios of hadrons would on the one hand be a great success for both fundamental theory and techniques of its application if calculated and observed rates observe. On the other hand, predictions of not yet observed resonances would complement incomplete experimental data in the compilation of a tentative full picture of hadron creation and decay needed for Monte Carlo generators. Furthermore, these predictions would of course act as a guide for the extension of the set of experimentally observed and investigated resonances and decays.

The investigation of a hadron spectrum involves several questions: Which spin, orbital angular momentum, and radial configuration do actually lead to bound states of a given flavour combination, and what are the masses of these states? Which decays take place at what rate, and what is the resulting width of the resonance? A mass prediction is of outstanding importance for the experimental identification of a resonance. Despite the complexity of QCD interaction of the constituents, mass predictions are possible in specific cases, primarily for mesons containing one heavy quark, which will be discussed below. Decay rates, since they involve a dynamic transition from one bound state to at least one other, are much more difficult, and only simple cases lead to useful predictions, like the investigation of semi-leptonic meson decays in lattice QCD. A consequence of the difficulty of predicting decay rates is that it is extremely problematic to predict the widths of hadronic resonances. This in turn complicates the experimental verification of hadronic spectra, especially the association of observed resonances with predicted states.

The case of mesons containing one heavy and one light quark turned out to be accessible to precise calculations and thus very interesting. This is due to the following concept pioneered by Isgur and Wise [60], Eichten and Hill [61], and mathematically streamlined by Georgi [62]. It is based on the assumption that for a large quark mass m_{Q} the four-momentum of the system consisting of the heavy and a light quark is dominated by the heavy quark mass, and thus the invariant mass of the bound state is close to the mass of the heavy quark:

$$P^{\mu} = m_{\mathrm{Q}} v^{\mu} + p^{\mu} \ , \tag{2.92}$$

where v is the four-velocity of the system, with $v_{\mu}v^{\mu} = 1$ and $v^0 > 0$. p is the correction due to off-shellness of the heavy quark and the light quark momentum. p is expected to be of the order of Λ_{QCD}. After an elastic scattering process with momentum transfer k^{μ}, the four-momentum is expressed as

$$P^{\mu} = m_{\mathrm{Q}} v'^{\mu} + p^{\mu} + k^{\mu} \ . \tag{2.93}$$

For $m \to \infty$ with constant k, and p still around Λ_{QCD}, four-momentum conservation immediately leads to $v' = v$. This means that in the infinite mass limit the four-velocity is an invariant

property of the heavy quark, and thus the theory can be re-formulated by replacing the original heavy quark wave function $\psi(x)$ by a phase-transformed variant,

$$h_v(x) = e^{im_Q \not{v}_\mu x^\mu} \psi(x) \ , \tag{2.94}$$

which simplifies the Lagrangian:

$$\begin{aligned}
\mathcal{L} &= \overline{\psi}(i\not{\partial} - m_Q)\psi && (2.95)\\
&= \overline{\psi}(i\not{\partial} - m_Q)e^{-im_Q \not{v}_\mu x^\mu} h_v && (2.96)\\
&= \overline{\psi}\left(i(\not{\partial} e^{-im_Q \not{v}_\mu x^\mu})h_v + ie^{-im_Q \not{v}_\mu x^\mu}(\not{\partial} h_v) - m_Q e^{-im_Q \not{v}_\mu x^\mu} h_v\right) && (2.97)\\
&= \overline{\psi}\left(m_Q(\not{\partial}\, \not{v}_\mu x^\mu)e^{-im_Q \not{v}_\mu x^\mu} h_v + ie^{-im_Q \not{v}_\mu x^\mu}(\not{\partial} h_v) - m_Q e^{-im_Q \not{v}_\mu x^\mu} h_v\right) && (2.98)\\
&= \overline{\psi} e^{-im_Q \not{v}_\mu x^\mu}\left(m_Q(\not{\partial}\, \not{v}_\mu x^\mu) + i\not{\partial} - m_Q\right) h_v && (2.99)\\
&= \overline{h}_v \left(m_Q(\not{\partial}\, \not{v}_\mu x^\mu) + i\not{\partial} - m_Q\right) h_v && (2.100)\\
&= \overline{h}_v i\not{\partial} h_v && (2.101)
\end{aligned}$$

In the last step $(\not{\partial}\, \not{v}_\mu x^\mu) = 1$ was used, which is straightforward to see if written without daggers:

$$\begin{aligned}
\not{\partial}\, \not{v}_\mu x^\mu &= \gamma^\mu \partial_\mu \gamma_\nu v^\nu v_\omega x^\omega && (2.102)\\
&= \gamma^\mu \gamma_\nu \partial_\mu v^\nu v_\omega x^\omega \ , \quad \gamma^\mu \gamma^\nu = \delta_{\mu\nu} && (2.103)\\
&= \partial_\mu v^\mu v_\omega x^\omega \ , \quad v = const && (2.104)\\
&= v^\mu v_\omega \partial_\mu x^\omega \ , \quad \partial^\mu x^\omega = \delta_{\mu\omega} && (2.105)\\
&= v^\mu v_\mu && (2.106)\\
&= 1 && (2.107)
\end{aligned}$$

The Lagrangian 2.101 has the important property that it does not depend on the mass of the heavy quark in the limit $m_Q \to \infty$. This is an additional symmetry arising in the heavy quark limit, which basically states that the spectrum of mesons containing a heavy quark should be independent of the heavy quark flavour. The ground state mass should be fixed by the heavy quark mass, but the mass difference of excited states with respect to the ground state should be flavour symmetric.

A second new symmetry in the heavy quark limit becomes evident when one considers the spin operator $\vec{S}$ with

$$S^i = \frac{1}{2}\gamma_5 \not{v} \not{s}^i \ , \quad i = 1, 2, 3 \ , \tag{2.108}$$

referring to a direction $\vec{s}$ orthogonal to v. An infinitesimal spin rotation

$$h_v \to (1 + i\vec{\epsilon}\cdot\vec{S})h_v \tag{2.109}$$

leaves the Lagrangian invariant:

$$\begin{aligned}
\mathcal{L}' &= (1 - i\vec{\epsilon}\cdot\vec{S})\overline{h}_v(i\not{\partial})(1 + i\vec{\epsilon}\cdot\vec{S})h_v && (2.110)\\
&= \overline{h}_v i\not{\partial} h_v - i(\vec{\epsilon}\cdot\vec{S})\overline{h}_v i\not{\partial} h_v + i\overline{h}_v i\not{\partial}(\vec{\epsilon}\cdot\vec{S})h_v + \mathcal{O}(\vec{\epsilon}^{\,2}) && (2.111)\\
&= \overline{h}_v i\not{\partial} h_v - i(\vec{\epsilon}\cdot\vec{S})\overline{h}_v i\not{\partial} h_v + i(\vec{\epsilon}\cdot\vec{S})\overline{h}_v i\not{\partial} h_v + \mathcal{O}(\vec{\epsilon}^{\,2}) && (2.112)\\
&= \mathcal{L} && (2.113)
\end{aligned}$$

Hence, the Lagrangian is independent of the heavy quark spin direction; the heavy quark spin decouples from the remaining angular momentum (light quark spin s_q, relative orbital angular

momentum L), and is separately conserved. The consequence for meson spectra in the heavy quark mass limit is that mass-degenerate doublets of states are expected which have identical total angular momentum of the light quark $j_{\mathrm{q}} = s_{\mathrm{q}} + L$, but different orientation of the heavy quark spin s_{Q}.

The approximation of infinitely heavy quark mass thus leads to a simplified QCD with additional heavy quark flavour and heavy quark spin symmetries, commonly designated as Heavy Quark Symmetry. It corresponds to a representation of a meson as a light quark moving in a static colour potential. b and c quarks, although classified as heavy quarks, have masses small enough that Heavy Quark Symmetry is only approximately valid; symmetry breaking effects are of the order of $\Lambda_{QCD}/m_{\mathrm{Q}}$. Improved precision can be obtained by representing observables like particle masses in a perturbation series in $1/m_{\mathrm{Q}}$. The infinite mass limit represents the zeroth order term of this expansion. Heavy Quark Effective Theory [63] provides systematic methods for treating the $1/m_{\mathrm{Q}}$ corrections. Further corrections can be applied by expanding in $\alpha_s(m_{\mathrm{Q}})$, but for calculations related to the topic of this thesis usually only lowest order interactions (one gluon exchange) are taken into account.

The Heavy Quark Symmetry relates meson spectra with different heavy quarks, and it predicts that the states within these spectra concentrate in doublets of similar properties. Unfortunately no absolute predictions of the properties are made. This is often done in a quasi-potential approach. The simplest parametrisation of a static colour potential that leads to useful results is the combination of a Coulomb-like one-gluon exchange term and a linear confinement term:

$$V(r) \propto \frac{\alpha_s}{r} + (Ar + B) \tag{2.114}$$

This formula neglects spin-dependent terms. Meson masses can then be obtained as solutions of a Schrödinger-type equation in the given potential.

A $\mathrm{D_{u,d}}$ meson mass spectrum as calculated by Ebert, Faustov, and Galkin [64] is shown in Figure 2.12. This calculation is based on a quasi-potential approach with a relativistic treatment of the light quark. The simple scalar confining potential introduced above is replaced by a combination of scalar and vector potentials. Heavy quark mass expansion is used to first order in $1/m_{\mathrm{Q}}$. As expected from Heavy Quark Symmetry, a doublet structure is visible, albeit broken at the $\Lambda_{QCD}/m_{\mathrm{Q}}$ level. Relative mass differences of the order of 10% are expected in the D meson system. The predictions are confronted with experimental results in Table 2.3. The parameters of the model, namely constituent quark masses ($m_{\mathrm{c}} = 1.55$ GeV/c^2, $m_{\mathrm{s}} = 0.50$ GeV/c^2, $m_{\mathrm{u}} = m_{\mathrm{d}} = 0.33$ GeV/c^2) and the parameters of the confinement potential term are not tuned to the D meson spectrum, but taken from charmonium states and radiative decays. The overall agreement is very good.

Different relative spin orientations of heavy and light quark lead to a pseudo-scalar and a vector meson comprising the ground state doublet. The four lowest-lying orbital excitations correspond to the isosinglet (total angular momentum $J = 0$) and isotriplet (total angular momentum $J = 1$, with component along the quantisation axis of -1,0,1) states expected from pure QCD. The decoupled heavy quark spin transforms this apparent 1+3 configuration into two doublets of the same total angular momentum of the light quark. The figure also shows the first doublet of radial excitations, denoted D' and $\mathrm{D}^{*\prime}$ for the pseudo-scalar and vector state, respectively.

It was already briefly mentioned that a prediction of the decay modes and the width of resonances is more difficult than the mass estimates. Some general remarks shall be made: The average life-time of heavy quarks is large, due to the small amplitude of weak decays. Therefore decays of all heavy mesons except the respective ground state are proceeding almost

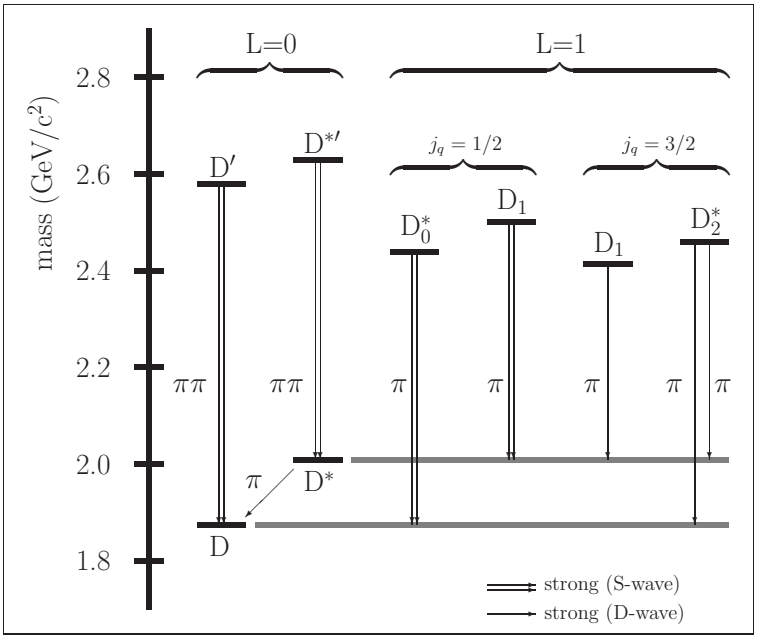

Figure 2.12: *Spectrum of* D *mesons as calculated in Ref. [64]. Also shown are the expected dominant decay modes of the excited* D *mesons. S-wave decays are expected to be fast, therefore the corresponding resonances are expected to be broad. D-wave decays are slow, and therefore the expected widths are small.* D, D^*, $\mathrm{D}_1(j_\mathrm{q} = 3/2)$, *and* D_2^* *are experimentally verified. Evidence is beginning to emerge for the broad* $L = 1$ *states [65]. Conflicting results are available for* $\mathrm{D}^{*\prime}$ *(see Chapter 5). No attempt has yet been made to reconstruct* D'.

state	J_j^P	predicted mass [GeV/c^2] [64]	observed properties [2]	
			mass [GeV/c^2]	width [MeV/c^2]
D	$0^-_{1/2}$	1.875	1.865	
D^*	$1^-_{1/2}$	2.009	2.010	< 0.131
D_0^*	$0^+_{1/2}$	2.438	} (2.461) [65]	(290) [65]
$\mathrm{D}_1(1/2)$	$1^+_{1/2}$	2.501		
$\mathrm{D}_1(3/2)$	$1^+_{3/2}$	2.414	2.422	18.9
D_2^*	$2^+_{3/2}$	2.459	2.459	23
D'	$0^-_{1/2}$	2.579		
$\mathrm{D}^{*\prime}$	$1^-_{1/2}$	2.629	(2.637) [66]	(< 15) [66]

Table 2.3: *Masses of charm mesons as predicted in Ref. [64]. Measurements of the meson masses and width are given where available [2]. Values in brackets are not from Ref. [2], but represent recent observations from CLEO [65] and DELPHI [66].* D_0^*, $\mathrm{D}_1(1/2)$, $\mathrm{D}_1(3/2)$, *and* D_2^* *are orbital excitations (the* $\mathrm{D}_1(1/2)$ *meson is also known as* D_1' *or* D_1^**).* D' *and* $\mathrm{D}^{*\prime}$ *are radial excitations.*

exclusively via the strong interaction. The decay of B^* mesons to B mesons in the $B_{u,d}$ system is an important exception. The mass splitting of these two states is too small (≈ 46 MeV/c^2) for a decay via strong interaction, because this would involve at least one pion in the final state. B^* mesons do therefore decay electro-magnetically: $B^* \to B\gamma$. In any case, decays of excited heavy-light mesons always proceed within the spectrum of the respective flavour combination, in one or more steps towards the ground state of the spectrum, which then decays weakly.

Decays via the emission of a single pion are favoured due to the available phase space. However, parity and angular momentum conservation restrict the possible single-pion transitions to the ones indicated by arrows in Figure 2.12. In the case of the orbitally excited D mesons, this leads to the five possible decay modes indicated in the figure. The decays of the $j_q = 3/2$ doublet involve higher partial waves (D-wave), which are expected to be much slower than S-wave decays. Therefore the $D_1(3/2)$ and D_2^* are comparatively narrow (measured widths ≈ 20 MeV/c^2), whereas the $j_q = 1/2$ doublet members are broad (≈ 300 MeV/c^2 [65]).

The kinematically favoured decay mode of the $D^{(*)\prime}$ is presumed to be the direct three-body decay into a $D^{(*)}\pi\pi$ final state. This is an S-wave decay and thus generally expected to be broad, although a model exists [67] which estimates the partial width of this decay mode to be less than 1 MeV/c^2. Decays via an intermediate orbitally excited D meson could also contribute to the same final state; these decay widths are estimated to be several MeV/c^2 by the same model. If enough phase space is available, $D^{(*)\prime}$ decays to a $D^{(*)}\rho$ state with $\rho \to \pi\pi$ might also be allowed. The decays via orbitally excited states include S-wave (e.g. $D^{*\prime} \to D_1(1/2)\pi$, $D_1(1/2) \to D^*\pi$), and D-wave transitions (e.g. $D^{*\prime} \to D_2^*\pi$, $D_2^* \to D^*\pi$). The decays involving a ρ are P-wave transitions. The higher partial waves are expected to be suppressed due to lack of phase space.

To summarise, the ability to predict properties of resonances from first principles of QCD is limited. Effective theories allow a rather precise calculation of the masses of mesons containing a heavy quark, but the prediction of decay rates and thus widths is at a clearly non-satisfactory level of semi-quantitative estimates. Further experimental input, especially concerning the wide orbital excitations and radial excitations is needed to develop and verify new mathematical approaches. Insights into the current experimental status of orbitally and radially excited D mesons will be given in Chapter 5 of this thesis.

2.6 Shortcomings and Possible Extensions of the Standard Model

Although it is technically very difficult to deal with QCD, the theory is beautifully consistent and symmetric. It might seem quite reasonable to suspect that QCD provides a fundamental description of the phenomena of Nature. Yet, viewed at the scale of the Standard Model, there is reason to believe that there is physics beyond what is experimentally accessible today. The last section of this chapter will briefly outline the shortcomings of the Standard Model, and it will mention a few important concepts for possible extensions.

A prime example for the incompleteness of the current Standard Model is the electroweak interaction. Without discussing the implications of this in detail, the gauge bosons $W^\pm$ and Z of the electroweak interaction were introduced as particles of large invariant mass in Table 2.2. In fact, gauge invariance requires that the gauge bosons be *massless*: Gauge bosons of mass M_G introduce mass terms of $M_G^2 A_\mu A^\mu$ into the Lagrangian, which are not gauge invariant unless $M_G = 0$. One possible mechanism which saves gauge invariance despite the obvious presence of

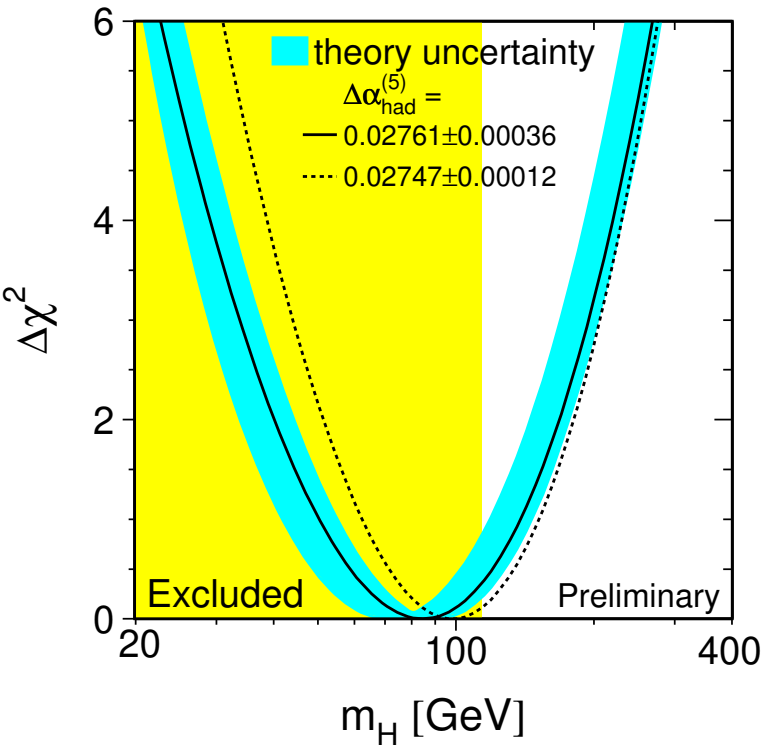

Figure 2.13: *Indirect estimate of the Standard Model Higgs mass by the LEP experiments and SLD [69], and mass region excluded by direct searches [70]. The curve corresponds to the Standard Model parameter fit quality relative to the best fit obtained for* $m_{Higgs} \approx 100$ GeV/c^2. *Two curves are given for two different estimates of the strong coupling constant* α_s. *The shaded region indicates the mass range which is excluded by direct Higgs searches at LEP.*

massive gauge bosons is the Higgs mechanism [68]. According to the Higgs picture, all gauge bosons are indeed initially massless. They acquire an *effective* mass by interaction with a scalar Higgs field. This field has a non-zero vacuum expectation value; therefore the interaction with the Higgs field does not vanish even at lowest energies. The Higgs field is can also be used to explain the fermion masses, for which no other satisfactory explanation has been found so far. The Higgs mechanism is thus an essential part of the Standard Model.

An important consequence of the presence of a Higgs field is the prediction of an associated scalar boson. This Higgs boson can be produced directly in reactions like the Higgsstrahlung process, where a e^+e^- annihilation produces a virtual Z which then decays into ZH. Besides direct production of Higgs particles, they, or something equivalent[12], produce noticeable loop corrections to well-known Standard Model processes. Unfortunately the Higgs loop corrections depend only logarithmically on the Higgs mass, and therefore estimates of the Higgs mass from these loop corrections are very imprecise. Direct measurements at LEP have set a lower limit on the Standard Model Higgs boson mass of 114.1 GeV/c^2 [70]. But, as Figure 2.13 shows, under the assumption that the Standard Model Higgs mechanism is realised in Nature, the Higgs mass should not be too far above 100 GeV/c^2. The Higgs mass should in any case be below about 1 TeV/c^2, because some Standard Model cross-sections can not be simply extrapolated beyond $\sqrt{s} \approx 1$ TeV: For example the WW $\rightarrow$ WW scattering cross-section diverges for large $\sqrt{s}$ if only γ- and Z-exchange graphs are taken into account. This WW cross-section violates

[12]Other models show for example that the Higgs mechanism would also work with composite instead of elementary Higgs bosons.

the unitarity boundary at about 1 TeV. The presence of a Higgs exchange graph fixes these problems by destructive interference with the other channels [71]. In summary, it is clear that the Standard Model with the particles discovered so far is only a low energy approximation. The Higgs boson as missing part of the Standard Model, or any alternative addition to or correction of the theory, has to appear below an energy scale of about 1 TeV.

A further hint that the Standard Model might not be a fundamental theory is the existence of more than one interaction between particles. At low energy, the four basic interactions mentioned in the beginning of this chapter are distinguishable. Electro-magnetic and weak force have been unified into a single electroweak interaction with different low-energy manifestations. This raises the question whether a similar unification with the strong and maybe even gravitational force might happen at higher energy scales. This idea is supported by the energy-dependence of the coupling constants described by the β functions of Equations 2.31 and 2.32:

$$\beta_{QCD}(\alpha_s(Q^2)) \approx \frac{2N_{flav} - 33}{12\pi}\alpha_s^2(Q^2) \tag{2.115}$$

$$\beta_{QED}(\alpha_{EM}(Q^2)) \approx \frac{4N_{chferm}}{12\pi}\alpha_{EM}^2(Q^2) \tag{2.116}$$

The running of the weak coupling constant $\alpha_{weak} = g'^2/4\pi$ is defined by a similar relation [8]:

$$\beta_{weak}(\alpha_{weak}(Q^2)) \approx \frac{2N_{ferm} - 22}{12\pi}\alpha_{weak}^2(Q^2) \tag{2.117}$$

N_{ferm} is the number of fermions participating in loop corrections. All coupling constants show a different energy dependence, and in fact it turns out their values converge towards each other. With N_{flav}, N_{chferm}, and N_{ferm} including only Standard Model particles, there is unfortunately no energy scale where all three couplings become identical (see Figure 2.14a). The introduction of new particles might change this; additional particles at higher energies modify the evolution of the coupling constants and can lead to a single unification scale, as indicated in Figure 2.14b.

The model that was used to calculate the energy dependence of the coupling constants in Figure 2.14b belongs to the class of supersymmetric theories [73]. Supersymmetric theories have of course not been introduced to support a unification of forces. Instead, they are theoretically very interesting extensions of the Standard Model. Supersymmetry is a symmetry between fermions and bosons, which is the only gauge symmetry not realised in the Standard Model. This symmetry is realised by adding "super-partners" to all Standard Model particles, leading to a 1:1 correspondence of fermions and bosons. Of course, if Supersymmetry is realised in Nature, it must be broken, because otherwise the super-partners would have the same mass as their Standard Model partners.

It was already mentioned that Supersymmetry could help in the unification of forces. Another advantage is related to the unification energy scale: The Standard Model offers no explanation for the large range of relevant energy scales. Whereas typical electroweak scales are in the region of 100 GeV, the regime where all forces become of comparable size is expected around 10^{16} GeV. This leads to problems because the Standard Model higher order corrections to the Higgs and W boson masses diverge quadratically at very large energy scales if there is no new physics below these large energy scales. This problem is solved in Supersymmetry, where equal numbers of fermions and bosons contribute to the corrections. Since fermions and bosons enter with opposite signs, their contributions cancel if the mass difference of the respective super-partners is not too large, i.e. the masses of the additional Supersymmetry should be of the order of 1 TeV [74].

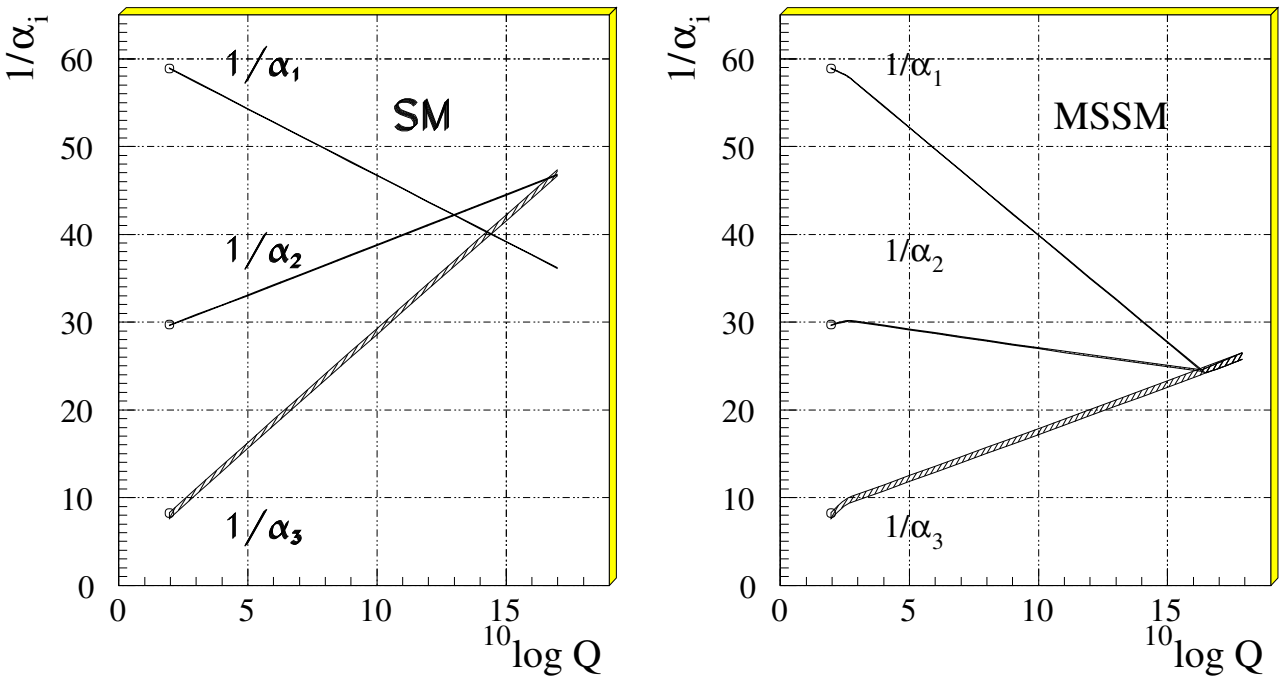

Figure 2.14: *Evolution of coupling constants* $\alpha_1 = \alpha_{QED}$, $\alpha_2 = \alpha_{weak}$, *and* $\alpha_3 = \alpha_s$ *[72]. a) Evolution with only Standard Model particles contributing to higher order corrections. b) Additional MSSM particles contributing to higher order corrections above* ≈ 1 TeV.

Another shortcoming of the Standard Model is the number of its parameters, which seems too large for a fundamental theory. A total of 18 parameters are needed [74]:

- 3 gauge couplings
- 6 quark masses
- 3 charged lepton masses
- 3 generalised Cabibbo weak mixing angles
- 2 weak boson masses
- 1 CP-violating Kobayashi-Maskawa phase

Possibly a CP-violating strong interaction parameter adds to the above list. Non-zero neutrino masses introduce at least seven more parameters:

- 3 neutrino masses
- 3 mixing angles
- 1 CP-violating phase

Supersymmetry, if leading to a single unification scale, could remove at least one parameter from this list: The weak mixing angle $\cos\theta_W$ is precisely predicted in the framework of this theory. It has to be pointed out that the most general formulation of a supersymmetric theory currently leads to about 100 free parameters, which might look as a serious drawback. However, the number of parameters can be reduced once a specific manifestation of Supersymmetry is

selected. In any case the question of whether it is possible to reduce the large number of parameters of the Standard Model significantly is still open.

Supersymmetry as a local symmetry would furthermore include gravity automatically, which addresses another point where the Standard Model proves to be incomplete. Gravity might also ultimately be explained in terms of a string theory, for which hints are available that it seems to require Supersymmetry [74]. Unfortunately the connection of local supersymmetry and gravity, as well as details of string theories, are not yet mathematically developed. So far only rough concepts of how such theories might look like are available.

Other approaches besides Supersymmetry might also deliver viable extensions of the Standard Model. The large number of different particles might for example be explained by a further level of substructure. Other models try to explain the large hierarchy of energy scales by additional space dimensions. The unitarity violation of the WW cross-section might be resolved by a significant increase of the W boson interaction strength at high energies. An overview of many alternative theories is given in Ref. [75].

In summary, the picture of the universe described in terms of physics is far from being complete. Three classes of problems remain: Even with existing and seemingly complete theories like QCD, it is often not possible to describe physical processes, due to mathematical problems. Secondly, crucial parts of today's theories have not yet been verified experimentally. Above all, experimental evidence for the Higgs mechanism is still lacking. The third class of problems is incompleteness of the theories. This refers to the fact that no satisfactory description has yet been found for gravity at small scales, and the Standard Model does in some respects give the impression that it can not be entirely fundamental. All this leads to the desire for further and improved experiments, like the TESLA linear collider project described in Chapter 6, to get first insights into how the Standard Model is embedded into a more fundamental theory.

Chapter 3

Experimental Setup

It was already indicated in the previous chapter that this thesis deals with investigations of e^+e^- annihilation events. Chapters 6 to 8 present pure simulation studies for the TESLA linear e^+e^- collider project, without reference to actual experimental data. The central part of this thesis, the b quark hadronisation study (Chapter 4) and the $D^{*\prime +}$ search (Chapter 5), make use of data that have been taken with the OPAL detector[1] at CERN[2]. This chapter is intended as short overview of the most important features of the LEP accelerator and the OPAL detector and dataset. Detailed descriptions of the detector are available elsewhere [76].

3.1 The LEP Accelerator

The source of e^+e^- collisions for the OPAL experiment, as well as the ALEPH, DELPHI, and L3 experiments, was the e^+e^- accelerator, storage ring and collider LEP[3], situated approximately 100 m below the Swiss and French surface near Geneva. LEP had a diameter of almost 10 km. In the time period from 1989 to 1995, it was operating at a beam energy of about 45.6 GeV or half of the Z mass, continuously accelerating electron and positron beams in opposite direction. This operation energy was chosen to take advantage of the Z resonance in the e^+e^- collision cross section, which enhances the total cross section by several orders of magnitude with respect to the non-resonant photon exchange cross section which is dominant at lower energies (see Section 2.3). This allowed about 4 million hadronic Z decays to be recorded by each experiment. Starting in 1996, the LEP energy was gradually increased up to a maximum of 209 GeV achieved in 2000. Main physics goals pursued in this LEP2 programme were a detailed investigation of $W^\pm$ properties, and the search for new phenomena beyond those previously accessible to accelerator-based particle physics. LEP was shut down and dismantled at the end of 2000.

3.2 The OPAL Detector

One of the four detector systems operating at LEP was OPAL. A perspective view of the OPAL detector can be seen in figure 3.1, cross-sections are shown in figure 3.2. Two coordinate

[1] **O**mni-**P**urpose **A**pparatus at **L**EP

[2] 'European Laboratory for Particle Physics' — the abbreviation has been kept from the first name of the laboratory: **C**entre **E**uropéen pour la **R**echerche **N**ucléaire.

[3] **L**arge **E**lectron **P**ositron collider

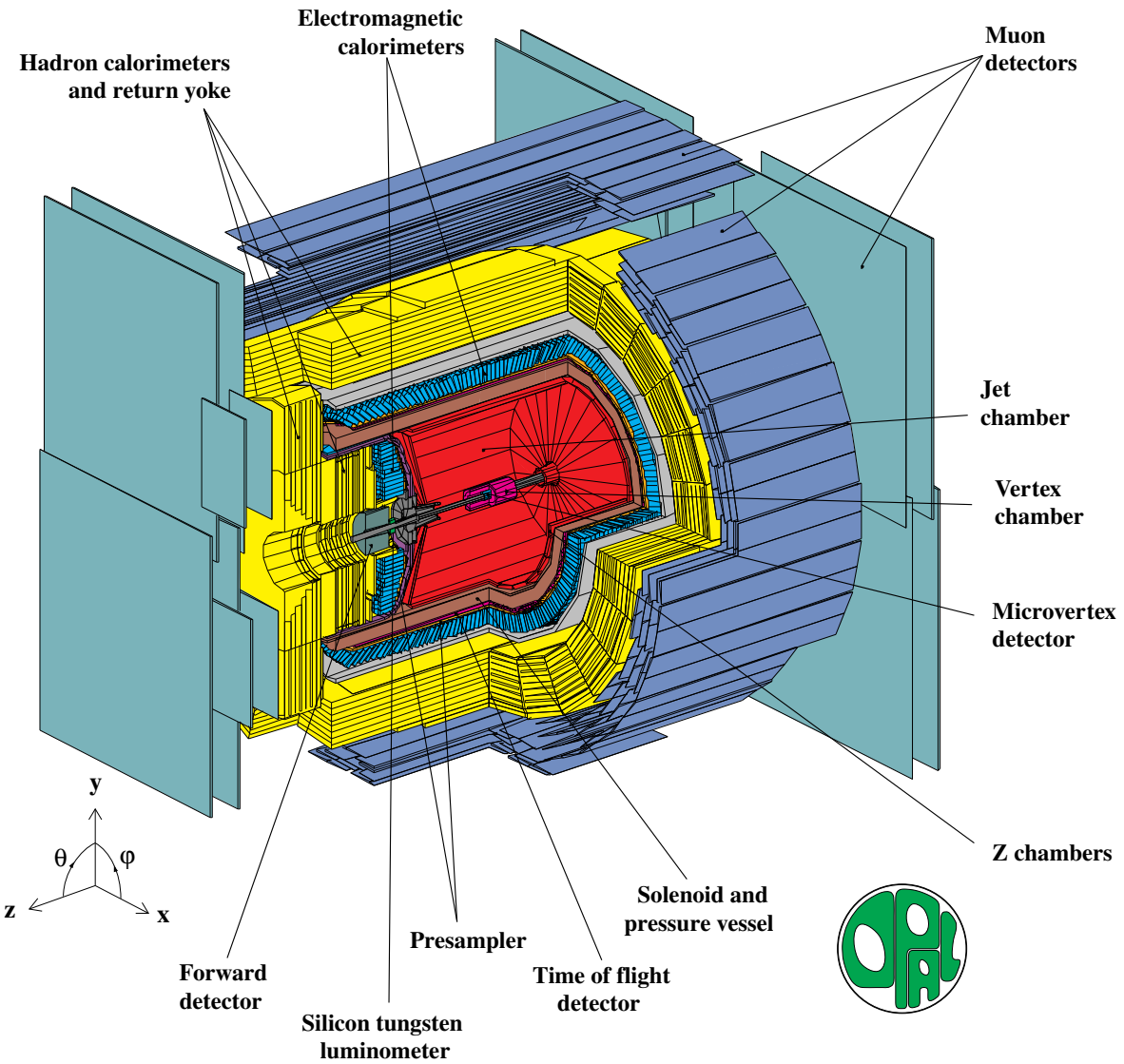

Figure 3.1: *Perspective view of the OPAL detector*

systems are usually chosen to describe geometrical issues concerning the detector: A right-handed Cartesian system is defined using the electron flight direction as z-axis, thus leaving the area perpendicular to the beam direction to be called xy-plane. The x-axis points towards the centre of the LEP ring. An equivalent, but polar coordinate system shares the same z-axis with the Cartesian one. The azimuthal angle φ is counted from the x-axis, the polar angle θ describes the angular distance to the z-axis. Because the e^+ and e^- beams at LEP had identical energy, all LEP detectors were symmetric with respect to the xy- or $r\phi$-plane cutting the beam at the (ideal) interaction point.

The tracking and particle identification system of the OPAL detector relied on the following sub-detectors:

- Silicon micro-vertex detector (SI)
- Central vertex chamber (CV)
- Central jet chamber (CJ)
- z-Chambers (CZ)

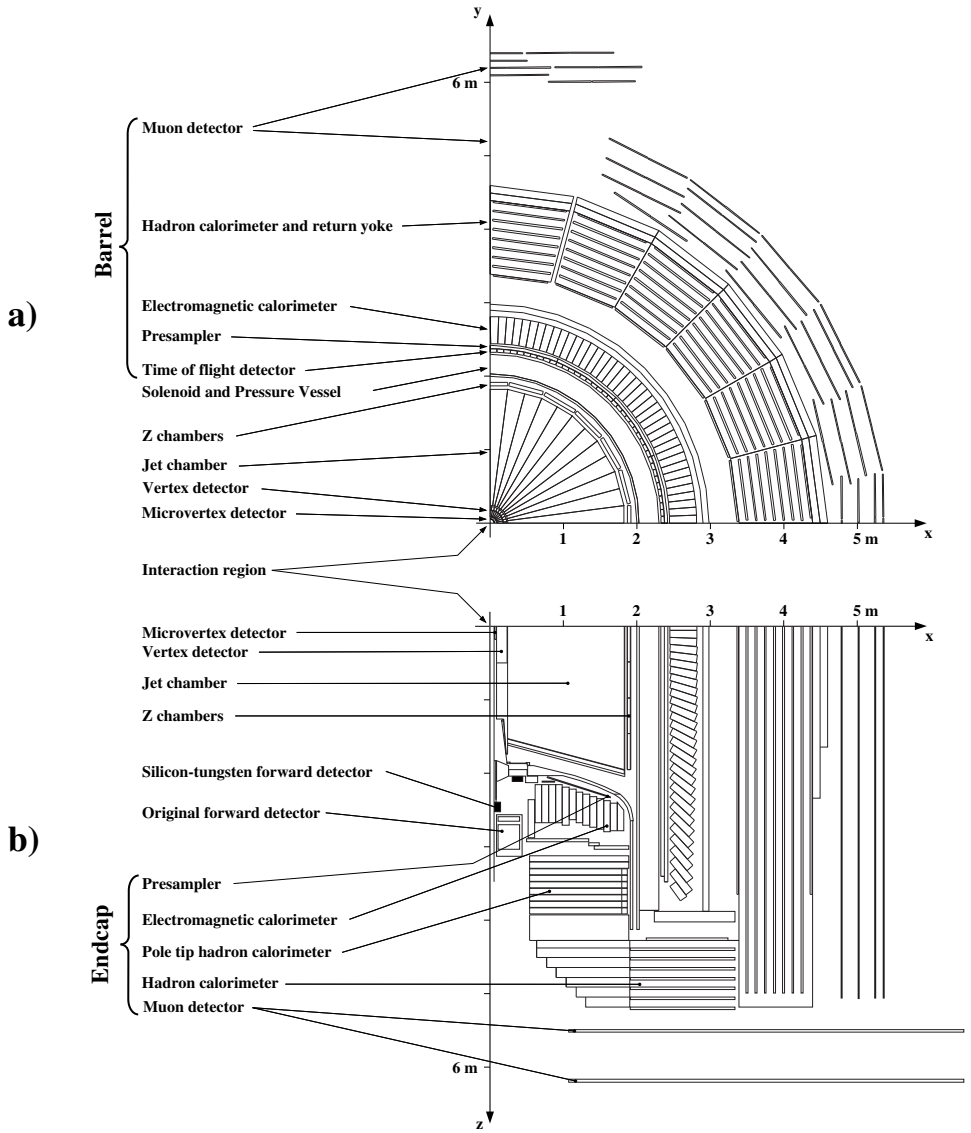

Figure 3.2: *Cross section of the OPAL detector perpendicular (a) and parallel (b) to the beam axis*

Directly outside a beryllium beam pipe, the silicon micro-vertex detector was mounted. It had been installed in 1991 and consisted of two concentric layers of silicon strip detectors. Each strip originally had three sections along the beam pipe. The inner layer, at a distance of 6.1 cm from the centre of the beam pipe, consisted of 11 silicon strips; another 14 strips made up the outer layer, whose radius was 7.5 cm. The length of the detector was 18.3 cm, covering an angular range of $|\cos\theta| < 0.83$ with the inner, and $|\cos\theta| < 0.77$ with the outer layer. The intrinsic spatial resolution in $r\phi$ was about 10 μm. No z measurement was possible until a detector upgrade in the 1992/1993 winter shutdown, where the detector was exchanged with an enhanced version, delivering readout capabilities in $r\phi$ and z. Since then, a z resolution of 15 μm had been achieved for particles that pass the silicon strips perpendicularly. At the end of 1995, a further upgrade extended the angular coverage of the detector.

Surrounding the silicon detector, a first drift chamber called 'central vertex detector' (CV) was installed. The axial CV occupied a radial range from 8.8 cm to 17.5 cm with 36 cells, each containing 12 staggered signal wires parallel to the beam direction. Within its acceptance region of $|\cos\theta| < 0.95$, it delivered an $r\phi$ resolution of 55 μm, and a z resolution of 4 cm. It

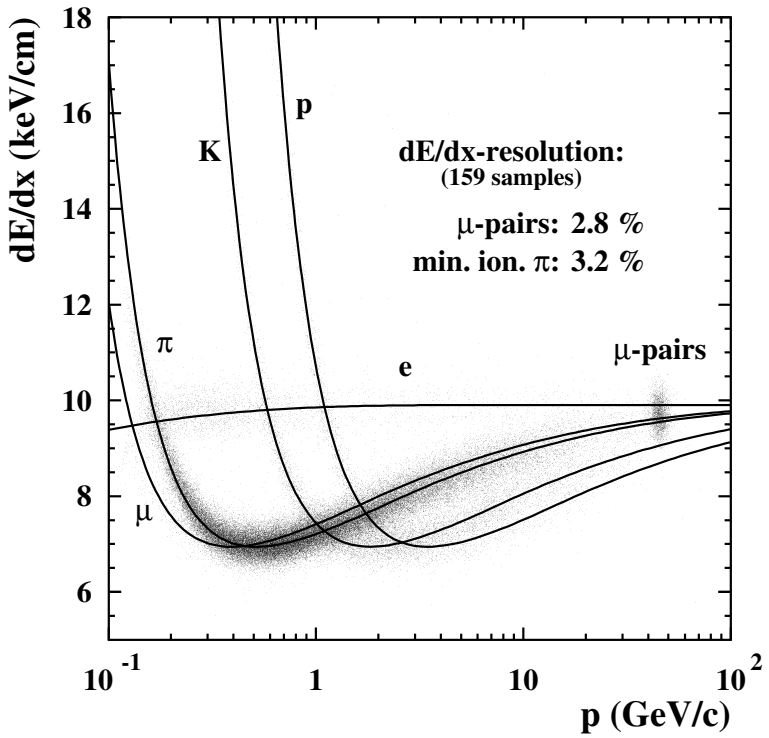

Figure 3.3: $\mathrm{d}E/\mathrm{d}x$ *distribution at OPAL. Each dot represents the* $\mathrm{d}E/\mathrm{d}x$ *value measured for a single track. The curves indicate the expected* $\mathrm{d}E/\mathrm{d}x$ *values depending on the momentum of a particle according to the Bethe-Bloch-equation for different particles. The agglomeration of muon pairs at the beam energy of about* 45.6 GeV/c *is caused by* $\mathrm{Z} \rightarrow \mu^+\mu^-$ *reactions. The plot is optimistic in the sense that only tracks are shown that feature 159* $\mathrm{d}E/\mathrm{d}x$ *measurements along the trajectory. This is only possible if the particle crosses the central jet chamber in its full radial extension and delivers a signal at every sense wire.*

was followed by a second part of the central vertex chamber which improved the z resolution: The 36 cells of the so-called CV stereo chambers were very similar to the axial chambers, apart from the orientation of the signal wires: The angle between a wire parallel to the beam axis and a stereo wire was 4°. The combined information of axial and stereo wires led to an overall z resolution of about 1 mm. The CV stereo chambers extended radially to 23.5 cm.

The largest component of the tracking system was the central jet chamber, a drift chamber with 24 sectors each having 159 signal wires. It extended over 4 m along the beam direction, with an inner radius of 25 cm and an outer radius of 185 cm. An angular range of $|\cos\theta| < 0.73$ was covered by all 159 wires, while particles in the range of $0.73 < |\cos\theta| < 0.98$ could be detected by at least 8 wires depending on the angle. The $r\phi$ resolution of the jet chamber of 135 μm was achieved by drift time measurement in combination with precise knowledge of the wire positions. For most hits, the z coordinate was reconstructed to within $4.5 - 6$ cm by charge division measurements on both ends of the wires. For tracks with $|\cos\theta| > 0.73$, the z resolution was improved by determining the position of the last signal wire that was hit.

For tracks in the barrel region of the detector, $|\cos\theta| < 0.72$, the z measurement was enhanced by the outermost detector subsystem of the central tracking devices, the z-chambers. These were flat drift chambers with wires perpendicular to the beam direction, thus allowing a precise measurement of z to within 100 to 300 μm, depending on the drift distance of a particle within the chambers. Here, the φ measurement was obtained by charge division with a resolution of 1.5 cm.

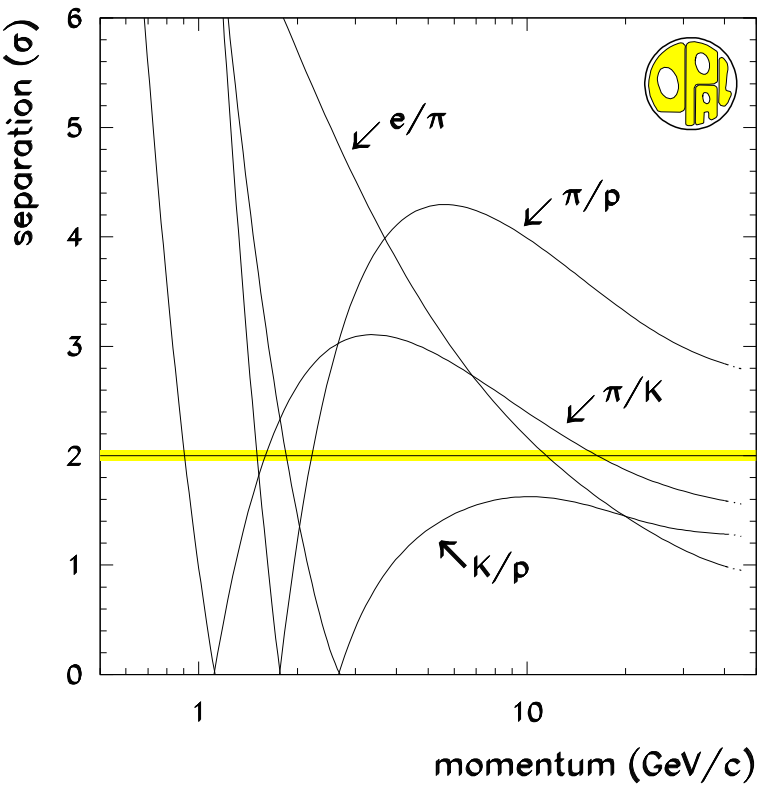

Figure 3.4: *Particle type separation power under realistic circumstances for tracks within hadronic* Z *events at OPAL*

The whole tracking system was encapsulated in a pressure vessel, keeping the chamber gas[4] at 4 bar. A high pressure allowed a more precise measurement of the specific energy loss, $\mathrm{d}E/\mathrm{d}x$, of a particle within the jet chamber, at the cost of enlarging the error on momentum measurement especially for low momenta due to multiple scattering. The choice of a suitable pressure was a compromise between both effects.

The specific energy loss of a particle depends on its velocity (Bethe-Bloch-equation). In combination with the momentum of a particle, the energy loss is used to estimate the mass and thus the type of a particle. With the OPAL detector, the specific energy loss was measured with an accuracy of 3.8% for minimum ionising particles in jets (see also figure 3.3). The resulting separation capabilities for charged hadrons are shown in figure 3.4.

The track fit within the central jet chamber included information from all parts of the central tracking system. The average momentum resolution obtained at OPAL, using the information of CV, CJ and CZ described above, has been found to be

$$\frac{\sigma_{p_t}}{p_t} = \sqrt{0.02^2 + (1.3 \times 10^{-3}(\ \mathrm{GeV}/c)^{-1})^2 \times p_t^2}\ . \tag{3.1}$$

The constant term is due to multiple scattering in the chamber medium. The second term describes the limitation of the resolution by geometrical issues and the magnetic field. Including the additional tracking information from the silicon micro-vertex detector, the coefficient of the second term improves to $1.25 \times 10^{-3}(\ \mathrm{GeV}/c)^{-1}$.

The entire tracking system was embedded in a solenoid providing a 0.435 T magnetic field parallel to the beam axis. The resulting curvature of the particle trajectories allowed a precise

[4]argon, butane and isobutane

momentum measurement of charged particles in the $r\phi$ plane. A set of scintillators for time of flight measurements surrounded the magnet solenoid. It was mainly used for fast triggering and rejection of events that were caused by cosmic rays.

A system of calorimetric detectors was mounted outside the solenoid. The electro-magnetic calorimeter, which consisted of approximately 12 000 lead glass blocks, provided an azimuthal coverage up to polar angles of $|\cos\theta| < 0.98$. To improve the shower energy and spatial resolution, a preshower detector (presampler) made of streamer chambers was mounted between the solenoid and the electro-magnetic calorimeter. For the analysis presented in Chapter 5, the barrel presampler at a radius of 2.4 m is used to improve the z information for tracks without z-chamber hits. The spatial resolution of the barrel presampler was measured to be $2-6$ mm.

A sampling hadron calorimeter was integrated into the iron return yoke, using limited streamer tubes. Its coverage of up to $|\cos\theta| < 0.91$ was extended to $|\cos\theta| < 0.99$ by a pole tip calorimeter operating on multi-wire proportional chambers. Outside the calorimeter barrel and endcaps additional drift chambers (barrel) and streamer tube arrangements (endcaps) were mounted to function as muon detectors.

Intended mainly for luminosity measurements, forward calorimeters with a polar angular acceptance between 25 and 120mrad were installed. The part closest to the beam pipe was covered by a silicon tungsten sampling calorimeter; other technologies in use included proportional tubes, scintillator sandwiches, and lead scintillator calorimeter modules.

3.3 OPAL Dataset and Monte Carlo Samples

The LEP accelerator was shut down for a few months each winter, when electrical power is most expensive in Geneva. These shutdown periods were used for machine and detector maintenance and upgrades. As a consequence, the detector setup, calibration, and data quality vary among the datasets of different years. Both OPAL analyses presented in this thesis require reconstruction of secondary vertices. The vertex reconstruction performance is insufficient for data that were taken without silicon micro-vertex detector, and therefore these datasets are not used here. This concerns a few 100k events that had been taken in 1989–1991. Part of the 1994 dataset, where SI became inoperational after a cooling system failure, is also not used. About 3.5 million hadronic events from the LEP1 period of 1989–1995 remain for analysis.

During this LEP2 programme, a further $\approx$ 400k events were recorded at the Z pole for detector calibration purposes. These calibration data have not been used for the $D^{*/+}$ search, because at the time this analysis was finalised the calibration data were systematically not understood well enough. This has changed over the last years, and so the full Z dataset of the years 1992–2000, except the aforementioned part of the 1994 data, could be used for the investigation of the b fragmentation function.

An overview of the OPAL datasets taken at or close to the Z resonance is given in Table 3.1. A few essential differences of the individual datasets are specified in the following: The first version of the silicon micro-vertex detector, used in 1992, had only $r\phi$ read-out. Silicon z read-out was introduced between 1992 and 1993. 1994 saw the extension of the outer SI layer. Before the 1995 run, also the inner layer was upgraded to a longer version. In 1997 (after the Z run), a sector of CV stereo became inoperational.

Dedicated Jetset 7.4 [17] Monte Carlo samples are available with detailed simulation of the detector setup of all years [77], and for all energies of data-taking. The OPAL tune of the Jetset 7.4 Monte Carlo generator uses the Lund string hadronisation scheme per default with a Bowler parametrisation for uds quarks ($a = 0.11; b = 0.52$), and a Peterson parametrisation

year	$\sqrt{s}$	sample size					
		data	JT $q\overline{q}$	JT $b\overline{b}$	JT $c\overline{c}$	HW5 $q\overline{q}$	HW6 $q\overline{q}$
1992	m_Z	0.76M	1.24M	0.40M	0.40M	—	—
1993	m_Z, $m_Z - 1.8$ GeV	0.57M	1.20M	0.33M	0.33M	—	—
1993	$m_Z + 1.8$ GeV	0.14M	0.28M	0.08M	0.08M	—	—
1994	m_Z	1.34M	3.99M	3.74M	2.00M	2.00M	5.00M
1995	m_Z, $m_Z - 1.8$ GeV	0.56M	1.20M	0.30M	0.30M	—	—
1995	$m_Z + 1.8$ GeV	0.13M	0.30M	0.08M	0.08M	—	—
1996	m_Z	0.03M	0.08M	—	—	—	—
1997	m_Z	0.05M	0.1M	—	—	—	—
1998	m_Z	0.09M	0.1M	—	—	—	—
1999	m_Z	0.12M	0.1M	—	—	—	—
2000	m_Z	0.12M	0.1M	—	—	—	—
sum		3.91M	8.69M	4.93M	3.19M	2.00M	5.00M

Table 3.1: *OPAL datasets at centre-of-mass energies $\sqrt{s} \approx m_Z$ (only data taken with silicon microvertex detector), and general purpose Monte Carlo samples used in this thesis. The sample sizes are given in units of a million events.* $q\overline{q}$ *denotes five-flavour hadronic event samples.* $b\overline{b}$ *and* $c\overline{c}$ *samples are dedicated heavy flavour datasets. Jetset 7.4 is abbreviated as JT, Herwig 5.9 as HW5, Herwig 6.2 as HW6. All OPAL data and Monte Carlo samples listed in this table are used for the* b *quark hadronisation study in this thesis. The* $D^{*\prime +}$ *analysis uses only data and Monte Carlo from 1992–1995, and only Jetset* $q\overline{q}$ *samples.*

for charm ($\epsilon_c = 0.031$) and bottom ($\epsilon_b = 0.0038$) quarks. A total of 8.69 million five-flavour hadronic events is available, plus 4.93 million $b\overline{b}$ and 3.19 million $c\overline{c}$ events. Further Monte Carlo samples were produced with the Herwig generator [22]. Two million five-flavour hadronic events are available from Herwig 5.9, along with another five million Herwig 6.2 events. A detailed list of all subsamples is shown in Table 3.1.

The $D^{*\prime +}$ search in Chapter 5 is comparatively insensitive to details of the detector configuration. The data are therefore not separated into subsets. The Monte Carlo simulation is mixed from samples of all detector setups in approximately the same ratio as the data. Since production of radially excited $D^{*\prime}$ mesons is not included in Jetset by default, 0.6 million $b\overline{b}$ and $c\overline{c}$ events with at least one $D^{*\prime +}$ meson per event were generated using Jetset 7.4.

The investigation of b quark hadronisation presented in Chapter 4 is sensitive to changes in the detector configuration and calibration, and therefore it is performed independently for different years. Furthermore, the data samples 2 GeV above the Z resonance have to be treated separately: As explained in Section 2.3, they are affected much more strongly by initial state radiation than the runs at or below the Z. The energy distribution of b hadrons is therefore noticeably different.

The full Jetset 7.4 $q\overline{q}$ sample with 1994 detector simulation, one million events of the Jetset 7.4 $b\overline{b}$ 1994 sample, and one million events of the Jetset 7.4 $c\overline{c}$ 1994 sample were created with Jetset 7.404, whereas all other samples were generated with Jetset 7.408. During the Monte Carlo studies performed for the b hadronisation analysis it was found that th older Jetset variant contains a coding bug which distorts the b hadron energy spectrum slightly. The average energy is shifted by 1.0%. The energy spectrum of primary charmed hadrons is not affected. The old $c\overline{c}$ sample is therefore used in both analyses. The $q\overline{q}$ and $b\overline{b}$ samples are corrected with energy correction weights obtained from a comparison of two million Jetset 7.404

events and two million Jetset 7.408 events created for this purpose. The correction weights fix only the energy distribution; it is unclear whether other observables, e.g. angular distributions, are also affected. The $b\overline{b}$ events of these samples, with correction weights enabled, are only used for cross-checks in the b hadronisation study and do not enter the final results. The effect on the $D^{*\prime +}$ search is only a small fraction of the systematic uncertainty assigned to the analysis due to limited knowledge of the b hadron energy distribution. Therefore the affected samples are used in this analysis.

The Jetset 7.4 $q\overline{q}$ sample differs from the remaining Monte Carlo (including the Jetset 7.404 $b\overline{b}$ and $c\overline{c}$ samples) in another respect. The Peterson fragmentation function is used with different parameters for b ($\varepsilon_b = 0.0057$) and c ($\varepsilon_c = 0.046$) quark hadronisation. These values are comparatively far from current estimates of these parameters, as for example obtained in Chapter 4.

Chapter 4

Bottom Hadronisation at 90 GeV

The theoretical difficulties arising in the description of the fragmentation and hadronisation of heavy quarks have been discussed in Chapter 2. The predictions of the parton shower/cluster hadronisation generator Herwig and of the parton shower/string hadronisation generator Jetset will now be compared and tuned to OPAL data.

A direct measurement of the light cone momentum fraction z describing the hadronisation is not possible, because the energy of the b quark after perturbative shower evolution and before hadronisation is not observable. Furthermore, the distinction between perturbative fragmentation and non-perturbative hadronisation is only valid in the framework of a specific model, and so is the definition of z itself. For example, z is not defined in the cluster model used by Herwig. A model-independent and observable quantity is the ratio x_{E} of the energy of a B hadron[1] and the energy of the b quark directly after pair creation, where both quantities are measured in the $\mathrm{e^+e^-}$ centre-of-mass system. This reference frame is usually approximated by the laboratory frame, which differs from the $\mathrm{e^+e^-}$ centre-of-mass frame only if electron or positron emit a photon before annihilation. This initial state radiation is modelled in the Monte Carlo. Likewise, the initial energy of the b quark is approximated as the beam energy. x_{E} will in the following often be referred to as "scaled energy" of a B hadron.

The hadronisation process would be best constrained by a measurement of the x_{E} distribution of primary B hadrons. Primary B hadrons are those that are produced directly in the hadronisation process, as opposed to secondary B hadrons that are decay products of the primary B hadrons. Unfortunately it is very difficult experimentally to identify the primary B hadrons, and therefore the weakly decaying B hadron will be reconstructed instead. The latter can be identified easily due to its long life-time and the large transverse momentum occurring in b quark decays due to the large mass difference to the c quark. The relation to the energy distribution of primary hadrons is then taken from the Monte Carlo model.

The investigation of the hadronisation process of b quarks requires a reconstruction of the energy of B hadrons with very good resolution. The B hadron reconstruction of the analysis presented here (as well as the presentation of this part of the analysis) follows closely a recent OPAL publication on orbitally excited B mesons [78], where similarly good energy resolution is required and the B hadron reconstruction is tuned accordingly. Main difference between the mentioned analysis and the work presented here is that the event-wise b tag has been replaced by a tag on the opposite hemisphere only. This is done at the cost of reduced reconstruction

[1] All hadrons containing a b quark will be called B hadrons throughout this thesis. This includes also baryons with a b quark. The name is chosen to reflect the fact that B mesons are the dominant contribution to the sample of hadrons containing a b quark.

efficiency at the same amount of impurity. Other than in the mentioned analysis, this efficiency loss is more than compensated for by a significant gain in systematic understanding of the data. Correlations between b tag result and B hadron energy reconstruction, which are not modelled well enough in Monte Carlo, are minimised.

4.1 Event Selection and Monte Carlo Optimisation

Hadronic events are selected as described in Ref. [79], giving a hadronic Z selection efficiency of $(98.4 \pm 0.4)\,\%$ and a background of less than $0.2\,\%$. A data sample of about 3.91 million hadronic events is selected, distributed over data taking periods as detailed in Chapter 3. Each event is divided into two hemispheres by the plane perpendicular to the thrust axis and containing the interaction point of the event. The thrust axis is calculated using tracks and electro-magnetic clusters not associated with any tracks. To select events within the fiducial acceptance of the silicon micro-vertex detector and the barrel electro-magnetic calorimeter, the thrust axis direction is required to satisfy $|\cos\theta_T| < 0.8$.

A total of 23.81 million Monte Carlo events are used: 16.81 million events were created with Jetset 7.4, 2 million events were generated with Herwig 5.9, and 5 million events were produced by Herwig 6.2. Detailed information on the individual samples is given in Chapter 3. The same reconstruction algorithms as for data are applied to simulated events.

Since this analysis requires as good as possible a simulation of the detector response, all steps are performed separately for the data of different years, where detector upgrades and recalibrations might lead to different conditions. Separate samples of Jetset Monte Carlo are available for all years. Herwig Monte Carlos are only available for the largest homogeneous dataset, taken in 1994, and therefore Herwig-related studies are performed exclusively for this dataset.

A specific situation is present in the 1993 and 1995 dataset, where part of the data has been taken not at the centre of the Z resonance, but at a centre-of-mass energy of about 1.8 GeV above and below. The measurement of the energy distribution of B hadrons performed here is intended to provide insights in the fragmentation/hadronisation process and the energy remaining for the B hadron after this process. However, the energy distribution is also affected by energy losses due to initial state radiation prior to the annihilation process. Initial state radiation is heavily suppressed at and just below the Z resonance, but it has significant impact in the dataset taken at an energy of $m_{\mathrm{Z}} + 1.8$ GeV. Therefore the latter samples are treated separately, with Monte Carlo samples simulated for the appropriate energy.

In some respects the Monte Carlo parameters used during generation do not reflect the current knowledge of data. Corrections are applied by reweighting the Monte Carlo. The fraction of b baryons and $\mathrm{B_s}$ in the sample of primary B hadrons are chosen to be 10.3% and 9.8%, respectively [80]. The fraction of orbitally excited B mesons is set to 28.4%, representing an error weighted average of measurements from all LEP collaborations [81, 82]. Due to their different masses, the different B hadrons have different energy distribution, and therefore wrong relative fractions in the sample would distort the overall distribution. To achieve the best possible estimate on the amount of background in the sample, the flavour fractions $\mathrm{R_b} = \Gamma_{\mathrm{b\bar{b}}}/\Gamma_{\mathrm{had}}$ and $\mathrm{R_c} = \Gamma_{\mathrm{c\bar{c}}}/\Gamma_{\mathrm{had}}$ are reweighted to their LEP/SLD combined measured values of 0.21646 and 0.1719, respectively [69]. Another set of quantities with important influence on background modelling in the simulation is the rate of heavy quarks produced via gluon splitting, which has been found to be underestimated by about a factor of two in the Jetset Monte Carlo. Gluon splitting rates of $\mathrm{R}_{g\to\mathrm{c\bar{c}}} = 0.0296$ and $\mathrm{R}_{g\to\mathrm{b\bar{b}}} = 0.00254$ (number of heavy

quark pairs from gluon splitting per event) are used [83]. Since this analysis relies on secondary vertex reconstruction, the B hadron reconstruction efficiency and thus the relative amount of background in the sample depends on the lifetime of b and c hadrons. These lifetimes have been set to current average values as suggested in Ref. [83].

Production of b baryons is almost completely suppressed in the Herwig 6.2 Monte Carlo sample, caused by the OPAL parameter tuning [35]. For Herwig 6.2 the relative amount of all other B hadron species is therefore scaled upwards to sum up to the total expected B hadron production rate. Also completely suppressed in the OPAL tune of Herwig 6.2 is the production of $b\overline{b}$ quark pairs in gluon splitting. This can be corrected by combining the Herwig 6.2 Monte Carlo with a sample of about 250000 hadronic Jetset/Pythia events with at least one gluon splitting into $b\overline{b}$ each, created for another OPAL analysis [84]. However, the $g \to b\overline{b}$ background in this analysis is small, and therefore the pure Herwig 6.2 sample has been used for the studies presented here.

All corrections described so far are applied at the level of the Monte Carlo tree, referring to external measurements of the corrected quantities. Additional correction are applied at a later stage of the analysis, when a direct comparison of data and simulation in the framework of the b hadronisation study are possible. These corrections will be described in Section 4.3.

4.2 Selection and Reconstruction of B Hadrons

B hadrons are reconstructed using an extended version of the method used in earlier analyses [85, 82]. Since the measurement of the energy of B hadrons is primary objective of this analysis, the B reconstruction is tuned to minimise the uncertainty on the B energy, while maintaining a high reconstruction efficiency.

4.2.1 Preselection of $Z \to b\overline{b}$ Events

To achieve optimal b-tagging performance, each event is forced to a 2-jet topology using the Durham jet-finding scheme [86]. In calculating the visible energies and momenta of the event and of individual jets, corrections are applied to prevent double counting of energy in the case of tracks with associated clusters [87]. A b-tagging algorithm is applied to each jet using three independent methods: lifetime tag, high p_t lepton tag and jet-shape tag (see Figure 4.1). This algorithm was developed for and used in the OPAL Higgs searches; a detailed description of the algorithm can be found in Ref. [88]. Its applicability to data on the Z pole was already proven in Ref. [89]. The b-tagging discriminants calculated for each of the jets in the event are combined to yield an event b likelihood $\mathcal{B}_{\text{event}}$. For each event, $\mathcal{B}_{\text{event}} > 0.2$ is required. After this cut, the $Z \to b\overline{b}$ event purity is about 57%. The cut on the direction of the event thrust axis, $|\cos\theta_T| < 0.8$, as described in Section 4.1, removes roughly a quarter of all $Z \to b\overline{b}$ events. At this stage, about 1.2 million B hadron candidates are selected.

4.2.2 Reconstruction of B Hadron Energy and Direction

The primary event vertex is reconstructed using the tracks in the event constrained to the average position and effective spread of the e^+e^- collision point. For the B hadron reconstruction, tracks and electro-magnetic calorimeter clusters with no associated track are combined into

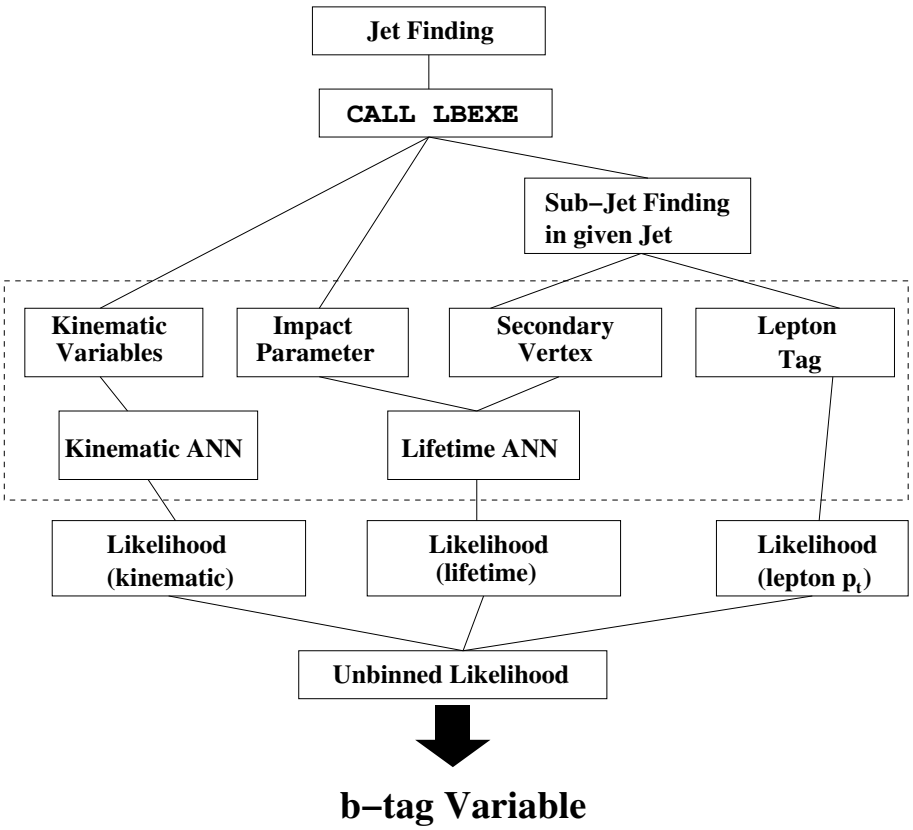

Figure 4.1: *Flow chart of the* b *tagging algorithm applied in this analysis. This figure is adapted from Ref. [91]. Artificial neural networks are abbreviated as ANN.*

jets using a cone algorithm[2] [90] with a cone half-angle of 0.65 rad and a minimum jet energy of 5.0 GeV. The two most energetic jets of each event are assumed to contain the B hadrons. Only jets where the opposite hemisphere yields a b jet probability of at least 0.8 are used in the analysis. The energy and direction of each remaining jet are reconstructed.

In each hemisphere defined by the jet axis, a weight is assigned to each track and each cluster, where the weight corresponds to the probability that this track or cluster is a product of the B hadron decay. The B hadron is reconstructed by summing the weighted momenta of the tracks and clusters. The reconstruction algorithm is applied to all B hadron species and is 100% efficient. Details of the reconstruction method are provided below.

Calculation of track weights

Two different types of weights are assigned to each track:

- ω_{vtx}, calculated from the impact parameter significances of the track with respect to both the primary and secondary vertices;
- ω_{NN}, the output of a neural network based on kinematics and track impact parameters with respect to the primary vertex.

[2]The cone jet-finder provides the best B hadron energy and direction resolution compared to other jet finders studied here.

The calculation of $\omega_{\rm vtx}$ requires the existence of a secondary vertex, whereas $\omega_{\rm NN}$ does not and is therefore available for all tracks. The search for detached secondary vertices proceeds as follows:

Each jet is searched for secondary vertices using a vertexing algorithm similar to that described in Ref. [82], making use of the tracking information in both the $r\phi$ and rz planes if available. If a secondary vertex is found, the primary vertex is re-fitted excluding the tracks assigned to the secondary vertex. Secondary vertex candidates are accepted and called 'good' secondary vertices if they contain at least three tracks and have a decay length greater than 0.2 mm. If there is more than one good secondary vertex attached to a jet, the vertex with the largest number of significant[3] tracks is taken. If there is a tie, the secondary vertex with the larger separation significance with respect to the primary vertex is taken. Jets without associated secondary vertex are rejected. A weight is calculated for each track in the hemisphere of the jet using the impact parameter significance of the track with respect to both the primary and secondary vertices. This weight is given by

$$\omega_{\rm vtx} = \frac{R(b/\eta)}{R(b/\eta) + R(d/\sigma)} \,, \tag{4.1}$$

where b and η are the impact parameter and its error with respect to the secondary vertex, and d and σ are the same quantities with respect to the primary vertex. R is a symmetric function describing the impact parameter significance distribution with respect to a fitted vertex. The $\omega_{\rm vtx}$ distribution for tracks of hemispheres with a good secondary vertex is shown in Figure 4.2a and compared with the corresponding Monte Carlo distribution. The weight $\omega_{\rm vtx}$ shows a weak correlation with the momentum of the track.

For each track, the weight $\omega_{\rm NN}$ is calculated using an artificial neural network [92] trained to discriminate B hadron decay products from tracks originating from other hadronisation products in a jet. The neural network was trained using as inputs the scaled track momentum $x_p = p/E_{\rm beam}$, the track rapidity relative to the estimated B direction, the impact parameters of the track with respect to the primary vertex in the $r\phi$ and rz planes and the corresponding errors on the impact parameters[4]. As a preliminary estimate, the jet axis is taken as the estimated B direction. The $\omega_{\rm NN}$ distribution is shown in Figure 4.2b. The track weight $\omega_{\rm NN}$ is combined with the vertex weight $\omega_{\rm vtx}$ using the prescription

$$\omega_{\rm tr} = \frac{\omega_{\rm NN} \cdot \omega_{\rm vtx}}{(1-\omega_{\rm NN}) \cdot (1-\omega_{\rm vtx}) + \omega_{\rm NN} \cdot \omega_{\rm vtx}} \,. \tag{4.2}$$

The weight $\omega_{\rm tr}$ in Equation 4.2 is approximately the probability that the track is a B hadron decay product. The combined weight $\omega_{\rm tr}$ for tracks of all hemispheres is shown in Figure 4.2c.

Calculation of cluster weights

Similar weights are calculated for energy clusters reconstructed in the electro-magnetic and hadronic calorimeters to represent the probability the clusters came from a B hadron decay. Weights $\omega_{\rm ecl}$ and $\omega_{\rm hcl}$ are assigned to each electro-magnetic and hadronic cluster in the hemisphere of the B hadron based on their rapidity with respect to the estimated B direction. The

[3] A track is called significant if its impact parameter significance with respect to the primary vertex is larger than 2.5.

[4] A similar neural network was already used in Ref. [93]

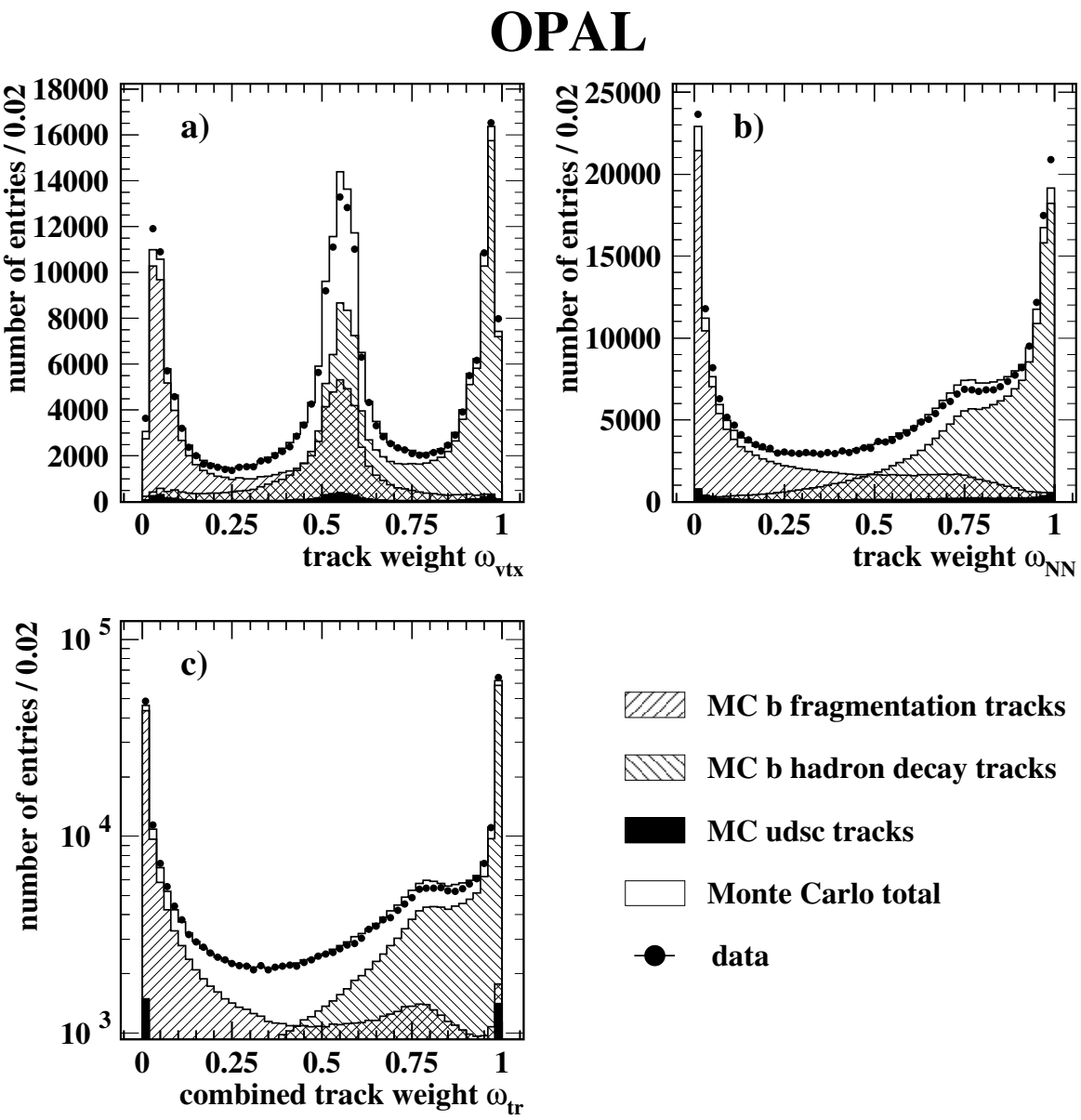

Figure 4.2: *a) The track weight* $\omega_{\rm vtx}$ *for all tracks in hemispheres with a good secondary vertex. The peaks near 0 and 1 correspond to tracks created by* b *hadronisation and* B *hadron decay tracks, respectively. The peak near 0.5 is produced by tracks which are not unambiguously assigned to the primary or the secondary vertex, as in the case of tracks matching both the primary and secondary vertex or matching no vertex at all. b) The track weight* $\omega_{\rm NN}$ *for tracks of all hemispheres (with or without a good secondary vertex). The separation power of* $\omega_{\rm NN}$ *is superior to the separation power of* $\omega_{\rm vtx}$*. c) The combined track weight* $\omega_{\rm tr}$ *calculated from* $\omega_{\rm vtx}$ *and* $\omega_{\rm NN}$ *for tracks of all hemispheres. Note that* $\omega_{\rm tr}$ *is shown on a logarithmic scale. This figure is taken from Ref. citebib-opalbss.*

weight is equal to the probability, calculated using the Monte Carlo simulation as a function of the cluster energy, that the cluster came from the decay of a B hadron. Clusters associated with a track have the estimated energy of the track subtracted.

Calculation of B direction

The B momentum is calculated iteratively by a weighted sum of all tracks and clusters in the hemisphere:

$$\vec{p} = \sum_{i=1}^{N_{\text{track}}} \omega_{\text{tr},i} \cdot \vec{p}_i + \sum_{i=1}^{N_{\text{ecal}}} \omega_{\text{ecl},i} \cdot \vec{p}_i + \sum_{i=1}^{N_{\text{hcal}}} \omega_{\text{hcl},i} \cdot \vec{p}_i \tag{4.3}$$

where N_{track}, N_{ecal} and N_{hcal} denote the number of tracks, electro-magnetic clusters and hadronic clusters, respectively. The rapidity calculation, for both tracks and clusters, is initially performed relative to an estimate of the B hadron direction[5]. The weights are then recalculated with the rapidity determined using the new B direction estimate.

An estimate of the B hadron direction is made for all B candidates based on the weighted momentum sum of the tracks and clusters in the jet. In addition, the vector from the primary vertex to the secondary vertex yields an estimate of the B direction. The weighted average of both estimators is taken, using the calculated uncertainties of each direction estimate. The covariance matrices of the primary and secondary vertices determine the error on the B flight direction. The error on the momentum sum is estimated by removing each term in turn from the sum in Equation 4.3, calculating the change in the B direction caused by this omission and adding up in quadrature the corresponding error contributions from each track and cluster. The final estimate of the B direction is obtained by taking the error-weighted sum of the B direction calculated with the momentum sum method and the B direction obtained from the primary and secondary vertex positions. The direction information in the rz plane of the secondary vertex is only used if the vertex is built with tracks that left at least four hits in the z-layers of the silicon micro-vertex detector (the maximum number of these hits per track is two).

The error $\Delta\alpha$ on the weighted sum of both B direction estimators described in the previous paragraph is a measure for the quality of the B direction. To improve the resolution on the B direction, which influences the B energy resolution, a cut on $\Delta\alpha$ is imposed.

Calculation of B energy

The resolution on the total energy of the B candidate can be significantly improved by constraining the total centre-of-mass energy, $E_{\text{CM}} = \sqrt{s}$, to twice the LEP beam energy. Assuming a two-body decay of the Z, one obtains:

$$E_{\text{B}} = \frac{E_{\text{CM}}^2 - M_{\text{recoil}}^2 + M_{\text{B}}^2}{2E_{\text{CM}}} \,, \tag{4.4}$$

where the mass of the B hadron is set to the B meson mass $M_{\text{B}} = 5.279\ \text{GeV}/c^2$ and M_{recoil} denotes the mass recoiling against the B hadron. The recoil mass and the recoil energy E_{recoil} are calculated by summing over all tracks and clusters[6] of the event weighted by $(1 - \omega_i)$

[5]The initial input for this axis is the jet direction calculated using tracks and unassociated electro-magnetic clusters.

[6]Tracks and clusters not contained in the hemisphere of the B hadron candidate have weights $\omega_i = 0$. ω_i denotes the weight $\omega_{\text{tr},i}$, $\omega_{\text{ecl},i}$ and $\omega_{\text{hcl},i}$ for tracks, electro-magnetic clusters and hadronic clusters, respectively.

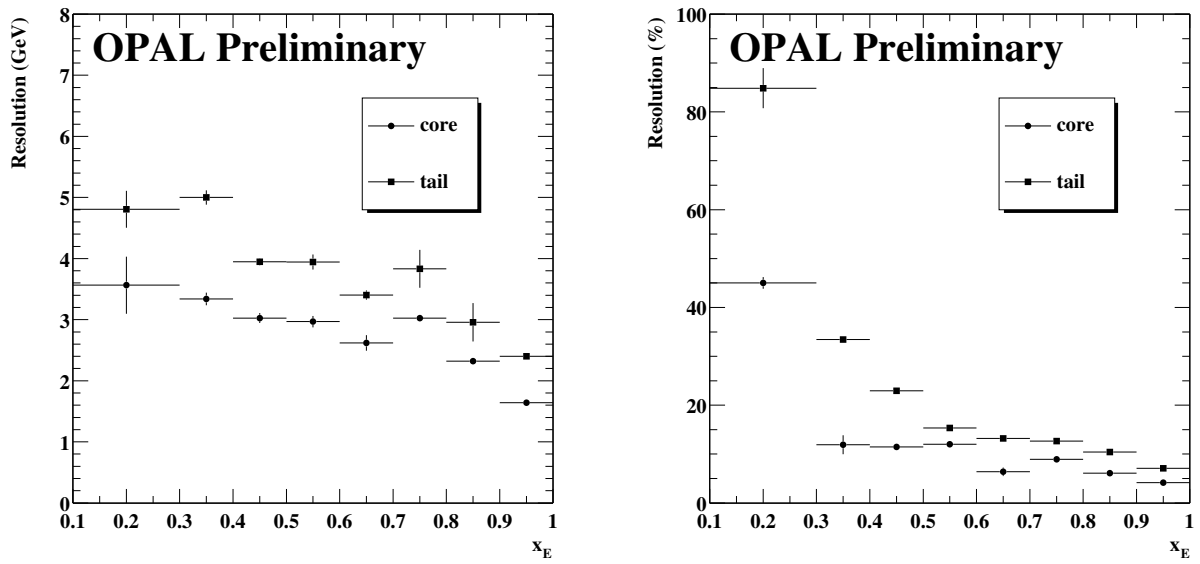

Figure 4.3: *Energy dependence of the* B *hadron energy resolution. The left plot shows the absolute resolution in GeV. It is only weakly energy-dependent. The corresponding relative resolution is shown on the right.*

and assuming the particle masses used in the calculation of the respective particle energy. To account for the amount of undetected energy mainly due to the presence of neutrinos, the recoil mass is scaled by the ratio of the expected energy in the recoil to the energy actually measured:

$$M_{\text{recoil,new}} = M_{\text{recoil,old}} \cdot \frac{E_{\text{CM}} - E_{\text{B}}}{E_{\text{recoil}}} \tag{4.5}$$

where E_{B} is taken from Equation 4.4. The new recoil mass value $M_{\text{recoil,new}}$ obtained from Equation 4.5 is substituted into Equation 4.4 and the calculation of E_{B} is iterated. After two iterations the uncertainty on the B hadron energy is minimised.

After all these cuts, the narrower Gaussian from a two Gaussian fit to the difference between the reconstructed and generated B hadron energy has $\sigma = 2.4$ GeV, and 90% of the entries are contained within 3σ. The broader Gaussian has a width of 5.3 GeV. Figure 4.3 shows the dependence of both the absolute and the relative energy resolution on the scaled energy.

The complete B hadron selection applied to the full data sample results in 270 707 tagged jets with a b purity of about 96%, as estimated from Monte Carlo[7]. The average B hadron selection efficiency is 16%, albeit with a significant energy dependence, shown in Figure 4.4.

4.3 Additional Monte Carlo Corrections

A comparison of reconstructed quantities in the B hadron samples obtained in data and Monte Carlo shows that further improvement of the simulation is possible despite the tree level corrections described earlier. The B hadron reconstruction efficiency of the sample suggested by Monte Carlo has been compared to the actual value in data using a double tag approach as described in Ref. [93]. The number of event hemispheres tagged as containing a B hadron is given by

$$N_t = 2 \times \text{R}_\text{b} \times N_{had} \times \epsilon_\text{b} \ , \tag{4.6}$$

[7]The purity depends on the dataset and varies in the range 95.6% to 96.3%

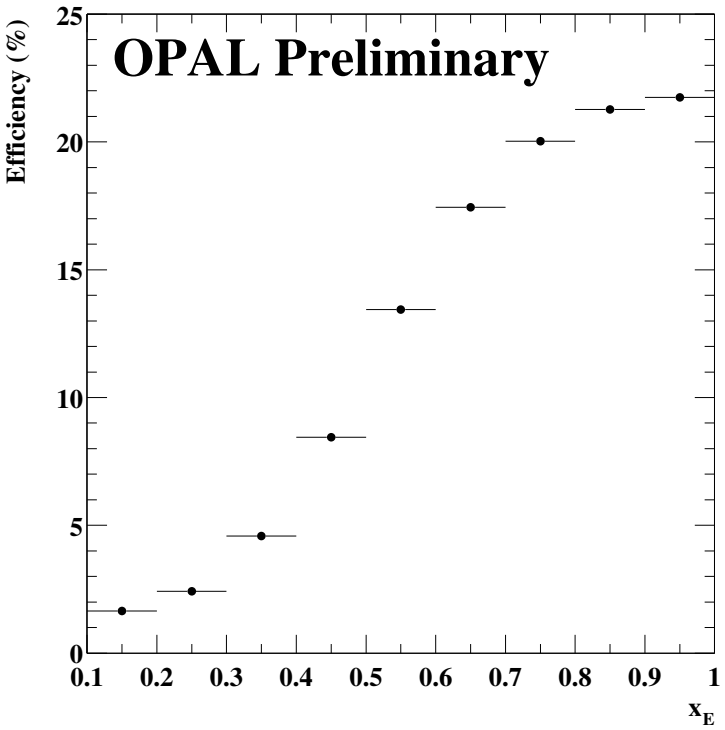

Figure 4.4: *Energy dependence of the* B *hadron reconstruction efficiency. An average efficiency of 16% is achieved, which is dominated by the highly efficient reconstruction of* B *hadrons with large energy and thus comparatively large decay length. The efficiency shown in this plot is calculated for Jetset Monte Carlo with all corrections described in the text.*

where N_{had} is the number of hadronic events in the sample, R_b is the hadronic branching ratio of Z into $b\overline{b}$ quark pairs, ϵ_b is the efficiency to reconstruct a B hadron. Background in the sample is neglected. The number of events with both hemispheres being tagged as containing a B hadron results to

$$N_{tt} = R_b \times N_{had} \times \epsilon_b^2 \ , \tag{4.7}$$

the ratio of the latter and the former number thus gives $1/2 \times \epsilon_b$. The numbers obtained this way in both simulation and real data are found to agree within 5% in all cases, however, a correction is applied to improve the agreement further. The value of ϵ_b shows a tendency towards smaller values in data with respect to Monte Carlo. The Monte Carlo efficiency is therefore scaled to match the data.

A further correction is derived from the observation that, although the b likelihood distribution agrees well in data and Monte Carlo, this is not separately true for all energy regions. The conclusion is that the energy dependence of the amount of background is not perfectly modelled in the simulation. To improve on this, the b likelihood is plotted for ten bins in x_E. The ratio of the distributions of data and Monte Carlo is calculated and fitted by a linear function in each bin separately. The slope of this function is an indicator for the quality of agreement of data and simulation. All fitted slopes are compatible with zero within two standard deviations. Still, all Monte Carlo events are then reweighted with this function to improve the modelling of the energy dependence of the background fraction.

4.4 Test of Hadronisation Models

The B hadron energy distributions predicted by the Jetset 7.4, Herwig 5.9, and Herwig 6.2 Monte Carlo models are compared to the OPAL data. The Herwig predictions are taken with OPAL standard settings only, without further variation of parameters in this analysis. This simplifies the model test to a mere comparison of the x_{E} distributions obtained with data and Monte Carlo. The Jetset Monte Carlo is reweighted to use the hadronisation parametrisations of Peterson et al., Collins/Spiller, Kartvelishvili et al., the Lund symmetric model, and the Bowler parametrisation, as described in Chapter 2. The parameters of the respective fragmentation functions are then tuned to achieve a best fit of the x_{E} distributions in data and Monte Carlo. In the case of the Peterson, Collins/Spiller, and Kartvelishvili models, one free parameter is available. The Lund and Bowler models each have two free fit parameters.

The amount and distribution of background in the B hadron candidate sample is estimated from Monte Carlo. The dominant background source are jets from primary charm quarks, which make up almost 3% of the B hadron candidate sample. Since the heavy quark fragmentation functions to be tested for b quarks are also applicable to charm quarks, the same hadronisation model is used to parametrise the charm background energy distribution like the model used in the respective fit.

The Jetset 7.4 Monte Carlo is reweighted relative to its original parametrisation, which in the samples used here is a Peterson fragmentation function with $\varepsilon_{\mathrm{b}} = 38 \times 10^{-4}$. But, as already noticed in earlier analyses [94], the resulting distribution of z values in a Jetset Monte Carlo sample does not correspond exactly to the chosen input distribution and parameters. This is due to the way Jetset deals with fragmentation functions peaked very close to one [95]: In order to put the heavy hadron itself on-shell (problematic if $z \approx 0$), and to ensure a remaining string fragment can decay to at least a single on-shell hadron if the remaining energy is small (problematic if $z \approx 1$), the z value is corrected:

$$z' = \frac{1}{2}\left(1 + \frac{m_{t,H}^2}{E_{rem}^2} - \frac{m_{t,R}^{(min)2}}{E_{rem}^2} + (2z-1)\sqrt{\left(1 - \frac{m_{t,H}^2}{E_{rem}^2} - \frac{m_{t,R}^{(min)2}}{E_{rem}^2}\right)^2 - 4\frac{m_{t,H}^2}{E_{rem}^2}\frac{m_{t,R}^{(min)2}}{E_{rem}^2}}\right) \quad (4.8)$$

Here, $m_{t,H}$ is the transverse mass of the heavy hadron, $m_{t,R}^{(min)}$ is the minimal transverse mass required for the remainder string assuming it decays into a single hadron. E_{rem} is the energy of the remaining string fragment. This correction constrains the z value away from zero and one. This is the practical realisation of the concept introduced in Subsection 2.4.2, where it was explained that the Lund model ensures on-shellness of hadrons by moving string breaks to suitable positions. Unfortunately, this method does not fully conserve the original shape of the fragmentation function. The effective ε_{b} turns out to be around 5% lower than the input parameter.

Not taking the ε_{b} shift into account in the reweighting fit would lead to a biased parameter estimation. Therefore the actual ε_{b} in the Monte Carlo sample used for the respective reweighting fit is measured by a fit to the z distribution, and the reweighting is performed relative to this effective ε_{b} value. The reweighting used in the fit is then applied to the original z distribution in the Monte Carlo sample, and the respective fragmentation function is fitted to this reweighted distribution. The fact that the parameters obtained this way agree with the expectations proves that the reweighting works as expected.

The results of the Jetset reweighting fit for all datasets are presented in Tables 4.1 and 4.2. The adequateness of the fit is measured in terms of the fit χ^2 (Table 4.3) and a Kolmogorov

	Bowler			Lund symmetric		
	a	bm_t^2	correl.	a	bm_t^2	correl.
1992	0.43 ± 0.14	45 ± 8	96.1%	1.1 ± 0.2	11.3 ± 1.6	98.5%
1993, $\sqrt{s} \leq m_Z$	1.4 ± 0.2	104 ± 15	97.6%	2.5 ± 0.4	22.2 ± 3.1	99.1%
1993, $\sqrt{s} > m_Z$	1.1 ± 0.5	84 ± 28	97.8%	2.0 ± 0.7	18.3 ± 5.3	99.1%
1994	0.67 ± 0.08	58 ± 5	96.3%	1.3 ± 0.1	13.1 ± 0.9	98.5%
1995, $\sqrt{s} \leq m_Z$	0.78 ± 0.15	65 ± 9	96.9%	1.5 ± 0.2	14.4 ± 1.7	98.7%
1995, $\sqrt{s} > m_Z$	1.9 ± 0.9	160 ± 70	98.7%	3.4 ± 1.5	30.4 ± 12.0	99.5%
1996	-0.07 ± 0.16	15 ± 5	79.0%	0.2 ± 0.2	4.3 ± 1.2	87.6%
1997	0.34 ± 0.29	28 ± 11	92.3%	0.8 ± 0.4	7.7 ± 2.5	96.0%
1998	0.18 ± 0.18	35 ± 10	84.7%	0.5 ± 0.3	8.2 ± 2.2	95.2%
1999	0.31 ± 0.20	36 ± 10	90.4%	0.7 ± 0.3	8.5 ± 2.2	96.5%
2000	0.96 ± 0.43	68 ± 24	96.1%	1.7 ± 0.6	15.3 ± 4.3	98.1%

Table 4.1: *Fit results of the Bowler and Lund symmetric parametrisations for all OPAL datasets.*

	Kartvelishvili	Peterson	Collins/Spiller
	α_b	$\varepsilon_b \times 10^4$	$\varepsilon_b \times 10^4$
1992	12.0 ± 0.3	40.4 ± 2.0	21.7 ± 1.9
1993, $\sqrt{s} \leq m_Z$	12.2 ± 0.2	39.8 ± 1.6	20.7 ± 1.6
1993, $\sqrt{s} > m_Z$	12.3 ± 0.5	39.6 ± 3.4	20.3 ± 3.2
1994	12.1 ± 0.1	39.7 ± 1.0	21.4 ± 0.9
1995, $\sqrt{s} \leq m_Z$	12.1 ± 0.2	40.1 ± 1.6	21.0 ± 1.5
1995, $\sqrt{s} > m_Z$	13.1 ± 0.5	34.5 ± 2.9	16.2 ± 2.6
1996	9.8 ± 1.0	61.3 ± 12.4	36.1 ± 13.8
1997	9.9 ± 0.8	57.4 ± 9.5	38.8 ± 10.9
1998	12.4 ± 0.8	38.5 ± 5.4	20.1 ± 5.4
1999	11.7 ± 0.7	41.7 ± 5.3	20.3 ± 5.1
2000	11.6 ± 0.6	43.3 ± 5.2	22.2 ± 5.1

Table 4.2: *Fit results of the Kartvelishvili, Peterson, and Collins/Spiller parametrisations for all OPAL datasets.*

	Bowler	Lund symm.	Kartvelishvili	Peterson	Collins/Spiller
1992	55/44	57/44	59/45	67/45	125/45
1993, $\sqrt{s} \leq m_{\mathrm{Z}}$	98/44	101/44	153/45	197/45	336/45
1993, $\sqrt{s} > m_{\mathrm{Z}}$	47/44	47/44	53/45	58/45	80/45
1994	59/44	69/44	90/45	153/45	398/45
1995, $\sqrt{s} \leq m_{\mathrm{Z}}$	38/44	38/44	51/45	77/45	179/45
1995, $\sqrt{s} > m_{\mathrm{Z}}$	35/44	35/44	47/45	54/45	85/45
1996	61/44	60/44	62/45	62/45	62/45
1997	26/44	27/44	26/45	29/45	34/45
1998	42/44	45/44	46/45	51/45	56/45
1999	53/44	53/44	53/45	56/45	66/45
2000	49/44	49/44	53/45	54/45	66/45

Table 4.3: *Overview of fit χ^2/d.o.f. achieved with Jetset and different fragmentation functions for all OPAL datasets.*

	Bowler	Lund symm.	Kartvelishvili	Peterson	Collins/Spiller
1992	0.71	0.50	0.27	3.8×10^{-2}	1.1×10^{-4}
1993, $\sqrt{s} \leq m_{\mathrm{Z}}$	2.0×10^{-2}	1.6×10^{-2}	4.9×10^{-6}	5.3×10^{-10}	1.9×10^{-17}
1993, $\sqrt{s} > m_{\mathrm{Z}}$	1.00	1.00	0.94	0.45	3.4×10^{-2}
1994	0.44	0.28	3.7×10^{-3}	2.6×10^{-7}	3.8×10^{-20}
1995, $\sqrt{s} \leq m_{\mathrm{Z}}$	0.98	0.92	0.12	9.6×10^{-4}	3.2×10^{-9}
1995, $\sqrt{s} > m_{\mathrm{Z}}$	0.96	0.99	0.65	0.17	5.1×10^{-3}
1996	0.98	0.97	0.95	0.99	0.88
1997	0.98	0.97	0.95	0.55	0.14
1998	0.69	0.68	0.72	0.38	5.7×10^{-2}
1999	0.52	0.41	0.50	0.27	4.0×10^{-2}
2000	0.99	0.99	0.39	4.4×10^{-2}	6.4×10^{-4}

Table 4.4: *Overview Kolmogorov compatibility test results achieved with Jetset and different fragmentation functions for all OPAL datasets.*

model	parameters	$\langle x_{\mathrm{E}} \rangle$	χ^2/d.o.f.	Kolmogorov test
Bowler	$bm_t^2 = 66.1 \pm 4.4$ $a = 0.78 \pm 0.07$	$0.7209^{+0.0006}_{-0.0010}$	59/44	0.44
Lund symmetric	$bm_t^2 = 14.7 \pm 0.8$ $a = 1.5 \pm 0.1$	$0.7201^{+0.0006}_{-0.0012}$	69/44	0.28
Kartvelishvili	$\alpha_{\mathrm{b}} = 12.1 \pm 0.1$	0.7157 ± 0.0006	90/45	3.7×10^{-3}
Peterson	$\varepsilon_{\mathrm{b}} = (40.3 \pm 0.7) \times 10^{-4}$	0.7029 ± 0.0006	153/45	2.6×10^{-7}
Collins/Spiller	$\varepsilon_{\mathrm{b}} = (21.4 \pm 0.7) \times 10^{-4}$	0.6876 ± 0.0006	398/45	3.8×10^{-20}
Herwig 6.2	cldir=1, clsmr(2)=0	0.7074	430/46	1.6×10^{-20}
Herwig 5.9	cldir=1, clsmr=0.35	0.6546	4454/46	$< 10^{-30}$

Table 4.5: *Results of the comparison of hadronisation models to OPAL data. The parameter fit results and corresponding x_{E} values are luminosity weighted averages over all datasets from the years 1992–2000. The parameter errors are statistical errors only. The errors on $\langle x_{\mathrm{E}} \rangle$ are the propagated parameter errors. The χ^2 are quoted for the 1994 dataset only, which is the largest coherent sample. The errors of the two parameters of the Lund and Bowler models are almost fully correlated. The parameters given for the Herwig Monte Carlo are not obtained from a fit. These are the values used for the generation of respective sample, as explained in Section 2.4.2.*

compatibility test (Table 4.4). The Kolmogorov test results agree nicely with the χ^2 fit quality estimate.

The luminosity weighted average parameter values are summarised in Table 4.5. For each parametrisation the corresponding model-dependent mean scaled energy of weakly decaying B hadrons is given. Data samples at $\sqrt{s} = m_{\mathrm{Z}} + 1.8$ GeV have been excluded in the calculation of the luminosity weighted average $\langle x_{\mathrm{E}} \rangle$. The table also compares the fit quality of all Jetset 7.4 fits and the Herwig 5.9 and Herwig 6.2 results on the 1994 data, which is the largest homogeneous data sample available. The ordering of the χ^2 in 1994 data agrees with all other large data samples; only in a few smaller samples a slightly different ordering is observed. The quoted χ^2 only take into account the statistical error of data and Monte Carlo. Systematic errors, although dominant in this analysis, are not included. The Bowler, Lund symmetric, and Kartvelishvili models with their respective χ^2 values of 59/44, 69/44, and 90/45 in 1994 data can therefore be seen as consistent with data.

Although the parametrisations with two degrees of freedom score generally better than the one-parameter fit results, this is accomplished with a larger spread of values in the individual datasets: All obtained values for the years 1992–2000 are contained within two (three) times their respective statistical error from the overall mean value for the Peterson and Collins/Spiller (Kartvelishvili) parametrisations. In contrast to this, the Lund and Bowler fit results are clearly less self-consistent, with values spread over more than five standard deviations from the mean value.

The Lund symmetric parametrisation was treated differently in earlier OPAL measurements [96], where a was fixed to a value of 0.18 to tune the distribution of event shape variables in Jetset 7.2 to the observed distributions [97]. However, with a fixed to this value, the Lund symmetric parametrisation provides a drastically worse description of the data, similar in qual-

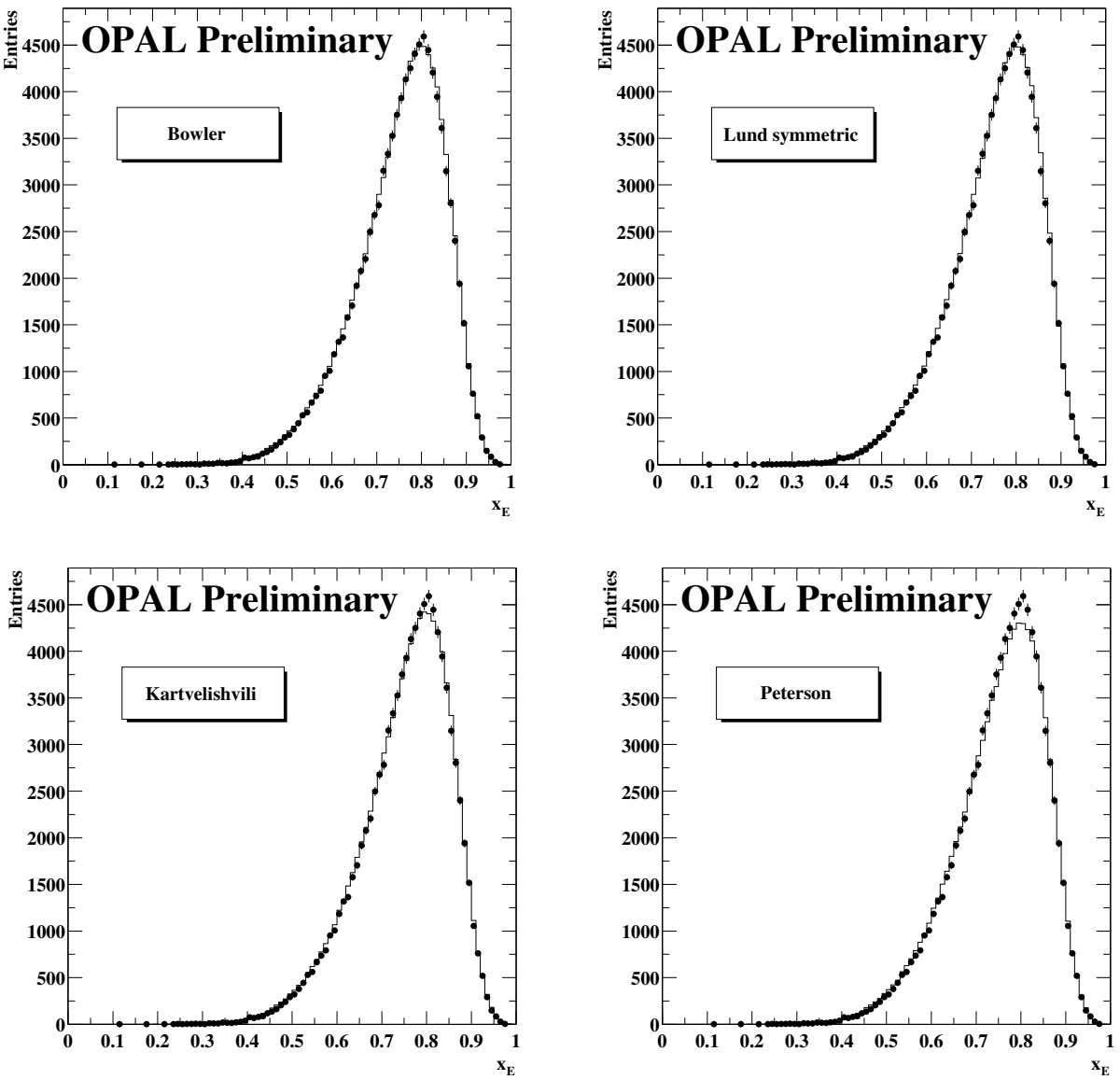

Figure 4.5: *Fit result of hadronisation models for Jetset 7.4. The points with error bars are the reconstructed scaled energy distribution in the 1994 data sample. The histogram represents the best match as obtained from the respective fragmentation function fit. The Kartvelishvili, Lund symmetric, and Bowler parametrisation provide an adequate description of the data. The Peterson parametrisation is too broad.*

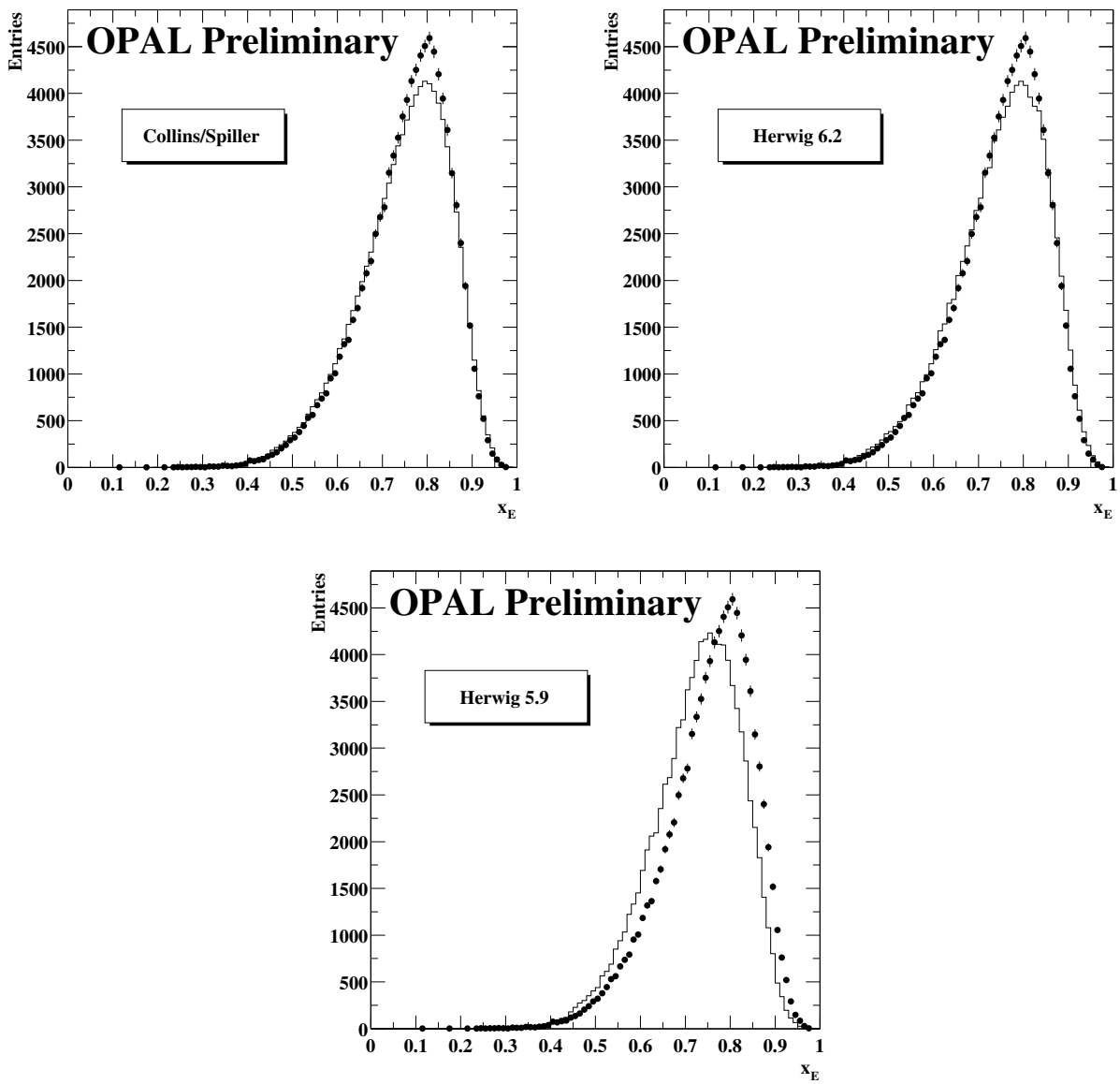

Figure 4.6: *Fit result of further hadronisation models. The Herwig 5.9 model is clearly too soft. Herwig 6.2 and the Collins/Spiller parametrisation for Jetset 7.4 are too broad.*

ity as Collins/Spiller. Therefore a is left free in this analysis, possibly neglecting constraints from other physics inputs. This is done in accordance with a recent b hadronisation study by SLD [98].

4.5 Model-independent Analysis

In the previous section information was extracted from the observed energy distribution making explicit use of a set of models to describe the data. A measurement which is to a lesser extent model-dependent will be presented is this section. For the purpose of this measurement, the scaled energy distribution of weakly decaying B hadrons will be solely characterised by its mean value $\langle x_{\mathrm{E}} \rangle$. This corresponds to usual practice as for example defined in Ref. [83].

The B hadron reconstruction efficiency is varying with the energy, as evident from Figure 4.4. For high energies, the reconstructed energy is biased towards smaller values by the beam energy constraint applied in the reconstruction. At low B hadron energies, the reconstructed value is shifted towards higher values due to the B mass constraint imposed during reconstruction. These effects prevent the mean reconstructed B hadron energy from being a useful observable. In contrary, even a slightly different choice of B hadron selection criteria might lead to a different mean reconstructed energy. It is therefore mandatory to purge analysis- and detector-dependent influences from the result as far as possible, and to try to obtain information on the distribution of the true energy of the weakly decaying B hadron. Its mean value $\langle x_{\mathrm{E}} \rangle$ can be measured with a minimum amount of model-dependence, because only weak assumptions have to be made on the production chain of the weakly decaying B hadrons to describe the measurement. Attempts to go back earlier in the event history, like ALEPH does in their attempt to reconstruct the mean scaled energy of leading B hadrons [99], introduce increasing model-dependences and are therefore more difficult to interpret outside a very limited scope.

To clarify, no measurement of B hadron properties will be entirely model-independent. However, to express the fact that the model-dependences of the measurement presented in this section are strongly reduced in comparison to the fit approach shown in the previous section, this analysis will be labelled "model-independent" in accordance with other publications on this topic [98, 99].

Two complementary approaches are used to unfold an estimate of the true x_{E} distribution from the observed distribution of the reconstructed scaled B hadron energy. The main method represents all distributions by smooth functions obtained by spline fits. The Monte Carlo is then reweighted to match the observed data distribution in a fit process. Details of how the result is stabilised are described later. This method is independent of the initial Monte Carlo distribution and thus reduces model-dependences in the unfolding process. Furthermore, the result is represented as unbinned spline function, which is optimal for the calculation of the mean value of the unfolded distribution. This algorithm is coded in the software package RUN by Blobel [100].

For the second approach, the observed and true B hadron energy distributions are represented as binned histograms, and the correspondence of these two distributions for Monte Carlo is put into a 20×20 matrix connecting the two. In principle, the unfolding process is reduced to a simple matrix inversion to obtain an estimate of the true data x_{E} distribution from the observed distribution. However, also this method requires a stabilisation, which in the case of the SVD-GURU software package by Hocker and Kartvelishvili [101] is provided by re-ordering and re-scaling rows of the matrix to isolate only significant relations as identified by singular value decomposition. This approach has stronger inherent model-dependences than the previously

mentioned method. To reduce these, the unfolding is performed iteratively, with the initial Monte Carlo distribution of the next iteration being reweighted to the unfolding result of the last iteration. The iteration is considered to have converged as soon as all bins of unfolded x_{E} distribution and the respective Monte Carlo distribution agree within one standard deviation. The storage of the unfolding result in a binned histogram might lead to undesirable binning effects in the calculation of $\langle x_{\mathrm{E}} \rangle$, however, for typical x_{E} distributions these effects are rather small in practice. Since in 3 out of 11 data samples the convergence criterion is not fulfilled after a large number of iterations, this second approach is only used as cross-check for the spline fit method described above. Furthermore, the iteration is prone to numerical instabilities. These are damped by smoothing the weights using a fourth order polynomial constrained to be flat at the lower end of the spectrum. A similar approach is used by ALEPH [99].

4.5.1 Stabilisation of the Unfolding Solution

Raw unfolding solutions often oscillate strongly around the solution expected in e.g. Monte Carlo studies. Especially in the case of a binned representation of the data, this effect can be easily understood by strong negative bin-bin correlations introduced by the finite detector resolution. These oscillations can be damped by reducing the number of freedoms of the unfolding solution. In the case of RUN the internal weighting function is represented by an expansion into a set of orthogonal functions. The number of functions to be used in a specific problem can be limited to reduce oscillating behaviour of the solution. RUN provides a mechanism to estimate the optimal number of orthogonal functions from noise analysis. This mechanism and further Monte Carlo studies show that three functions are sufficient for the problem to be solved here.

A similar mechanism is implemented in SVD-GURU, where by matrix rotation the number of significant equations is estimated, and the most significant ones can be isolated. The internal mechanism for an estimate of this effective rank of the linear system of equations in the unfolding agrees with Monte Carlo studies and the choice of RUN parameters in that it suggests three independent equations to perform the unfolding.

Another means to regularise the unfolding solution is foreseen in the RUN package. Of all remaining solutions to the unfolding problem, the one can be chosen that best fulfils a regularisation criterion, which by default is to minimise the integral over the second derivative

$$\int [f''(x)]^2 dx \ ,$$

which minimises the overall curvature of the solution. However, for a sharply peaked distribution like the one of x_{E}, this regularisation criterion is not adequate and was found to lead to biased results. Instead, a so-called linear regularisation criterion has been used in this analysis, which minimises

$$\int [f'(x)]^2 dx$$

instead. It has been checked on Monte Carlo that this regularisation leads to essentially bias-free results on all samples.

The unfolding has been performed separately for data from all years of 1992–2000. 1993 and 1995 datasets at a centre-of-mass energy around $m_{\mathrm{Z}} - 1.8$ GeV show x_{E} distributions that are compatible with those of m_{Z}-samples in Monte Carlo. The 1993 and 1995 datasets at $m_{\mathrm{Z}} + 1.8$ GeV show a significantly lower $\langle x_{\mathrm{E}} \rangle$. This is caused by a large amount of initial state radiation affecting them. The quark energy prior to hadronisation is lower on average than

dataset	$\langle x_{\mathrm{E}} \rangle$ ($E_{cms} \leq m_{\mathrm{Z}}$)	$\langle x_{\mathrm{E}} \rangle$ ($E_{cms} > m_{\mathrm{Z}}$)
1992	0.7172 ± 0.0042	
1993	0.7229 ± 0.0038	0.7052 ± 0.0078
1994	0.7204 ± 0.0024	
1995	0.7180 ± 0.0038	0.7205 ± 0.0080
1996	0.7209 ± 0.0151	
1997	0.7159 ± 0.0129	
1998	0.7175 ± 0.0091	
1999	0.7276 ± 0.0081	
2000	0.7056 ± 0.0075	

Table 4.6: *Resulting $\langle x_{\mathrm{E}} \rangle$ of the unfolding process with RUN and Jetset 7.4 Monte Carlo for all individual datasets. The quoted errors include the statistical errors of data and Monte Carlo, and the statistical uncertainty of the Monte Carlo efficiency.*

the beam energy in this case, and since the beam energy is used as estimator for the quark energy prior to hadronisation, the average x_{E} value is lower than in samples without significant amount of initial state radiation.

Both RUN and SVD-GURU are performed with Monte Carlo that has been reweighted to match the best result of the model-dependent reweighting fits for the respective dataset. This is also done by SLD in their latest b hadronisation analysis [98]. This way it is intended to reduce the dependence of the unfolding result on the Monte Carlo sample used for unfolding. The effect of not using the best parametrisation, but the second and third best instead, have been studied as systematic effect.

4.5.2 Results of the Unfolding Analysis with RUN

Table 4.6 shows the unfolding results obtained in all datasets. Jetset 7.4 Monte Carlo samples are used for unfolding; unfolding results with Herwig are compared to these results in the discussion of systematic effects below. The luminosity weighted average for all datasets at or below the Z resonance is

$$\langle x_{\mathrm{E}} \rangle = 0.7194 \pm 0.0016(stat) \ ,$$

where the error includes the statistical uncertainties due to limited data and Monte Carlo sample sizes, and the statistical error on the Monte Carlo efficiency. The mean scaled energy observed in the $m_{\mathrm{Z}} + 1.8$ GeV samples is found to be

$$\langle x_{\mathrm{E}} \rangle = 0.7128 \pm 0.0056(stat) \ .$$

The difference of these two values is in excellent agreement with the prediction obtained from Monte Carlo samples at similar energies. The agreement of this model-independent measurement with the $\langle x_{\mathrm{E}} \rangle$ values in the framework of the best models as seen in Table 4.5 is very good. The unfolding result spline for the 1994 dataset is plotted in Figure 4.7.

4.5.3 Results of the Unfolding Analysis with SVD-GURU

The results obtained with the unfolding program SVD-GURU are shown in Table 4.7. Especially the results for the large samples are in very good agreement with the ones achieved with RUN. This is also demonstrated in Figure 4.7, where the results obtained for 1994 data by both

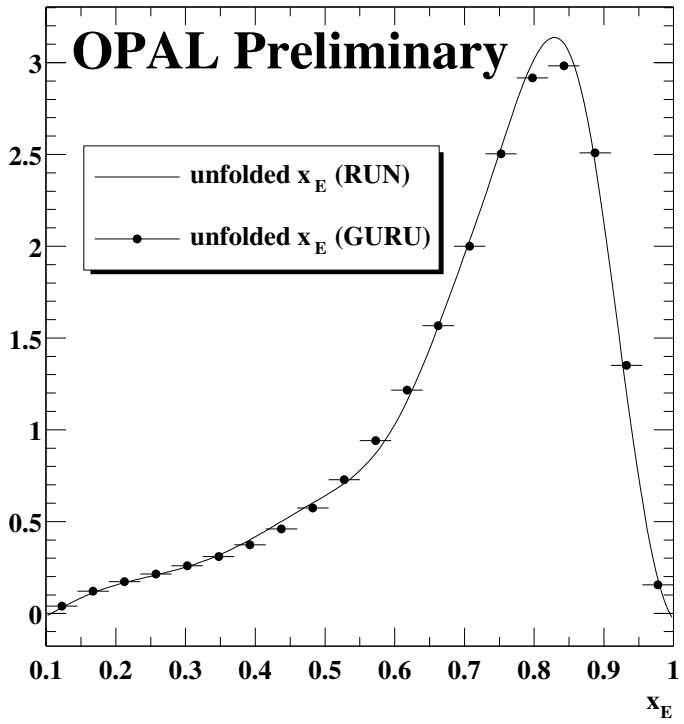

Figure 4.7: *Spline representation of the RUN unfolding result (line), and binned GURU unfolding result (points with error bars), both for 1994 data. The area under both distributions is normalised to one. Despite the different ansatz, the results of both methods are in excellent agreement.*

dataset	$\langle x_{\mathrm{E}} \rangle$ ($E_{cms} \leq m_{\mathrm{Z}}$)	$\langle x_{\mathrm{E}} \rangle$ ($E_{cms} > m_{\mathrm{Z}}$)
1992	0.7155 ± 0.0039	
1993	0.7223 ± 0.0036*	0.7080 ± 0.0074
1994	0.7206 ± 0.0023	
1995	0.7195 ± 0.0036	0.7256 ± 0.0076*
1996	0.7239 ± 0.0145	
1997	0.7180 ± 0.0124	
1998	0.7104 ± 0.0087	
1999	0.7559 ± 0.0081*	
2000	0.7102 ± 0.0074	

Table 4.7: *Resulting $\langle x_{\mathrm{E}} \rangle$ of the unfolding process with SVD-GURU and Jetset 7.4 Monte Carlo for all individual datasets. The quoted errors include the statistical error of the data sample, and the statistical uncertainty of the Monte Carlo efficiency. The statistical error of the Monte Carlo samples is neglected. Samples indicated with a * failed to fulfil the convergence criterion. The values quoted for these samples are therefore calculated without iteratively repeating the unfolding process.*

algorithms are compared. Also the errors agree very well, the reason for the small difference being the fact that the Monte Carlo statistical uncertainty is not taken into account in the errors quoted by SVD-GURU. In three out of 11 samples, the iterative approach fails to converge to an agreement of Monte Carlo and unfolded data distribution of better than one standard deviation in each bin. In these cases the result of the iteration is rejected and replaced by the result obtained without iterations. The luminosity weighted average $\langle x_{\mathrm{E}} \rangle$ value for the datasets at or below the Z resonance is

$$\langle x_{\mathrm{E}} \rangle = 0.7202 \pm 0.0015(stat) \ ,$$

and the value for the $m_{\mathrm{Z}} + 1.8$ GeV samples is

$$\langle x_{\mathrm{E}} \rangle = 0.7167 \pm 0.0053(stat) \ .$$

The errors include the statistical error of the data, and the statistical uncertainty of the Monte Carlo efficiency. Contrary to the RUN result, the Monte Carlo statistical error is not included. The agreement of the SVD-GURU result with the RUN result is excellent, and so is the agreement of the SVD-GURU result with the result of the model-dependent reweighting fit for the best models.

4.6 Systematic Studies

Given the large data sample collected with the OPAL detector, and given the inclusive character of the analysis presented here, the statistical error obtained in the results of the previous sections is expected to be small compared to the systematic uncertainties introduced by limited knowledge of physics parameters with possible impact on the measured quantities. In the following, an overview of all systematic checks will be given separately for the reweighting fit and for the unfolding analysis.

4.6.1 Systematic Uncertainties of the Model-dependent Fit

The Jetset 7.4 Monte Carlo samples used for the reweighting fit were created with Peterson fragmentation function at $\varepsilon_{\mathrm{b}} = 38 \times 10^{-4}$. The fit result for data is $\varepsilon_{\mathrm{b}} = (40.3 \pm 0.7) \times 10^{-4}$. The fact that the Monte Carlo tuning and the data fit result are close is advantageous in the sense that adverse effects due to weights far from 1.0 are not expected. However, additional efforts have been made to prove that the closeness of the two values is not introduced by improper reweighting. In order to achieve this, a sample of 4 million hadronic Jetset 7.4 events with Peterson fragmentation function at $\varepsilon_{\mathrm{b}} = 57 \times 10^{-4}$ is used to repeat the fit for the 1994 data sample[8]. The fit result obtained with this sample is in excellent agreement with the result obtained with the main $\varepsilon_{\mathrm{b}} = 38 \times 10^{-4}$ Monte Carlo. It is thus concluded that the reweighting fit works as expected.

All further systematic checks that are performed for the reweighting fit are presented in the following. For an overview of all error contributions for all models see Table 4.8.

- The resolution of the OPAL calorimeters is varied $\pm 10\%$ around the best estimate.

[8]See note on this sample in Chapter 3.

- The resolution of the $r\phi$-related track parameters d_0 (transverse impact parameter), ϕ_0 (initial azimuth), and κ (curvature) is varied in the range $\pm 5\%$.
- The resolution of the rz-related track parameters z_0 (longitudinal impact parameter) and $\tan\lambda$ (dip angle, $\lambda = \pi/2 - \theta$) is varied by $\pm 10\%$.
- The relative fraction of different B hadron species in the sample of primary B hadrons influences the measurement, because different B hadron species have different energy distributions. All values obtained in this analysis are calculated with Monte Carlo samples that are reweighted to reflect the current best knowledge of the hadron fractions. The LEP/SLD/CDF average estimate of the amount of b baryons is $(10.3 \pm 1.8)\%$ [80]. For the systematic analysis it is varied within the quoted error.
- The fraction of B_s in the sample is varied in the range $(9.8 \pm 1.2)\%$ [80].
- The amount of orbitally excited $B_J^{(*)}$ mesons was measured by all LEP collaborations [81, 82]. An error weighted average is calculated to be $(28.4 \pm 3.5)\%$. The value is varied within its error.
- The average multiplicity of charged particles from a B hadron decay was found at LEP to be 4.955 ± 0.062 [83]. Although the variation of the hadron species fractions explained above covers most of this range, a variation within the full error is performed additionally.
- The average lifetime of weakly decaying B hadrons affects the efficiency of secondary vertex reconstruction, and is therefore varied in the range 1.577 ± 0.0016 ps [2][9].
- The average lifetime of weakly decaying charm hadrons determines the amount of charm background found in the B hadron candidate sample. The D^0, D^+, D_s, and Λ_c lifetimes are varied within the errors proposed in Ref. [83].
- The charm background in the Monte Carlo samples is reweighted to the same fragmentation function as the B hadron distribution in the respective fit. The central values and errors of the charm hadronisation parameters are taken from earlier OPAL measurements [102]. For the evaluation of the systematic uncertainty the parameters are varied within their errors.
- The background contribution from gluon splitting to $b\overline{b}$ quark pairs depends on the rate of such splittings. The average LEP result is 0.00254 ± 0.00051 $b\overline{b}$ pairs per hadronic event [83].
- The number of $c\overline{c}$ pairs from gluon splitting per hadronic event is changed within the LEP errors of 0.0296 ± 0.0038 [83].
- The partial width of the Z into $b\overline{b}$ quark pairs, normalised to the total hadronic width of the Z, is measured to be $R_b = 0.21646 \pm 0.00065$ [2]. Varying this fraction in the quoted errors leads to varying background levels in the unfolding Monte Carlo sample and might thus affect the fit result.

[9] The average inclusive B hadron lifetime as obtained from secondary vertex techniques is most appropriate for this analysis and is therefore used here. Ref. [2] also gives a combined average with measurements from exclusive channels.

- The analogous quantity for charm quark pairs, R_c, is less well known, with a current best value of 0.1719 ± 0.0031 [2].
- Limited knowledge of the LEP beam energy propagates into a corresponding uncertainty of x_E, although the dependency of x_E on the beam energy information is reduced due to the fact that the beam energy does also enter into the calculation of the reconstructed B hadron energy via the beam energy constraint. Nevertheless, wrong assumptions on the LEP beam energy can lead to shifted estimates of the hadronisation parameters. The assumed LEP beam energy is varied within 8 MeV, which is the largest reported error for any sample at or close to the Z resonance [103]. A correlation of the energy uncertainties of 100% is assumed conservatively.
- The parameter values depend slightly on the x_E range taken into account for the fit. The lower end of the fit range is varied in the range $x_E = 0.5 \pm 0.1$, and the upper range is varied within $x_E = 0.95 \pm 0.05$. The largest deviation from the result obtained using the central values is included into the systematic uncertainty.
- The bin width used in the fit is varied by $\pm 10\%$. Any deviations from the result with standard binning are taken into account as systematic uncertainty.

4.6.2 Systematic Uncertainties of the Unfolding Analysis

The following systematic checks are performed to check the stability of the result of the model-independent measurement of $\langle x_E \rangle$:

- Model-dependence: The unfolding procedure is repeated using not the best reweighting fit result, but the second and third best fit results as initial estimators of the true distribution. This study is performed independently for all datasets. The unfolding is also performed with the Monte Carlo replaced by Herwig 5.9 and 6.2 samples. The latter checks can only be performed for the 1994 dataset due to lack of Herwig Monte Carlo samples for the other years. However, it dominates the model error in negative direction, which is taken as the largest observed deviation from the central $\langle x_E \rangle$ value, and therefore a same size effect is assumed for all datasets, with 100% correlation between the sets. The error in positive direction is dominated by use of the third best model, which in almost all datasets is the Kartvelishvili parametrisation. The resulting model uncertainty is found to be $^{+0.0025}_{-0.0028}$.
- The calorimeter resolution is varied by $\pm 10\%$. This results in a change of the measured $\langle x_E \rangle$ of ± 0.0021, taken as systematic uncertainty.
- The resolution of the $r\phi$-related track parameters d_0, ϕ_0, and κ is varied in the range $\pm 5\%$. A systematic uncertainty of ± 0.0004 is found this way.
- The resolution of the z-related track parameters z_0 and $\tan\lambda$ is varied by $\pm 10\%$, resulting in a systematic error of ± 0.0004.
- A variation of the b baryon rate within the error range of the LEP/SLD/CDF estimate of $(10.3 \pm 1.8)\%$ leads to systematic deviations of $^{+0.0005}_{-0.0001}$.

	Bowler bm_t^2	Bowler a	Lund bm_t^2	Lund a	Kartv. α_b	Peterson ε_b	Coll./Spi. ε_b
calo resolution	$^{+2.0}_{-8.5}$	$^{+0.03}_{-0.11}$	$^{+0.4}_{-1.8}$	$^{+0.06}_{-0.21}$	± 0.2	± 1.1	± 1.2
$r\phi$ tracking	± 2.6	± 0.03	± 0.6	± 0.06	± 0.2	± 1.3	± 1.3
z tracking	± 0.1	< 0.01	< 0.1	< 0.01	< 0.1	± 0.2	± 0.3
b baryons	± 0.5	± 0.01	± 0.1	± 0.02	< 0.1	± 0.2	$^{+0.2}_{-0.1}$
B_s fraction	$^{+0.0}_{-0.2}$	< 0.01	< 0.1	< 0.01	< 0.1	< 0.1	< 0.1
$B_J^{(*)}$ fraction	$^{+1.9}_{-2.4}$	± 0.02	$^{+0.2}_{-0.3}$	$^{+0.02}_{-0.03}$	± 0.3	$^{+2.4}_{-2.3}$	$^{+2.2}_{-2.1}$
b decay mult.	$^{+1.7}_{-2.1}$	± 0.03	$^{+0.4}_{-0.5}$	$^{+0.05}_{-0.06}$	< 0.1	$^{+0.1}_{-0.0}$	$^{+0.1}_{-0.0}$
b lifetime	< 0.1	< 0.01	< 0.1	< 0.01	< 0.1	$^{+0.0}_{-0.1}$	< 0.1
c lifetime	$^{+0.7}_{-1.0}$	± 0.01	$^{+0.1}_{-0.2}$	± 0.02	< 0.1	$^{+0.2}_{-0.1}$	$^{+0.2}_{-0.1}$
charm fragm.	± 0.1	< 0.01	< 0.1	< 0.01	< 0.1	± 0.1	± 0.1
$g \to b\overline{b}$ rate	± 0.2	< 0.01	< 0.1	< 0.01	< 0.1	< 0.1	< 0.1
$g \to c\overline{c}$ rate	± 0.6	± 0.01	± 0.1	± 0.01	< 0.1	± 0.1	± 0.1
R_b	< 0.1	< 0.01	< 0.1	< 0.01	< 0.1	< 0.1	< 0.1
R_c	< 0.1	< 0.01	< 0.1	< 0.01	< 0.1	< 0.1	< 0.1
beam energy	± 0.3	< 0.01	± 0.1	± 0.01	< 0.1	± 0.1	± 0.1
fit range	$^{+2.5}_{-3.9}$	$^{+0.04}_{-0.05}$	$^{+1.1}_{-0.9}$	$^{+0.16}_{-0.10}$	$^{+0.2}_{-0.1}$	$^{+1.1}_{-0.9}$	$^{+1.3}_{-3.3}$
binning effects	< 0.1	< 0.01	± 0.1	± 0.01	< 0.1	< 0.1	< 0.1
total	$^{+\ 5.0}_{-10.3}$	$^{+0.07}_{-0.13}$	$^{+1.4}_{-2.2}$	$^{+0.19}_{-0.25}$	$^{+0.5}_{-0.4}$	$^{+3.2}_{-3.0}$	$^{+3.1}_{-4.3}$

Table 4.8: *Overview of systematic error contributions to the model-dependent reweighting fits. The Peterson and Collins/Spiller contributions are given in units of* 10^{-4}.

- The fraction of B_s in the sample is varied in the range $(9.8 \pm 1.2)\%$. The resulting error is $^{+0.0006}_{-0.0003}$.
- Variation of the amount of orbitally excited $B_J^{(*)}$ mesons within the uncertainty of the error weighted average value of $(28.4 \pm 3.5)\%$ gives systematic shifts of ± 0.0006.
- Changing the average multiplicity of charged particles from a B hadron within 4.955 ± 0.062 leads to a systematic uncertainty of $^{+0.0004}_{-0.0005}$.
- The average lifetime of weakly decaying B hadrons is varied in the range 1.577 ± 0.0016 ps. The effect on the $\langle x_E \rangle$ measurement is found to be ± 0.0001.
- Varying the D^0, D^+, D_s, and Λ_c lifetimes within the errors proposed in Ref. [83] leads to a systematic error on the $\langle x_E \rangle$ measurement of ± 0.0001.
- The charm background in the Monte Carlo samples used for the unfolding procedure is used with a Peterson fragmentation function with $\varepsilon_c = 0.031$. A variation of ε_c by ± 0.006 reflects the precision of the parameter estimate as obtained by OPAL [102]. The resulting variations in the $\langle x_E \rangle$ result are found to be below $\pm 10^{-4}$ and are neglected.
- An error on the rate of gluon splitting to $b\overline{b}$ quark pairs of 0.00254 ± 0.00051 $b\overline{b}$ pairs per hadronic event propagates to an uncertainty of ± 0.0001 on $\langle x_E \rangle$.
- The number of $c\overline{c}$ pairs from gluon splitting per hadronic event is changed within the LEP errors of 0.0296 ± 0.0038. This results in a systematic error on $\langle x_E \rangle$ of $^{+0.0006}_{-0.0005}$.
- Varying $R_b = 0.21646 \pm 0.00065$ in the quoted errors leads to differences of $\langle x_E \rangle$ of less than $\pm 10^{-5}$. This effect is neglected.
- The effect of the uncertainty on $R_c = 0.1719 \pm 0.0031$ on the analysis result is below $\pm 10^{-5}$ and is neglected.
- The assumed LEP beam energy is varied within 8 MeV, which is the largest reported error for any sample at or close to the Z resonance [103]. A correlation of the energy uncertainties of 100% is assumed conservatively. The resulting change in $\langle x_E \rangle$ is found to be ± 0.0001.

Summing all systematic errors in quadrature results in a total systematic error on $\langle x_E \rangle$ of $^{+0.0035}_{-0.0037}$. As expected, the systematic uncertainty is larger than the statistical precision. The difference of the RUN and SVD-GURU results is only about one fifth of the total measurement error, and since the SVD-GURU approach is not as stable and robust as the RUN algorithm, the SVD-GURU result is not used for the final result, and no additional systematic error is introduced to account for the difference. A summary of all contributions is shown in Table 4.9.

4.7 Discussion

The mean scaled energy of weakly decaying B hadrons in Z decays is measured to be

$$\langle x_E \rangle = 0.7194 \pm 0.0016(stat)^{+0.0035}_{-0.0038}(syst) \ .$$

	error contribution
model dependence	$^{+0.0025}_{-0.0028}$
calo resolution	± 0.0021
$r\phi$ tracking	± 0.0004
z tracking	± 0.0004
b baryons	$^{+0.0005}_{-0.0001}$
B_s fraction	$^{+0.0006}_{-0.0003}$
$B_J^{(*)}$ fraction	± 0.0006
b decay mult.	$^{+0.0004}_{-0.0005}$
b lifetime	± 0.0001
c lifetime	± 0.0001
charm fragm.	< 0.0001
$g \to b\overline{b}$ rate	± 0.0001
$g \to c\overline{c}$ rate	$^{+0.0006}_{-0.0005}$
R_b	< 0.0001
R_c	< 0.0001
beam energy	± 0.0001
total	$^{+0.0035}_{-0.0037}$

Table 4.9: *Summary of all contributions to the total systematic error of the* $\langle x_E \rangle$ *measurement.*

model	this analysis	ALEPH 2001	SLD 2002
Bowler	$bm_t^2 = 66.1 \pm 4.4^{+\ 5.0}_{-10.3}$	—	$b = 1.2$
	$a = 0.78 \pm 0.07^{+0.07}_{-0.13}$	—	1.4
Lund symmetric	$bm_t^2 = 14.7 \pm 0.8^{+1.4}_{-2.2}$	—	$b = 0.4$
	$a = 1.5 \pm 0.1^{+0.19}_{-0.25}$	—	1.4
Kartvelishvili	$\alpha_\mathrm{b} = 12.1 \pm 0.1^{+0.5}_{-0.4}$	$13.7 \pm 0.7 \pm 1.1$	10.0
Peterson	$\varepsilon_\mathrm{b} = (40.3 \pm 0.7^{+3.2}_{-3.0}) \times 10^{-4}$	$(31 \pm 3 \pm 5) \times 10^{-4}$	55×10^{-4}
Collins/Spiller	$\varepsilon_\mathrm{b} = (21.4 \pm 0.7^{+3.1}_{-4.3}) \times 10^{-4}$	$(18.5 \pm 2.5 \pm 4.1) \times 10^{-4}$	30×10^{-4}

Table 4.10: *Comparison of model parameters obtained by recent* b *hadronisation analyses. SLD does not quote errors on their parameter estimates. Comparison of the OPAL and SLD results for the Lund and Bowler models is difficult due to different parameters used in the fit. The transverse mass, included in the parameter set chosen for this analysis, is calculated from the* b *quark mass* m *as* $m_t^2 = m^2 + p_t^2$*, where* p_t *is the transverse momentum with respect to the Jetset hadronisation axis. The average* p_t *is of the order of* 0.1 GeV*. With a* b *quark mass of* 5 GeV*,* $b = 1.2$ *therefore corresponds to* $bm_t^2 \approx 30$*, and* $b = 0.4$ *yields* $bm_t^2 \approx 10$*.*

This is the most precise available measurement of this quantity. It is cross-checked using a second unfolding algorithm, and it is in excellent agreement with this second method, and with the result of model-dependent reweighting fits. The result obtained here agrees very well with a recent result from the ALEPH collaboration [99], who find $\langle x_\mathrm{E} \rangle = 0.716 \pm 0.006(stat) \pm 0.006(syst)$. ALEPH uses exclusive semi-leptonic B decays, leading to a smaller candidate sample and thus a larger statistical error. Another new measurement by SLD [98] obtains a somewhat lower value of $\langle x_\mathrm{E} \rangle = 0.709 \pm 0.003(stat) \pm 0.003(syst) \pm 0.002(model)$, however, the difference between the two measurements has a statistical significance of only 1.8σ taking only the uncorrelated errors into account. Another $\langle x_\mathrm{E} \rangle$ measurement by the OPAL collaboration was performed recently, using inclusive $\mathrm{b} \to \ell$ decays [104]. Modelling of the $\mathrm{b} \to \ell$ energy spectrum introduces large additional systematic errors in the lepton-based analysis, and therefore the result of $\langle x_\mathrm{E} \rangle = 0.709 \pm 0.003(stat) \pm 0.003(syst) \pm 0.013(model))$ is absolutely compatible with the analysis presented here, especially given that the result in Ref. [104] was not calculated model-independently, but based on a Peterson parametrisation. The LEP average result for $\langle x_\mathrm{E} \rangle$ in the framework of the Peterson model, obtained from earlier analyses, is 0.702 ± 0.008, again in excellent agreement with the value of $0.7029 \pm 0.0006(stat)$ found in this analysis.

The best description of the data with a fragmentation function with one free parameter is achieved with the Kartvelishvili model. The Peterson model is significantly worse, and the Collins/Spiller model results in a much too broad energy distribution to describe the data. The same ordering of adequateness has been observed by SLD and ALEPH in their recent publications. The Bowler and Lund parametrisations with two free parameters each achieve better χ^2 in this analysis and are clearly compatible with the data. The same is seen by SLD. ALEPH did not test these models. The Herwig cluster model is clearly disfavoured. The main difference of the two Herwig versions tested in this analysis is the amount of smearing of the B hadron direction around the initial b quark direction. Significant smearing is used in the Herwig 5.9 sample, softening the spectrum clearly too much. The Herwig 6.2 sample is used without any smearing. This leads to a maximum of the x_E distribution roughly at the same

place as in data, but the width of the x_{E} distribution is too large in Herwig. Similar results are obtained by SLD.

Less agreement is observed among the experiments when it comes to a comparison of the actual values for the parameters describing the individual models (Table 4.10). These values depend critically on details of the Monte Carlo tuning, which is not identical in all respects among the collaborations, although efforts have been made to correct most relevant Monte Carlo parameters to a common set of values.

Estimates of the parameters of several models have been brought forward in Chapter 2. In the Peterson model, ε_{b} is expected from mass scale considerations to be of the order of 50×10^{-4}, which is remarkably close to the observed value of $(40.3 \pm 0.7^{+3.2}_{-3.0}) \times 10^{-4}$. Kartvelishvili et al. estimate α_{b} to be around 9 from Regge intercepts of bottomonia. The observed value of $12.1 \pm 0.1^{+0.5}_{-0.4}$ is in acceptable agreement with this expectation.

The data seem to indicate a preference for a large z behaviour of the fragmentation function of $(1-z)^r$ with $r \approx 1$: The Lund and Bowler a parameters are both compatible with $r = 1$; the Kartvelishvili parametrisation, as best one-parameter function, also shows a $r = 1$ behaviour. The Peterson parametrisation, with $r = 2$, is less well matching. This may be understood as confirmation of the dimensional counting arguments of Brodsky et al. [50], against the more recent claims of Ref. [54]. One has to keep in mind, though, that the behaviour at z very close to one has only minor impact on the fit quality; other factors like the overall width of the distribution and the position of the maximum impose much stronger constraints on the parameter fit results.

A general conclusion of the analysis presented here is that the parton shower plus string hadronisation Monte Carlo models deliver an adequate description of the data to current precision. The fragmentation functions modelled according to intrinsic symmetries of the string model (Lund symmetric, Bowler) are favoured against the phenomenological approaches. The cluster model of Herwig only comes close to matching the data when essential features of the cluster model are replaced by more string-like concepts: Isotropic cluster decay leads to an energy spectrum much too soft, while the conservation of the initial heavy quark direction in the heavy hadron improves the model, yet at a level of still significantly worse agreement with data than Jetset.

Limitations of the analysis presented here are obvious: The OPAL detector resolution is not sufficient to resolve the subtle differences of the Lund symmetric and Bowler parametrisations. The precision of parameter estimates (both model-dependent and -independent) are dominated by imperfect modelling of the detector resolution. The $\langle x_{\mathrm{E}} \rangle$ measurement suffers furthermore from the weak separation power between different models, introducing a large model-dependence error. A simple study on possible improvements of the investigation of b quark hadronisation at a future $\mathrm{e^+e^-}$ experiment is presented in Chapter 8 of this thesis.

Chapter 5

Excited D Mesons at OPAL

The following part of this thesis deals with the spectrum of charmed $D_{u,d}$ mesons, introduced in Figure 2.12. Both production in the hadronisation of charm quarks and in decays of B hadrons is investigated. The reconstruction of orbitally and radially excited states of this spectrum is at the edge of being possible at LEP: The narrow orbital excitations $D_1(3/2)$ and D_2^* were seen by ALEPH [105], DELPHI [106], and OPAL [107], but the measurement of their properties and production rates is imprecise due to large background and a relatively small signal. This is especially true for excited D mesons produced in B hadron decays, because their average energy is lower, and therefore closer to the large background of arbitrary combinations of low-energy tracks produced during b quark hadronisation and decay. The broad orbital excitations D_0^* and $D_1(1/2)$ were not identified at LEP, because it is difficult to separate their contribution from the continuous combinatorial background. Similarly, the prospects of observing the radial excitations D' and $D^{*\prime}$ at LEP depend crucially on the width of these states. Common expectation is that due to their decay kinematics these states have a width similar to that of the broad orbital excitations. This would render an observation at LEP practically impossible. However, mass predictions of $m_{D'} = 2.579$ GeV/c^2 and $m_{D^{*\prime}} = 2.629$ GeV/c^2 exist [64], with an uncertainty of the order of 20 MeV/c^2 estimated from the difference between the values obtained in computations [64] and observations [2] of the masses of the narrow orbitally excited states. Furthermore, educated guesses of favoured decay final states are available. In fact, the DELPHI collaboration has published an observation of a narrow resonance decaying to[1] $D^{*+}\pi^+\pi^-$ [66] at a mass of $2.637 \pm 0.002(stat) \pm 0.006(syst)$ GeV/c^2, close to the theoretical prediction of the $D^{*\prime}$ mass. The DELPHI measurement of the width of the state is limited by their detector resolution and quoted to be smaller than 15 MeV/c^2 at 95% C.L. Their result is shown in Figure 5.1. Although DELPHI quotes a theoretical model which predicts the $D^{*\prime}$ width to be of the order of 1 MeV/c^2, this is in disagreement with most other models. Therefore the identification of the observed resonance as $D^{*\prime}$ is disputed [108, 109].

This chapter presents a search for the state reported by DELPHI in hadronic Z decays recorded with the OPAL detector. The search covers both the region of the resonance measured by DELPHI as well as any other narrow resonance in the vicinity of the predicted $D^{*\prime}$ mass. Therefore the particle being searched for will be referred to as $D^{*\prime+}(2629)$ throughout this Chapter[2]. A preliminary version of this analysis was developed during the Diploma thesis

[1] Charge conjugates will be implied throughout this thesis.

[2] This choice for the name was agreed upon by the OPAL collaboration to reflect the fact that the identification of the resonance as radial excitation $D^{*\prime}$ is disputable, due to the small width. On the other hand, no alternatives to this identification were offered by theorists. The name chosen here is thought to reflect that the mass of the

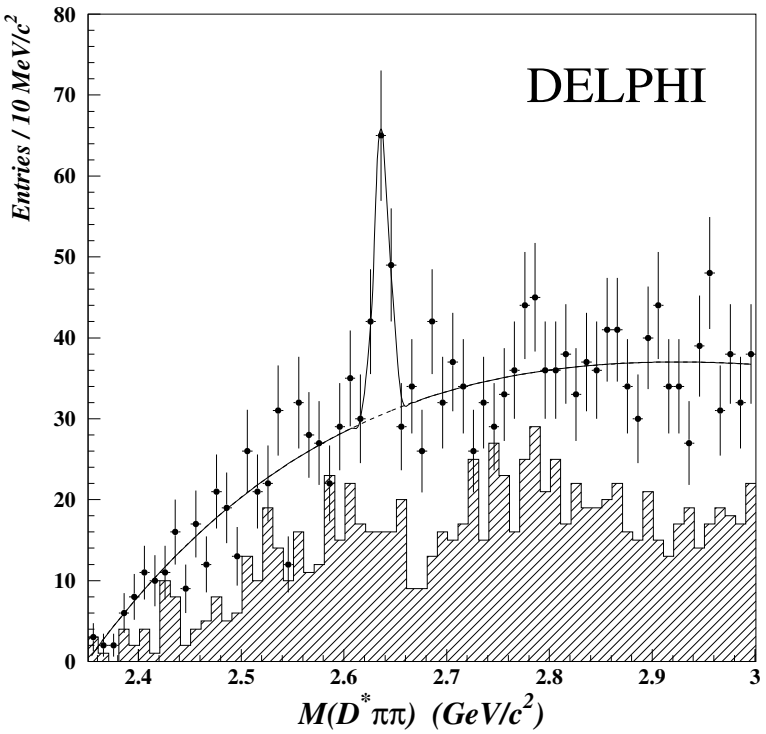

Figure 5.1: *Mass spectrum of* $D^{*+}\pi^+\pi^-$ *combinations observed by DELPHI [66]. A narrow peak is found at a mass of* $2.637 \pm 0.002(stat) \pm 0.006(syst)$ GeV/c^2. 66 ± 14 *candidates are exceeding the background level, corresponding to a significance of* 4.7σ*, taking only statistical errors into account. The shaded histogram shows the corresponding distribution of wrong charge combinations.*

preceding this PhD thesis [110] and was contributed to the International Conference on High Energy Physics 1998 [111]. The refined analysis presented here is published by the OPAL collaboration [112].

A further topic of this chapter is a close investigation of the production rates of the narrow orbital excitations $D_1^0(3/2)$ and D_2^{*0}, commonly referred to as $D_J^{(*)0}$ throughout this chapter. The reconstruction of $D_J^{(*)0}$ is utilised as simple cross-check analysis of the $D^{*\prime+}(2629)$ reconstruction. Unfortunately the LEP measurements of their production rate in B hadron decays spread over a wide range, and surprisingly large differences were found between the rates observed in the analysis presented here and a previous OPAL publication on this topic [107]. Possible reasons and the significance of this difference are evaluated and discussed.

5.1 Event Selection and Monte Carlo Optimisation

Hadronic Z decays are selected based on the number of reconstructed tracks and the energy deposited in the electro-magnetic calorimeter, as described in Ref. [113]. The analysis uses a sample of 3.5 million hadronic decays of the Z collected with the OPAL detector between 1992 and 1995.

All five-flavour Jetset 7.4 Monte Carlo samples described in Section 3.3 for the 1992–1995 detector configuration are used in this analysis. In addition, samples with simulated $D^{*\prime}(2629)$

presumed resonance is most important for the analysis presented here. However, this choice is not necessarily consistent. The Particle Data Group adopted the notation $D^*(2640)$.

decays were generated since Jetset does not include $D^{*\prime}(2629)$ production by default. For the production of the $D^{*\prime}(2629)$ Monte Carlo samples, excited D mesons states were implemented into Jetset with the masses set to 2.579 GeV/c^2 and 2.629 GeV/c^2, according to the most recent calculation [64], and the width set to zero. The possible effects of a non-zero width are treated later as systematic uncertainty. DELPHI only measured the ratio of the $D^{*\prime+}(2629)$ and $D_J^{(*)0}$ production rates [66], and therefore this measurement was combined with the OPAL measurement of $D_J^{(*)0}$ production [107] to calculate the expected absolute $D^{*\prime+}(2629)$ production rate. $D^{*\prime}(2629)$ production is simulated in charm quark hadronisation and in B meson decays. In the latter case, the production channels for the $D^{*\prime}(2629)$ were chosen to be the same as those for the D_2^*, with equal branching fractions. Four samples of $D^{*\prime}(2629)$ Monte Carlo events were generated: production in $Z \to c\overline{c}$ and $Z \to b\overline{b}$ events and the decay channels $D^{*\prime+} \to D^{*+}\pi^+\pi^-$ and $D^{*\prime+} \to D_1^0(1/2)\pi^+$. The signal Monte Carlo sample contains 600,000 events in total, with at least one charged $D^{*\prime}(2629)$ meson in each event.

The following corrections are applied to the Monte Carlo samples: The fractions of $c\overline{c}$ and $b\overline{b}$ events among the hadronic events, R_b and R_c, are reweighted to match the current world average values [2]. This is done to ensure realistic background levels. A Peterson fragmentation function is chosen with parameters as determined from LEP data[3] [114]. The production rates of D^* mesons [102] and $D_J^{(*)0}$ mesons [107] are corrected to the values measured by OPAL. The production rates quoted in these earlier measurements are highly correlated with the values of R_b and R_c. Since the estimates of these values have changed noticeably after the publication of these results, the values are corrected for the most recent world average flavour fractions [2]. The only significant shift is observed in the $b \to D^*$ production rate, where the published value of $f(b \to D^{*+}) = 0.173 \pm 0.016 \pm 0.012$ using $R_c = 0.180 \pm 0.011 \pm 0.012 \pm 0.006$ has to be corrected to $f(b \to D^{*+}) = 0.234$ (without error estimate) for the current average $R_c = 0.1719 \pm 0.0031$. The Monte Carlo is furthermore corrected for the rates of $b\overline{b}$ and $c\overline{c}$ pair production in gluon splitting, that are matched to world average values [2]. The Monte Carlo samples are then analysed in the same manner as the data.

5.2 Reconstruction of $D^{*\prime+}(2629)$ Candidates

The reconstruction of $D^{*\prime+} \to D^{*+}\pi^+\pi^-$ decays involves D^{*+} reconstruction and, subsequently, the combination of accepted D^{*+} candidates with additional pion candidates. The D^{*+} reconstruction follows closely a recent OPAL publication [102], with the exception of the cut on the kaon particle identification probability which has been tightened for this analysis, in order to reduce combinatorial background.

The following decay sequence is reconstructed exclusively:

[3] A Peterson fragmentation function with parameters close to the ones determined from LEP data is used in the largest fraction of the uncorrected samples. (The 1994 Monte Carlo sample uses a Peterson function with significantly different parameters — see Chapter 3.) The use of a Peterson parametrisation is therefore leading to correction weights generally close to unity and minimises possible adverse reweighting effects. Furthermore, the official recommendations for LEP heavy flavour analyses [83] do not yet take the recent b hadronisation studies into account and favour the use of a Peterson function for LEP publications.

$$\begin{aligned} \mathrm{D}^{*\prime+}(2629) \rightarrow & \mathrm{D}^{*+}\pi^+\pi^- \\ & \hookrightarrow \mathrm{D}^0\pi^+ \\ & \quad \hookrightarrow \mathrm{K}^-\pi^+ \end{aligned}$$

All tracks are considered for the construction of $\mathrm{D}^{*\prime+}(2629)$ candidates that pass loose quality cuts requiring $|d_0| < 0.5$ cm, $|z_0| < 20$ cm, $p > 0.5$ GeV/c, and $p_{xy} > 0.150$ GeV/c. Here $|d_0|$ is the distance of closest approach of the track to the primary vertex, measured in the plane perpendicular to the beam, z_0 the distance along the beam at this point, p the momentum, and p_{xy} the momentum in the plane perpendicular to the beam. Only tracks with more than 40 hits out of a maximum of 159 in the main tracking chamber are used. The primary vertex in a collision is reconstructed from the tracks in the event and constrained by the known average position and spread of the $\mathrm{e^+e^-}$ interaction point. To improve the mass resolution, a track is required to have a precise z measurement at the exit point of the tracking chamber, either from an associated hit in the z-chamber surrounding the central drift chamber, or from the presampler. In cases where the particle exited the tracking chamber in the endcap region, i.e. $|\cos\theta| > 0.73$, the exit point is determined precisely from the last sense wire used for the track measurement.

Only combinations of tracks that have the correct charge assignments, and which pass intermediate requirements imposed by the reconstruction of the D^{*+}, are taken into account. The two pions produced in the initial $\mathrm{D}^{*\prime+}(2629)$ decay will be referred to as "$\mathrm{D}^{*\prime+}(2629)$ pions", whereas the pion coming from the D^{*+} decay will be referred to as "slow pion".

Two tracks of opposite charge are accepted as a D^0 candidate if their invariant mass lies within the range $1.79-1.94$ GeV/c^2, assigning the pion mass to one particle and the kaon mass to the other [2]. D^0 candidates are combined with tracks of charge opposite to that of the kaon candidate to form D^{*+} candidates. The scaled energy x_E of the D^{*+} candidate, i.e. the ratio of the energy sum of all participating tracks over the beam energy, is required to be larger than 0.2 in order to reject combinatorial background from low-energy hadronisation tracks. The difference of the invariant masses of D^{*+} and D^0 candidates, $\Delta m = m_{\mathrm{D}^*} - m_{\mathrm{D}^0}$, must lie within the interval from 142 to 149 MeV/c^2.

Background in the sample is further reduced by cutting on the helicity angle θ^* measured between the direction of the D^0 candidate in the laboratory frame and the direction of the kaon in the rest frame of the D^0 candidate. The kaon candidate from the D^0 decay is expected to be isotropically distributed in $\cos\theta^*$, while the background peaks at $\cos\theta^* = -1$ and, particularly at small x_E, at $\cos\theta^* = +1$. This effect is taken into account by requiring $\cos\theta^* > -0.9$ for $x_\mathrm{E} > 0.5$ and $|\cos\theta^*| < 0.8$ for $x_\mathrm{E} < 0.5$.

At low x_E, where the background is most pronounced, the particle identification power of the OPAL detector is used to enrich the sample in true kaons from D^0 decays. A probability W_K is computed from the ionization energy loss measurement of a track in the drift chamber, the track momentum, and the theoretical expectation for a kaon. At least 20 $\mathrm{d}E/\mathrm{d}x$ out of a possible 159 measurement points and $W_\mathrm{K} > 10\%$ are required for the kaon candidate in a D^{*+} candidate with $x_\mathrm{E} < 0.5$.

A fraction (1.5%) of all D^{*+} candidates share the same slow pion candidate with another D^{*+} candidate in the same event. In this case only the D^{*+} candidate with a D^0 invariant mass closest to the mean value obtained from a fit to the D^0 mass distribution is kept for the further analysis. The D^{*+} candidates surviving the cuts described above are combined with

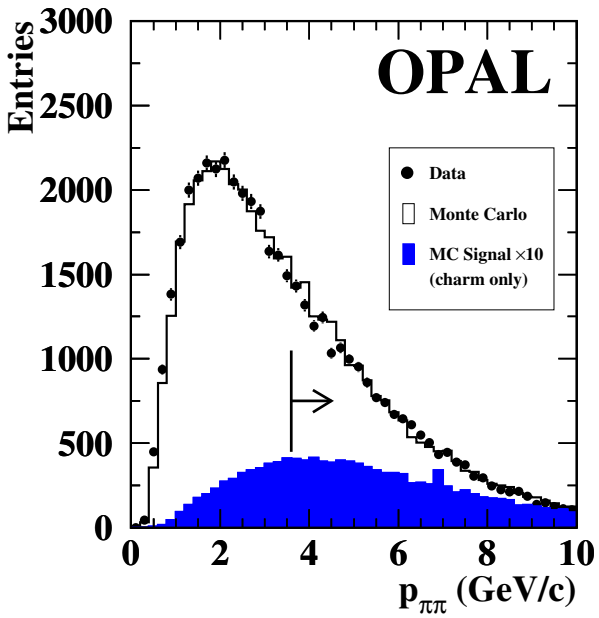

Figure 5.2: *Magnitude of the vector sum of the* $D^{*\prime}(2629)$ *pion momenta,* $p_{\pi\pi}$*, for data (points with error bars), Monte Carlo (open histogram, scaled to the same number of entries as data) and true* $D^{*\prime+}(2629)$ *(shaded, scaled up by a factor of 10). The arrow indicates the selected region.*

all remaining pairs of oppositely charged tracks. For these combinations, a mass difference $\Delta m^{'} = m_{D^{*\prime}} - m_{D^{*}}$ is calculated.

In order to suppress background from uds events, charm and bottom tags are used. The mean fractional energy of $D^{*\prime+}(2629)$ mesons in $Z \rightarrow c\overline{c}$ events is expected to be large compared to $D^{*\prime+}(2629)$ from B decays, and especially compared to fake $D^{*\prime+}(2629)$ candidates in events of all flavours consisting of low-energy hadronisation tracks. Since most of the energy of the $D^{*\prime+}(2629)$ is transferred to the D^{*+}, a charm enriched sample is selected by imposing a cut on the energy fraction of the D^{*+} of $x_E > 0.4$. Additionally, in the Monte Carlo simulation, the $D^{*\prime+}(2629)$ pions have a higher momentum if the $D^{*\prime}(2629)$ is produced in $c\overline{c}$ events compared to the production via the decay of B hadrons. This information has been exploited by selecting only candidates for which the magnitude of the vector sum of the two $D^{*\prime}(2629)$ pion momenta is greater than 3.6 GeV/c (Figure 5.2). The mass resolution in the charm enriched sample is improved by constraining all $D^{*\prime+}(2629)$ candidate tracks except those from the D^0 decay to the primary event vertex.

A bottom-enriched sample is selected by requiring an apparent D^0 decay length of at least 0.3 mm, defined as the distance between the reconstructed D^0 vertex and the primary event vertex, measured in the plane perpendicular to the beam. D^0 candidates from light quark (uds) events and $c\overline{c}$ events are expected to be made up from tracks in the vicinity of the primary vertex. In contrast, D^0 candidates in $b\overline{b}$ events tend to have a larger decay length with respect to the primary vertex, due to the B hadron lifetime.

The separation significance of two vertices is defined as the distance between them in the plane perpendicular to the beam, divided by the uncertainty on this quantity. The separation significance of the D^0 vertex and the reconstructed vertex formed by the $D^{*\prime+}(2629)$ pion tracks is required to be between -2.0 and $+4.0$. The distribution of this variable is not centred at zero, because the D^0 has a lifetime large enough to be observed. The separation significance between the $D^{*\prime+}(2629)$ pion vertex and the D^0 vertex is shown in Figure 5.3. A positive sign indicates that the D^0 vertex is farther from the primary interaction point than the $D^{*\prime+}(2629)$

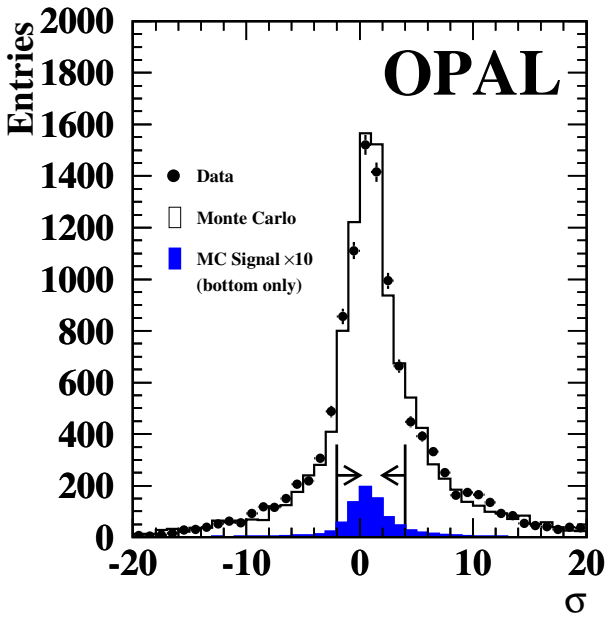

Figure 5.3: *Separation significance σ between the* D^0 *vertex and the reconstructed vertex of the* $D^{*\prime+}(2629)$ *decay pion tracks for data (points with error bars), Monte Carlo (open histogram, scaled to the same number of entries as data) and true* $D^{*\prime+}(2629)$ *(shaded, scaled up by a factor of 10) for candidates passing all selection criteria except for the cut on the quantity shown here. The arrows indicate the selected region.*

flavour	charm enriched	bottom enriched	combined sample
uds	12%	10%	11%
c	60%	15%	31%
b	28%	75%	58%

Table 5.1: *Flavour composition of the charm enriched, bottom enriched and combined Monte Carlo samples.*

pion vertex. Positive values are expected for signal, because the D^0 occurs later in the decay chain.

The Monte Carlo flavour composition of the $D^{*\prime+}(2629)$ candidates passing all selection criteria is shown in Table 5.1. For $D^{*\prime+}(2629)$ mesons from primary charm and bottom quarks, the reconstruction efficiencies are estimated from Monte Carlo analysis to be 14.1% and 7.1%, respectively. The combined efficiency for $D^{*\prime+}(2629)$ from both sources is 11.4%, assuming equal rates for production in charm and bottom events. This assumption is motivated by the range of production rate ratios observed for $D^{*\pm}$ [102] and orbitally excited $D_J^{(*)0}$ mesons [107]. The analysis has also been performed with several other assumptions, and the dependence of the results on these different scenarios is included as a systematic error.

5.3 Selection Results

In order to maximise the expected sensitivity of the analysis, the charm and bottom enriched samples with 1765 and 3051 candidates, respectively, in the $\Delta m' = m_{D^{*\prime}} - m_{D^*}$ region between 2.3 GeV/c^2 and 3.0 GeV/c^2 are merged into a combined sample. The overlap of 324 candidates between charm and bottom sample is taken into account; candidates that have been tagged as

charm and bottom are used only once. This sample contains a total of 4492 $D^{*\prime +}(2629)$ candidates in 2192 events. The results for the combined sample and the b and c enriched samples are discussed below.

The $\Delta m'$ distribution of the combined charm and bottom enriched sample is shown in Figure 5.4a. No narrow resonance is observed anywhere in the $\Delta m'$ region between 0.3 and 1.0 GeV/c^2, although the Monte Carlo simulation with a $D^{*\prime}(2629)$ production rate fixed at the value published by DELPHI [66] shows a clear signal (see Figure 5.4b). This is also separately true for the c and b enriched samples, shown in Figures 5.5 and 5.6, respectively. Shape and normalisation of the background differ in data and simulation, especially in the b enriched sample. This is due to $D^{*\prime +}(2629)$ candidates in the Monte Carlo where one track is incorrectly assigned to the $D^{*\prime +}(2629)$ candidate. These candidates lead to a broad enhancement in the mass distribution. The mean scaled energy x_{E} of these candidates is small. Therefore, they contribute more to the b enriched sample than to the c enriched sample. The analysis has also been performed on a Monte Carlo sample without $D^{*\prime}(2629)$ production. It has been found that in this case the background shape and normalisation agree very well with the data. This absence of a significant enhancement over the expected background in data provides additional confidence that the $D^{*\prime +}(2629)$ production rate must be small.

The Monte Carlo distributions shown in Figures 5.4–5.6 are created from a subsample of the available Monte Carlo events which has similar size as the data sample. This facilitates a visual impression of the expected significance of a possible signal with DELPHI parameters.

A limit on the $D^{*\prime +}(2629)$ production rate is calculated by defining a mass window in the $\Delta m'$ range of 0.58 GeV/$c^2 < \Delta m' <$ 0.66 GeV/c^2, corresponding to a $D^{*\prime}(2629)$ mass window of $2.59 - 2.67$ GeV/c^2. This includes the $\pm 2\sigma$ range of both the theoretical prediction of the $D^{*\prime}$ [64] and the excess observed by DELPHI [66]. The background distribution is fitted using a parametrisation of the form [66, 107]

$$\mathrm{f}(\Delta m') = \alpha \, (\Delta m' - m_0)^{\beta} \, \mathrm{e}^{-\gamma(\Delta m' - m_0)} \, , \tag{5.1}$$

where $m_0 = 0.28$ GeV/c^2 is the kinematic limit for $D^{*+}\pi^+\pi^-$ combinations, and α, β and γ are the fit parameters. The signal region has been excluded from the fit. The number of $D^{*\prime +}(2629)$ candidates in the mass window is determined to be 14 ± 28 by subtracting the integrated interpolated background function from the observed number of candidates in the signal interval. The quoted statistical error is obtained by combining the Gaussian variance of the number of entries in the mass window (± 25) and the uncertainty on the background integral obtained by propagating the uncertainties on the fit parameters (± 14), taking into account the correlations.

5.4 Reconstruction of $D_J^{(*)0}$ Candidates

The $D^{*\prime +}(2629)$ analysis is checked by applying a similar selection to $D^{*+}\pi^-$ final states, looking for the narrow orbital resonances D_1^0 and D_2^{*0}. The D^{*+} selection criteria are as described earlier. Accepted D^{*+} candidates are combined with pion candidates passing selection criteria similar to those applied to the $D^{*\prime +}$ pions, except for the cuts on the pion-pion momentum sum and the pion-pion vertex separation, which are inappropriate here. Instead, the pion momentum is required to be larger than 2.0 GeV/c, as was done in an earlier OPAL publication on orbitally excited D mesons [107]. The efficiency of the $D_J^{(*)0} \to D^{*+}\pi^-$ reconstruction is about 7.3%. The results achieved on data and simulated events can be compared in Figure 5.7. The method used

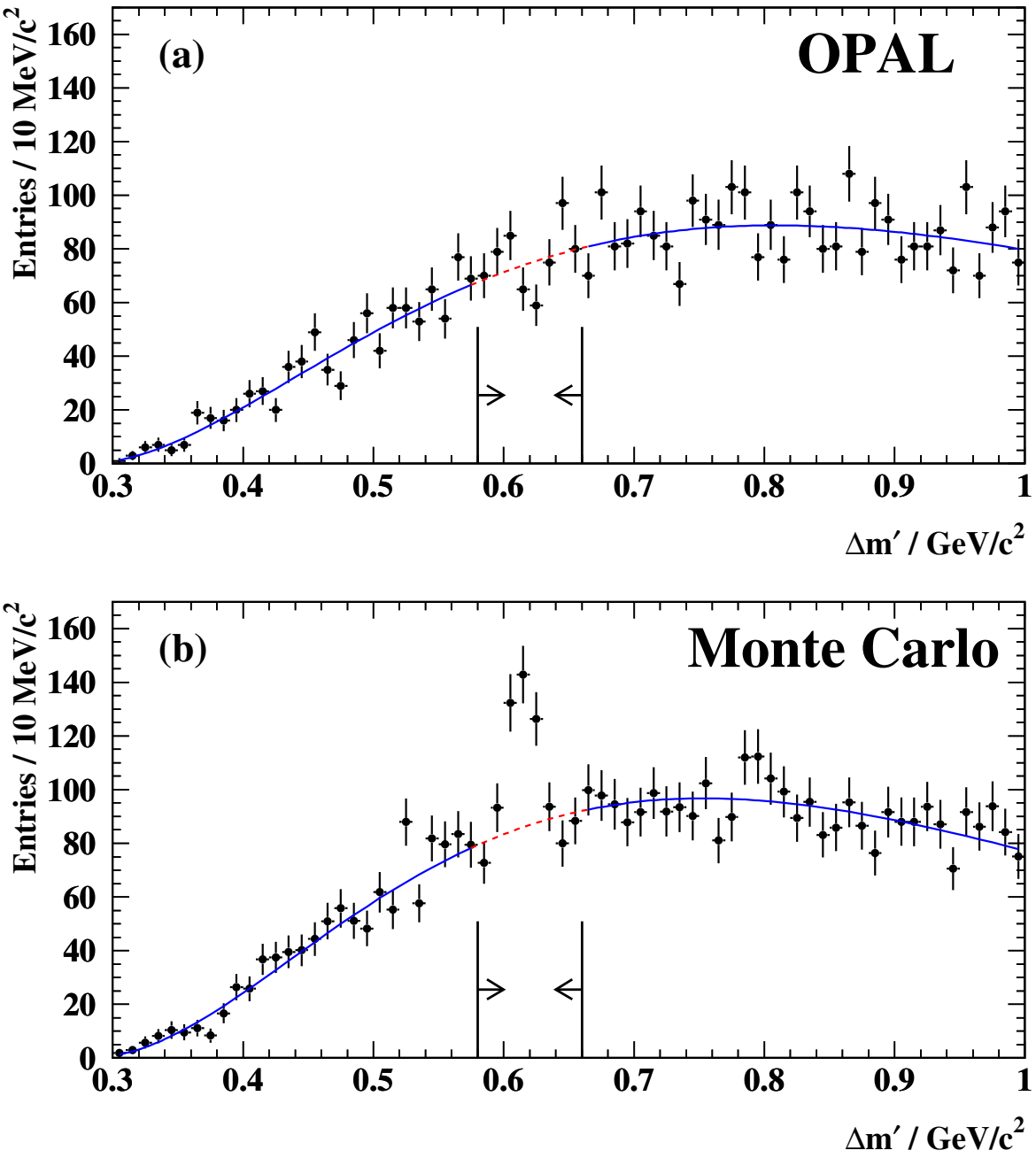

Figure 5.4: *Distribution of the mass difference* $\Delta m' = m_{\mathrm{D}^{*\prime}} - m_{\mathrm{D}^*}$ *of* $\mathrm{D}^{*\prime+}(2629)$ *candidates in the combined charm and bottom sample, for (a) data and (b) Monte Carlo. The calculation of* $\Delta m'$ *as well as the background parametrisation superimposed on the histogram are described in the text. The Monte Carlo histogram is scaled to the number of hadronic events in data. Furthermore, the* D^{*+} *Monte Carlo production rate is adjusted to an OPAL measurement of this quantity [102], and the* $\mathrm{D}^{*\prime+}(2629)$ *production rate is fixed at the value published by DELPHI [66] and the OPAL* $\mathrm{D}_J^{(*)0}$ *measurement [107]. The Monte Carlo plot presented here is created from a subsample of the available events that has roughly the same size as the data sample. The arrows indicate the mass window defined as the signal region. The line represents the result of the background fit, where the line is dashed in regions that are excluded from the fit. The* χ^2*/d.o.f. of the background fit is 1.23 for data, and 0.99 for the Monte Carlo simulation.*

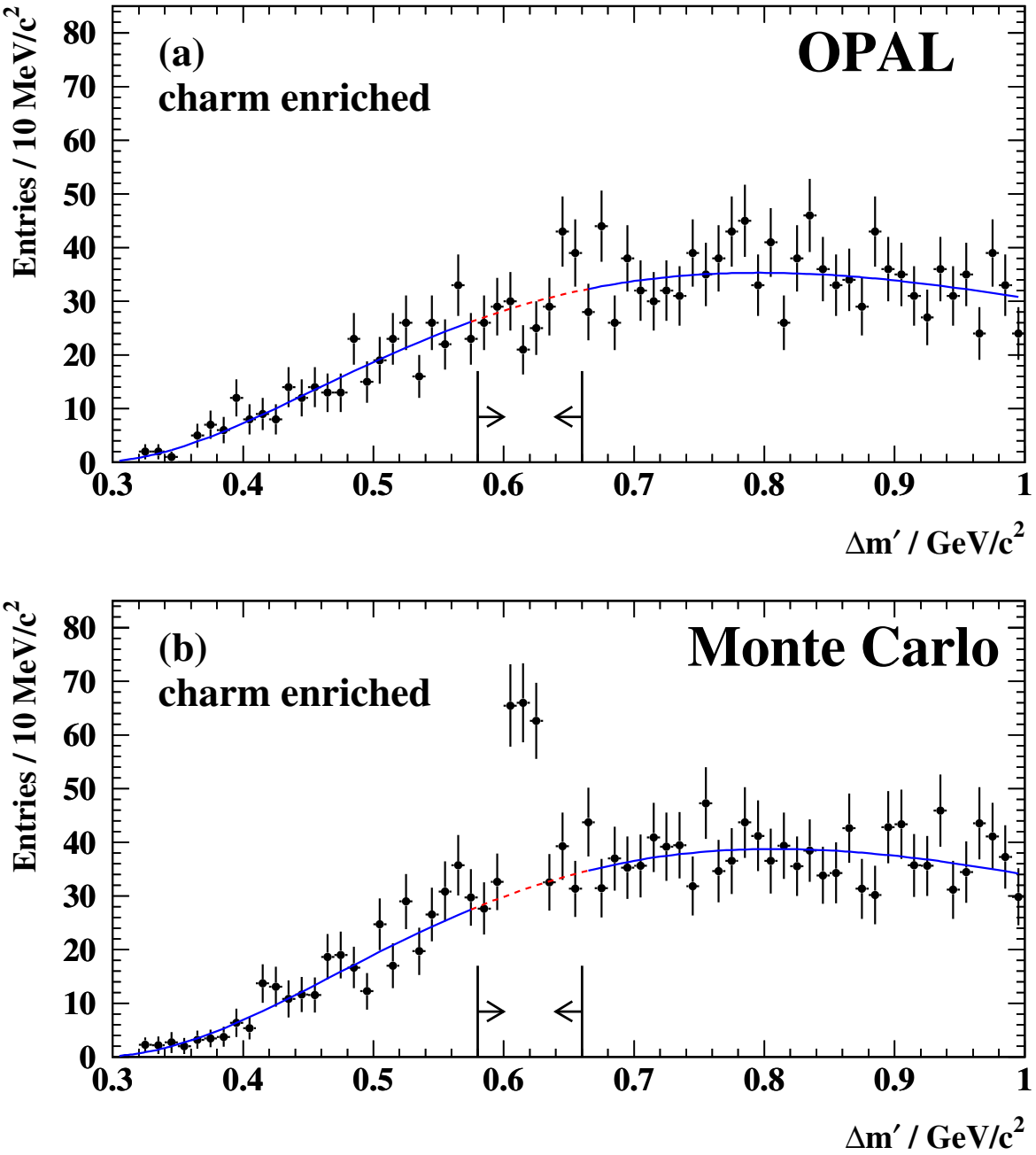

Figure 5.5: *Distribution of the mass difference* $\Delta m' = m_{\mathrm{D}^{*\prime}} - m_{\mathrm{D}^*}$ *of* $\mathrm{D}^{*\prime+}(2629)$ *candidates in the charm enriched sample, for (a) data and (b) Monte Carlo. The* χ^2*/d.o.f. of the background fit is 0.80 for data, and 0.70 for the Monte Carlo simulation.*

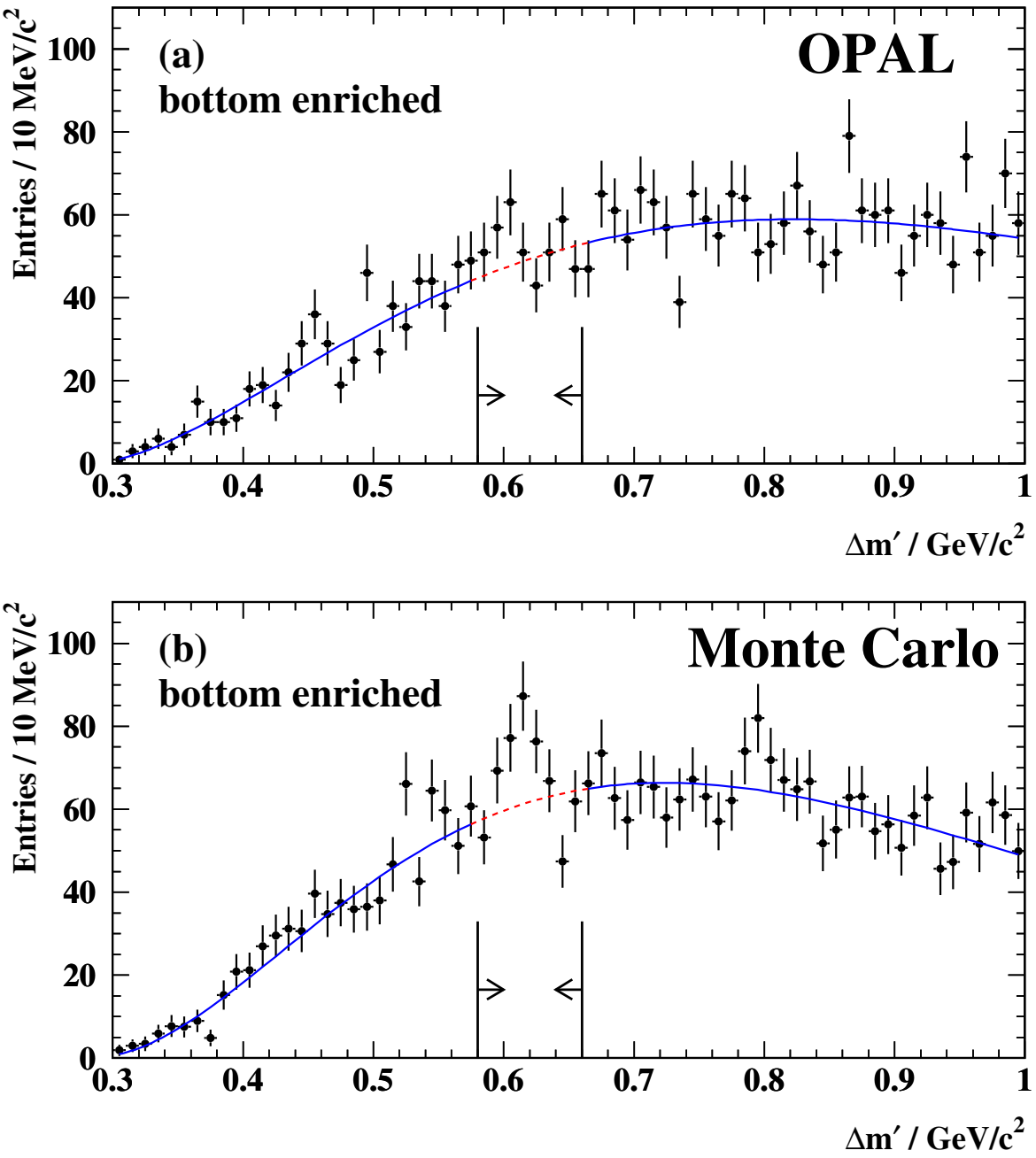

Figure 5.6: *Distribution of the mass difference* $\Delta m^{'} = m_{\mathrm{D}^{*\prime}} - m_{\mathrm{D}^{*}}$ *of* $\mathrm{D}^{*\prime+}(2629)$ *candidates in the bottom enriched sample, for (a) data and (b) Monte Carlo. The* χ^2*/d.o.f. of the background fit is 1.20 for data, and 1.07 for the Monte Carlo simulation. The difference in shape and normalisation of the background is explained by a large number of partially reconstructed* $\mathrm{D}^{*\prime+}(2629)$ *candidates which, due to their low mean scaled energy, mainly contribute to the* b *enriched sample. The analysis is also performed on a Monte Carlo sample without* $\mathrm{D}^{*\prime}(2629)$ *production. It is found that in this case the background shape and normalisation agree very well with the data.*

sample	data (fit)	Monte Carlo (fit)	Monte Carlo (true)
charm enriched	122 ± 23	108 ± 15	$122 \pm 39 \pm 22$
bottom enriched	83 ± 27	174 ± 22	$159 \pm 46 \pm 23$

Table 5.2: *Number of* $\mathrm{D}_J^{(*)0}$ *signal candidates observed in data and Monte Carlo tuned to published OPAL* $\mathrm{D}_J^{(*)0}$ *production rates [107]. The errors quoted with the true number of selected Monte Carlo* $\mathrm{D}_J^{(*)0}$ *account for the statistical as well as systematic uncertainties of the published OPAL measurement.*

for determining the number of signal events is the same as was used for the $\mathrm{D}^{*\prime+}(2629)$. The lower mass window boundary is set to 2.382 GeV/c^2, two D_1^0 widths below the world average D_1^0 mass. The upper boundary is chosen to be 2.507 GeV/c^2, two D_2^{*0} widths above the world average D_2^{*0} mass. The production rates of the two narrow $\mathrm{D}_J^{(*)0}$ resonances are adjusted in the simulation to match the previous OPAL measurement [107]. The amount of signal found in Monte Carlo is 281 ± 16, whereas in data the excess is 189 ± 41 in a sample of 4711 selected $\mathrm{D}_J^{(*)0}$ candidates. The analysis presented here and the previous OPAL publication on orbitally excited D mesons [107] that was used to adjust the $\mathrm{D}_J^{(*)0}$ production rates in Monte Carlo use a similar dataset. Both results are therefore expected to be correlated. Nevertheless, it is found that the overlap of the selected $\mathrm{D}_J^{(*)0}$ candidate samples of old and new analysis is small, and the results can thus be considered almost statistically independent. This leads to the conclusion that the measured rates are statistically compatible, although detailed studies uncover hints that a large part of the difference is actually caused by improved correction routines for OPAL data, and not by statistical fluctuations, as detailed in the following.

Details of the $\mathrm{D}_J^{(*)0}$ Fit Results

The Monte Carlo sample used for the $\mathrm{D}^{*\prime+}(2629)$ and $\mathrm{D}_J^{(*)0}$ analyses has its $\mathrm{D}_J^{(*)}$ production rates tuned to the values previously published by OPAL [107]. The observed amount of signal in both data and tuned Monte Carlo is presented in Table 5.2. While there is very good agreement in the charm enriched selection, a possible discrepancy is observed in the bottom sector. The difference between data fit result and true number of selected Monte Carlo $\mathrm{D}_J^{(*)}$ is only 1.3σ if all errors can be taken as independent. But since both measurements are using the same data sample, it is highly questionable whether this is adequate. Numerous checks are therefore performed to investigate the actual significance and nature of the observed difference.

Re-evaluation of the $\mathrm{D}_J^{(*)0}$ Production Rates Published Previously by OPAL

The $\mathrm{D}_J^{(*)0}$ production rates published in Ref. [107] were obtained from an analysis finalised in 1996 and published in 1997. Since then, many updates of the OPAL reconstruction software, calibration database, and further improvements of detector modelling had been performed before the finalisation of the analysis presented here in 2001. In order to evaluate possible effects on the observed $\mathrm{D}_J^{(*)0}$ production rates in OPAL data, the part of the previous OPAL analysis dealing with $\mathrm{b} \to \mathrm{D}_J^{(*)0}$ was repeated during the studies performed for this thesis. The principal author of the respective $\mathrm{b} \to \mathrm{D}_J^{(*)0}$ part of the OPAL $\mathrm{D}_J^{(*)0}$ publication, Matthew Jones, kindly agreed to provide his original analysis software for further studies, and also supported the work with useful hints. A minimal amount of changes was applied to adapt the software to the latest version of the OPAL reconstruction environment; private calls to data correction routines have been removed in order not to interfere with the recently established

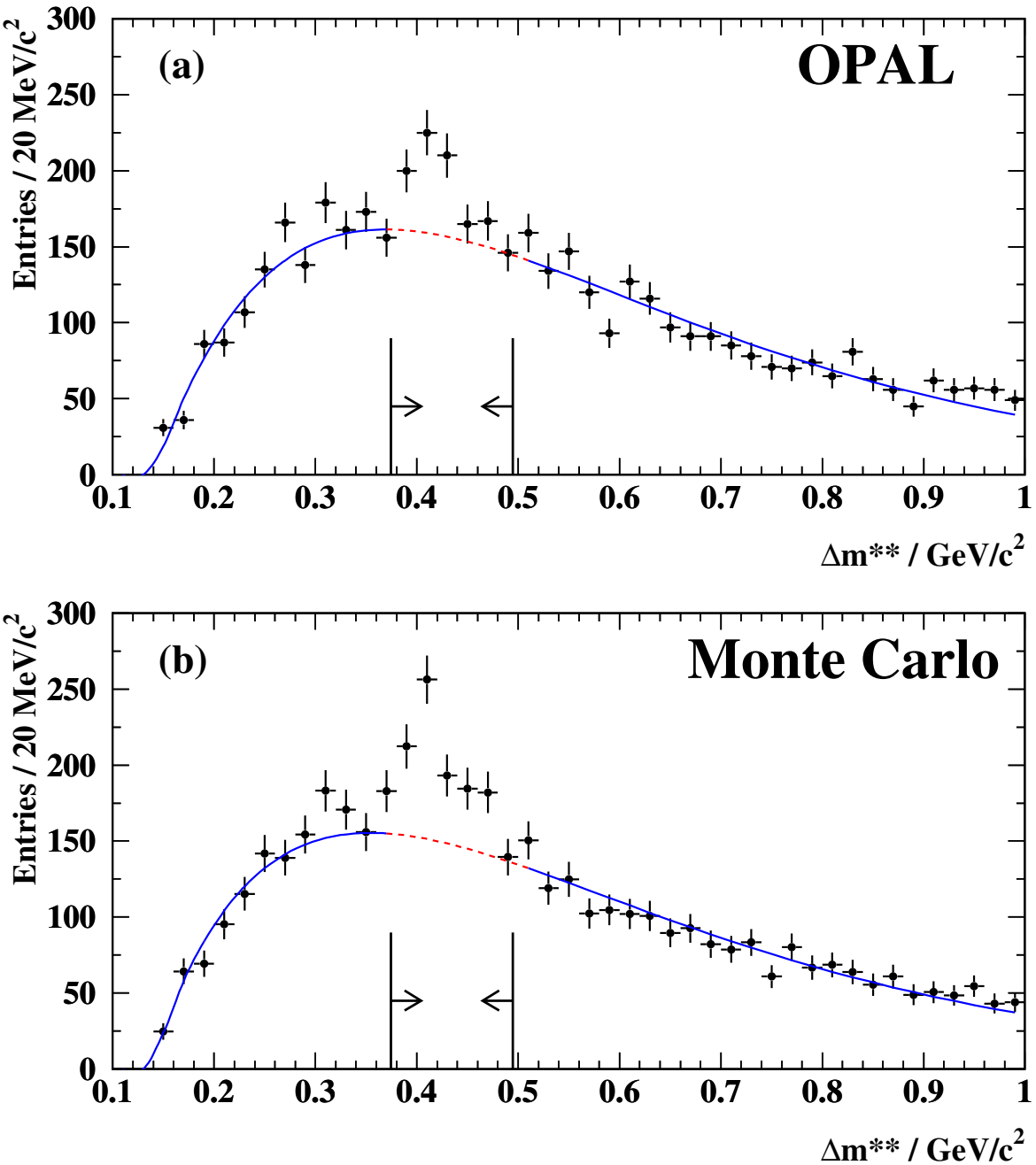

Figure 5.7: *Distribution of the mass* $\Delta m_{**} = m_{\mathrm{D}^{*+}\pi^-} - m_{\mathrm{D}^{*+}}$, *for (a) data and (b) Monte Carlo. The production rates of* $\mathrm{D}_J^{(*)0}$ *mesons in the Monte Carlo are adjusted to the values measured in data [107]. The same parametrisation as in the* $\mathrm{D}^{*/+}(2629)$ *analysis is used to describe the background. The* χ^2*/d.o.f. of the fit is 1.43 for data, and 1.22 for the Monte Carlo simulation. The Monte Carlo histogram is scaled to the number of hadronic events in data.*

global data correction scheme[4]. All 1992–1995 OPAL data with active silicon micro-vertex detector along with a sample of 4 million Monte Carlo events were processed with Jones's software. Figure 5.8 shows the resulting $D_J^{(*)0}$ mass distributions for data and Monte Carlo; the fit that is shown in the histograms will be explained later. Figure 5.9 is taken from the 1997 OPAL $D_J^{(*)0}$ publication for comparison. The re-evaluated mass distribution clearly shows an increased amount of background with respect to the original result. The background level of the re-evaluation agrees nicely with the Monte Carlo expectation. The amount of signal will be investigated in the following.

Matthew Jones's software reconstructs 146 $D_J^{(*)0}$ in the Monte Carlo, out of which 122 were produced in $b\overline{b}$ events. A total number of 1844 $D_J^{(*)0}$ in $b\overline{b}$ and 1655 $D_J^{(*)0}$ in $c\overline{c}$ events that decay in the investigated channel are present in the Monte Carlo. This gives a tag efficiency of $(6.6 \pm 0.6)\%$ for b, and $(1.5 \pm 0.3)\%$ for c. The efficiencies quoted in the publication were 5.5% and 0.7%, respectively.

The fit to determine the $D_1^0(3/2)$ and D_2^{*0} production rates in $b\overline{b}$ and $c\overline{c}$ events in the 1997 publication takes decay angular distributions into account to improve the separation of the $D_1^0(3/2)$ and D_2^{*0} contributions. A simultaneous fit is performed for charm enriched and bottom enriched candidate samples. Because only the b enriched selection is repeated here, a simple fit with the same background parametrisation as in the main analysis presented in this chapter, plus two Gaussians with fixed means and widths for the two $D_J^{(*)0}$ peaks is performed for this study. The means are fixed to the world average values of the $D_J^{(*)0}$ masses [2], the widths are set to a quadratic sum of the Gaussian equivalent of the Breit-Wigner widths and a term for the detector resolution (7 MeV/c^2, as in the 1997 publication). The result of this fit is presented in Figure 5.8; the Monte Carlo fit estimates the number of events in the peaks to be 122 ± 22, which is compatible with the actual Monte Carlo content of 146 to within roughly one sigma. 78 ± 21 events are found in data (published: 106 ± 24). The fraction of candidates in the D_1^0 peak is 0.71 (published: $0.77^{+0.16}_{-0.14}$), where the error is presumably large. If the $D_J^{(*)0}$ production rates are not significantly different in $b\overline{b}$ and $c\overline{c}$ than what is used in the Monte Carlo, the assumption holds that the $b\overline{b}$ purity in the selected signal sample is roughly the same as observed in Monte Carlo. With thus 65 ± 18 b $\to D_J^{(*)0}$ candidates in the reconstructed decay channel, and a reconstruction efficiency in this channel of $(6.6 \pm 0.6)\%$, an estimated total number of 1000 $D_J^{(*)0}$ decays in this channel is expected in the whole data sample of 3.5 million events. The production rate of $D_J^{(*)}$ in $b\overline{b}$ events is thus

$$\mathrm{BR}(b \to D_1^0) = 0.025 \ , \tag{5.2}$$

$$\mathrm{BR}(b \to D_2^{*0}) = 0.032 \ , \tag{5.3}$$

corrected for the combined branching ratio of $D_J^{(*)0} \to D^{*+}\pi^-$, $D^{*+} \to D^0\pi^+$, $D^0 \to K^-\pi^+$, and for the fraction of $b\overline{b}$ events in the sample. No error is calculated, but realistically one can assume the relative error to be of the order of 50%. These values are to be compared with the published rates of

$$\mathrm{BR}(b \to D_1^0) = 0.050 \pm 0.014(\mathrm{stat}) \pm 0.006(\mathrm{syst}) \ , \tag{5.4}$$

$$\mathrm{BR}(b \to D_2^{*0}) = 0.047 \pm 0.024(\mathrm{stat}) \pm 0.013(\mathrm{syst}) \ . \tag{5.5}$$

Obviously data reprocessing and data correction routines have enough impact on the measurement of the production rate of $D_J^{(*)0}$ in $b\overline{b}$ events to decrease the measured values by almost

[4]In OPALists terms, the older analysis did not yet use the global DST fixup routine ODFIX.

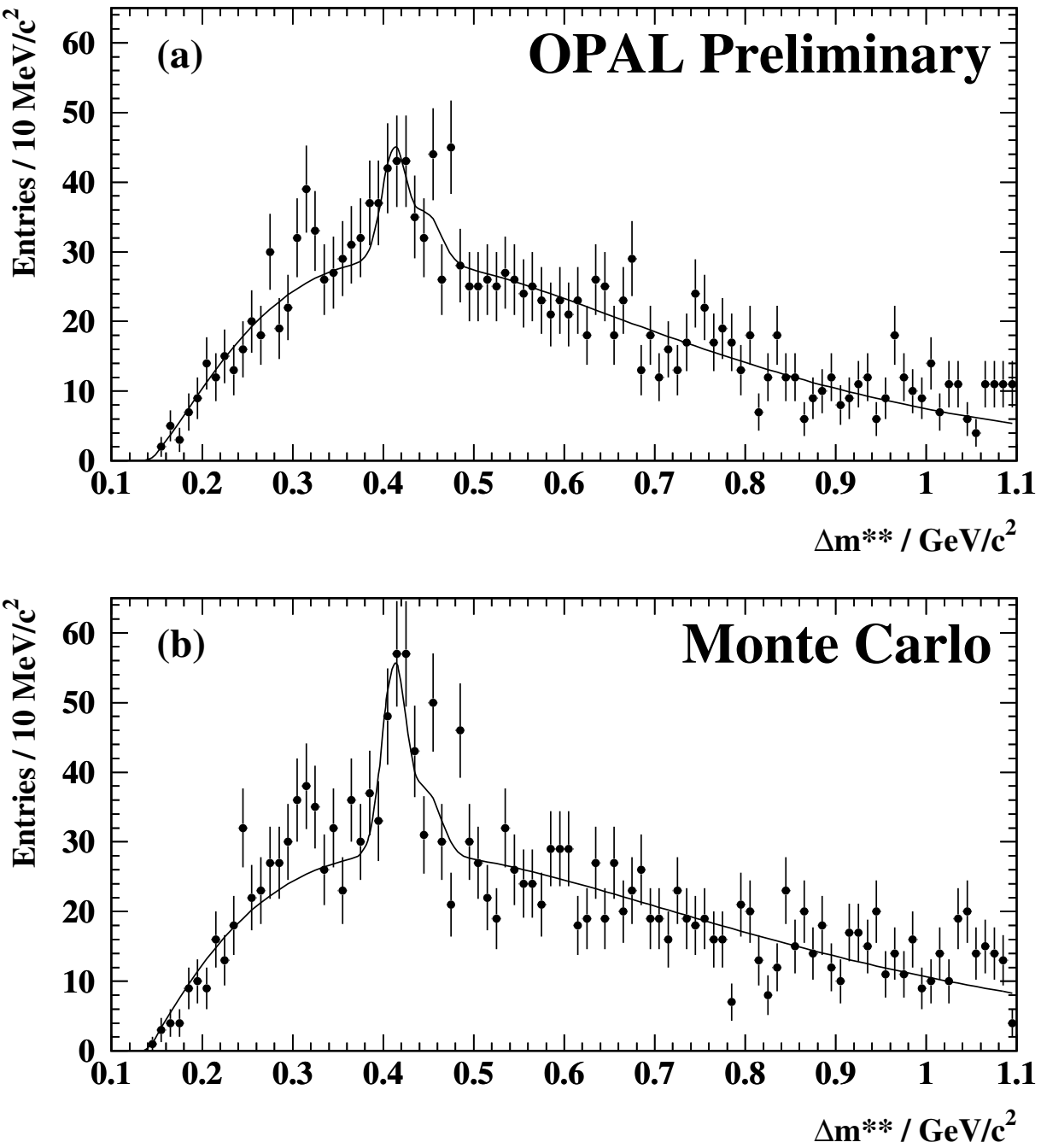

Figure 5.8: *Reprocessed version of Matthew Jones's analysis. The upper plot shows the result for OPAL data 1992-1995, for the lower plot 4 million Monte Carlo events were used. The fits are explained in the text; the χ^2/d.o.f. is 0.98 for data and 1.41 for Monte Carlo.*

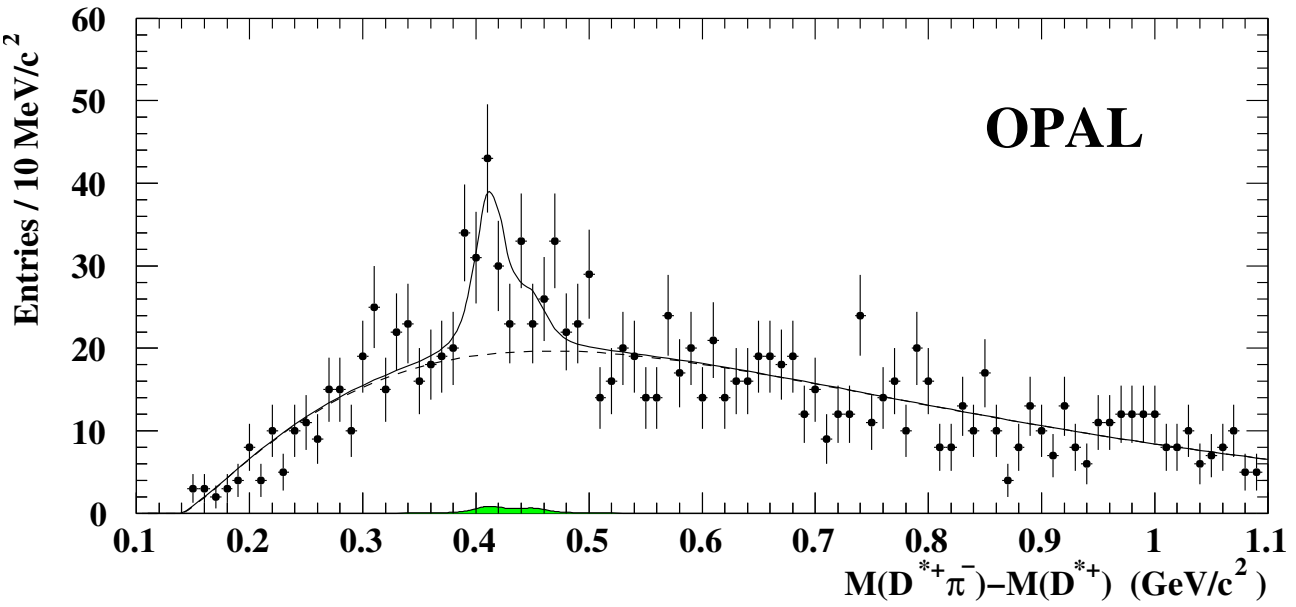

Figure 5.9: *Published* $D_J^{(*)}$ b *sample mass distribution from the OPAL* $D_J^{(*)}$ *paper [107].*

sample	data (fit)	new Monte Carlo (fit)	new Monte Carlo (true)
charm enriched	122 ± 23	100 ± 15	118 ± 60
bottom enriched	83 ± 27	136 ± 21	114 ± 60

Table 5.3: *Number of* $D_J^{(*)0}$ *signal candidates observed in data and Monte Carlo tuned to re-evaluated OPAL* $D_J^{(*)0}$ *production rates. The errors quoted with the true number of selected Monte Carlo* $D_J^{(*)0}$ *mirror the rough estimate of production rate uncertainty given in the text.*

a factor of two. This is not completely unexpected, given that $D_J^{(*)0}$ reconstruction in $b\overline{b}$ is a measurement at the limit of what can be done with the OPAL detector. Nevertheless, this change is not covered by the systematic error of the published result. It is not possible anymore to reconstruct the statistical overlap of the selected $D_J^{(*)0}$ candidate samples of the original publication version software and the recent re-runs of Matthew Jones's software. Therefore no information about the degree of correlation of both samples (and thus their statistical errors) are available. This leads to the conclusion that it is not clear whether the original and the re-evaluated versions of this measurement are compatible or not.

With $D_J^{(*)0}$ rates used in the Monte Carlo samples for the $D^{*\prime+}(2629)$ cross-check analysis adapted to the re-evaluated rates, the formerly observed discrepancy is much smaller, although the tendency remains — see Table 5.3.

Correlation of the Measurements

It is impossible to judge the significance of the observed differences without knowing to what extent the re-evaluated Jones analysis and the $D^{*\prime+}(2629)$ cross-check analysis are correlated. Both are using the same initial sample of OPAL data. Nevertheless, looking at all candidates selected in the signal region, one finds that out of 450 candidates found by the re-evaluated published analysis and out of the 436 candidates from the cross-check analysis, only 28 candidates are present in both selections. Even fully accounting this amount to the signal, the overlap of the selections is roughly one third of the signal. It is rather likely that a large part of the

overlap are real $D_J^{(*)0}$, because the overlap observed in Monte Carlo signal is higher: With 146 (179) true $D_J^{(*)0}$ correctly reconstructed by the published (the cross-check) analysis in Monte Carlo, the number of candidates selected by both analyses is 61, i.e. also roughly one third. With more than 300 independent background events present in each analysis' signal region, it is easy to explain a fluctuation of the fit results of the observed magnitude.

Impact on the $D^{*\prime+}(2629)$ Analysis

$D_J^{(*)0}$ production rates are used in two parts of the $D^{*\prime+}(2629)$ analysis: The cross-check $D_J^{(*)0}$ reconstruction is one aspect. Its result has to be compared to a reference production rate. The other point is the normalisation of the $D^{*\prime+}(2629)$ production rate in Monte Carlo, which requires the assumption of a $D_J^{(*)0}$ rate to translate the relative rate compared to $D_J^{(*)0}$ production that was published by DELPHI into an absolute rate. This absolute rate is necessary to estimate the sensitivity of the analysis.

$D_J^{(*)0}$ rates are measured by OPAL [107], DELPHI [106], and ALEPH [105]. The most natural choice would be to calculate absolute $D^{*\prime+}(2629)$ cross-sections with the DELPHI $D_J^{(*)0}$ measurement, which is essentially the same analysis on the same dataset as the cross-check analysis in the DELPHI $D^{*\prime+}(2629)$ paper, while comparing the OPAL cross-check analysis with the previously published OPAL $D_J^{(*)0}$ results. Unfortunately, both parts are problematic: The DELPHI $D_J^{(*)0}$ production rates (ALEPH likewise) are not yet final; they are available only as conference reports. The OPAL $D_J^{(*)0}$ measurement is not fully reproducible, though all recent measurements agree within the statistical errors, as shown above for the analyses relevant to the $D^{*\prime+}(2629)$ analysis presented in this chapter.

Since no other final and published $D_J^{(*)0}$ production rate measurement exists than from the 1997 OPAL paper, this publication is used as basis for cross-check reference as well as Monte Carlo tuning. Following the investigations described above, it can be stated that the cross-check analysis of the OPAL $D^{*\prime+}(2629)$ analysis is compatible with the previous OPAL publication. Referring to the OPAL measurement for Monte Carlo tuning of the $D^{*\prime+}(2629)$ is somewhat more of an issue: The sensitivity of the $D^{*\prime+}(2629)$ reconstruction depends on the amount of signal that is to be expected, which again depends on the choice of the reference $D_J^{(*)0}$ rates. Among all published as well as preliminarily measured $D_J^{(*)0}$ rates, the OPAL rates are the highest, thus giving a rather optimistic signal expectation. It seemed infeasible, though, to wait for any of the other LEP collaborations to finalise their results, since both of them have been in the state of preliminary announcements for a few years now; therefore it is concluded that there is no other choice for a final OPAL $D^{*\prime+}(2629)$ publication than to refer solely to the OPAL $D_J^{(*)0}$ paper. It has to be pointed out that the core of the analysis, the calculation of $D^{*\prime+}(2629)$ production rate limits, does itself not depend on external $D_J^{(*)0}$ rate measurements. The limitations of the sensitivity of the analysis are not defined by an expected signal rate, but by the upper limit on $D^{*\prime+}(2629)$ production rates in absence of a significant signal.

5.5 Systematic Checks of the $D^{*\prime+}(2629)$ Reconstruction

Having confirmed in the case of $D^{*+}\pi^-$ final states as described in the previous section that the reconstruction procedure performs as expected, the results of the search in the $D^{*+}\pi^+\pi^-$ final state are used to place limits on the production rate of the $D^{*\prime+}(2629)$. The efficiency

of $\mathrm{D}^{*\prime+}(2629)$ reconstruction is taken from Monte Carlo simulation. The efficiency calculation accounts for several sources of systematic uncertainties. They are evaluated as follows:

- The efficiency is calculated from a simulation with zero $\mathrm{D}^{*\prime+}(2629)$ width. To quantify the effect of a non-zero width, the analysis is repeated with a $\mathrm{D}^{*\prime+}(2629)$ width of 15 MeV/c^2, the 95% C.L. upper limit obtained by DELPHI [66]. This results in a relative decrease of the efficiency of 16.5%, taken as systematic uncertainty.

- The simulated detector resolutions of momentum, impact parameters and track angles are varied by $\pm 10\%$, as in previous publications [107, 102], around the values that best describe the data. The largest relative deviation in the selection efficiency $(^{+4.9\%}_{-5.7\%})$ is taken as systematic uncertainty.

- Equal production rates of $\mathrm{D}^{*\prime+}(2629)$ in charm hadronisation and B hadron decays are assumed. Other possible assumptions include the same ratio as observed in $\mathrm{D}^{*\pm}$ production [102], or in $\mathrm{D}_J^{(*)0}$ production [107]. Equal numbers of $\mathrm{D}^{*\prime}(2629)$ from both primary heavy flavours are simulated as well as the ratio of candidates from $\mathrm{b\overline{b}}$ and $\mathrm{c\overline{c}}$ events observed by DELPHI [66], corrected for the different reconstruction efficiencies of the respective analyses. The ratios thus obtained cover a $^{+33\%}_{-23\%}$ range around the central assumption of equal production rates in $\mathrm{b\overline{b}}$ and $\mathrm{c\overline{c}}$ events. The largest observed variations in the efficiency in both directions, $^{+3.8\%}_{-4.6\%}$, are taken as systematic uncertainty.

- A Peterson function is used to parametrise the heavy quark hadronisation in the Monte Carlo samples. The hadronisation models by Collins and Spiller [47] and Kartvelishvili [48] are also tested. The fragmentation function parameters are varied in the limits implied by the measurement of the mean x_E distribution of D^{*+} mesons at LEP [114]. The largest resulting uncertainty of $^{+1.7\%}_{-2.3\%}$ is taken as systematic uncertainty.

- The efficiency depends on the performance of the particle identification by $\mathrm{d}E/\mathrm{d}x$ measurements. The $\mathrm{d}E/\mathrm{d}x$ calibration for kaons was checked in a previous analysis [115] under identical circumstances. An error of $\pm 3.2\%$ was found for the total rate of kaons passing the selection. Because this cut is applied only for candidates with $x_\mathrm{E} < 0.5$, the expected contribution to the uncertainty on the efficiency is $\pm 2.1\%$.

- The D^0 lifetime is currently measured with a precision of 0.7%, whereas the average B hadron lifetime is known to 0.9% [2]. The cut on the D^0 apparent decay length and thus the b flavour enrichment is sensitive to the modelling of this quantity. The cut value is therefore varied within the combined uncertainty on D^0 and B lifetime. The resulting deviation of $^{+0.2\%}_{-0.0\%}$ is taken as systematic uncertainty.

- The calculated production limit depends on the branching ratio $\mathrm{Br}(\mathrm{D}^{*+} \to \mathrm{D}^0\pi^+) \times \mathrm{Br}(\mathrm{D}^0 \to \mathrm{K}^-\pi^+)$. The world average value is $(0.677 \pm 0.005) \times (0.0383 \pm 0.0009)$ [2]. The relative uncertainty on the product branching ratio is $\pm 2.5\%$.

- The reconstruction efficiencies of the decay chains $\mathrm{D}^{*\prime+} \to \mathrm{D}_1^0(1/2)\pi^+$, $\mathrm{D}_1^0(1/2) \to \mathrm{D}^{*+}\pi^-$ and $\mathrm{D}^{*\prime+} \to \mathrm{D}^{*+}\pi^+\pi^-$ are identical within the statistical uncertainties. No systematic uncertainty is introduced.

- The reconstructed number of $\mathrm{D}^{*\prime+}(2629)$ in Monte Carlo is compared to the actual number of $\mathrm{D}^{*\prime+}(2629)$ in the sample. The excess over the background fit is 138 ± 30, with 175

error source	relative contribution		
	c enriched	b enriched	combined
relative errors on Monte Carlo efficiency			
$D^{*\prime+}(2629)$ width	$^{+0.0\%}_{-17.9\%}$	$^{+0.0\%}_{-10.6\%}$	$^{+0.0\%}_{-16.5\%}$
detector resolution	$^{+5.2\%}_{-6.1\%}$	$^{+4.5\%}_{-5.7\%}$	$^{+4.9\%}_{-5.7\%}$
relative production rates in b and c	none	none	$^{+3.8\%}_{-4.6\%}$
hadronisation modelling	$^{+3.6\%}_{-3.7\%}$	$^{+1.1\%}_{-0.3\%}$	$^{+1.7\%}_{-2.3\%}$
kaon $\mathrm{d}E/\mathrm{d}x$	$^{+1.3\%}_{-1.3\%}$	$^{+2.6\%}_{-2.6\%}$	$^{+2.1\%}_{-2.1\%}$
B and D^0 lifetimes	none	$^{+0.5\%}_{-0.0\%}$	$^{+0.2\%}_{-0.0\%}$
Monte Carlo statistics	$^{+0.1\%}_{-0.1\%}$	$^{+0.08\%}_{-0.08\%}$	$^{+0.07\%}_{-0.07\%}$
total	$^{+6.5\%}_{-19.3\%}$	$^{+5.3\%}_{-12.3\%}$	$^{+6.8\%}_{-18.4\%}$
relative errors on external branching ratios			
branching ratio $D^{*+} \to D^0\pi^+,\ D^0 \to K^-\pi^+$	$\pm 2.5\%$	$\pm 2.5\%$	$\pm 2.5\%$
error on $\Gamma_{b\overline{b}}/\Gamma_{\mathrm{had}}$ and $\Gamma_{c\overline{c}}/\Gamma_{\mathrm{had}}$	$\pm 2.9\%$	$\pm 0.3\%$	none
total	$^{+7.5\%}_{-19.7\%}$	$^{+5.9\%}_{-12.6\%}$	$^{+7.2\%}_{-18.6\%}$

Table 5.4: *Overview of the systematic error sources contributing to the total uncertainty.*

entries due to $D^{*\prime+}(2629)$ with all tracks reconstructed. It is thus concluded that the fit is free of significant bias.

- The width of the signal region is varied from 90% to 130% of the nominal value to check whether the resulting counting rate variations are consistent with statistical effects. All results are clearly within the statistical error. Thus no additional systematic uncertainty is assigned.

- The bin width of the $\Delta m'$ histograms in which the fit is performed is varied from 75% to 125% of the value used for the analysis. No significant impact on the rate is observed.

The contributions to the systematic uncertainty are summarised in Table 5.4.

5.6 Calculation of $D^{*\prime+}(2629)$ Production Limits

The limit is calculated assuming that the candidate sample in the signal region is composed of a large background and a small signal sample. Each contribution has a Poisson probability density function although the background can be approximated by a Gaussian distribution $\mathcal{G}(n; e_{\mathrm{bck}}, \sigma)$ since the background expectation is large. The width of the Gaussian, $\sigma = 28$, has two contributions, one accounting for the statistical uncertainty in the signal window, the other one taking into account the fit error. $n_0 = 610$ candidates are observed in the signal window. The probability to count n_0 candidates or less is given by

$$P(n_0; e_{\mathrm{sig}}) \;=\; \sum_{n=0}^{n_0} \sum_{n_{\mathrm{sig}}=0}^{n} \mathcal{P}(n_{\mathrm{sig}}; e_{\mathrm{sig}})\; \mathcal{G}(n - n_{\mathrm{sig}}; e_{\mathrm{bck}}, \sigma)\ , \tag{5.6}$$

where $e_{\rm sig}$ is the unknown expectation value of the signal and $\mathcal{P}$ its Poisson distribution. The summation is performed over all possible combinations of n, the total number of candidates in the mass window, and $n_{\rm sig}$, the amount of signal within these n candidates, where $n \leq n_0$. Assuming no narrow $\mathrm{D}^{*\prime+}(2629)$ are produced, i.e. $e_{\rm sig} = 0$, a probability of 0.70 is obtained to observe 610 candidates or less. Given the prior knowledge of the maximum amount of background, the 95% C.L. limit is obtained at $P(n_0; e_{\rm sig}) = 0.70 \times 0.050$. At large n (≈ 10) the systematic uncertainties affecting the efficiency start playing a role in calculating the limit. They are considered by substituting the Poisson distribution of the signal with a Gaussian distribution at $n > 10$ and adding in quadrature the asymmetric systematic uncertainty of the efficiency to the width of the Gaussian given by $\sqrt{n}$. The limit obtained is:

$$f(\mathrm{Z} \to \mathrm{D}^{*\prime\pm}(2629)) \times Br(\mathrm{D}^{*\prime+}(2629) \to \mathrm{D}^{*+}\pi^+\pi^-) < 3.1 \times 10^{-3} \quad (95\%\ \mathrm{C.L.}). \tag{5.7}$$

This corresponds to a 95% C.L. upper limit of 66 on the number of reconstructed $\mathrm{D}^{*\prime+}(2629)$ in the signal region. The approach used here is similar to a Bayesian approach with a flat prior distribution for positive $\mathrm{D}^{*\prime+}(2629)$ production rates and zero elsewhere, but superior in the fact that negative expectation values are excluded in principle by using the proper Poisson distribution.

Limits on the $\mathrm{D}^{*\prime+}(2629)$ production rate in charm and bottom events are also calculated. In the charm and bottom enriched samples, the numbers of events in the signal region, relative to the expectations derived from the fitted background functions, are 5 ± 18 and 29 ± 23, respectively. In using these results to calculate limits, a further systematic uncertainty arises due to the experimental uncertainties on[5] $\mathrm{R_c} = \Gamma_{\mathrm{c\overline{c}}}/\Gamma_{\rm had} = 0.1671 \pm 0.0048$ and $\mathrm{R_b} = \Gamma_{\mathrm{b\overline{b}}}/\Gamma_{\rm had} = 0.21644 \pm 0.00075$ [2]. Under the conservative assumption that $\mathrm{D}^{*\prime+}(2629)$ are only produced in $\mathrm{Z} \to \mathrm{c\overline{c}}$ events, i.e. that the measured excess can be fully assigned to $\mathrm{D}^{*\prime+}(2629)$ candidates in $\mathrm{c\overline{c}}$ events, a production limit of

$$f(\mathrm{c} \to \mathrm{D}^{*\prime+}(2629)) \times Br(\mathrm{D}^{*\prime+}(2629) \to \mathrm{D}^{*+}\pi^+\pi^-) < 0.9 \times 10^{-2} \quad (95\%\ \mathrm{C.L.}) \tag{5.8}$$

is obtained from the charm enriched sample, while under the opposite assumption that all $\mathrm{D}^{*\prime+}(2629)$ are only produced in the decay of b-hadrons, a limit of

$$f(\mathrm{b} \to \mathrm{D}^{*\prime+}(2629)) \times Br(\mathrm{D}^{*\prime+}(2629) \to \mathrm{D}^{*+}\pi^+\pi^-) < 2.4 \times 10^{-2} \quad (95\%\ \mathrm{C.L.}) \tag{5.9}$$

is computed using the bottom enriched sample. The systematic uncertainties assumed for the calculations in the separate samples are given in Table 5.4.

5.7 Discussion

The result of the OPAL $\mathrm{D}^{*\prime+}(2629)$ search does not agree with the published DELPHI results [66]. Both analyses apply standard selection criteria to obtain a high-purity D^{*+} sample. In contrast to the OPAL analysis, DELPHI reconstructs D^0 candidates in two decay channels, $\mathrm{D}^0 \to \mathrm{K}^-\pi^+$ and $\mathrm{D}^0 \to \mathrm{K}^-\pi^+\pi^+\pi^-$. The loss in efficiency associated with using only the $\mathrm{K}^-\pi^+$ channel is in part compensated by the softer kinematic cuts and a slightly larger hadronic event sample. Combinatorial background is reduced by applying a best candidate selection to D^{*+}

[5]The more recent $\mathrm{R_b}$ and $\mathrm{R_c}$ from LEP/SLD [69] used in Chapter 4 were not yet available when the $\mathrm{D}^{*\prime+}(2629)$ analysis was finalised.

candidates which share tracks. These candidates can produce correlated entries in the $\Delta m'$ distribution if they are combined with the same $\mathrm{D}^{*\prime+}(2629)$ pions. The expected sensitivity of the analysis to the existence of a narrow resonance in the mass region including the theoretical predictions for the $\mathrm{D}^{*\prime}$ as well as the mass of the published DELPHI result, produced at a rate published by DELPHI, is demonstrated in Figure 5.4. The excess observed in the Monte Carlo sample with comparable size to the data sample has a significance of 4.7σ (statistical error only), or 3.5σ including all systematic uncertainties.

The OPAL and DELPHI selection criteria used to select charm and bottom enriched samples, and for the pions from the $\mathrm{D}^{*\prime+}(2629)$ decay, have been optimised in different ways. For example, the kinematic cuts for the pion candidates from the $\mathrm{D}^{*\prime+}(2629)$ are less restrictive, 0.5 GeV/c in this analysis while DELPHI requires 1.0 GeV/c.

The sensitivity of the OPAL analysis is checked with the $\mathrm{D}_J^{(*)0}$ reconstruction described above, where agreement between data and simulation is observed. The selection criteria that are specific to either the $\mathrm{D}^{*\prime+}(2629)$ or $\mathrm{D}_J^{(*)0}$ analysis are checked by performing the analysis without these cuts. This did not change the result of the $\mathrm{D}^{*\prime+}(2629)$ search.

Overall, the sensitivities of the OPAL and DELPHI analyses are found to be similar, although the background in this analysis is higher. A comparison between the analyses can be made by calculating the $\mathrm{D}^{*\prime+}(2629)$ versus $\mathrm{D}_J^{(*)0}$ rate for which DELPHI published a number [66]:

$$\begin{aligned} R &= \frac{\langle N_{\mathrm{D}^{*\prime+}}\rangle \mathrm{Br}(\mathrm{D}^{*\prime+}(2629) \to \mathrm{D}^{*+}\pi^+\pi^-)}{\langle N_{\mathrm{D}_1^0}\rangle \mathrm{Br}(\mathrm{D}_1^0 \to \mathrm{D}^{*+}\pi^-) + \langle N_{\mathrm{D}_2^{*0}}\rangle \mathrm{Br}(\mathrm{D}_2^{*0} \to \mathrm{D}^{*+}\pi^-)} \\ &= 0.49 \pm 0.18(\mathrm{stat.}) \pm 0.10(\mathrm{syst.}) \ , \end{aligned} \tag{5.10}$$

where $\langle N_{\mathrm{D}^{*\prime+}}\rangle$ denotes the expected number of $\mathrm{D}^{*\prime+}(2629)$ in a sample with $\langle N_{\mathrm{D}_1^0}\rangle$ and $\langle N_{\mathrm{D}_2^{*0}}\rangle$ being the corresponding quantities for the D_1^0 and D_2^{*0}. Based on the numbers presented in Sections 5.3 and 5.5,

$$R = 0.05 \pm 0.10(\mathrm{stat.}) \pm 0.002(\mathrm{syst.}) \tag{5.11}$$

is calculated. The statistical error of the fit and the systematic uncertainties resulting from the $\mathrm{D}^{*\prime+}(2629)$ width and relative production rates in b and c are included. In the ratio calculation, all other systematic uncertainties largely cancel and have therefore been neglected. Using a statistical approach analogous to the one described earlier, a limit of

$$R < 0.22 \ \ (95\% \text{ C.L.}) \tag{5.12}$$

is computed.

Detailed investigations of a rather large difference of $\mathrm{b} \to \mathrm{D}_J^{(*)0}$ rates found in this analysis with respect to an earlier OPAL publication lead to the conclusion that this difference is not significant. Furthermore, it is shown that a large fraction of this difference can be attributed to improvements in the OPAL reprocessed data quality, and of the reconstruction software.

Due to the fact that DELPHI only published a ratio of $\mathrm{D}^{*\prime+}(2629)$ and $\mathrm{D}_J^{(*)0}$ production rates, the OPAL $\mathrm{D}_J^{(*)0}$ measurement enters the $\mathrm{D}^{*\prime+}(2629)$ signal expectation of the analysis in this chapter. However, the $\mathrm{D}^{*\prime+}(2629)$ production rate limit obtained here does not depend on the signal expectation, and thus it does not depend on the $\mathrm{D}_J^{(*)0}$ production rates assumed in the Monte Carlo. The limit on the ratio R of the $\mathrm{D}^{*\prime+}(2629)$ and $\mathrm{D}_J^{(*)0}$ production rate is normalised to the $\mathrm{D}_J^{(*)0}$ rate observed in this analysis, and therefore it is also independent of the $\mathrm{D}_J^{(*)0}$ rate in Monte Carlo. Hence, if significantly smaller production rates of $\mathrm{D}_J^{(*)0}$ mesons in B

	relative prod. rate R		$f(c \to D^{*\prime+}(2629)) \times Br(D^{*\prime+}(2629) \to D^{*+}\pi^+\pi^-)$	
	95% C.L.	90% C.L.	simple (95% C.L.)	conservative (95% C.L.)
DELPHI	$0.49 \pm 0.18 \pm 0.10$			
OPAL	< 0.22	< 0.17	$< 0.78 \times 10^{-2}$	$< 0.9 \times 10^{-2}$
CLEO ($c\bar{c}$)		< 0.16		
ZEUS ($c\bar{c}$)			$< 0.7 \times 10^{-2}$	

Table 5.5: *Comparison of* $D^{*\prime+}(2629)$ *production rate limits obtained by CLEO [116], ZEUS [117], and in this thesis (published by OPAL [112]) with the DELPHI measurement [66]. The published OPAL limits are calculated in a more conservative way than the ZEUS and CLEO limits. To allow a comparison of the results obtained by the collaborations, recalculated OPAL limits with matching conditions are given in this table. A comparison of the 90% C.L. R limits of OPAL and CLEO remains difficult, because the OPAL value still contains the contribution from* $b\overline{b}$ *events, which has a smaller signal reconstruction efficiency than achieved in* $c\overline{c}$ *events, and therefore leads to a larger limit. The general conclusion is that the OPAL results are competitive in* $c\overline{c}$ *and unique in* $b\overline{b}$.

hadron decays were assumed in the simulation, the results of this analysis would not change. The sensitivity of this analysis to the resulting smaller $f(b \to D^{*\prime+}(2629))$ rates would rapidly approach zero, as evident from Figure 5.6, but this fact is reflected in the comparatively large upper limit on $f(b \to D^{*\prime+}(2629))$.

In summary, the evidence of $D^{*\prime+}(2629)$ production in hadronic decays of the Z published by the DELPHI collaboration [66] is not confirmed with OPAL data. Conference contributions on this topic exist from the CLEO [116] and ZEUS [117] collaborations, which both confirm the non-observation of a narrow radial excitation of the $D^{*\pm}$ in $c\overline{c}$ events. The limit obtained by CLEO is

$$R < 0.16 \text{ (90\%C.L.)}. \tag{5.13}$$

CLEO is not sensitive to $D^{*\prime+}(2629)$ production in $b\overline{b}$ events, because the lower average energy of $D^{*\prime+}(2629)$ produced in B hadron decay is smaller and the background at low energies is too large. The restriction to $c\overline{c}$ events leads to a limit which seems better than the one obtained in this thesis, where also $b\overline{b}$ events with smaller $D^{*\prime+}(2629)$ reconstruction efficiency are taken into account. Furthermore, the CLEO limit is given at 90% C.L., whereas a conservative 95% C.L. is preferred here. The CLEO result is shown in Figure 5.10.

The production cross-section of b quarks is strongly suppressed in ep collisions at HERA, and therefore also ZEUS is insensitive to $D^{*\prime+}(2629)$ production in B hadron decays. However, the large sample of charm jets accumulated at HERA leads to a very strong limit on $D^{*\prime+}(2629)$ production in c quark hadronisation of

$$f(c \to D^{*\prime+}(2629)) \times Br(D^{*\prime+}(2629) \to D^{*+}\pi^+\pi^-) < 0.7 \times 10^{-2} \text{ (95\%C.L.)}. \tag{5.14}$$

Also this limit is calculated in a less conservative way than the OPAL result. ZEUS obtain their limit by a simple frequentist statistical approach, not taking care of the unphysical region of production rates below zero. Table 5.5 summarises the available $D^{*\prime+}(2629)$ results, and it also provides recalculations of the limits obtained in this thesis which match the CLEO and ZEUS calculations as close as possible. The mass distribution observed by ZEUS is shown in Figure 5.11.

Two questions are left open following the discussed results: On the one hand, it is not clear whether there is a narrow resonance with mass around 2.63–2.64 GeV/c^2. On the other hand

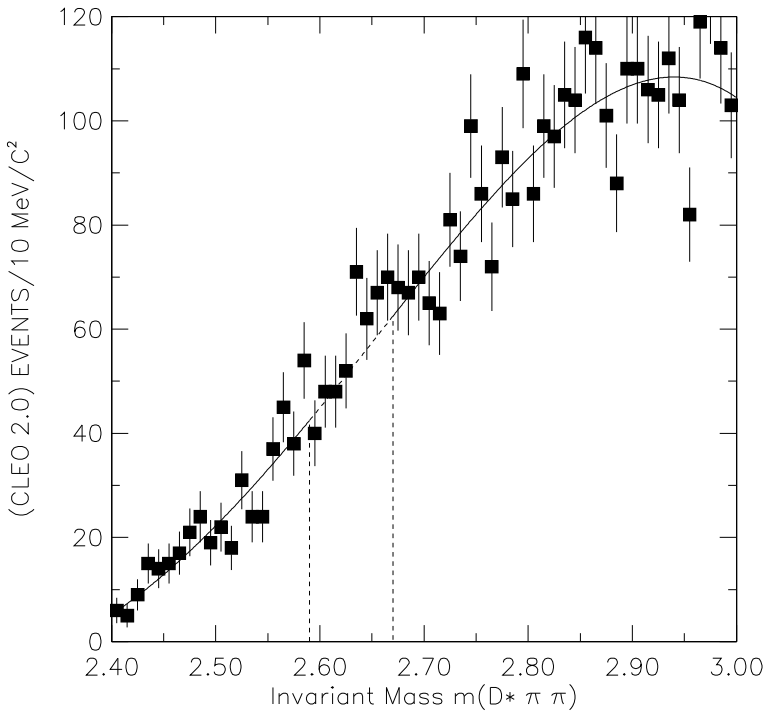

Figure 5.10: *Mass distribution of* $D^{*+}\pi^+\pi^-$ *combinations as seen in a preliminary CLEO analysis [116]. No narrow resonance is observed in the mass spectrum. A visible signal is only expected in* $c\overline{c}$ *events. The mass region used for the calculation of a* $D^{*\prime+}(2629)$ *production rate limit is indicated by dashed lines.*

it is not known whether such resonance, if it exists, can be associated with the radial excitation $D^{*\prime+}(2629)$. A few short consideration on these two questions will conclude this chapter.

In light of the conflicting results obtained from CLEO, ZEUS, and OPAL data in comparison to the DELPHI measurement, it is still not known to satisfactory degree of certainty whether a narrow resonance in the mass region of 2.63–2.64 GeV/c^2 exists. Two scenarios to reconcile the results are considered most likely:

- The peak in the mass spectrum observed by DELPHI might be a fluctuation instead of an actual resonance. The peak consists of only three bins. The calculation of the significance of the excess does not take systematic uncertainties into account. Furthermore, DELPHI uses $D^0 \to K^-\pi^+\pi^-\pi^+$ candidates in addition to $D^0 \to K^-\pi^+$ candidates to construct $D^{*\prime+}(2629)$ candidates. These decays were not used in the analysis presented here because they caused correlated entries in the mass distribution, consisting of several candidates sharing tracks. The correlated entries were found to accumulate mostly in the same or in nearby mass bins, leading to strong fluctuations of the mass distribution. However, fluctuations of the size seen by DELPHI were not observed in OPAL data. Another source of correlated entries are candidates which share the same $D^{*\prime+}(2629)$ pions, but have a different D^{*+} candidate. These are removed in this analysis, but not by DELPHI.

- The signal seen by DELPHI might be exclusively due to $D^{*\prime+}(2629)$ production in B hadron decays. CLEO and ZEUS are not sensitive to this production channel, and the sensitivity of the analysis presented here is limited. This explanation is improbable for three reasons: DELPHI claims that $(57 \pm 10)\%$ of the candidates in the peak are observed in $c\overline{c}$ events. Furthermore, if the full signal would be attributed to production in B

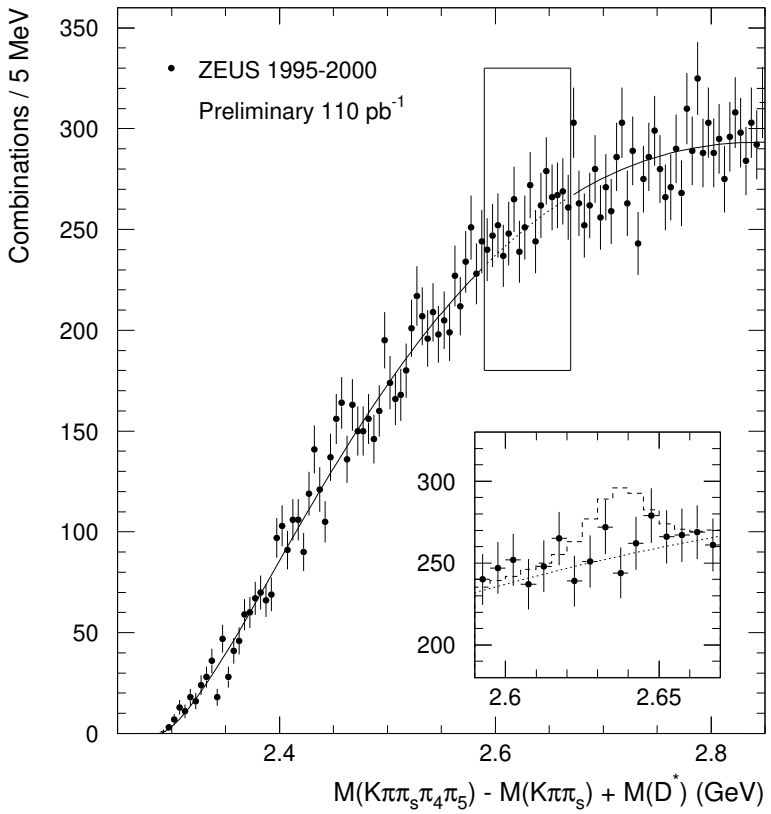

Figure 5.11: *Preliminary* $m' = \Delta m' + 2.01$ GeV/c^2 *distribution at ZEUS. No narrow resonance is observed. The inset shows an enlargement of the mass region used for the calculation of a* $D^{*\prime +}(2629)$ *production rate limit. The dashed line indicates the expected signal according to the DELPHI results. The ZEUS analysis is not sensitive to* $D^{*\prime +}(2629)$ *production in* B *hadron decays.*

hadron decays, the resulting $f(b \to D^{*\prime +}(2629))$ production rate would be large enough to be safely observed at OPAL. Thirdly, no physical reason is known why one of the two production channels should be almost completely suppressed in favour of the other one. No such case has been observed so far.

Under the assumption that there is in fact a resonance with a mass as measured by DELPHI, it remains to be clarified whether this can really be associated with the $D^{*\prime +}$ meson. Melikhov and Péne estimate a lower limit of 50 MeV/c^2 for the width of a radial excitation like the $D^{*\prime}$ [108], where they take the strong model-dependence into account[6]. An identification as higher orbital excitation ($L = 2$, $L = 3$) is clearly disfavoured because then two peaks with similar mass difference as the narrow $D_J^{(*)0}$ states were expected. Furthermore the expected mass should be larger, and the width should still be around 50 MeV/c^2. Page emphasises again that all explanations other than $D^{*\prime}$ are excluded due to their mass [109].

In conclusion, the claim by the DELPHI collaboration of the observation of a narrow radial excitation in the D meson system is theoretically questionable and can not be confirmed experimentally. However, the doubts expressed by theorists are exclusively based on the predicted width of the $D^{*\prime}$, which is prone to large theoretical uncertainties. On the experimental side, both observation and non-confirmations suffer from limited statistics and a large background. This is especially true for the investigation of possible $D^{*\prime +}(2629)$ decays in $b\bar{b}$ events and has

[6]Original statement in Ref. [108]: "conservatively estimated to be significantly larger than about 50 MeV"

been demonstrated with $b \to D_J^{(*)0}$ reconstruction in this chapter. A similar statement holds as in the previous chapter: Significant improvements might be gained for analyses of this type with a detector of better mass resolution to suppress background, and with a larger data sample than the one collected by the LEP experiments. These prospects are illustrated in Chapter 8 with a simple reconstruction of $D_J^{(*)0}$ mesons in $b\overline{b}$ events in a simulated future e^+e^- experiment.

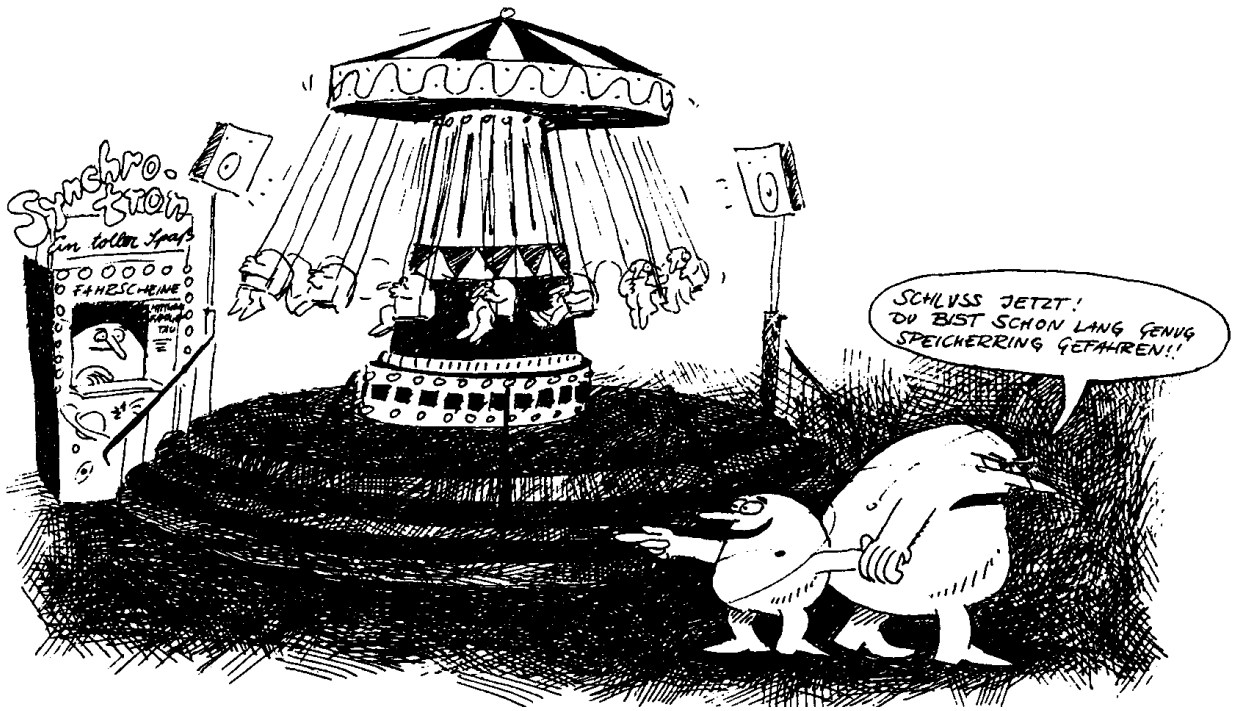

"Stop it now! You have been riding storage ring long enough!"

from: Peter Evers, "Die wundersame Welt der Atomis", Wiley-VCH 2002. Printed with kind permission from Wiley-VCH.

Chapter 6

The TESLA Project

The overview of the current status and the limitations of the Standard Model that was given in Chapter 2 mentioned many problems and open questions. Probably the most important problem arises from the fact that the physics we know today cannot be simply extrapolated to an energy regime of beyond 1 TeV. Either at least one Higgs boson, or any other significant deviation from today's Standard Model must occur below this boundary. The Large Hadron Collider LHC, currently under construction at CERN and expected to be commissioned in 2007, will collide proton beams at a centre-of-mass energy of 14 TeV. It is therefore very likely that the LHC will discover the new particles and effects waiting in the 1 TeV region. However, in comparison to lepton colliders, the precise analysis of particles and their interactions is complicated due to large background of the hadron remainders, and due to the unknown energy of the actually interacting particles. In contrast to this, lepton colliders have a well-defined initial state with less background. The centre-of-mass system is precisely known, as well as the centre-of-mass energy, which can furthermore be adjusted to any desired value the collider supports. Another advantage of lepton colliders is the possibility of polarised beams.

The highest energy lepton collider so far was the LEP accelerator introduced in Chapter 3. With centre-of-mass energies of up to 209 GeV and a large data-sample, it accomplished tests of the Standard Model and determination of its parameters with unprecedented precision. For example the $W^{\pm}$ and Z bosons had already been discovered at the CERN SPS proton-anti-proton collider with a centre-of-mass energy of 540 GeV [118], but the precise measurement of their properties would have been impossible without LEP as a complementing lepton collider. The same concept applies for the physics ahead: All new phenomena discovered by the LHC will have much more impact on the development of the theory of elementary particles and their interaction if they can be investigated also in precision analyses performed at a lepton collider of suitable energy. The centre-of-mass energy of a lepton collider has to be matched to a typical collision energy scale of a hadron collider, not the centre-of-mass energy of the complete hadron system. The average momentum fraction of the colliding partons in a hadron is smaller, typically about 1/6 of the hadron momentum. Therefore the energy of lepton collider beams can be much smaller than the hadron collider beam energy, still covering a similar energy region with a significant fraction of the luminosity.

A lepton collider to complement the LHC should therefore reach a centre-of-mass energy not too far below 1 TeV. Unfortunately it is not possible to simply scale up the LEP technology to increase the energy by a factor 2–5: Particles orbiting circularly in a storage ring lose energy

due to synchrotron radiation, where the power radiated by a beam particle follows the relation

$$P_{rad} \propto \frac{E^4}{r^2 m^3} \ . \tag{6.1}$$

Here, E is the beam energy, r is the radius of the curvature, and m is the mass of the particle. Energy loss due to synchrotron radiation is mainly a problem for electron beams and is suppressed for hadron beams because of the m^{-3} dependence. Larger electron beam energies with manageable energy loss due to synchrotron radiation can therefore only be attained by increasing the radius of the collider/storage rings. Because the radiation loss increases with the fourth power of the energy, and a larger radius enters only to the second power, a simple scaling of storage rings does not work. At 200 GeV centre-of-mass energy, already 44 MW electrical power were needed to compensate the synchrotron radiation energy loss of LEP[1] [119]. A circular electron positron collider of larger energy than LEP is commonly regarded as unrealistic.

One possibility to extend the energy reach of lepton colliders beyond LEP could be to replace electrons by muons, which would suppress synchrotron radiation by seven orders of magnitude. However, the technology to cool muon beams sufficiently well and sufficiently fast to obtain useful luminosities still requires long-term development [120].

The most realistic option for the near future is a linear e^+e^- collider, although of course this technology is challenging as well. A linear collider imposes much more stringent criteria on the final focus of the beams to achieve high luminosity, because the beams are crossing only once before they are dumped. Furthermore, the accelerating gradient must be increased with respect to circular collider/storage rings, because the full beam energy has to be reached in a single acceleration pass. The research and development of these technologies directed towards construction of a high energy and high luminosity linear collider has seen good progress over the last decade. Three next generation linear collider projects are being pursued worldwide. The American NLC project [121] and the Asian JLC project [122] are both based on copper-cavities operated at room temperature. Both projects intend to increase the accelerating gradient by using a higher frequency in the cavities (11 GHz). A similar, but more long-term development line is followed at CERN, where the CLIC project evaluates possibilities for a next-to-next generation linear collider are with up to 5 TeV centre-of-mass energy [123]. Another project with development mainly centred in Europe is TESLA (**T**eV **E**nergy **S**uperconducting **L**inear **A**ccelerator). As first of the three near-term projects it has already submitted a full technical design report [124]. The simulation studies described in the two subsequent chapters are performed in the TESLA framework. Hence, an overview of the accelerator design and the detector proposal will be given in the following. Nevertheless, this chapter can only provide a small fraction of the information gathered for the TESLA project. A comprehensive review is given in the Technical Design Report [75, 124, 125].

6.1 The TESLA Accelerator

The TESLA design is based on superconducting cavities operating at 1.3 GHz. This leads to larger cavities and thus larger spacings between the electron bunches than at NLC/JLC, which makes the identification of the primary reaction vertex in a corresponding particle physics detector easier. Problem and main subject to TESLA accelerator research and development is the limitation of the field gradient in the cavities that can be achieved before the superconductivity

[1] Plus about the same amount for magnet operation and cryogenics.

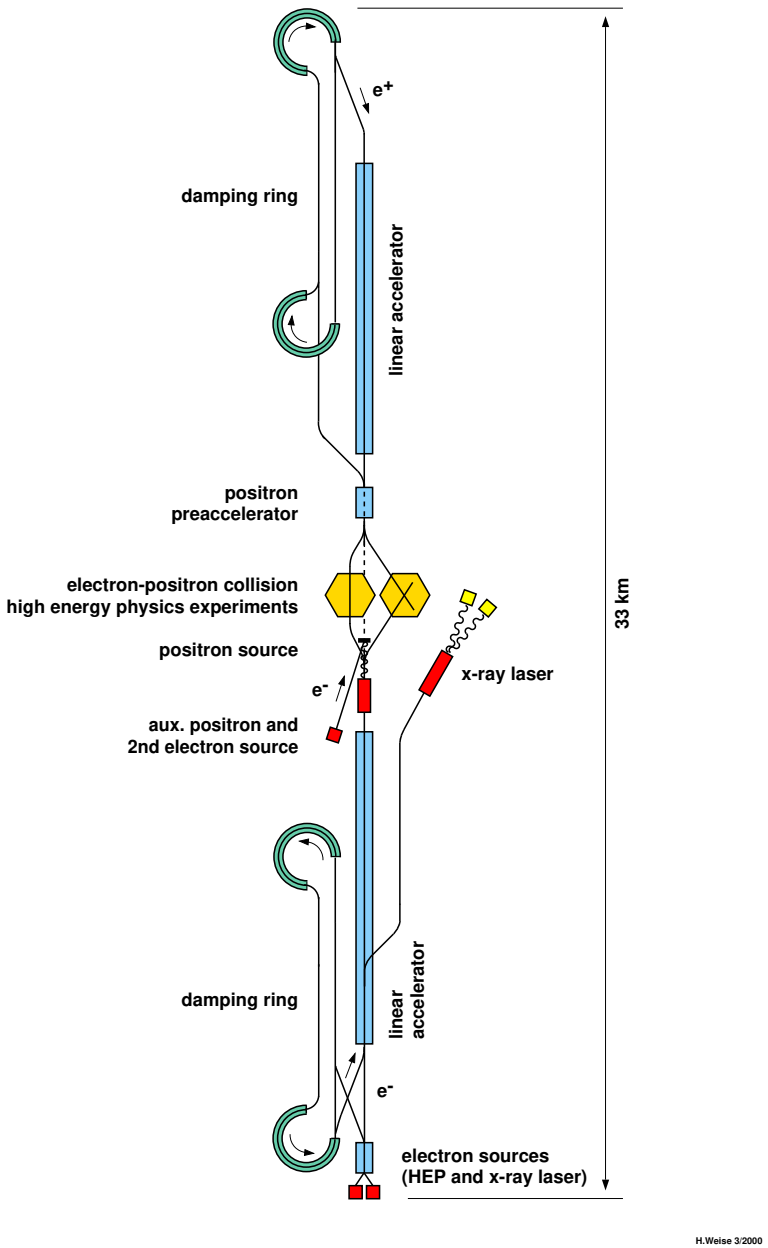

Figure 6.1: *Layout of the proposed linear* e^+e^- *collider TESLA. Two main linear accelerators each are equipped with a damping ring for beam cooling. Positrons are created by pair production of a high intensity synchrotron radiation beam created by the electron beam passing through undulator magnets. Two interaction regions for particle physics are proposed. Also shown is an X-ray laser facility which is included in the TESLA design. This Figure is taken from Ref. [124].*

parameter	LEP	TESLA	
collision energy (GeV)	209	500	800
luminosity ($cm^{-2}s^{-1}$)	$\approx 10^{32}$	3.4×10^{34}	5.8×10^{34}
beam size at IP (μm $\times$ μm)	$\approx 100 \times 10$	0.553×0.005	0.391×0.0028
acceleration gradient (MV/m)	7	23.4	35

Table 6.1: *Essential parameters of the TESLA linear collider [124] in comparison to LEP. The accelerating gradient has to be increased to achieve full collision energy in a single pass. The beam focus at the interaction point (IP) has to be improved to obtain a high luminosity at a single pass collider.*

breaks down. The technology to achieve a centre-of-mass energy of 500 GeV with a collider of 33 km total length is already available; prototype cavities have already fulfilled the design criteria for a 800 GeV machine. Important machine parameters are summarised in Table 6.1. The layout of the collider facility is shown in Figure 6.1.

6.2 The Physics Program

A large amount of physics studies to evaluate the physics capabilities of TESLA and other high energy linear colliders has been performed and is continuously extended [126]. Only a few examples will be given here. Although all studies mentioned here are available with similar results from the NLC and JLC projects, all numbers and plots in this chapter will for simplicity be taken from the TESLA project. A comprehensive review of physics at TESLA is available in Ref. [75]. A general review centred more towards NLC/JLC studies was compiled for the Snowmass 2001 workshop [127].

Major task of a linear e^+e^- collider will be the analysis of the electroweak symmetry breaking, probably due to a Higgs mechanism, which would then also solve the problem of the divergent WW cross-section. Theoretical boundaries lead to the expectation that the mass of at least one Higgs boson should be within reach of the linear collider in almost any model. Contrary to the situation at hadron colliders, the observation of such Higgs bosons is possible independent of its decay modes. This advantage comes from the possibility to investigate the recoil mass spectrum of the Higgs against the remainder of the final state, e.g. the Z decay in Higgs-Bremsstrahlung reactions $e^+e^- \rightarrow Z \rightarrow ZH$. An example of such a recoil mass spectrum is given in Figure 6.2, where the reconstruction of a 120 GeV/c^2 Higgs boson is simulated with an integrated luminosity of 500 fb^{-1} at $\sqrt{s} = 350$ GeV.

The small background in e^+e^- reaction allows measurements of the Higgs couplings to many fermions and bosons (e.g. b, c, τ, W, γ) with high precision, where only ratios of some couplings are accessible at hadron colliders like the LHC. Knowledge of these couplings is necessary to identify the suitable Higgs model. Even self-coupling of Higgs bosons should be measurable, providing direct access to the Higgs potential. However, it is expected that this measurement can only be done with large uncertainties ($\approx 20\%$).

Also supersymmetric theories require Higgs bosons, and in addition they predict a full spectrum of supersymmetric partner particles that remain to be discovered. Depending on the details of the symmetry breaking mechanism and the parameters of the model, a large fraction of the new particles is expected within the energy reach of a linear collider, although full coverage of the spectrum with a next generation collider can presumably only be provided by the LHC.

A large class of measurements is the precision analysis of Standard Model parameters and

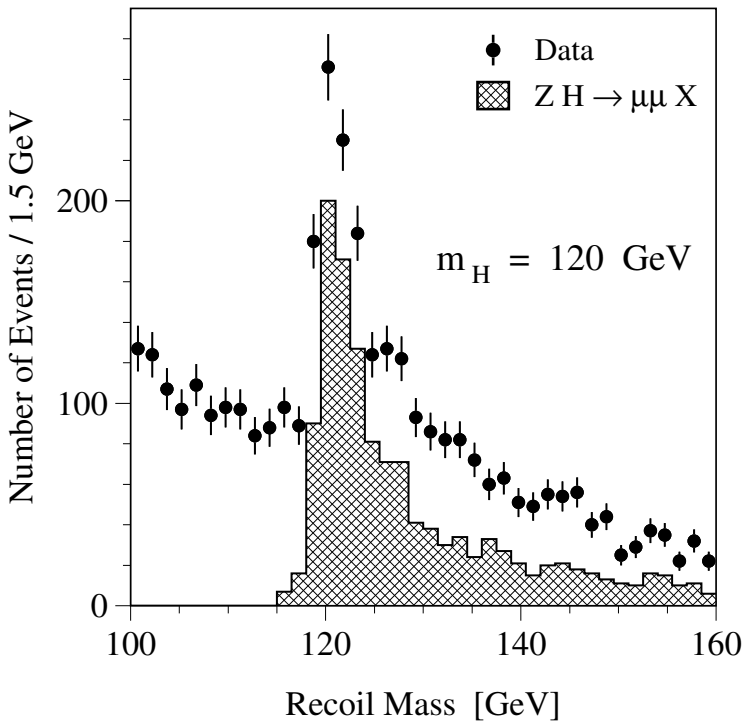

Figure 6.2: *Higgs recoil mass spectrum of* $e^+e^- \to Z \to ZH \to \mu\mu H$ *reactions at a centre-of-mass energy of* 350 GeV *and an integrated luminosity of* 500 fb^{-1} *[75].*

predictions. These measurements are crucial tests of the theory and are often sensitive to physics beyond the Standard Model far above the centre-of-mass energy, due to the impact of virtual corrections. The precision measurements will also provide means to identify alternative scenarios in case no Higgs boson is found. A prime example for precision measurements is the top quark mass: The mass of the heaviest known quark is known with highest precision of all quarks. Due to its size, it is especially sensitive to corrections caused by even heavier particles. The LHC will be able to improve the precision of the top quark mass to 1–2 GeV/c^2 [128], but a linear e^+e^- collider could achieve a precision of around 100 MeV/c^2 with a dedicated threshold scan as indicated in Figure 6.3.

A similar threshold scan would lead to a precision of the $W^\pm$ mass of about 6 MeV/c^2 [129], where polarised beams and an integrated luminosity of 100 fb^{-1} are assumed. This enables stringent tests of the electroweak model. Of special interest are the electroweak self-couplings; clear evidence for the existence of triple-gauge vertices in a LEP WW threshold scan is shown in Figure 2.2. The triple-gauge couplings are very sensitive to deviations from Standard Model physics, and the sensitivity to such deviations at a linear collider is expected to be up to an order of magnitude better than achievable at the LHC [75].

The study of Quantum Chromodynamics is the main topic of this thesis. A high energy linear e^+e^- collider offers promising possibilities also for this field. The strong coupling constant α_s can be determined with improved precision, and its evolution can be compared to the expectation 2.31 over a large energy range. Simulated measurements are compared to existing data in Figure 6.4.

Although the main motivation for the construction of a linear e^+e^- collider is seen in precision physics at high energies, it would also provide enormous prospects for the improvement

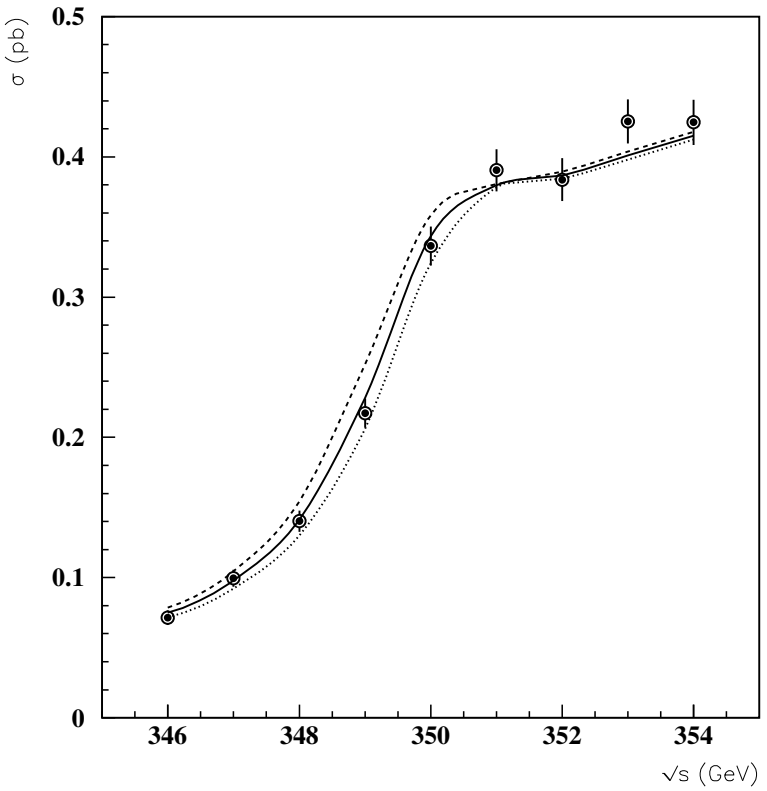

Figure 6.3: *Top quark threshold scan at TESLA [75]. A total luminosity of* 500 fb^{-1}*, corresponding to 1–2 years of operation, is assumed. The dashed and dotted lines represent the effect of a top mass shifted by* $\pm 100\ \mathrm{MeV}/c^2$*.*

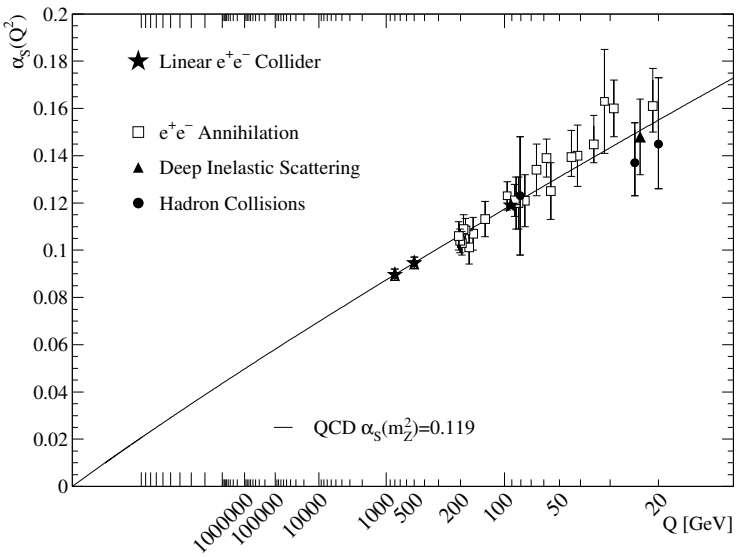

Figure 6.4: *Evolution of* $\alpha_s(Q^2)$ *according to existing measurements at* $\mathrm{e^+e^-}$ *and hadron colliders, as well as in deep inelastic scattering experiments. Simulated measurements at a linear* $\mathrm{e^+e^-}$ *collider are indicated by stars. This plot is taken from Ref. [75].*

of existing analyses at lower energies. The so-called GigaZ scenario for TESLA suggests a run at a centre-of-mass energy on the Z resonance. With an expected luminosity of 5×10^{33} cm^{-2}s^{-1} about 10^9 Z bosons could be produced in 50–100 days of running [75]. Important LEP/SLD results like the measurement of the weak mixing angle could be improved during such a run.

6.3 TESLA Detector Design

The development of linear e^+e^- accelerators is accompanied by studies of suitable particle physics detector systems. The detectors have to be able to exploit fully the physics capabilities offered by the accelerator. This section summarises the detector design foreseen for TESLA, as it is defined in the Technical Design Report [125].

The detector design is based on the LEP detectors and SLD, with improvements as required by e^+e^- physics at up to 1 TeV, e.g. narrower jets due to higher boost, and by the specific machine environment, e.g. larger beam-related background due to reduced beam cross-section at the interaction point. Furthermore the experience of more than a decade of data analysis is incorporated to reduce the specific weaknesses of the LEP detectors and SLD. It has been learned for example that the design of tracking and calorimetric detectors should be optimised for the possibility to match tracks and calorimeter clusters. The aim is a full reconstruction of both charged and neutral particles, which gives essential improvements in the analysis of hadronic jets[2].

The TESLA detector proposal shown in Figure 6.5 shows a strong resemblance to the LEP detectors and SLD. It continues the concept of a barrel detector supplemented by endcaps. A system of tracking detectors forms the inner part, enclosed in a shell of calorimeters. A solenoidal magnet coil provides an axial magnetic field of 4 T for charged particle momentum measurement. The coil will be outside electro-magnetic and hadronic calorimeters to reduce the amount of material in front of the calorimeters, which leads to a better energy resolution. The magnet flux return yoke is instrumented as muon detector. Details and dimensions of the detector layout are best visible in Figure 6.6.

Performance goals for the tracking detectors are excellent vertex resolution for heavy quark and τ identification, together with an accurate momentum determination, high redundancy to ensure good jet-jet reconstruction and good hermeticity in the forward direction. Vertex reconstruction will be needed to study new physics which involves heavy flavours, like Higgs and top decays. The higher energy at a linear collider compared to LEP will produce more energetic and therefore narrower jets. Redundant information in a many-layered tracker will be mandatory to resolve high energy jets into several particles. Many of the top, WW and SUSY channels are characterised by missing energy signatures, which will need a hermetic detector to identify these events. Hermeticity is also an important requirement for the calorimeter, for the same reason as for the tracker. A fine granularity of both electro-magnetic and hadronic calorimeters is required for optimal matching of tracks and calorimeter clusters, and for the reconstruction of non-pointing photons. The energy resolution has to be as good as possible.

The simulation studies in this thesis are based on tracking detector information only. The proposed setup of tracking detectors will therefore be discussed in detail in the following section. No description of the suggested technology and expect performance of the calorimeter design will be given here; details are available in Ref. [125].

[2]The matching of tracking and calorimeter signals for this purpose is often referred to as “energy flow algorithm”.

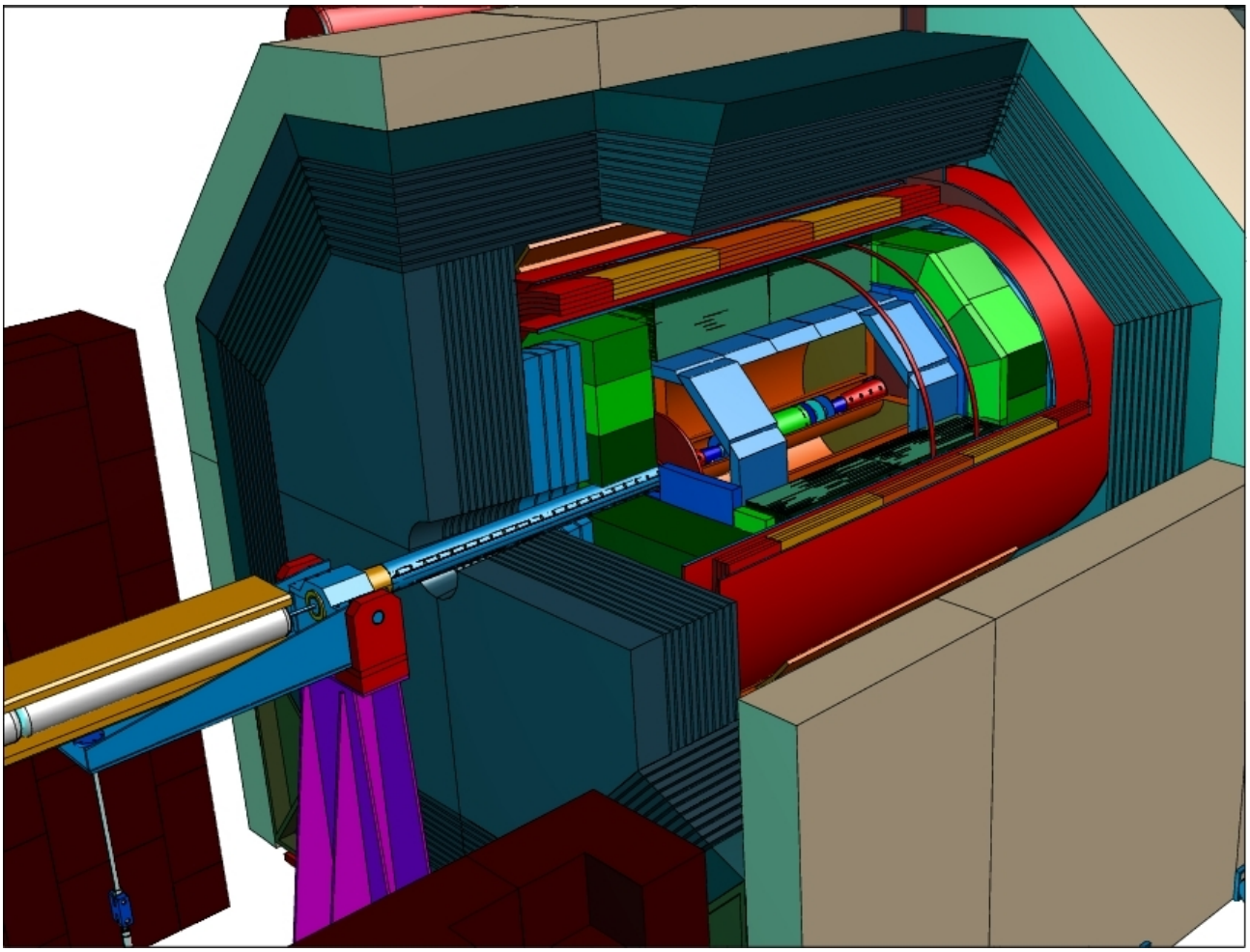

Figure 6.5: *Cut-away view of the proposed TESLA detector [125]. The electro-magnetic and hadronic calorimeters are easily recognisable due to their octagonal shape. A set of silicon detectors in the centre of a large TPC constitutes the tracking system inside the calorimeters. The calorimeters are surrounded by a* 4 T *magnet coil, the return yoke of which is instrumented and will be used as muon detector. A concrete shielding encloses the whole detector system.*

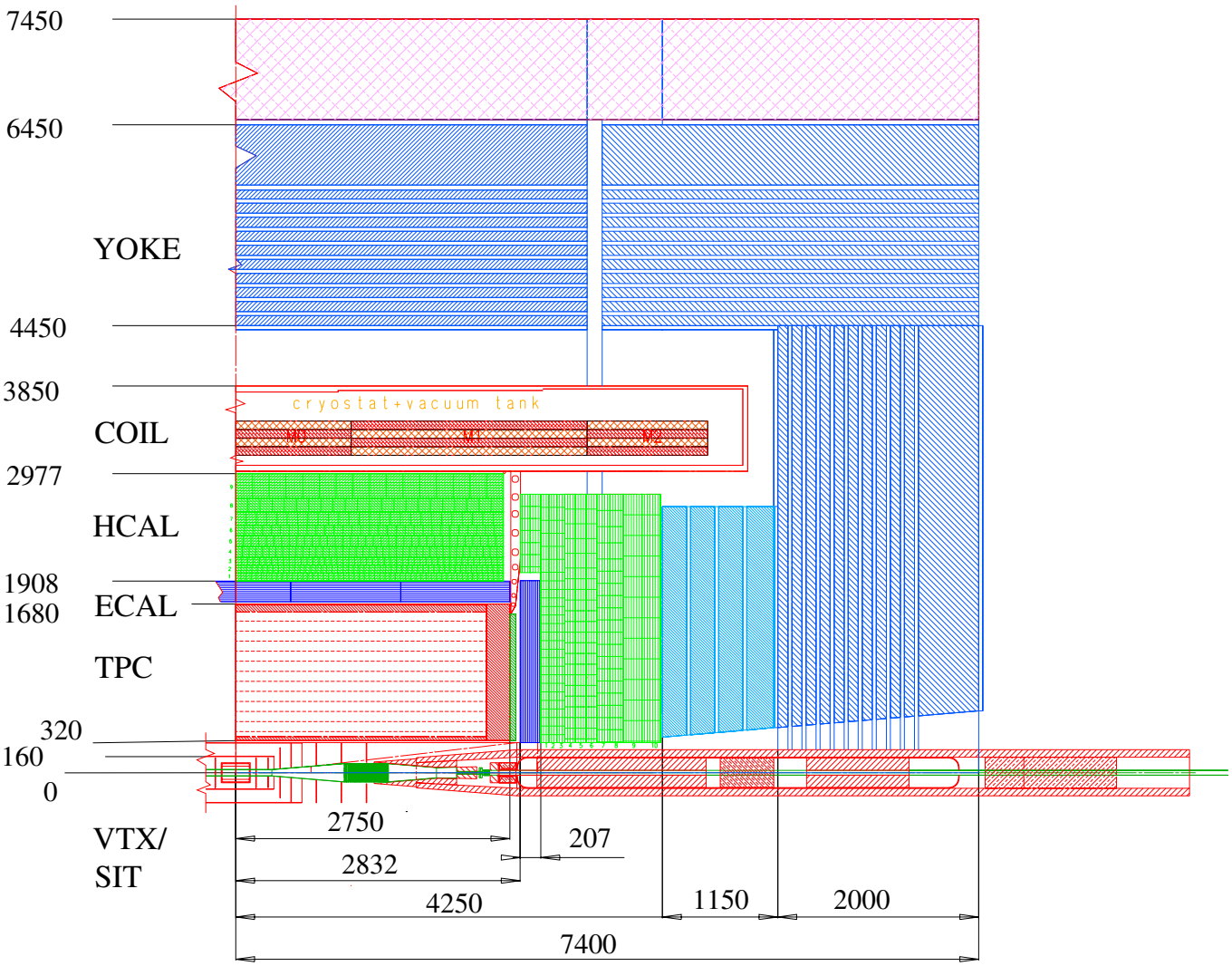

Figure 6.6: *A schematic view of one quadrant of the proposed TESLA detector. All dimensions are in mm. This Figure is taken from Ref. [125].*

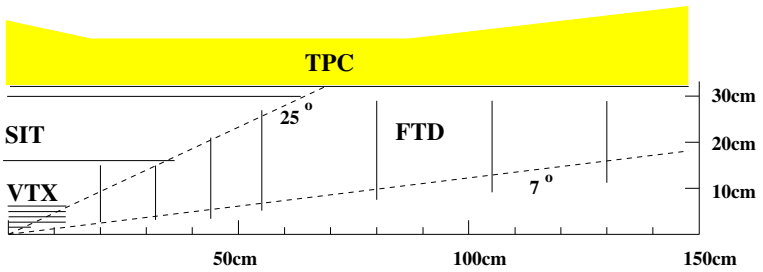

Figure 6.7: *Detailed view of the inner detector part as foreseen in the CCD option. This Figure is taken from Ref. [125].*

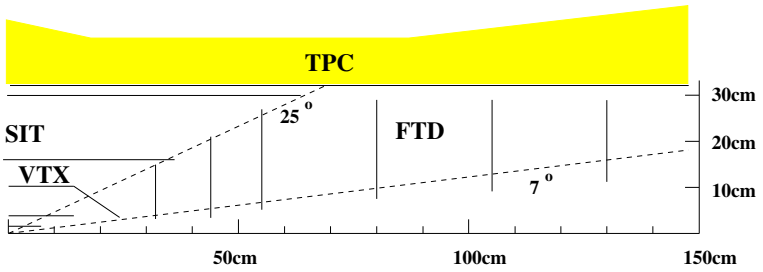

Figure 6.8: *Detailed view of the inner detector part as foreseen in the APS option. In comparison to the CCD variant, 3 vertex detector layers and one conical endcap are used instead of the five layer CCD device, and the innermost FTD layer as present in the CCD option is not foreseen in the APS design.*

The full detector system is simulated in the GEANT 3.21-based detector simulation program BRAHMS [130]. For the simulation of large numbers of events the fast parametric simulation program SIMDET [131] is available, where the detector performance is parametrised according to BRAHMS performance studies including the ones presented in Chapter 7.

6.4 Tracking Detector Setup

In this section a short overview over the tracker design is given. The two design variants in the Technical Design Report differ in the choice of the central vertex detector technology. Either Charged Coupled Devices (CCD) or hybrid Active Pixel Sensors (APS) could provide the performance required for the vertex detector. Additional technological options like CMOS pixel detectors are being developed [132], but have not yet led to a full mechanical design. In the following, both the CCD and the APS design are briefly discussed. More information can be found in Ref. [125].

The central detector region of the CCD design variant is shown in Figure 6.7. The innermost detector is a five layer CCD pixel detector (VTX), followed by two layers of double sided silicon strip detectors (SIT) and the TPC as the principal tracking detector. The forward direction is covered by 7 additional discs (FTD), 3 pixel layers and 4 layers of double sided silicon detectors. The momentum resolution of muons in the forward region is improved by a forward tracking chamber (FCH) behind the TPC endcaps. The FCH is supposed to consist of 12 layers of straw tubes in three different orientations.

Figure 6.8 shows the alternative design option for the central detector system, where the five layer CCD device is replaced by three layers of active pixel detectors (APS) with a conical

detector	radial coverage [cm]	z coverage [cm]	$\|cos(\Theta)\|$ range	comment
VTX (CCD)	1.55	-5.0..+5.0	0..0.955	
	2.4	-12.5..+12.5	0..0.982	
	3.6	-12.5..+12.5	0..0.961	
	4.8	-12.5..+12.5	0..0.934	
	6.0	-12.5..+12.5	0..0.902	
VTX (APS)	1.55	-7.30..+7.30	0..0.978	
	3.75	-14.3..+14.3	0..0.967	
	10.0	-14.3..+14.3	0..0.820	coverage without endcap
		-24.3..+24.3	0..0.990	including conical endcap
FTD	2.8..15.0	±20.0	0.800..0.990	CCD option only
	3.3..15.0	±32.0	0.906..0.995	
	4.3..22.0	±44.0	0.894..0.995	
	5.3..28.0	±55.0	0.891..0.995	
	7.4..30.0	±80.0	0.936..0.996	
	9.4..30.0	±105	0.962..0.996	
	11.5..30.0	±130	0.974..0.996	
SIT	16.0	-38.0..+38.0	0..0.922	
	30.0	-66.0..+66.0	0..0.910	
TPC	38.6..162.6	-250..+250	0..0.988	200 pad rows
FCH	32.0..160	±273..±279	0.863..0.994	12 layers

Table 6.2: *Subdetector coverage for the proposed TESLA detector for APS and CCD vertex detector options.*

detector endcap on the outermost layer. This goes along with a modification of the FTD system in the sense that the innermost disk foreseen for the CCD option will not be used in the APS design. The coverage of the different detector components is summarised in Table 6.2.

6.4.1 Detector Specifications

A Time Projection Chamber (TPC) is foreseen as large tracking device for the linear collider detector, with a single hit design resolution varying between 50μm and 200μm in the $r\phi$ plane, depending on the drift distance [133]. The simulation software represents the z dependence of the resolution in a linear approximation. A resolution of 1 mm is expected along the z direction. A TPC combines several advantages: The number of pad rows and thus the redundancy for track reconstruction can be very large. The TESLA detector TPC is assumed to have 200 pad rows, allowing easy kink-finding and reconstruction of neutral particle decay vertices far from the interaction region. Resolution degradation due to multiple scattering is minimised, because the TPC gas is rather thin, and in the barrel region there is no additional material than the inner field cage. Furthermore particle identification is easily performed with $\mathrm{d}E/\mathrm{d}x$ measurements. The number of pad rows is optimised for momentum and $\mathrm{d}E/\mathrm{d}x$ resolution [133, 134]. Disadvantages of a TPC clearly are rather thick endcaps and a limited capability to resolve very close tracks. Conservative values of 3.3 mm in $r\phi$ and 14 mm in z are assumed as double hit resolution.

Major task of a Silicon micro-vertex detector is the precise measurement of impact param-

eters in order to allow efficient vertex reconstruction. The high density of tracks in narrow jets close to the interaction region increases the demands imposed on a vertex detector. A pixel device with a point resolution of not more than several micrometer is therefore mandatory for a linear collider detector. Three alternative designs are under study. The highest possible resolution and very thin detector layers are expected to be achievable with either CCD or CMOS detector systems. Detailed studies are especially available for CCD devices and show that a detector with 3.5 micron point resolution and 0.06% radiation length thickness per layer is feasible [135]. This would allow to operate a five layer CCD detector in a cryostat with still very good material budget.

A CCD detector is read out by shifting the information stored in the individual pixels cell by cell along readout columns. In the TESLA bunch structure environment, the physics and background hits of 60 bunch crossings are therefore accumulated until the signal enters the front-end electronics. A pattern recognition algorithm for a CCD vertex detector will thus have to deal with a much larger number of background (and physics) hits than that for a detector with immediate readout of every individual pixel.

Another proposal for a vertex detector for the TESLA linear collider uses hybrid active pixel sensors (APS), which feature readout drivers integrated into the active detector material. This provides simpler and faster readout capabilities, but at the cost of larger pixels and thicker detector layers. At the current level of technological development it is expected that three APS layers are the optimal compromise between material and tracking performance. A point resolution of 7 μm is envisioned. Full GEANT simulation is available in the BRAHMS software package for CCD and APS option.

Neither TPC nor vertex detector provide sufficient coverage to perform track reconstruction with good momentum resolution in the angular region very close to the beam pipe. Therefore dedicated Silicon disk-shaped detectors are proposed to achieve a maximal degree of hermeticity with the tracking detectors. Three Silicon disks within less than 50 cm on both sides of the interaction region provide pixels with roughly 50 μm $\times$ 15 μm resolution to complement the CCD vertex detector. The innermost pair of disks is replaced by conical detector endcaps attached to the outer vertex detector layer in the APS design. Farther away than 50 cm from the collision region double sided strip detectors can easily cope with the remaining background and track density; four disks of 25 μm effective point resolution are assumed at z coordinates of $\pm$55 cm to $\pm$130 cm. The standard BRAHMS simulation approximates the strip detectors as pixel devices. A strip detector simulation was performed in a worst case scenario with strips running exactly in the r and $r\phi$ direction, and no significant degradation of the performance was seen [136]. This simulation is however not yet included in the study presented here.

TPC, vertex detector and forward tracker are the main track detectors of the proposed linear collider detector. Special emphasis lies on the fact that these subdetectors are capable of independent track reconstruction, with restrictions in the case of the APS vertex detector. These stand-alone capabilities are considered advantageous for internal alignment of the silicon detectors, and for the redundancy of the track reconstruction in general. Further detector systems are added, though, to improve the overall performance in specific tasks.

Two layers of high resolution double-sided silicon strip detectors, the Silicon Intermediate Tracker (SIT), are foreseen to bridge the gap between vertex detector and TPC inner radius. With a per-layer hit resolution of 10 μm in $r\phi$, and 50 μm in z, the outer layer at its radius of 30 cm and thus large lever-arm with respect to the precise vertex detector layers plays an important role in achieving the global momentum resolution designed to be $\delta(\frac{1}{p_t}) \leq 5 \times 10^{-5}(\mathrm{GeV}/c)^{-1}$. The inner layer at 16 cm radius was added to the proposal to

subdetector	resolution	space points
VTX (CCD)	3.5 μm	5
VTX (APS)	7 μm	3
pixel FTD	15 μm $\times$ 50 μm	2, 3 (APS, CCD)
strip FTD	25 μm	4
SIT	10 μm $\times$ 50 μm	2
TPC	90..190 μm ($r\phi$), 1 mm (z)	200
FCH	100 μm	12 strips

Table 6.3: *Subdetector specifications for the proposed TESLA detector as present in the simulation software [130]. The simulation matches the technical proposal, with the exception of SIT and outer FTD detectors. These are proposed as double strip detectors, whereas the simulation contains pixel readout.*

improve reconstruction of vertices from long-lived strange particles in the otherwise uncovered radial range of 6 (CCD) or 10 (APS) cm and 31 cm, the inner edge of the TPC field cage. The APS vertex detector furthermore relies on the additional silicon layers to ensure the possibility of performing pattern recognition independently from the TPC. No simulation of silicon strip detectors is currently implemented in BRAHMS. However, the hit densities on the SIT layers are comparably low, and thus no noticeable effect on the track reconstruction performance is expected from the imprecise modelling of this detector. This is especially true since the availability of full 3d information both inside (VTX) and outside (TPC) the SIT will allow very good discrimination between true and mirror hits.

The full system of silicon based high precision detectors is designed to ensure a coverage of at least five space points throughout the whole angular reach of the tracking devices. In addition to the stand-alone pattern recognition capabilities of vertex detector and forward tracker, this provides a good basis for a combined silicon detector pattern recognition, which is advantageous in the overlap region between vertex detector and forward tracker.

Tracks passing through the TPC endcaps do in general not traverse all TPC pad rows. Smaller number of hits for use by a track fit and the shorter track length in the TPC at decreasing polar angle degrade the momentum resolution achievable for these tracks. Additional Forward Chambers (FCH) are proposed behind the TPC endcaps to recover from this degradation at least for muons. Other particles are expected to be scattered significantly in the approximate 30% of a radiation length material in the endcaps. Twelve layers of straw tubes in three different orientations are the technology of choice for the FCH, which allows internal pattern recognition. A resolution of 100 μm is foreseen, and a double hit resolution of the same size is assumed.

Table 6.3 gives an overview of the detector specifications as implemented in the full detector simulation BRAHMS. The simulation matches the detector proposal in Ref. [125], with the exception of the few details mentioned above.

6.4.2 Beam-related Background

Sources of background are beam-beam effects, synchrotron radiation and back-scattered particles from the final quadrupole, as well as muon background from upstream sources [125]. Beam-beam effects are especially pronounced at a high energy and high luminosity linear e^+e^- collider due to the strong focus of the beams close to the interaction point. For the purpose of this study the effects due to e^+e^- pair production are dominant, and their effects are

subdetector	hits per bunch crossing			
	500 GeV		800 GeV	
	3 T	4 T	3 T	4 T
CCD layer 1	548	350	616	422
CCD layer 2	224	132	264	119
CCD layer 3	76	42	80	57
CCD layer 4	72	26	31	23
CCD layer 5	26	17	23	11
APS layer 1	800	511	899	616
APS layer 2	87	48	92	65
APS layer 3	21	15	18	10
APS cone	71	34	84	54
FTD layer 1	71	34	84	54
FTD layer 2	58	33	68	35
FTD layer 3	38	24	37	26
FTD layer 4	24	16	27	26
FTD layer 5	26	16	32	16
FTD layer 6	22	13	16	14
FTD layer 7	12	12	11	11
SIT layer 1	22	23	16	17
SIT layer 2	15	7	9	5
FCH, per layer	19	10	9	11
TPC (tracks)	7	5	7	8

Table 6.4: *Number of background hits per bunch crossing originating from* e^+e^- *pair production in all detector systems [125]. FTD and FCH rates are summed over both sides. The amount of background entering the reconstruction has to be multiplied by 60 for the CCD vertex detector layers, because the CCD readout takes the time equivalence of 60 bunch crossings [135].*

incorporated in the simulation package.

Table 6.4 gives an overview of the expected amount of background hits per bunch crossing in each tracking detector [125]. A conservative estimate of 1% total background occupancy is assumed for the TPC. It is assumed that all other subdetectors except the CCD vertex detector option can be read out once per bunch crossing; thus, the numbers given in Table 6.4 reflect directly the amount of background present in the reconstruction chain. The CCD vertex detector accumulates background over 60 bunch crossings before the event data enter the reconstruction [135]; therefore each event in the CCD is overlaid by 60 times the number of background hits given in the table.

The large background expected close to the beam pipe poses a challenge to the track reconstruction. Another potential problem is the limited double hit resolution of a gaseous detector like the TPC in the expected dense jet environment. In order to prove that track reconstruction of good performance is possible in such an environment, a realistic track reconstruction package for BRAHMS was set up during the work performed for this thesis, and the performance of the track reconstruction was evaluated. Details of the reconstruction method and the performance are discussed in the following chapter.

Chapter 7

Track Reconstruction at a TESLA Detector

As a result of the studies performed for the TESLA Technical Design Report, a baseline tracker design with two options for the vertex detector is proposed [125]. The specifications of both variants are implemented into the simulation package BRAHMS [130]. The subject of this chapter is to document the performance of both designs and to ensure that both meet the physics requirements. This work was contributed as supplemental note [137] to the TESLA Technical Design Report. A complete pattern recognition package to reconstruct charged tracks was developed based on existing LEP software in order to obtain realistic results from the simulation data. This allows to study reconstruction efficiencies and rates of fake reconstructed tracks, as well as vertexing and momentum resolutions. At the same time effects of machine backgrounds and double track resolutions are taken into account. For the study the solenoid magnetic field is assumed to be 3 T. The proposed coil for the TESLA detector is designed for a 4 T field, but one intention of this chapter is to prove that track reconstruction with sufficient quality will also work in a more difficult environment than foreseen in the design. Therefore several system parameters are chosen with safety margins.

This chapter will begin with a detailed description of the track reconstruction algorithm. The second part is then dedicated to the evaluation of track reconstruction efficiencies and the amount of fake track candidates. A short discussion of the results will close the chapter. The track reconstruction efficiency and related quantities describe the detector performance on a rather technical level. A more physics oriented evaluation of the tracking performance was also performed for this thesis; it will be presented in Chapter 8.

7.1 The Full Reconstruction Package

The track reconstruction system that is implemented in the BRAHMS detector simulation software package is designed modularly. A global steering package collects hits from all tracking subdetectors in a common bank structure. These hits are then passed over to pattern recognition packages that perform a local track search in the respective subdetector, or combination of subdetectors. Currently three pattern recognition packages are in use: A dedicated TPC pattern recognition is optimised to cope with specific TPC properties like limited double-track resolution and a large number of space points. A full Silicon pattern recognition exploits the homogeneous design of the inner tracking to combine the information delivered by vertex detector, forward tracker and SIT for performing a track search. A Forward Chamber pattern

recognition package is specifically designed for wire chamber signal processing.

The track candidates found by the local pattern recognition are passed back to the steering routine, which converts track candidates from the local pattern recognition routines into a common data format to be used by the global track search. All hits found in the silicon detectors are also passed on to the global track search separately. This is done because the silicon detector pattern recognition suffers most from background, and therefore the local silicon pattern recognition is improved in a second step, including additional information from the TPC and FCH.

A high efficiency is maintained by performing the global track search without taking care of ambiguities. Any sensible combination of hits and local tracks is selected if certain minimal quality criteria are fulfilled, and track candidate sharing one or more hits are not excluded at this stage. The resolving of these ambiguities is done in a final step, where all track candidates found in the event are treated at once to optimise the overall fit result.

The structure of the track search implemented in the BRAHMS linear collider detector simulation software is adapted from the DELPHI experiment at LEP, where this strategy has proven itself highly successful. An overview of the structure of the track reconstruction system in BRAHMS is given in Figure 7.1.

7.1.1 Global Steering

The execution of the reconstruction package is controlled by a global steering. It serves as the interface to the simulation package for receiving the information. Necessary conversions between different ways of parameterising hits and helices are done. The simulation data, intermediate results and the reconstructed event are stored in an event data space (ZEBRA) which allows to cope with the huge memory requirements due to simulated backgrounds. The global steering calls the different reconstruction processors which are discussed in the following.

7.1.2 Local Reconstruction Packages

The first layer of pattern recognition involves a local pattern recognition for the different subdetectors. First all hits in the subdetectors are converted into space points used in the later reconstruction. Three subsystems have a detailed local pattern recognition to exploit the standalone tracking capability of the devices. The first is the full system of silicon tracking detectors, comprising the CCD or APS detector, the SIT and the FTD. Another detector having a local pattern recognition is the TPC. A third local track search deals with the information obtained from the forward chambers. The task of those local reconstruction codes is to find short local track elements which will be used in the later processing as seeds for the final track searches.

Pattern Recognition for the Silicon Trackers

The silicon trackers feature cylindrical layers of pixel detectors (CCD or APS vertex detector), cylindrical layers of double-sided strip detectors (SIT), silicon pixel detector disks (inner FTD), and double-sided strip detector disks (outer FTD). The APS design also includes conical pixel detector endcaps. Combining all these different detector types in such a way that a common pattern recognition program can treat them simultaneously is clearly a non-trivial task. Although the strip detector simulation for SIT and outer FTD is not yet used in this study, a structure to cope with these detector types has already been included in the track search. This approach starts with transforming the strip detector readout into pseudo-pixels.

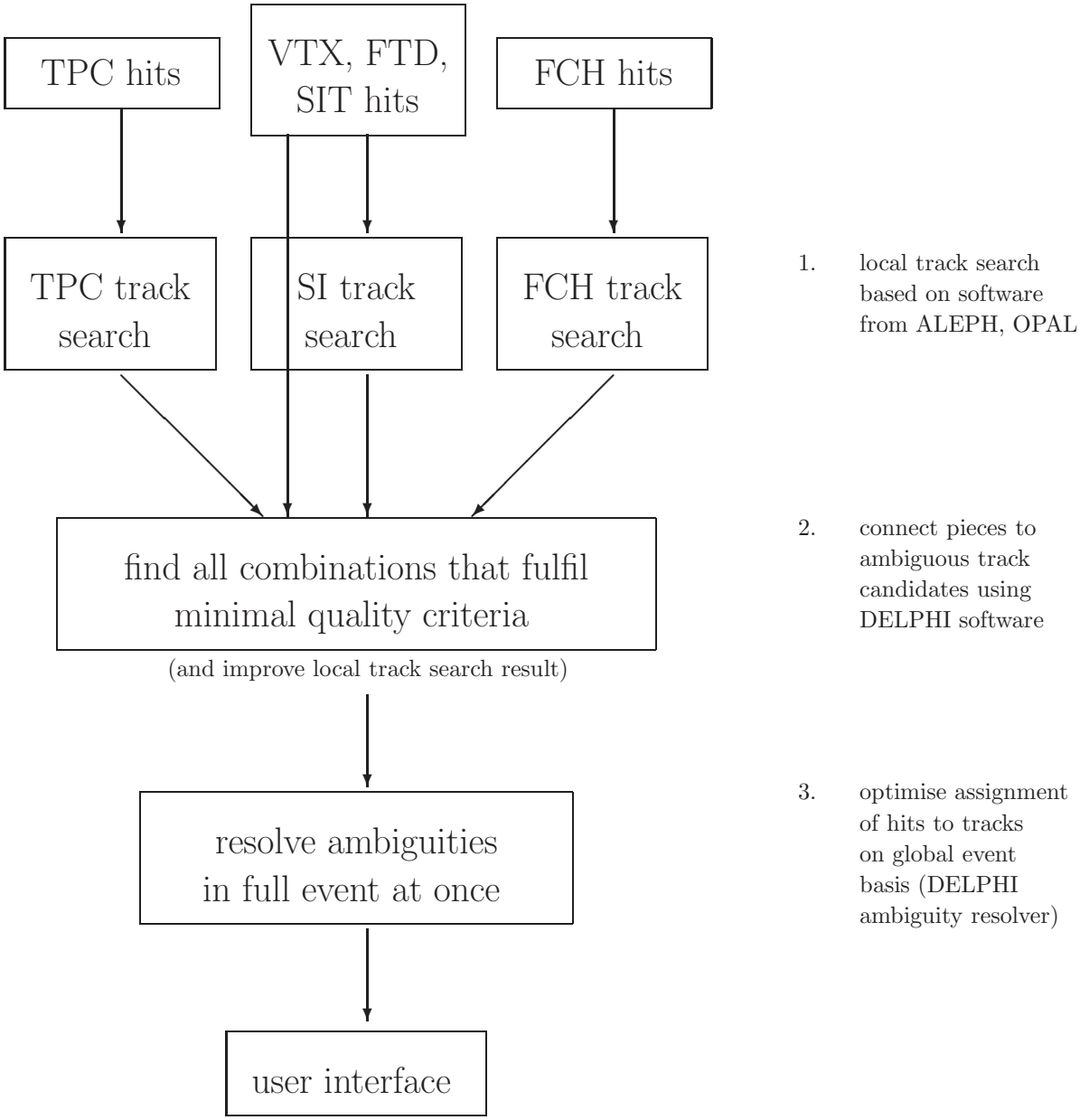

Figure 7.1: *A schematic view of the track reconstruction system. The three main stages of data processing are explained in the text. Each box corresponds to a separate software module. Additional packages that are not represented in this overview are the track fit module, and the global steering that controls data flow between and storage for all packages.*

All positions where a front side strip with a signal crosses a back side strip with a signal are assumed to be separate hits, although in general different assumptions on where the actual hits took place are mutually exclusive. Solutions that are mutually excluded are marked as such (see Section 7.1.5), but these exclusions are ignored until later in the track reconstruction process, where information from other subdetectors is included to help decide which solution is most likely correct. This way the number of hits that has to be taken care of by the track search is generally much larger than in the case of true pixel detectors, but on the other hand the track search can be performed with a very simple algorithm that only has to be able to cope with 3d pixels.

Once all (pseudo- and real) pixels are made available, the track search starts with all combinations of hits from the outermost three layers with hits in a number of angular subdivisions of the silicon detectors. A helix fit is attempted for each such combination, and if the fit succeeds with acceptable χ^2, matching hits on the next inner layer are added to the candidate. All layers with matching hits are thus successively being scanned for hits to be added to the track candidates. Chains that are found in neighbouring angular subdivisions are finally merged together if they match. This algorithm was written by R.J. Hawkings and is described in detail in Ref. [138].

It has to be pointed out that two or more local track candidates in the silicon detectors may share one or more hits. Although these candidates are in fact mutually exclusive, none of these is rejected. Even candidates that do not share hits may be excluded against each other if they contain pseudo-hits from double-sided strip layers that are mutually exclusive, as indicated above. Candidates of either type are marked as being excluded against each other, but they are kept for further analysis. The decision which candidate is most likely correct is not taken before the information from other subdetectors can be taken into account, at a later stage in the track reconstruction.

The silicon vertex detector is the device that is closest to the interaction region. Therefore it suffers most from beam-related background (see Table 6.4). This is especially true for the CCD option, where background hits are accumulated over 60 bunch crossings. In this case, the track search has to deal with between 10^4 and 10^5 background hits overlaid over each physics event. It was shown that this is feasible using the simple algorithm described above [138]. An additional option, which is used in this study, is to exclude the innermost one or two vertex detector layers from the initial local track search, and to collect hits on this layer only at a very late stage, where track candidates including information from all other detectors can be extrapolated towards the IP with maximal precision. Both options are foreseen in the track reconstruction software, but the latter has proven advantageous in terms of CPU time consumption, while the reconstruction performance is similar in both cases.

TPC Pattern Recognition

The track search in the TPC is performed by a modification of the ALEPH TPC pattern recognition software. The first version of the TESLA detector adaptation was contributed by G.W. Blair. Hits in the TPC are sorted by radius and by ϕ coordinate. Chains of tracks are created by combining hits of the outermost pad rows, and then subsequently adding hits at smaller radii by a Kalman Filter algorithm, i.e. comparing the coordinates of hits in question with predicted coordinates calculated from a helix extrapolation of the current chain of hits. Deviations from a helix trajectory due to multiple scattering of particles in the TPC gas are taken into account.

Special care is taken to minimise disturbance by limited double hit resolution, which mainly

affects the inner part of the TPC, where the distance of tracks in jets is frequently smaller than what can be resolved. TPC readout signals that are merged contributions from more than one actual hit are expected to have coordinates that are an average of the coordinates of the contributing hits. Including these hits into a track fit would therefore effectively degrade the resolution and decrease the efficiency of merging those track candidates with information from the silicon detectors. Merged hits can in principle be tagged by looking at the pulse height or shape. A different, purely geometrical approach is being followed in the software described here: The initial track search starting at the outermost pad row stops in the middle of the TPC sensitive radial range, safely outside the region where significant effects of limited double hit resolution are observed. The track candidates assembled in this initial search are then extrapolated into the inner radial region of the TPC volume, and regions are being searched for where at least two tracks come closer to each other than the expected double hit resolution. All hits in these regions are assumed to be distorted due to merging of several contributions, and are removed from the database. Only the remaining hits are then used in the second part of the local track search.

Forward Chamber Track Search

Since the forward chambers are supposed to be constructed from twelve layers of straw tubes on each side of the detector, they do not provide space points, but only wire information. However, the chamber is designed to support full 3d track reconstruction following a principle already used at DELPHI. The twelve layers are grouped into six double-planes of parallel, but staggered wires. The wire orientation of each double plane is rotated by 60° with respect to the neighbouring double planes. This amounts to three different orientations in two sets of double-planes each.

Main task for the forward chambers is the reconstruction of high energy muons. The momentum resolution achieved by TPC and inner detectors alone degrades in the forward direction. Other particles than muons suffer from scattering in the TPC endcaps, and therefore the momentum resolution for these particles can hardly be improved by the FCH. As a consequence, the FCH track finding algorithm can be optimised for straight tracks originating from close to the IP without affecting the physics performance of the overall track reconstruction.

The first step is a search for hits on two near-by wires within each double plane. Only combinations that are compatible with a straight track coming from close to the IP are kept for further processing. For each hit both possible drift directions are taken into account. The second step is performed separately for the inner and outer set of three double-planes: From the hit combinations space points are reconstructed, where most of the fake combinations are rejected because of the redundant information in the three double planes. Pairs of such space-points from the inner and outer three double-planes are checked for being compatible with coming from a straight track originating in the IP. If they are, a full helix fit is performed using the information from all twelve planes. The Forward Chamber pattern recognition package was mainly written by I. Božović-Jelisavčić, using fit software from DELPHI.

7.1.3 Kalman Filter Track Fit

A common track fit algorithm is applied to all local track candidates found by the subdetector pattern recognition packages, and to combinations of those (global track candidates). The track fit can operate on hits as well as full track parts. This is for example exploited in the final

track fit, where the TPC contribution is not entered as single hits, but as a full set of track parameters as obtained from the local TPC track fit.

The track fit algorithm used is a Kalman Filter [139] which was developed for the DELPHI experiment and was adapted for use in the BRAHMS simulation software by K. Mönig. It is a fast recursive algorithm implemented using the weight matrix formalism. A Kalman Filter is an estimator for a linear system, while a track in a solenoid field is described by a helix. Therefore a Taylor expansion around a reference trajectory is used as a starting point to obtain a linear system. The fit is iterated to ensure good convergence.

The track fit takes into account the effects of multiple scattering and energy loss in the material. A simplified description of the detector material is sufficient for the purpose of track fitting. The geometry of the detailed detector material description of the TESLA detector simulation is approximated in the track fit by a sequence of surfaces, which are either cylinders around or planes perpendicular to the beam pipe. For each of these surfaces an apparent thickness is specified in terms of radiation length and energy loss of a minimal ionising particle (for a particle crossing at 90°). Additional surfaces are introduced in the TPC drift volume to account for the $\mathrm{d}E/\mathrm{d}x$ of particles in the drift gas.

In the track fit the effect of the multiple scattering is taken into account by increasing the error contour of the track extrapolation after crossing the material surface. The momentum dependent effect of the energy loss is taken into account by changing the curvature of the reference trajectory used for the Taylor expansion in the fit.

Another important feature of the fit is the logic to remove outliers. The fit is able to remove up to 3 measurements from a track candidate if it fails a fit χ^2 probability cut of 0.1%. This is a very effective filter to remove wrong associations of hits to tracks. A ranking of detectors to be removed is used in order not to remove the most precise measurement (e.g. the TPC track element) from the track. Called from the track search packages the fit always retains the track element which was used as a starting point to reconstruct the track.

7.1.4 Global Track Search

The task of the global track searches is to find all possible track candidates. A generic track search engine in use by the DELPHI collaboration [140] was converted for use in the TESLA detector framework in collaboration with M. Elsing, and it is used to implement several track search strategies. For each of those strategies a two stage algorithm is executed. First, the track element used as a starting point is extrapolated to other detectors which do not yet contribute to the reconstruction. For each of those detectors a list of candidate hits or track elements within a road around the extrapolation is selected. Then a sorted loop over all candidate lists is done in order to find the longest possible track combinations. Here the Kalman Filter track fit is used as the major filter for rejecting fake combinations.

In the first stage of the processing an attempt is made to merge the track elements in the silicon tracker system with those in the TPC, which were both found by the local pattern recognitions. Starting from the silicon all matching TPC track elements are combined to track candidates and vice versa. Before each track candidate is fitted, the track elements in the silicon tracker system are replaced by the individual hits in the different layers. This allows to correctly take into account the multiple scattering and energy loss in the silicon tracker material by using the momentum estimate from the full track. Also, single fake hits can be removed from the track if the fit of the full track is rejected by the outlier logic of the Kalman Filter. Furthermore, the information that hits in the silicon are missing is used in the second stage of

the processing to improve the association efficiency.

After the first searches, the track candidates are extrapolated to all detectors (or silicon layers) which do not yet contribute to the reconstruction. This is done in steps. First, all candidates are extrapolated to the SIT layers and to the forward chambers and missing hits are added into the candidates. Then all FTD discs are scanned for additional hits. Missing hits in the VTX are added in three steps to allow for the background levels in the first layers. Hits in the outermost layers 3-5 (or layer 3 and the conical endcap in the APS option) are searched in a first step. For those candidates which already include VTX hits and have therefore very small extrapolation uncertainties, also the second layer is scanned for additional hits. Extrapolation onto the first vertex detector layer is performed in the final step.

At the end of this process all candidates found by the searches are stored in the event data space and sent to the ambiguity processor for resolving the left over ambiguities in the hit association to tracks.

7.1.5 The Concept of Exclusions

The result of track searches is a set of ambiguous track candidates with many possible associations of individual hits to different track candidates. Also the local pattern recognition of the different detectors can create ambiguous hit combinations. For example in the Silicon Intermediate Tracker space points are supposed to be reconstructed out of hits on the back-to-back module by combining the measurements in both orientations, as indicated above, so that hits from n tracks on a module lead to $n(n-1)$ mirror images. Such ambiguities need to be resolved in the process of the track reconstruction. It is beneficial to leave the decisions to the stage of the global event solution, since at this stage the full information of the reconstructed track candidates can be used to minimise mistakes.

All results from the different reconstruction packages are stored in the event data space. The structure allows for so-called "logical exclusions" between objects like hits or track candidates. An "exclusion" signals that two objects use conflicting or common detector information and that for the final solution of the event such conflicts need to be resolved.

7.1.6 Event Ambiguity Processing

The ambiguity solution is a combinatorial problem. It is solved by the same algorithm as used in the DELPHI experiment, modified for TESLA detector purposes by D. Wicke. The task of the ambiguity processor is to decide about the association of hits and to select the best tracks out of the set of mutually excluded candidates found by the search algorithms. The design of the ambiguity processor [141] was done in order to find a balance between performance and CPU consumption.

The ambiguity processor maximises a score function for a given event. The score of each track in the solution is determined by the number of hits associated to the track and the quality of the fit. A simple algorithm to resolve the event can start by selecting the track with the highest score. The hits associated to that track are removed from all other candidates. This implies refitting the candidates from which a hit has been dropped. The list of candidates is therefore changing in the course of the process. The process is iterated by selecting the next best track until no more candidates are left over. This algorithm is very fast, but any mistake at the beginning propagates through the rest of the event analysis. Another algorithm, which does not have this problem, would be to create all possible lists of tracks, which contain no

exclusions anymore, in the same way as before. Here the list with the highest score would be selected. This algorithm is limited by combinatorics, because the number of lists increases very rapidly with the number of candidates.

The ambiguity processor is a mixture of both algorithms. It is a recursive algorithm, which in each step subdivides the event into sets of mutually excluded tracks to resolve them independently. For each set all possible lists of tracks are tried. One track after the other is taken out of the set and each time the subset is resolved in the next recursion level. For each recursion the maximum possible score of the subset is calculated to truncate combinations below the current maximum. A fall back solution is implemented, which uses the simpler algorithm for a set in case it is not resolved after more than one second or the recursion depth is exceeding 9 levels.

Additional protections are needed. Sub-tracks created during the processing are rejected if they are only generated by splitting a long track. A list of bad track types is used to reject detector combinations of poor quality or high risk of being fake.

The scoring function is tuned to optimise the track reconstruction efficiency and the hit association purity at the same time. For each track a score of 100 is assigned, while a detector measurement associated to the track is given a score between 1 and 20, depending on the quality of the measurement, and a logarithm of the χ^2 probability of the track fit is added to disfavour bad track candidates.

The result of the ambiguity processing is the final reconstruction result which is then stored in the event data space and used for analysis.

7.2 Performance of the Proposed Detector

Two reference event samples that represent different pessimistic scenarios are used for the evaluation of the linear collider detector tracking performance. Two-jet events created by $e^+e^- \rightarrow Z \rightarrow d\overline{d}$ reactions at 500 GeV centre-of-mass energy without initial state radiation constitute the main reference sample. These events contain high-multiplicity jets which are highly boosted and thus comparatively narrow. A second sample is mainly chosen to push track reconstruction in the TPC to its limit by providing tracks that are extremely close to each other. $e^+e^- \rightarrow Z \rightarrow \tau^+\tau^-$ events at 800 GeV without initial state radiation, where each τ is forced to decay into three charged particles, are selected for this task. Example events of both samples are shown in Figure 7.2.

Only tracks that fulfil certain quality cuts are being accounted for in the performance analysis. In order to avoid normalisation of the reconstruction efficiency to tracks which would not have been found even with ideal track reconstruction, all tracks are excluded that leave less than three hits anywhere in the detector. The hermetic detector design ensures that the fraction of tracks outside the beam pipe that cause less than three hits is practically zero. A minimal momentum of 1 GeV/c is required, and tracks that originate from secondary interactions with the detector material (e.g. conversion electrons) are rejected. The full angular extent of $|\cos(\theta)| < 0.995$ is evaluated. Both samples are processed with full background simulation in all subdetectors, including the equivalent of 60 bunch crossings of background in the CCD vertex detector.

7.2.1 Performance of the Local Pattern Recognition Packages

The result of the local track searches in the TPC, the silicon detectors and in the Forward Chambers are the starting point of the track reconstruction. Only tracks that are reconstructed in at

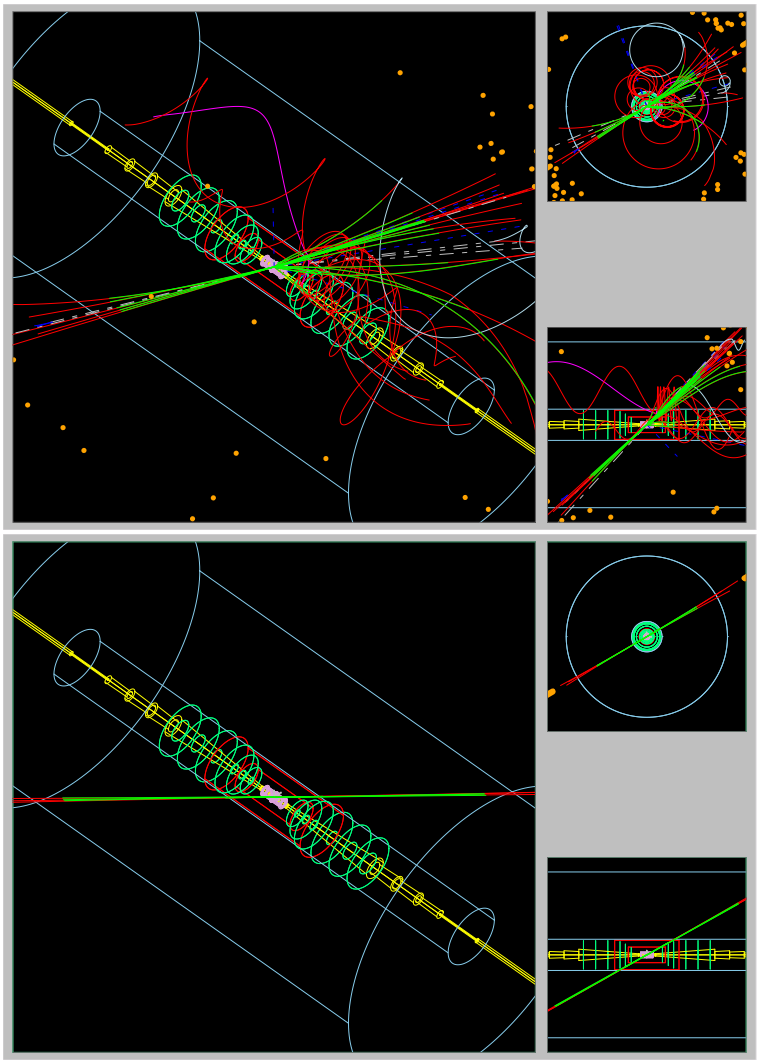

Figure 7.2: *BRAHMS event displays [142] of two reconstructed events after the complete processing. A* $Z \rightarrow d\bar{d}$ *event at* 500 GeV *(top), and a* $Z \rightarrow \tau^+\tau^-$ *3-prong event at* 800 GeV *(bottom). Charged tracks are shown in red, and the respective reconstructed tracks are overlaid in green.*

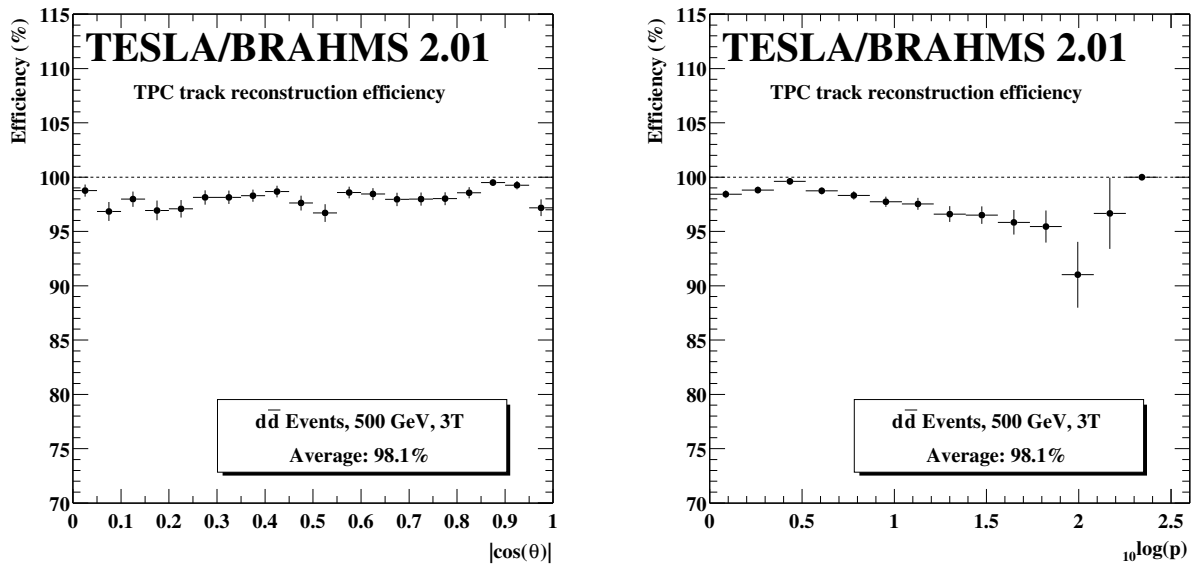

Figure 7.3: *Local track search efficiency in the TPC, with full background simulation on the $d\bar{d}$ reference sample, over $|\cos(\theta)|$ (left) and over the track momentum (right).*

least one of these three detector systems will show up in the sample of globally reconstructed tracks. The detector is designed to provide at least two independent systems capable of providing local track reconstruction over a maximal angular range. Thus a high level of redundancy is foreseen and evident in the performance figures presented in the following. Nevertheless, in order to achieve the full design performance of the detector as far as momentum and vertex resolution are concerned, maximal contribution of all available subdetectors to the reconstructed tracks is mandatory. Therefore, the local track search efficiency is a central figure of merit.

The reconstruction of tracks in the TPC performs well as expected even for the narrow jets typical for $d\overline{d}$ events. A reconstruction efficiency of 98.1% despite a background occupancy of 1% is found in this sample. As visible in Figure 7.3, mainly high momentum tracks contribute to the inefficiency. This is presumably due to jets with significantly less than the average multiplicity, where few high-momentum tracks traverse the TPC closer to each other than can be resolved given the limited double-hit resolution. This effect is much more prominent in the $\tau^+\tau^-$ reference sample (Figure 7.4), where almost all jets are of this type. As a consequence, the local reconstruction efficiency drops to just above 90% there. It will be shown later that this loss in efficiency is fully compensated by the redundant track searches in other subdetectors, mainly the silicon detectors. The fraction of fake tracks among the track candidates is 0.4% for $d\overline{d}$ events, and raises to 2.1% in the $\tau^+\tau^-$ sample. A fraction of between 3% ($d\overline{d}$) and 8% ($\tau^+\tau^-$) of all tracks has been reconstructed in more than one piece, although no interaction other than multiple scattering took place during their traversal of the TPC. This effect is caused by hits that are merged with background hits or hits from close-by tracks. These hits appear shifted away from the track, or are removed by the hit-merging finder and interrupt the track search trying to follow tracks through the TPC. No attempts are currently made to merge this split tracks together in a later step of the track reconstruction, although this is foreseen in the reconstruction code.

The silicon detector track search is investigated separately for the CCD and APS options. The APS design achieves a reconstruction efficiency of 97.4% with full background, where mainly low-momentum tracks in the forward direction are lost (see Figure 7.5). Almost 10% of all track candidates are noise tracks, which is reasonable given the large background on the

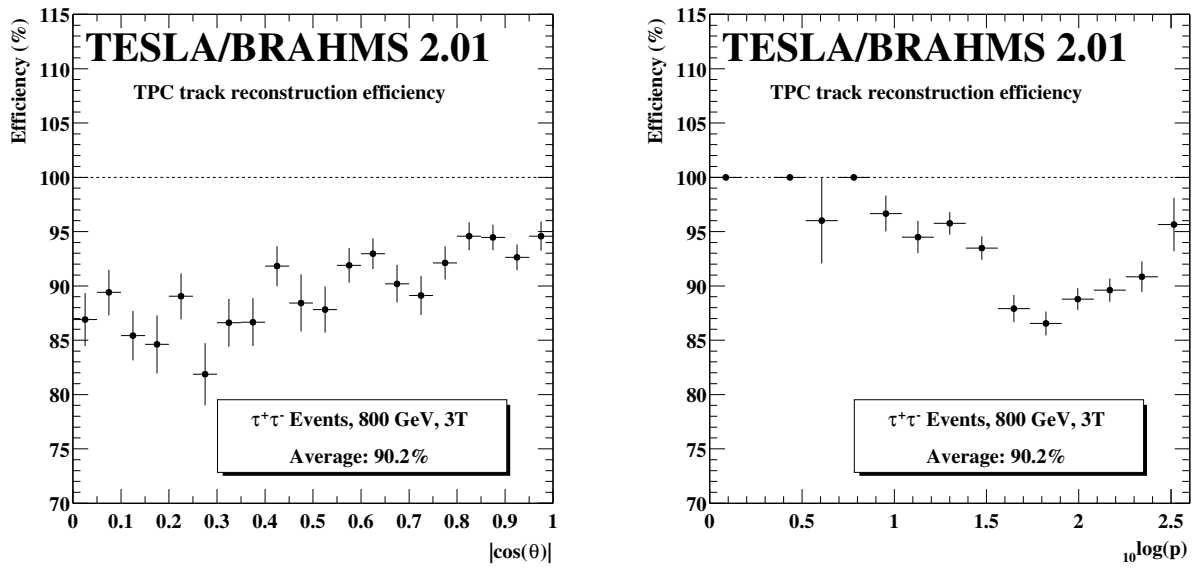

Figure 7.4: *Local track search efficiency in the TPC, with full background simulation on the $\tau^+\tau^-$ reference sample, over $|\cos(\theta)|$ (left) and over the track momentum (right).*

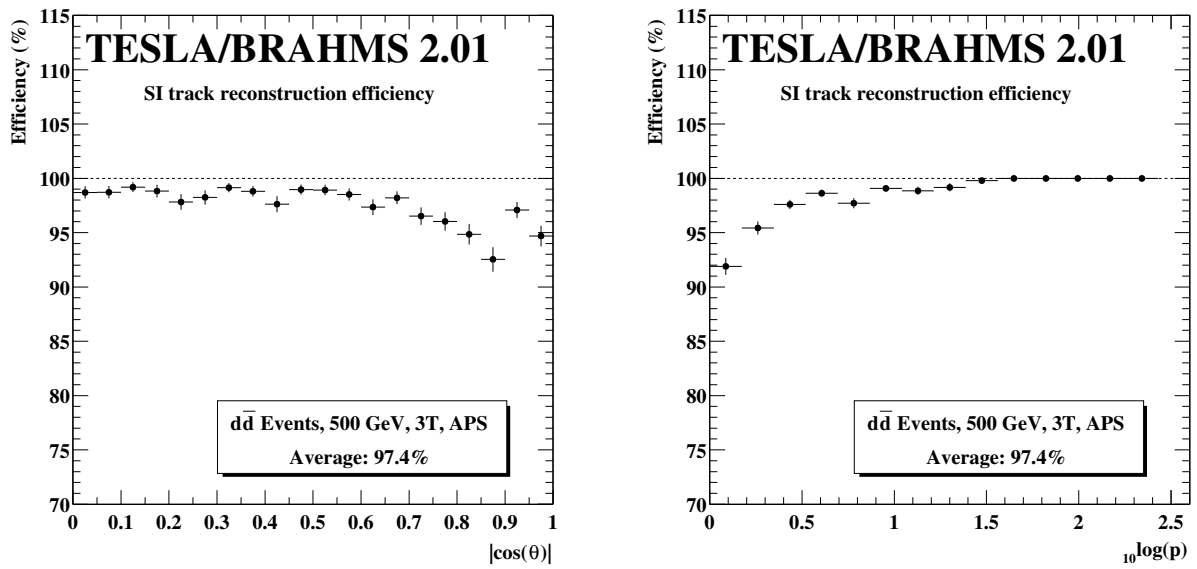

Figure 7.5: *Local track search efficiency in the APS variant of the central silicon detector system (APS-VTX, SIT, FTD), with full background simulation on the $\mathrm{d\bar{d}}$ reference sample, over $|\cos(\theta)|$ (left) and over the track momentum (right).*

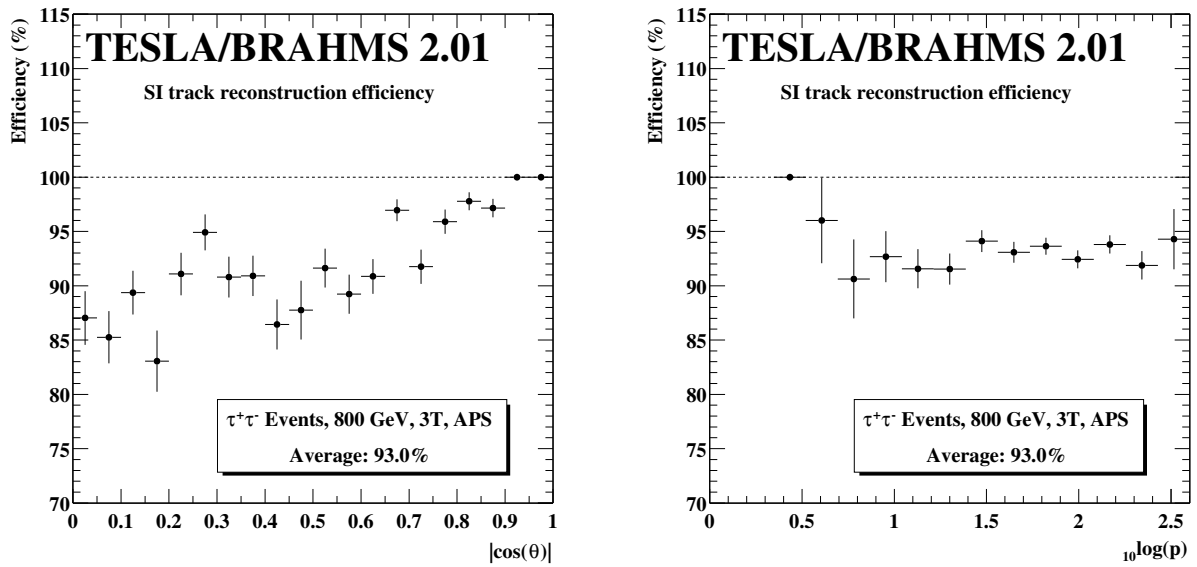

Figure 7.6: *Local track search efficiency in the APS variant of the central silicon detector system (APS-VTX, SIT, FTD), with full background simulation on the $\tau^+\tau^-$ reference sample, over $|\cos(\theta)|$ (left) and over the track momentum (right).*

inner vertex detector layers. Most fake tracks are however removed in the later stages of track reconstruction, when information especially from the TPC is taken into account additionally.

The APS performance on the $\tau^+\tau^-$ sample is slightly degraded; only 93% of all tracks are found. Figure 7.6 shows that tracks of all momenta are equally affected, but that the efficiency loss is restricted to the barrel region, whereas the forward direction is hardly affected. The explanation for this effect is found in a significant number of τ 3-prong decays that involve intermediate neutral resonances like K^0_S, a fraction of which decays outside the first vertex detector layer. The number of layers which are hit by the charged products of these decays in the APS option is thus four or even less, which causes inefficiencies in the reconstruction of these tracks. Due to the redundant design of the track reconstruction detector system, full efficiency is recovered during the following global track search, where unassociated SIT and APS hits are matched to TPC track elements (see below).

The CCD vertex detector option is equipped with more barrel layers than the APS, which suppresses effects like the one observed for τ decay products in the APS version, but the CCD suffers from a much higher background level. With moderate background like expected for a CMOS pixel detector design of otherwise similar specifications to the CCD proposal, average reconstruction efficiencies of above 99% are achieved. With full background simulation, the first two CCD layers are excluded from the local track search, which negatively affects the reconstruction efficiency mainly for tracks with significant curvature, i.e. with a momentum below about 5 GeV/c. An efficiency of 92.4% is found for $d\bar{d}$ events in this environment (see Figure 7.7), with a fraction of fake candidates of only 0.7%. The $\tau^+\tau^-$ sample contains mainly high momentum tracks which are not affected by the efficiency loss described above, and thus a reconstruction efficiency of 97.8% is measured independent of the background level (Figure 7.8). 12% of all local track candidates found in the full background scenario are fakes.

The third local track search takes place in the system of forward chambers (FCH) behind both TPC endcaps. As mentioned already, the large amount of material in front of the FCH restricts useful measurements in the FCH to very high-momentum tracks. Figure 7.9 shows that this goal is certainly met. A reconstruction efficiency of around 90% for tracks above

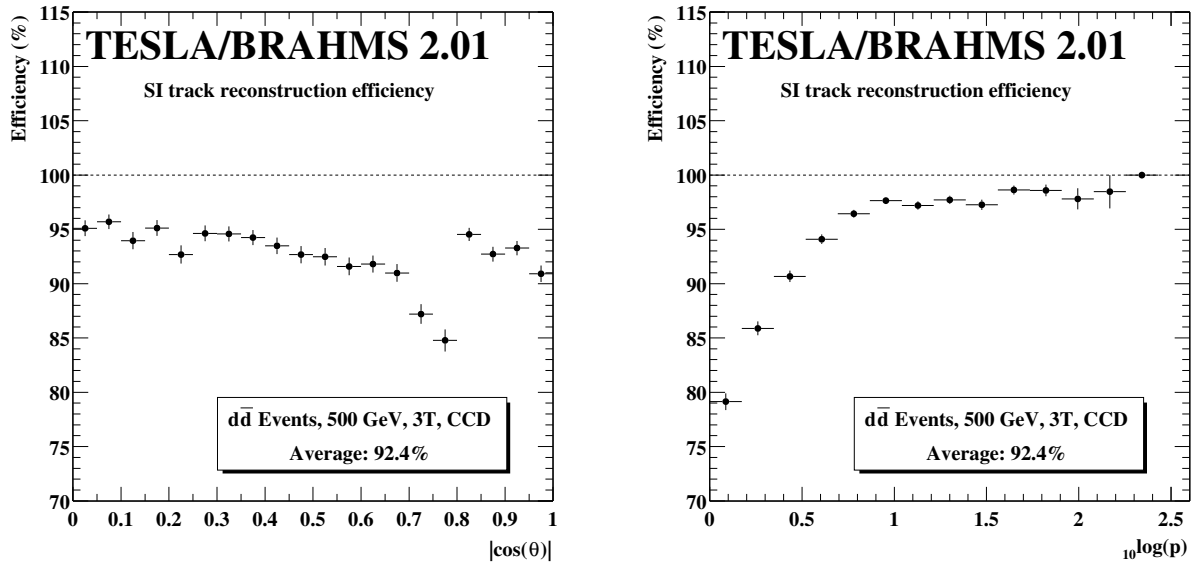

Figure 7.7: *Local track search efficiency in the CCD version of the central silicon detector system (CCD-VTX, SIT, FTD), with full background simulation on the* $\mathrm{d\bar{d}}$ *reference sample, over* $|\cos(\theta)|$ *(left) and over the track momentum (right).*

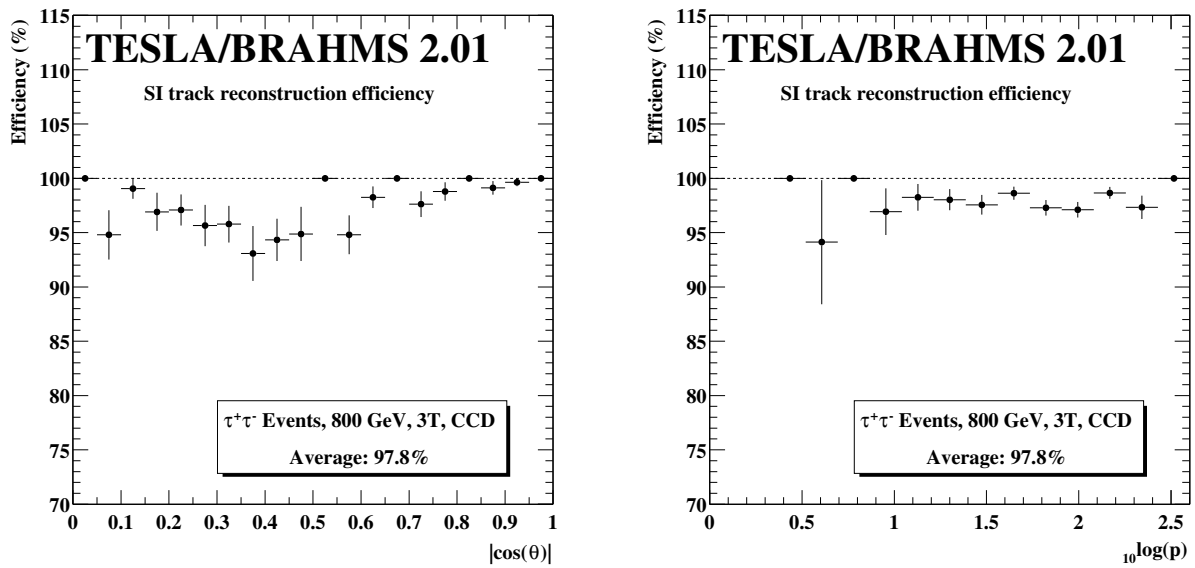

Figure 7.8: *Local track search efficiency in the CCD version of the central silicon detector system (CCD-VTX, SIT, FTD), with full background simulation on the* $\tau^+\tau^-$ *reference sample, over* $|\cos(\theta)|$ *(left) and over the track momentum (right).*

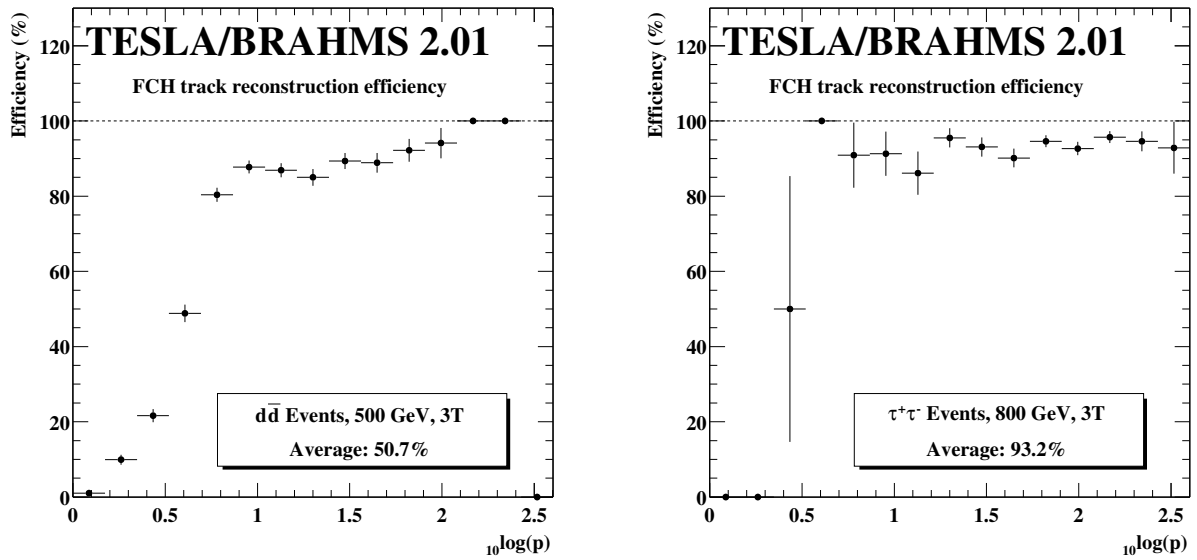

Figure 7.9: *Local track search efficiency in the FCH over track momentum, with full background simulation, on the* $\mathrm{d\bar{d}}$ *(left) and the* $\tau^+\tau^-$ *reference sample (right).*

10 GeV/c is observed. Between 7% ($\mathrm{d\bar{d}}$) and 23% ($\tau^+\tau^-$) of all candidates are noise tracks, including tracks where the wrong drift direction is guessed in more than 3 out of 12 layers.

7.2.2 Track Efficiencies and Fake Rates in $Z \rightarrow \mathrm{d\bar{d}}$ Events at 500 GeV

It was mentioned during the discussion of the local track search performance in the previous section that most inefficiencies are cured during the later stages of track reconstruction, namely the global track search and ambiguity resolving. In the CCD option detector, for example, the silicon detector pattern recognition suffers slightly from the high background level. However, after merging the information delivered by all subdetectors, the global track reconstruction efficiency turns out to be 98.4%, higher than both the TPC and the silicon detector reconstruction efficiencies. The APS design, with its better reconstruction performance due to less background, achieves even 99.2% efficiency (see Figure 7.10).

The fraction of fake tracks among the global track candidates is less than 1% for both vertex detector options. Roughly half of this sample consists of short track pieces dominated by noise in the silicon detectors. The remaining fake tracks are mainly short track pieces in the TPC which consist of merged hits from two or more close-by tracks. Less than 6% of the fake tracks, i.e. less than 0.06% of all track candidates, are caused by incorrect merging of correctly reconstructed local track candidates from the different subdetectors.

About 4% of all tracks are split up into at least two parts during the reconstruction. More than half of these splittings occur within the TPC; the remainder is mainly cut between the inner edge of the TPC and the silicon detectors. An explanation for the splittings within the TPC was given above; this is probably caused by distorted signals due to hit merging. The second contribution is not investigated in detail, but could presumably be suppressed by further optimising the global track search parameters.

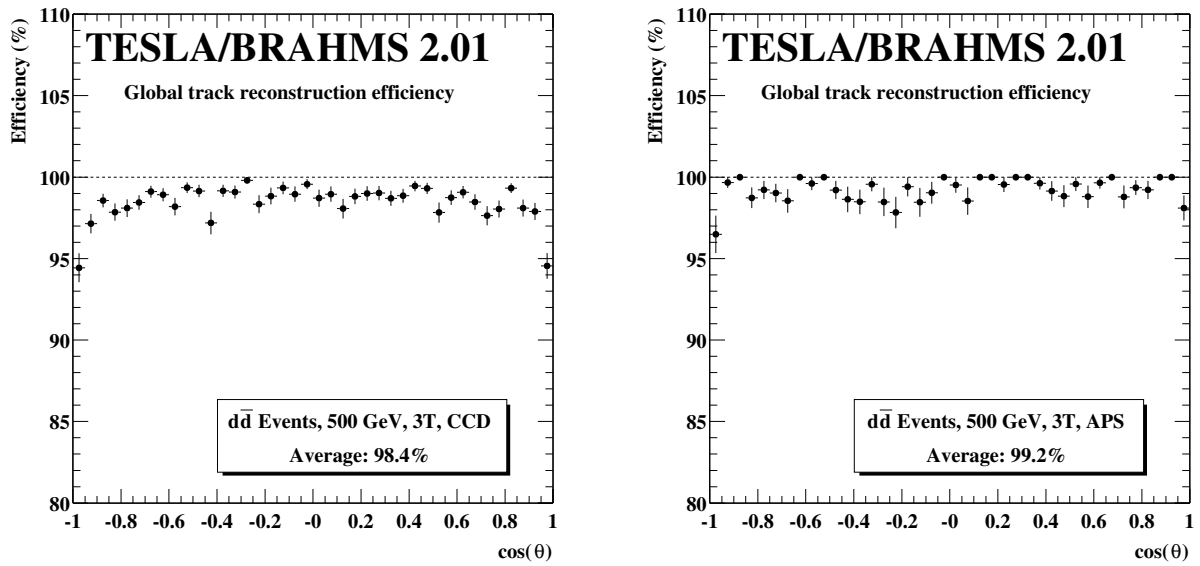

Figure 7.10: *Global track reconstruction efficiency over* $\cos(\theta)$*, with full background simulation, for the* $\mathrm{d\bar{d}}$ *reference sample, CCD (left) and APS (right) option.*

7.2.3 Track Efficiencies and Fake Rates in $Z \longrightarrow \tau^+\tau^-$ 3-prong Events at 800 GeV

The extreme case of a sample of pure τ 3-prong jets pushes the demands imposed on the track reconstruction at a TESLA detector even further. As Figure 7.11 shows, tracks in these events are reconstructed with an overall efficiency of almost 98% for both investigated detector design variants.

The fake track fraction is significantly higher than in the $\mathrm{d\bar{d}}$ sample, namely between 4% and 5%. The same sources as in the $\mathrm{d\bar{d}}$ sample contribute: Short noisy track pieces in the silicon detectors and short TPC track elements with a mixup of two or more close tracks, where this distorted piece is separated from other, unaffected parts of the TPC tracks which are then correctly merged to their silicon counterparts. The $\tau^+\tau^-$ sample is however much more affected by a third class of fake tracks, which are correctly reconstructed silicon track elements merged to noisy TPC track parts.

The fraction of tracks that are split into at least two parts is also higher than in the case of $\mathrm{d\bar{d}}$ events. 9% of all tracks are affected. With an increasing number of tracks that cannot be separated from nearby tracks in the inner region of the TPC, finding corresponding track pieces in TPC and silicon detectors becomes increasingly difficult. At the same time, due to more hits being lost due to merging, also the fraction of track splittings within the TPC is larger. Both effects are related, and thus it is well understandable that the relative size of their contributions to the total rate of track splittings remains the same as in the $\mathrm{d\bar{d}}$ sample.

7.2.4 Hit Efficiencies and Fake Rates for the Different Detector Components

It has been pointed out that it is not sufficient to exploit the redundant design of the tracking detector system in the sense that each track is only reconstructed in one subdetector system, while reconstruction in other systems fails frequently. All systems have to contribute information to global track candidates to make the full system meet the design criteria. In this section,

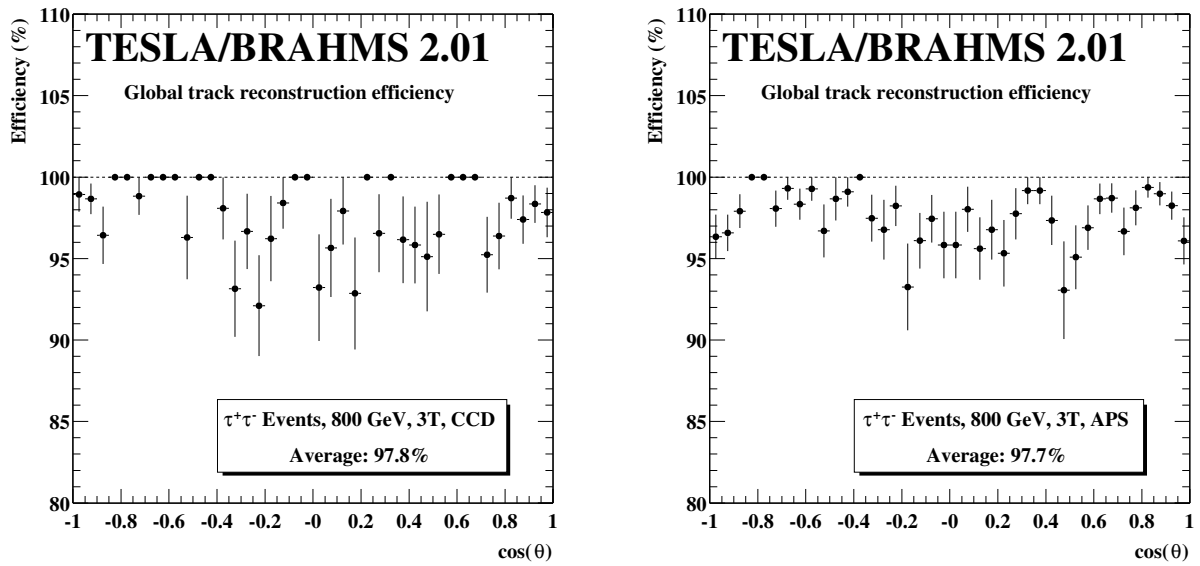

Figure 7.11: *Global track reconstruction efficiency over* $\cos(\theta)$*, with full background simulation, for the* $\tau^+\tau^-$ *reference sample, CCD (left) and APS (right) option.*

it will be shown that the proposed detectors do exploit the contributions from all subsystems to an almost optimal extent. This can be investigated by looking at the association efficiency of hits in a subdetector to the track they are caused by.

The global track search and ambiguity resolving algorithms that are performed during the track reconstruction process are designed to check for subdetectors that do not yet contribute to a track candidate, and attempts are made to add the missing hits. This is especially important in the case of the CCD vertex detector, where the first two layers are not used in the initial local track search. It turns out that in $d\bar{d}$ events 94.9% and 94.3% of all hits on CCD layers 1 and 2, respectively, are correctly merged into the global track candidate. Despite the enormous background level on these layers, only 5.1% and 0.9% of all tracks pick up wrong hits on layer 1 and 2, respectively.

Differences between local track search efficiency and association efficiency are caused by two competing effects: A small fraction of hits or track elements is usually lost due to merging inefficiencies. On the other hand, additional hits are included during the global track search. In the case of good local track search performance, both numbers are expected to be about equal. For example, the APS option silicon detector system reconstructs 97.4% of all tracks traversing it in $d\bar{d}$ events correctly. 97.5% of all global track candidates include correct silicon detector information. A slightly different situation is evident in the case of the CCD track search: Whereas the local CCD track search reconstructs only 92.4% of all tracks passing the silicon detectors, in the end 96.7% of those tracks are correctly reconstructed and include silicon detector information (see Figure 7.12).

For almost all considered scenarios, the association efficiencies for silicon hits and TPC track elements are very close to the local pattern recognition efficiencies, with the exception of the two innermost CCD layers, where no local pattern recognition is performed, as described above. The reason for these two figure of merits being close together is that the merging of the local track search result works with only small inefficiencies, and on the other hand the performance of the local track searches is good enough to leave not much room for improvement during the later reconstruction phases. The only case which is therefore to be mentioned explicitly here, in addition to the examples given above, is the inclusion of FCH track candidates into

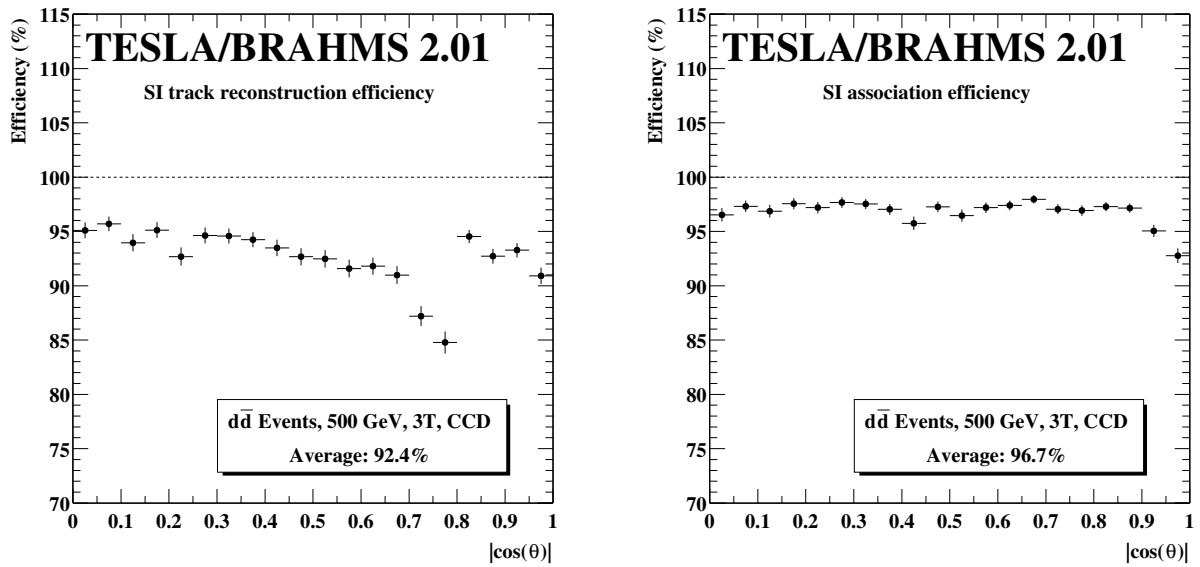

Figure 7.12: *Local silicon (CCD option) track reconstruction efficiency over* $\cos(\theta)$*, with full background simulation, for the* $\mathrm{d\bar{d}}$ *reference sample (left). The right plot shows the global efficiency for the silicon detector system, or the efficiency to associate hits from the silicon detector systems correctly to the tracks that traverse this detector. The fact that the association efficiency is higher than the local track reconstruction efficiency over essentially the full angular range shows the impact of improving the local track search during the global track search and ambiguity resolving phase.*

global tracks (see Figure 7.13). The local FCH track is not improved during the global track search, and therefore the local track reconstruction efficiency represents an upper boundary for the association efficiency; only tracks that are found locally in the FCH can include FCH information. The association efficiency has been found to be about 7% lower than the local track reconstruction efficiency, i.e. 7% of all reconstructed FCH tracks are not successfully merged to global track candidates. This reflects the difficult situation caused by a large amount of material in the TPC endcaps between FCH and all other parts of a track. The fraction of fake associations is however only 0.6%.

7.2.5 Momentum, Vertex, and Direction Resolutions

The realistic track reconstruction package described in this chapter was used by S.M. Xella-Hansen and K. Mönig to study whether the design criteria imposed on the tracking detector system can be fulfilled. A transverse momentum resolution of $\delta(\frac{1}{p_t}) \leq 5 \times 10^{-5}(\mathrm{GeV/c})^{-1}$ is required for physics analysis [125]. Figure 7.14 shows that this criterion can be met, and that a good momentum resolution is maintained over a large angular range.

An impact parameter resolution of $\frac{5\mu\mathrm{m} \oplus 10\mu\mathrm{m\ GeV/c}}{p \sin(3/2\Theta)}$ [125] is mandatory for b and c tagging and separation with sufficient quality. The actual performance of the CCD vertex detector simulation is measured to be $\frac{4.2\mu\mathrm{m} \oplus 4.00\mu\mathrm{m\ GeV/c}}{p \sin(3/2\Theta)}$ [143] (see Figure 7.15).

For angles close to the beam pipe, a major requirement is given by the desire to measure Bhabha acollinearity, which needs precise measurement of the polar angle θ. $\delta_\theta < 50\mu$rad down to $\theta \approx 7^\circ$ for muons with momentum above 10 GeV/c has been set as aim [125]. The distribution plotted in figure 7.16 shows that this can be achieved.

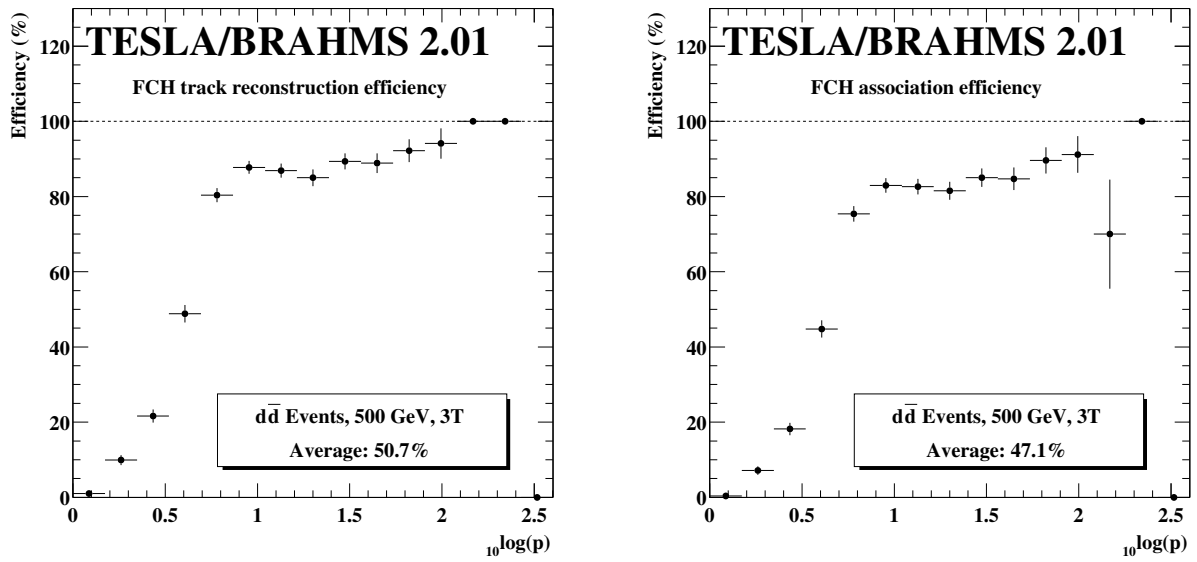

Figure 7.13: *Local FCH track reconstruction efficiency over track momentum, with full background simulation, for the* $\mathrm{d\bar{d}}$ *reference sample (left). The right plot shows the global efficiency for the FCH, or the efficiency to associate track candidates from the FCH correctly to reconstructed global track candidates. Merging inefficiencies of about 7% are visible.*

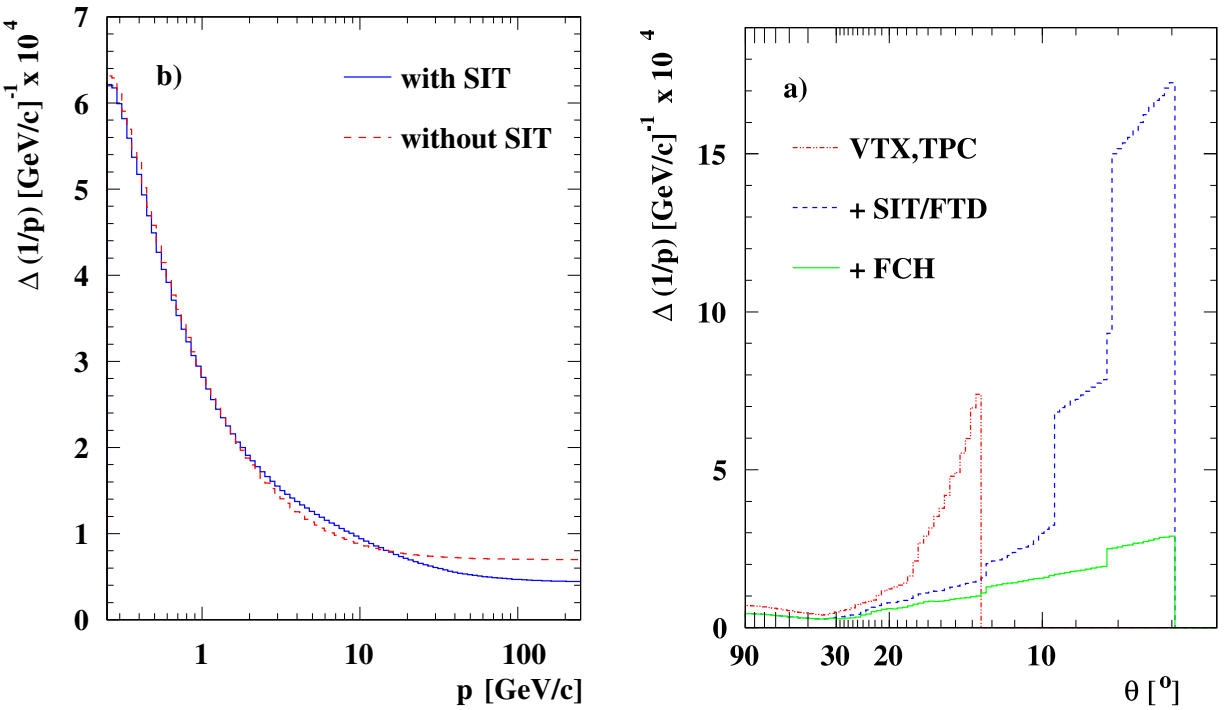

Figure 7.14: *Momentum resolution as a function of the momentum for tracks perpendicular to the beam axis (left). Momentum resolution for* 250 GeV/c *muons as a function of the polar angle (right). These figures are taken from Ref. [125].*

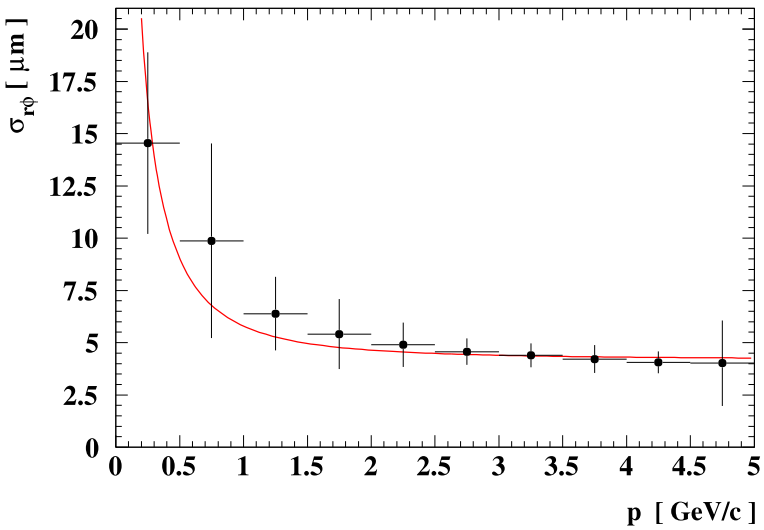

Figure 7.15: *Impact parameter resolution over momentum* ($\theta = 90°$) *as achieved with the CCD vertex detector option in the simulation framework described in this chapter. The fit to the distribution results to* $\frac{4.2\mu\text{m} \oplus 4.00\mu\text{m GeV/c}}{p \sin(3/2\Theta)}$. *This figure is taken from Ref. [143].*

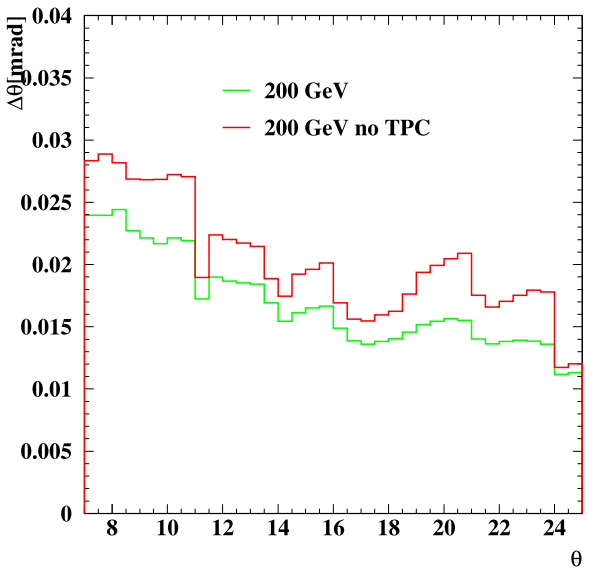

Figure 7.16: *Polar angle resolution for* 200 GeV/c *muons as a function of the polar angle. This figure is taken from Ref. [125].*

7.3 Summary

A realistic track reconstruction package is compiled that operates on a full simulation of a detector for the TESLA linear collider, with only minor deviations from the detector design brought forward in the technical design report [125]. The performance of the detector is evaluated with background in all detectors and pessimistic assumptions on properties of events to be reconstructed with this detector. It is shown that in all investigated scenarios the detector clearly fulfils all design criteria.

Of special interest is the comparison of the performance of the APS and CCD vertex detector options. Under realistic assumptions on material, resolution, background rate, and readout technology, it is shown that both options provide very good pattern recognition capabilities and fulfil the performance goals set by the expected physics tasks at a next generation linear collider.

Chapter 8

Physics Capabilities of a TESLA Detector

Both OPAL measurements presented in this thesis could profit from increased statistics, but even more from a detector with improved momentum and energy resolution. The tools presented in the previous chapter provide the environment for a realistic estimation of the possible improvements at the TESLA linear collider. It is by no means intended to repeat the OPAL analyses in full detail on the simulated TESLA detector; only critical points will be addressed here. The prospects for an improved investigation of b quark hadronisation are represented by a study of B hadron energy resolution at TESLA. The achievable B hadron energy resolution is of course very interesting beyond the scope of a hadronisation study. The analysis of excited D mesons at OPAL is contrasted with a $b \to D_J^{(*)0}$ study for TESLA in this chapter.

The studies in this chapter are performed in the GigaZ framework, albeit with only a fraction of the expected sample size. However, both studies can as well be performed in high energy runs, although the performance might be slightly different due to the energy dependence of mass and energy resolution.

Due to CPU constraints, both analyses presented here are performed with the parametric detector simulation SIMDET [131]. Detailed studies involving the GEANT-based simulation program BRAHMS are foreseen. However, the essential tracking features like energy- and angular dependence of the track reconstruction efficiency are well modelled in SIMDET according to BRAHMS results. The results presented here are therefore generally reliable.

8.1 B Hadron Energy Reconstruction at TESLA

The B hadron energy reconstruction presented in Chapter 4 is based on more than a decade of experience with the OPAL detector. Information from most subdetectors and assumptions on the underlying physics are gathered to obtain an estimate of the B hadron energy with approximately 2.4 GeV resolution. Still, the SLD collaboration achieves, despite a much smaller data sample and despite basing the full energy reconstruction only on tracking information with special emphasis on vertex detector information, a measurement of the mean scaled energy of B hadrons with only marginally larger errors [98]. This is essentially due to the fact that SLD can maintain a good relative energy resolution over the full x_{E} range, whereas the resolution at OPAL decreases significantly for smaller B hadron energies (see Figure 4.3).

The most significant advantage of SLD is the small SLC beam spot in combination with their precise knowledge of the position of B hadron decay vertices in space, made possible by

a CCD vertex detector of excellent spatial resolution. The precise determination of the vertex position in combination with measurement of the momentum sum of tracks associated with the vertex allows, in a novel approach described below, to obtain a very good estimate of the B hadron energy without the need for external constraints. The proposed TESLA detector will include a vertex detector of even better performance, and with a very detailed simulation of the TESLA tracking system available already now, all tools are in place to estimate the B hadron energy resolution achievable with the TESLA detector using the same method as SLD. Further improvements will certainly be possible if calorimeter information is taken into account, and therefore the study presented here is to be regarded as a mere lower limit of the expected performance. The analysis described here is very similar to the original analysis presented by SLD [98], with only a few selection cuts adapted to the TESLA detector environment.

8.1.1 Selection of B Decay Vertices

A sample of 10 million hadronic $e^+e^- \to Z/\gamma^* \to q\overline{q}$ reactions at a centre-of-mass energy of 91.2 GeV was generated with the Pythia 6.136 generator [21] and was passed through the parametric TESLA detector simulation program SIMDET 4.01 [131]. The beam energy spectrum and beam-related background were simulated by CIRCE 1.31 [144]. All events are forced into a two-jet topology by a Durham jet finding algorithm [86]. In order to ensure good momentum and impact parameter resolution for all B decay tracks, the thrust axis is required to point to the barrel part of the detector, $|cos\theta_{thrust}| < 0.85$. Here the longer barrel detector compared to SLD is fully exploited, where a cut on the cosine of the thrust polar angle is imposed at 0.71.

Secondary vertices are reconstructed in each hemisphere using the topological vertex finder ZVTOP [145]. This algorithm represents charged particle trajectories as Gaussian tubes of enhanced vertex probability in three-dimensional space. The position in space and track parameter uncertainty is taken into account while superposing the vertex probability distributions of all tracks. Maxima in this total probability distribution are then taken as seed vertex positions. Only tracks with transverse impact parameter with respect to the interaction point of $|d_0| < 3$ mm with an error of less than 250 μm, and longitudinal impact parameter of $|z_0| < 10$ cm are taken into account. The intention of these cuts is to remove cosmic and off-momentum beam background, which are both not simulated in SIMDET. The cuts are nevertheless used in order to achieve a realistic estimate of the reconstruction efficiency. A minimal transverse momentum of 150 MeV/c is required for each track; in the region below 150 MeV/c, the reconstruction efficiency is essentially zero, and track candidates have a high probability of being noise (see Chapter 7).

Only seed vertices with a decay length from the interaction point of between 1 and 23 mm are retained for further analysis. The lower boundary rejects fake vertices with tracks which should have been assigned to the primary vertex. The upper limit is used to reduce the contamination of decay vertices of long-lived secondary particles like K^0_S. The latter contribution is also reduced by removing all outermost vertices in a hemisphere with two tracks and an invariant mass between 0.47 and 0.53 GeV/c^2, assuming the pion mass for both attached particles.

In a second step of the vertex reconstruction, additional tracks are attached to the remaining seed vertices. All tracks are considered that fulfil less stringent track quality criteria than those for the seed vertices; the $|d_0|$ range is extended to 5 cm without any requirement on the error. All other track quality cuts remain the same. The distance of closest approach of the candidate track to the axis between primary and seed vertex has to be less than 1 mm, and the point of closest approach on the vertex axis has to be separated from the interaction point by more than

30% and less than 250% of the seed vertex decay length in order to have the track attached to the seed vertex.

8.1.2 Vertex Mass b Tag

The existence of a secondary vertex fulfilling the above requirements is a good tag criterion for the decay of a heavy quark in the respective hemisphere. But still only about 70% of all hemispheres with at least one reconstructed non-primary vertex are in $b\overline{b}$ events; $c\overline{c}$ events form almost the complete remainder. An improvement of the $b\overline{b}$ purity can be achieved by a simple vertex mass tag. The vertex mass M_{ch} is defined as the invariant mass of the system of all tracks associated with the b decay vertex. The B decay vertex is assumed to be the outermost vertex. In hemispheres with more than one non-primary vertex, one might assume that the outermost vertex is caused by decay of the secondary charm quark in a b hemisphere. However, Monte Carlo studies show that, with the track attachment criteria described above, even in this case most B decay tracks are attached to the outermost vertex. 92.4% of all reconstructed B decay tracks (including tracks from subsequent charm and strange decays) are attached to this vertex, and 99.1% of all attached tracks are B decay products. SLD sees an efficiency 91.9%, and a purity of 98.0%.

The average of the vertex mass M_{ch} of B hadron decay vertices is larger than that of secondary vertices in charm or light quark hemispheres. A cut on the vertex mass can therefore be used to select b hemispheres. A better efficiency and purity can be achieved by looking at the P_t corrected vertex mass M_{P_t}, the calculation of which will be described in the following.

In the rest frame of a decaying B hadron, the B mass can be written as:

$$M_{\mathrm{B}} = E_{\mathrm{B}}^{(rest)} = E_0^{(rest)} + E_{ch}^{(rest)} = \sqrt{M_0^2 + P_{0,t}^2 + P_{0,l}^{(rest)2}} + \sqrt{M_{ch}^2 + P_{ch,t}^2 + P_{ch,l}^{(rest)2}} \tag{8.1}$$

Momentum conservation requires $|P_{ch,t}| = |P_{0,t}| = P_t$, and thus:

$$M_{\mathrm{B}} = \sqrt{M_0^2 + P_t^2 + P_{0,l}^{(rest)2}} + \sqrt{M_{ch}^2 + P_t^2 + P_{ch,l}^{(rest)2}} \tag{8.2}$$

In the B rest frame, $P_{ch,l}^{(rest)} = -P_{0,l}^{(rest)}$. M_0, $P_{0,l}^{(rest)}$, and thus $P_{ch,l}^{(rest)}$, are unknown. (The charged longitudinal momentum in the laboratory frame $P_{ch,l}^{(lab)}$ is of course measurable, but due to missing information on neutral particles, the B rest frame and thus the transformation of the longitudinal momentum into the B rest frame are not known.) Therefore one obtains a lower limit for M_{B} by setting all unknown squares to zero:

$$M_{\mathrm{B}} \geq \sqrt{P_t^2} + \sqrt{M_{ch}^2 + P_t^2} = \sqrt{M_{ch}^2 + P_t^2} + |P_t| =: M_{P_t} \tag{8.3}$$

P_t is obtained as follows: The charged momentum $P_{ch}^{(lab)}$ is the sum of all momenta of tracks associated to the vertex. $P_t = P_{ch,t}^{(lab)}$ is the component perpendicular to the vertex flight direction. This transverse momentum component is Lorentz-invariant under transformation into the B rest frame, because this is a transformation along the B flight direction. The charged mass is calculated under the assumption that all particles are pions.

A further improvement in a separation of B and non-B vertices can be achieved by taking into account that the B flight direction is not measured with unlimited precision. Varying both primary and secondary vertex within their 1σ error ellipses will result in a variation of P_t. Using the minimal value for P_t in the vertex mass calculation gives a stable and reliable lower limit for

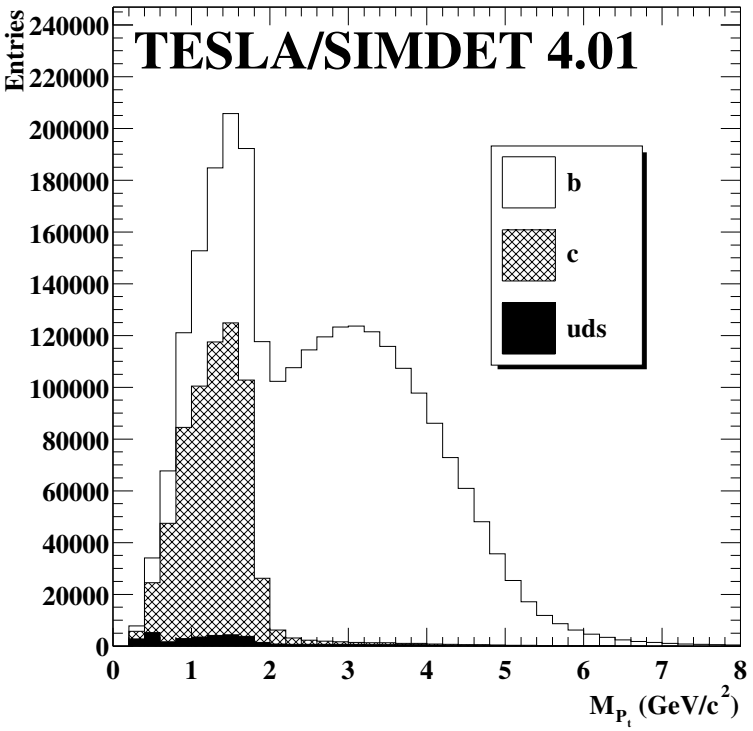

Figure 8.1: *P_t-corrected vertex mass distribution with minimised P_t for one million hadronic* Z *decays.*

the mass of the decaying hadron. Non-B vertices tend to have lower P_t-corrected vertex masses than B vertices. The distribution of the P_t-corrected vertex mass with minimised P_t is shown in Figure 8.1. For the selection of B vertices, $M_{P_t} > 2$ GeV$/c^2$ is required. Vertices with P_t-corrected vertex mass larger than twice the uncorrected vertex mass tend to be of poor quality and are rejected. The resulting sample of event hemispheres consists of 98.8% b hemispheres (SLD: 98.2%). The efficiency to reconstruct a B hadron using this analysis is 34.4%, compared to 27.3% achieved by SLD[1]. A large fraction of the efficiency increase is simply due to the longer barrel part of the TESLA detector.

8.1.3 B Hadron Energy Reconstruction

Only about half of the energy of a decaying B hadron ends up in charged long-lived particles; only slightly more than 90% of these charged particles are assigned to the reconstructed B decay vertex. The part of the B hadron energy carried by these particles ("charged energy") can be reconstructed easily and with good precision by adding up the energy contribution of each track assuming a pion rest mass. The missing (or "neutral") energy is unknown, since calorimeter information is not used for this analysis. However, from the comparison of vertex momentum (sum of momenta of attached tracks) and B hadron flight direction (vector from primary vertex to seed vertex position), an upper limit M_{0max} on the missing mass M_0 can be calculated, which then constrains the B energy. This method relies on a good resolution of the B hadron flight direction, which was not good enough at LEP, but is very well measured at SLD and the TESLA detector, due to the small beam-spots and the high-resolution vertex

[1]The efficiency quoted by SLD is 43.6%, however, this is normalised to the number of B hadrons after event selection cuts like the cut on the thrust axis direction. The SLD efficiency expressed with respect to all B hadrons in the Monte Carlo is 27.3%.

detectors.

The B hadron energy in the laboratory frame $E_{\mathrm{B}}^{(lab)}$ is the sum of charged energy $E_{ch}^{(lab)}$ and neutral energy $E_0^{(lab)}$. $E_{ch}^{(lab)}$ is easily calculated, and $E_0^{(lab)}$ can be expressed as

$$E_0^{(lab)} = M_0^2 + P_t^2 + P_{0,l}^{(lab)2} \ . \tag{8.4}$$

As explained above, the transverse momentum of the neutral particles has to balance the charged contribution, and therefore the neutral transverse momentum is known from the charged tracks attached to the vertex. Both longitudinal momentum of the neutral particles in the laboratory frame, $P_{0,l}^{(lab)}$, and the neutral mass, M_0, are not known. The following inequality can be derived from Equation 8.3 by setting the unknown B rest frame longitudinal momenta to their minimum value of zero:

$$\sqrt{M_{ch}^2 + P_t^2} + \sqrt{M_0^2 + P_t^2} \leq M_{\mathrm{B}} \tag{8.5}$$

If M_{B} is fixed to the world average B meson mass [2], Equation 8.5 can be interpreted as a constraint on M_0:

$$M_0^2 \leq M_{0max}^2 := M_{\mathrm{B}}^2 - 2M_{\mathrm{B}}\sqrt{M_{ch}^2 + P_t^2} + M_{ch}^2 \tag{8.6}$$

Since $M_0 \geq 0$, M_0 is bounded from both sides and is well constrained especially for small M_{0max}. Monte Carlo studies performed by SLD [98] show that for true B decay vertices, M_0 peaks sharply at M_{0max}, and thus M_{0max} is taken as estimator for M_0. Figure 8.2 shows the M_{0max}^2 distribution obtained in simulated hadronic events at TESLA. The average M_{0max}^2 coincides approximately with the square of half the B meson mass, which is expected given that about half of the particles produced in B hadron decays are neutral. A tail of negative values of M_{0max}^2 is observed, the contributions to which mainly come from poorly reconstructed vertices.

With M_0 estimated following the above consideration, only $P_{0,l}^{(lab)}$ remains unknown. It can be eliminated from the calculation of E_{B} by imposing the additional constraint

$$E_{\mathrm{B}}^2 = M_{\mathrm{B}}^2 + P_{\mathrm{B}}^{(lab)2} \ , \quad P_{\mathrm{B}}^{(lab)} = P_{ch,l}^{(lab)} + P_{0,l}^{(lab)} \ . \tag{8.7}$$

This constraint can be solved for $P_{0,l}^{(lab)}$ [146]:

$$P_{0,l}^{(lab)} = \frac{M_{\mathrm{B}}^2 - (M_{ch}^2 + P_t^2) - (M_0^2 + P_t^2)}{2(M_{ch}^2 + P_t^2)} P_{ch,l}^{(lab)} \tag{8.8}$$

Again, the average B meson mass is used for M_{B}. Thus all ingredients for the calculation of an estimator for the laboratory frame energy of a B hadron are available. The energy resolution of this estimator is further improved by requiring that the upper limit of the squared neutral mass, M_{0max}^2, be larger than -1. This rejects mostly poorly reconstructed vertices. B hadrons with a large fraction of neutral energy are characterised by a large value of M_{0max}^2, and therefore M_{0max}^2 is required to be below an energy-dependent upper limit. The energy dependence was chosen by SLD to achieve an almost energy-independent efficiency. The same parametrisation, albeit with different parameters, is used in this thesis:

$$M_{0max}^2 < 0.9\{1.1 + 0.004\ \mathrm{GeV}^{-1}(E_{beam} - E_{\mathrm{B}}^{rec}) + 4.7e^{-(E_{\mathrm{B}}^{rec} - 5.5\ \mathrm{GeV})/5\ \mathrm{GeV}}\}^2 \tag{8.9}$$

In addition, all vertices are required to have at least three tracks attached with $|d_0/\Delta d_0| > 2$, which improves the B flight direction resolution. After all cuts, the B hadron reconstruction

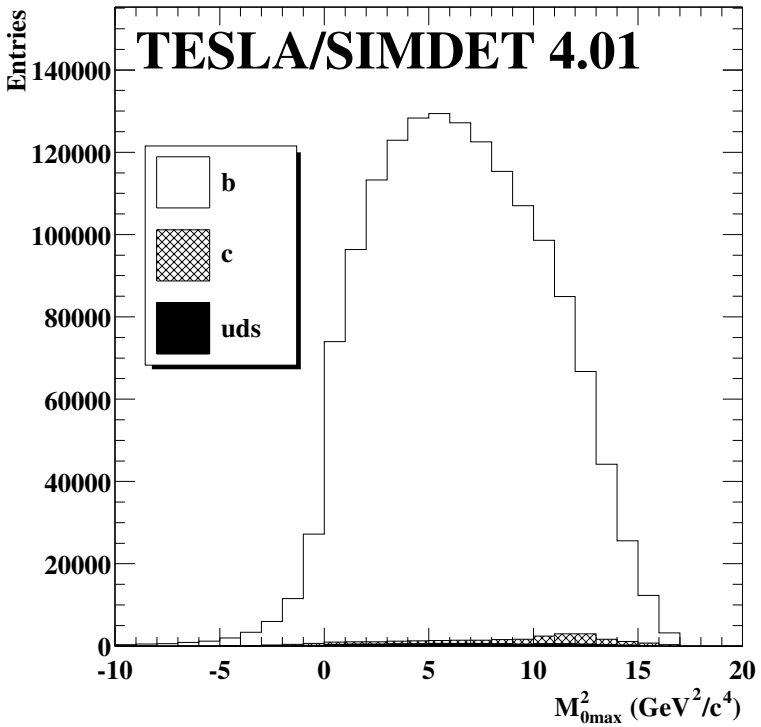

Figure 8.2: *Square of upper limit on missing mass.*

efficiency is 2.78%, compared to 2.61% for SLD[2]. Part of the initial efficiency advantage of the TESLA analysis is used up by the different tuning of the M_{0max} cut to achieve a better energy resolution. With this cut a similarly flat energy dependence of the reconstruction efficiency is achieved as SLD. It is shown in Figure 8.3.

The energy resolution achieved with the TESLA detector is found to be 9.1% (SLD: 10%) in the core Gaussian of a two-Gaussian fit. The resolution in the tail, which contains 17.7% (SLD: 16.4%), is found to be 22.1% (SLD: 21.2%). Similar to what was observed by SLD, the core resolution is almost constant over the full energy range. The tail resolution increases towards lower energies at SLD, but is kept almost constant in the analysis presented here (see Figure 8.4).

8.1.4 Discussion

The novel approach taken by SLD to reconstruct weakly decaying B hadrons and their energy is proven to be viable also for the TESLA detector. The B hadron energy resolution could not be improved significantly; at the level of performance of both SLD and TESLA CCD vertex detectors, it is obviously dominated completely by intrinsic limits of the method, not so much by the detector resolution. Still, an improvement in efficiency of up to 20% compared to SLD can be achieved with the TESLA detector, mainly due to its longer barrel part. The working point chosen for the analysis presented here makes use of the additional efficiency margin to improve the energy resolution by slightly more tight selection criteria. Any B hadron reconstruction at TESLA will further profit from the much larger luminosity. In addition, it has to be pointed out

[2]Again, SLD quotes an efficiency of 4.17% normalised to the number of B hadrons in the sample after event selection cuts. The number used for the comparison with the analysis presented in this thesis has been re-calculated to refer to all B hadrons in the initial sample.

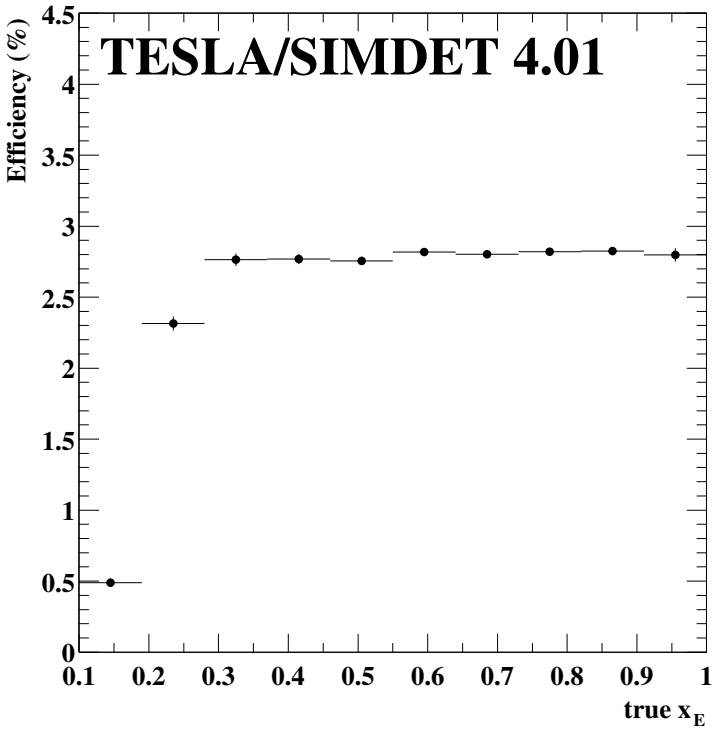

Figure 8.3: *Energy dependence of the* B *hadron reconstruction efficiency.*

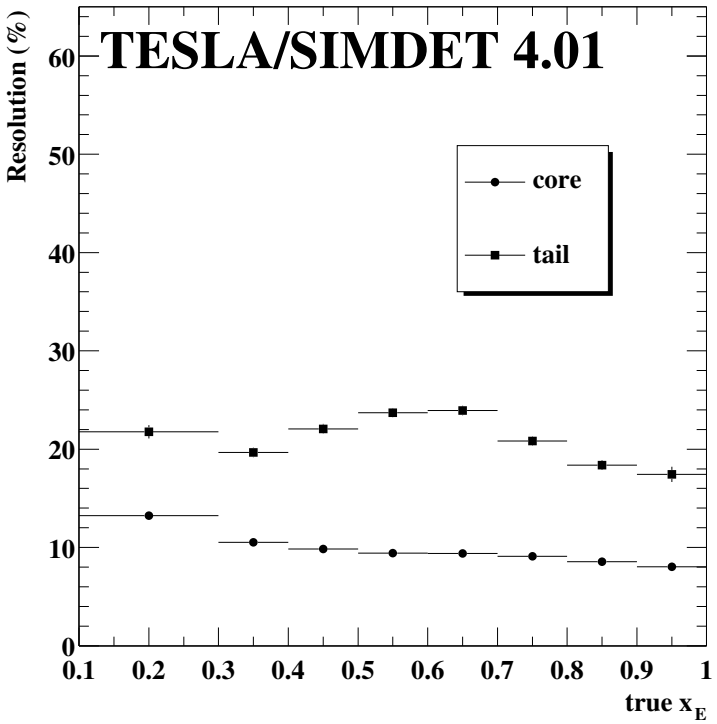

Figure 8.4: *Energy dependence of the relative energy resolution, obtained from a two-Gaussian fit. The widths of both core and tail Gaussian are shown in this plot.*

that possible future B hadron reconstruction will most likely also take calorimeter information into account to find better constraints for the neutral part of the B hadron energy than possible with the simple approach used by SLD. Further improvements in resolution and efficiency are therefore to be expected.

Another, if not the most important issue of the analysis presented in this section is the proof that all tools for sophisticated vertex analyses with the simulated TESLA detector are in place, and that they perform as expected. This adds to the reliability and credibility of analyses performed for TESLA. And although the motivation for the study presented here was to evaluate the prospects for future measurements of the B hadron energy distribution, its scope is much wider: A reliable and performant B hadron reconstruction is of central importance for many other fields in the rich physics program of a linear e^+e^- collider, like for example Higgs and top quark physics.

8.2 Excited D Mesons at TESLA

One conclusion from Chapter 5 is that the reconstruction of excited D mesons at OPAL suffers from large background and insufficient mass resolution. Especially the reconstruction of D resonances in $b\overline{b}$ events is difficult. In these events, D mesons are produced in the decay of B hadrons, and therefore their average energy is lower than in the primary production of D mesons in $c\overline{c}$ events. Due to their lower energy in combination with their decay into a comparatively large number of particles due to cascade decays, the combinatorial background from low energy tracks produced during hadronisation is large. An especially problematic case is the reconstruction of the orbital excitations $D_J^{(*)}$. The two narrow states D_1 and D_2^* have a mass difference in the same order as their intrinsic width. Additional contributions to the apparent width by the detector resolution tend to smear out the double peak structure (see e.g. Figures 5.7, 5.9). The broad peak of the combinatorial background, and possibly contributions of the broad $D_J^{(*)}$ doublet contribute to the difficulty to establish a clean signal, leading to the problems encountered and discussed in Chapter 5.

This section is dedicated to a reconstruction of the two narrow $D_J^{(*)0}$ states with the proposed TESLA detector. The improved mass resolution of the TESLA detector is exploited to achieve a clearer separation of the two resonances, but also to achieve a lower background level by imposing tighter cuts on the mass of D^{*+} and D^0 mesons in the $D_J^{(*)0}$ decay chain. The most important improvement with respect to typical LEP analyses is achieved by making use of the excellent vertex reconstruction possible with the TESLA detector.

8.2.1 Event and Track Selection

The Pythia 6.136 event generator [21] was used to simulate 10 million $e^+e^- \to Z/\gamma^* \to q\overline{q}$ reactions at a centre-of-mass energy of 91.2 GeV. The masses of the narrow $D_J^{(*)0}$ mesons were set to current world average values [2] during the creation of the Monte Carlo sample. A D_1^0 production rate in b quark decays of 5.0% and a D_2^{*0} rate of 4.7% are assumed, corresponding to the production rates published by OPAL [107], which were also used to create Figure 5.7. The simulation of the TESLA detector was done with the parametric detector simulation program SIMDET [131]. The beam energy spectrum and beam-related background were simulated by CIRCE 1.31 [144].

Secondary vertices are reconstructed exactly as in the previous section: All events are forced into a two-jet topology with a Durham jet finder [86], and the ZVTOP vertex finder [145] was

applied to each hemisphere in events with a thrust axis with $|cos\theta_{thrust}| < 0.85$. No further b tag is applied, because it is found that the $D_J^{(*)0}$ candidates found with the method described in the following are almost exclusively created in B hadron decays.

Only tracks attached to the outermost secondary vertex are considered for the construction of $D_J^{(*)0}$ candidates. Due to the high purity of track assignments to B candidate vertices this leads to a significant suppression of combinatorial background.

8.2.2 Reconstruction of $D_J^{(*)0}$ Candidates

$D_J^{(*)0}$ mesons are reconstructed in their decay mode

$$\begin{aligned} D_J^{(*)0} \rightarrow & D^{*+}\pi^- \\ & \hookrightarrow D^0\pi^+ \\ & \quad \hookrightarrow K^-\pi^+ \end{aligned}$$

With the $D_J^{(*)0}$ production rates given above, and the decay branching ratios $BR(D_1^0 \rightarrow D^{*+}\pi^-) = 0.67$, $BR(D_2^{*0} \rightarrow D^{*+}\pi^-) = 0.21$, $BR(D^{*+} \rightarrow D^0\pi^+) = 0.677$, and $BR(D^0 \rightarrow K^-\pi^+) = 0.0383$ [2], approximately 1100 of these decay chains are expected per 10^6 $b\overline{b}$ events.

All pairs of oppositely charged vertex tracks with momentum above 1 GeV/c and with a combined invariant mass in a range of ± 15 MeV/c^2 around the nominal D^0 mass of 1.8645 GeV/c^2 are taken as $D^0 \rightarrow K^-\pi^+$ candidates. The invariant mass is calculated assuming pion mass for the pion candidate, and kaon mass for the kaon candidate. The energy of the D^0 candidate is required to be at least 20% of the beam energy. Analyses at LEP usually exploit particle identification capabilities to enrich the kaon candidate tracks in true kaons, however, the D^0 mass distribution obtained here (Figure 8.5a) shows clearly that this is not necessary in the analysis presented here. Also a cut on the kaon decay helicity angle, which is usually applied in LEP analyses like the one in Chapter 5, is not applied here.

Figure 8.5 shows only D^0 candidates for which suitable tracks are found to combine them to $D_J^{(*)0}$ candidates. Two conclusions can be drawn from this distribution: Any background left in the $D_J^{(*)0}$ reconstruction is not due to fake D^0 candidates, and the D^0 mass resolution obtained at TESLA is about a factor of four better than at LEP. A typical D^0 mass cut range, as also used in Chapter 5, is indicated by the full width of the histogram.

D^{*+} candidates are formed by combination of D^0 candidates with an additional vertex track with opposite charge with respect to the kaon candidate, and with momentum larger than 0.5 GeV/c. The mass difference of D^{*+} candidate and D^0 candidate, shown in Figure 8.5b, has a nominal value of 0.1454 GeV/c^2. D^{*+} candidates are accepted if the reconstructed mass difference lies within a mass window of 1 MeV/c^2 around the nominal value. Again, the plot shows candidates which are subsets of $D_J^{(*)0}$ candidates. Similar conclusions apply as above: The D^{*+} selection is essentially free of background. The mass resolution is about a factor of four better than at LEP. The full width of the histogram represents the cut range used in Chapter 5 and in many other LEP analyses.

Additional vertex tracks with opposite charge than the D^{*+} decay pion and a momentum above 1 GeV/c are combined with the D^{*+} candidates to form $D_J^{(*)0}$ candidates. $D_J^{(*)0}$ candidates are accepted if their energy is larger than 20% of the beam energy.

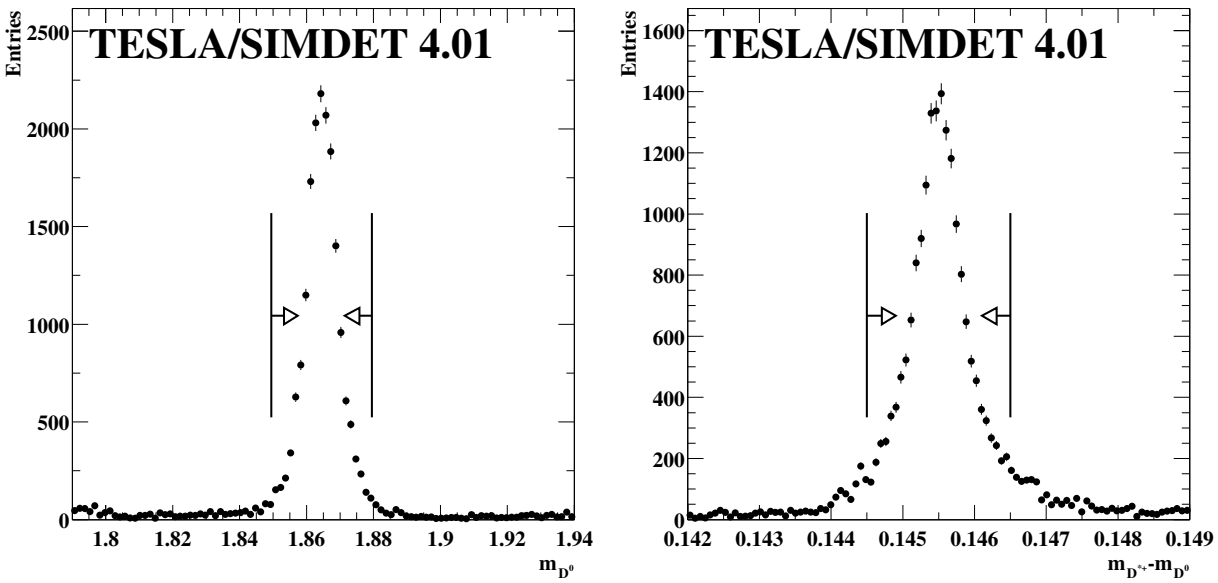

Figure 8.5: *Invariant mass of* D^0 *candidates (left). Distribution of mass difference of* D^{*+} *and* D^0 *candidates (right).*

The invariant mass distribution of $D_J^{(*)0}$ candidates is shown in Figure 8.6. The double-peak structure can clearly be resolved with the mass resolution expected for the TESLA detector. The observed width of the resonances is dominated by the intrinsic width of 19 MeV/c^2 (D_1^0) and 23 MeV/c^2 (D_2^{*0}). The detector mass resolution is measured with a double Gaussian fit, where the width of the narrower peak amounts to 1.3 MeV/c^2 (LEP: typically 6–7 MeV/c^2 [107, 66]), the width of the tail is 3.6 MeV/c^2. The reconstruction efficiency of $D_J^{(*)0}$ mesons in the investigated decay channel is 22%.

8.2.3 Discussion

The analysis presented in this section demonstrates that the inconclusive results in D meson spectroscopy obtained by the LEP experiments could be clarified by the proposed TESLA detector. Similar results might be obtained e.g. in the sector of excited B mesons, where the limitations of the LEP detectors led to similarly inconsistent results [147]. Improved reconstruction of excited D and B mesons is not only interesting for hadron spectroscopy itself, but could for example also support flavour oscillation analyses, where the pion emitted in the decay of orbitally excited resonances provides a tag for the initial (or production) flavour, as opposed to the flavour observed in the weak decay.

The $D_J^{(*)0}$ reconstruction described above is by far not optimal; one could for example introduce a distinction between tracks that are most likely attached to a secondary (B hadron decay) vertex, and tracks that are most likely attached to a tertiary (charmed hadron decay) vertex. This way one could possibly reduce the background of fake $D_J^{(*)0}$ decay pions. These are by far the dominant background source in this analysis, given that the D^0 and D^{*+} reconstructions are essentially free of background. However, the performance of the analysis as it is presented here is sufficient to demonstrate the nice prospects offered by the TESLA detector proposal.

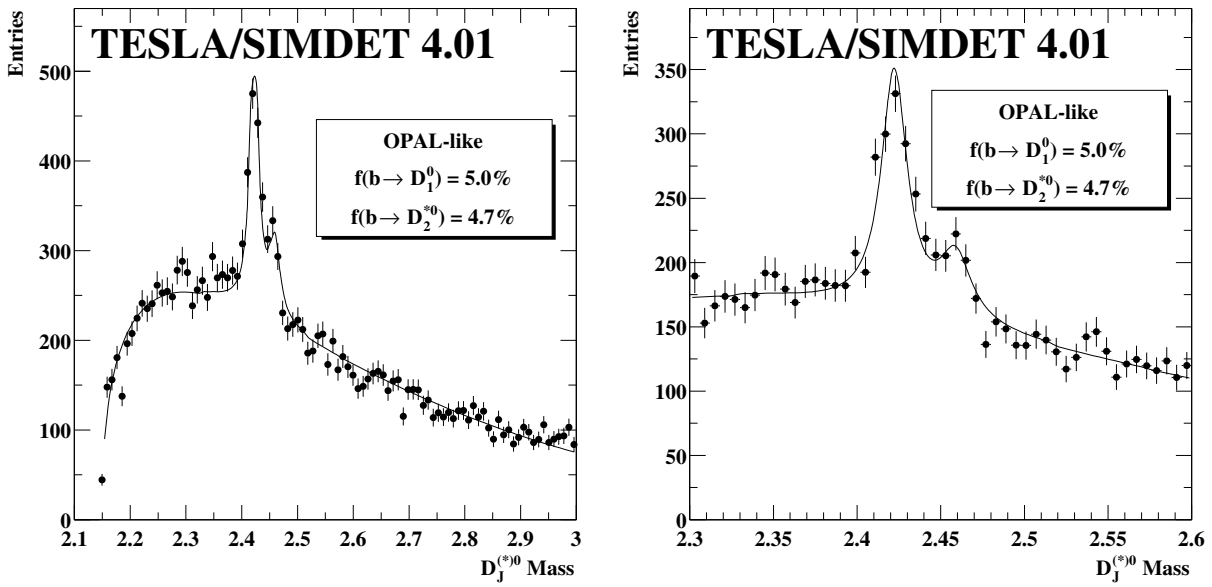

Figure 8.6: *Result of simple* $b \to D_J^{(*)0}$ *reconstruction at TESLA. Invariant mass distribution of* $D_J^{(*)0}$ *candidates (left), close-up view of the resonance structure (right). The* $D_J^{(*)0}$ *production rates are adjusted to the values published by OPAL [107]. The line represents a fit with the a background parametrisation according to Equation 5.1, plus a Breit-Wigner smeared by a Gaussian with width fixed to the detector resolution for each resonance.*

8.3 Summary

After an evaluation and discussion of the technical performance of the proposed TESLA detector in Chapter 7, the studies presented here provide insights into the resulting performance for actual analyses performed with the proposed detector. A B hadron energy reconstruction at a TESLA detector is performed using a method pioneered at SLD, and it it shown that this method has significant advantages compared to the much more complicated approach used in the OPAL analysis in Chapter 4. Furthermore, this study demonstrates, by giving reasonable improvements in comparison with SLD, that the simulated b tag and B hadron reconstruction performance leads to credible results.

A reconstruction of the narrow orbital excitations $D_J^{(*)0}$ of the D meson system, it is shown that the improved performance of the TESLA detector compared to the LEP experiments will help to resolve many not satisfactorily answered questions remaining in the LEP heritage. The $D_J^{(*)0}$ provide but one example to demonstrate that valuable experimental input can be expected for potential models of Heavy Quark Effective Theory, as discussed in Section 2.5 of this thesis. Further applications are possible, where the identification of the production flavour in oscillation studies is only one example.

Chapter 9

Conclusion

This thesis deals with aspects of quantum chromodynamics in e^+e^- annihilation experiments. The non-perturbative phase of the transition from isolated b quarks to hadrons is investigated at OPAL. A comparison of different hadronisation models leads to the conclusion that the string hadronisation model with fragmentation functions that are based on intrinsic symmetries of the problem (Bowler, Lund symmetric) provide the best description of the data. However, the parameters obtained for these fragmentation functions show a large spread over the OPAL data subsamples, and therefore the suspicion may be appropriate that the main advantage of these models is the larger number of fit parameters. However, of the one-parameter phenomenological approaches, the fragmentation function by Kartvelishvili et al. delivers also an acceptable description of the data. The measurement of the model-independent mean scaled energy of weakly decaying B hadrons leads to the most precise measurement of this quantity so far:

$$\langle x_{\mathrm{E}} \rangle = 0.7194 \pm 0.0016(stat)^{+0.0035}_{-0.0038}(syst)$$

This measurement could be improved significantly with a detector of better B hadron energy resolution for a better separation between different models. It is shown in this thesis that the proposed detector for the linear e^+e^- collider TESLA would indeed offer noticeable improvements.

Another difficult topic is the bound state problem of QCD. The confinement of quarks in hadrons leaves room for complicated hadron mass spectra caused by different excited states of the valence quarks in the hadron. Comparatively precise mass predictions are available for mesons containing a heavy quark, however the experimental verification of these spectra at LEP does not lead to definite results in all cases. An observation of the first radial excitation of the D^{*+} meson, the $\mathrm{D}^{*\prime+}$, was published by DELPHI, but a similar analysis performed at OPAL for this thesis can not confirm this observation, and an upper limit on the production rate of a narrow resonance in the vicinity of the DELPHI observation is obtained:

$$f(\mathrm{Z} \to \mathrm{D}^{*\prime\pm}(2629)) \times Br(\mathrm{D}^{*\prime+} \to \mathrm{D}^{*+}\pi^+\pi^-) < 3.1 \times 10^{-3} \quad (95\%\ \mathrm{C.L.})$$

Additional confusion was caused by the fact that the observation of the doublet of narrow orbital D excitations, the $\mathrm{D}_J^{(*)0}$ mesons, is difficult at LEP, at least as their production in $\mathrm{b\overline{b}}$ events is concerned. A possible discrepancy of a measurement performed in this thesis with a previous OPAL publication is investigated. The difference of the two measurements is traced back to changes in the OPAL analysis environment, possibly enlarged by statistical fluctuations due to the small correlation of the large combinatorial background of the two selections.

The difficulties with $b \to D_J^{(*)0}$ reconstruction at LEP motivated an analogue analysis for the TESLA detector. The TESLA $D_J^{(*)0}$ reconstruction is novel in the sense that it relies on the excellent secondary vertex reconstruction of the TESLA detector to select $D_J^{(*)0}$ decay candidate tracks exclusively from tracks identified as B hadron decay tracks by the vertex finder. The results, although not fully optimised, show that the improvements offered by the TESLA detector will resolve many of the open questions in hadron spectroscopy. This is especially important due to the fact that hardly any other collider than a linear e^+e^- collider will have access to the full spectrum of excited mesons in the foreseeable future.

Reliable and credible simulations of analyses with the TESLA detector can only be performed if the simulation of the detector and the methods to analyse data with the simulated detector are as realistic as possible. Realistic track reconstruction software for the GEANT-based TESLA detector simulation was developed in the context of this thesis, and the track reconstruction performance is evaluated. With this work, a sound foundation is laid for TESLA analyses relying on tracking information, like the ones presented in this thesis.

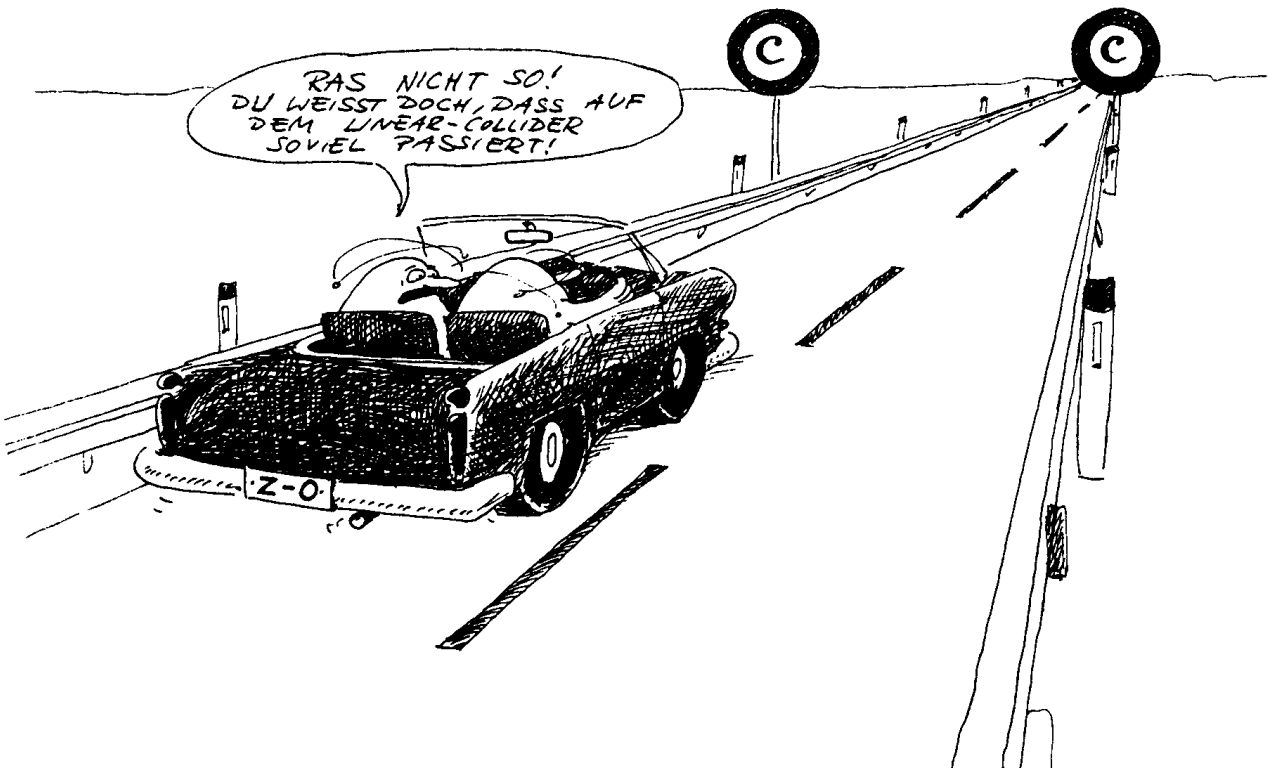

"Slow down! You should know how many things happen on the linear collider!"

from: Peter Evers, "Die wundersame Welt der Atomis", Wiley-VCH 2002. Printed with kind permission from Wiley-VCH.

Bibliography

[1] M. Gell-Mann, Phys. Lett. 8 (1964) 214;
G. Zweig, *An SU(3) Model for Strong Interaction Symmetry and its Breaking*,
CERN TH-401 and CERN TH-412.

[2] Particle Data Group, D.E. Groom et al., Eur. Phys. J. C15 (2000) 1.

[3] J.L. Rosner, *The Standard Model in 2001*, hep-ph/0108195.

[4] C.N. Yang, R.L. Mills, Phys. Rev. 96 (1954) 191.

[5] ALEPH, DELPHI, L3, and OPAL Collaborations, *LEP W-pair, Z-pair, and Single W Cross Section Results for the Summer 2001 Conferences*, LEPEWWG/XSEC/2001-03, OPAL TN702 (EPSHEP 2001, Budapest).

[6] J.R. Ellis, *Deep Hadronic Structure*, Les Houches Lecture 1976.

[7] S. Bethke, J. Phys. G26 (2000) R27.

[8] T. van Ritbergen, J.A.M. Vermaseren, S.A. Larin, Phys. Lett. B400 (1997) 379.

[9] M.G. Schmidt, C. Schubert, Phys. Rev. D53 (1996) 2150.

[10] H.D. Politzer, Phys. Rept. 14 (1974) 129.

[11] JADE and OPAL Collaborations, P. Pfeifenschneider et al., Eur. Phys. J. C17 (2000) 19.

[12] R.D. Kenway, *Lattice Field Theory*, hep-ph/0010219 (ICHEP 2000, Osaka).

[13] OPAL Collaboration, G. Abbiendi et al., Eur. Phys. J. C13 (2000) 553.

[14] J.R. Ellis, M.K. Gaillard, G.G. Ross, Nucl. Phys. B111 (1976) 253.

[15] L.W. Garland, T. Gehrmann, E.W.N. Glover, A. Koukoutsakis, E. Remiddi,
Nucl. Phys. B627 (2002) 107.

[16] K. Hagiwara, D. Zeppenfeld, Nucl. Phys. B313 (1989) 560.

[17] T. Sjöstrand, Comp. Phys. Comm. 82 (1994) 74.

[18] V.N. Gribov, L.N. Lipatov, Sov. J. Nucl. Phys. 15 (1972) 438;
V.N. Gribov, L.N. Lipatov, Sov. J. Nucl. Phys. 15 (1972) 675.

[19] G. Altarelli, G. Parisi, Nucl. Phys. B126 (1977) 298.

[20] C.F. von Weizsäcker, Z. Phys. 88 (1934) 612;
E.J. Williams, Phys. Rev. 45 (1934) 729.

[21] T. Sjöstrand et al., Comp. Phys. Comm. 135 (2001) 238.

[22] G. Marchesini et al., Comp. Phys. Comm. 67 (1992) 465;
G. Corcella et al., JHEP 0101 (2001) 010.

[23] B. Andersson, G. Gustafson, T. Sjöstrand, Nucl. Phys. B197 (1982) 45;
T. Meyer, Z. Phys. C12 (1982) 77.

[24] B. Andersson, G. Gustafson, T. Sjöstrand, Phys. Scripta 32 (1985) 574.

[25] A. Krzywicki, B. Petersson, Phys. Rev. D6 (1972) 924;
J. Finkelstein, R.D. Peccei, Phys. Rev. D6 (1972) 2606;
F. Niedermayer, Nucl. Phys. B79 (1974) 355;
A. Casher, J. Kogut, L. Susskind, Phys. Rev. D10 (1974) 732.

[26] R.D. Field, R.P. Feynman, Nucl. Phys. B136 (1978) 1.

[27] R.D. Field, R.P. Feynman, Phys. Rev. D15 (1977) 2590.

[28] R. Odorico, Comp. Phys. Comm. 72 (1992) 238.

[29] H. Baer, F.E. Paige, S.D. Protopopescu, X. Tata, *ISAJET 7.48 – A Monte Carlo Event Generator for pp, $\bar{p}p$, and e^+e^- Reactions*, hep-ph/0001086.

[30] D. Amati, G. Veneziano, Phys. Lett. B83 (1979) 87;
A. Bassetto, M. Ciafaloni, G. Marchesini, Nucl. Phys. B163 (1980) 477;
G. Marchesini, L. Trentadue, G. Veneziano, Nucl. Phys. B181 (1981) 335.

[31] R. Hagedorn, Nuovo Cim. Suppl. 3 (1965) 147;
S.C. Frautschi, Phys. Rev. D3 (1971) 2821.

[32] E.L. Berger, G.C. Fox, Phys. Lett. B47 (1973) 162;
C.J. Hamer, R.F. Peierls, Phys. Rev. D8 (1973) 1358.

[33] T.D. Gottschalk, Nucl. Phys. B239 (1984) 325;
T.D. Gottschalk, Nucl. Phys. B239 (1984) 349.

[34] B.R. Webber, Nucl. Phys. B238 (1984) 492.

[35] R.J. Hemingway, *An OPAL Tune of HERWIG 6.1 Using Z^0 Data*, OPAL TN652, 2000.

[36] K.G. Wilson, Phys. Rev. D10 (1974) 2445.

[37] M.G. Bowler, Z. Phys. C11 (1981) 169.

[38] X. Artru, G. Mennessier, Nucl. Phys. B70 (1974) 93.

[39] T.D. Gottschalk, D.A. Morris, Nucl. Phys. B288 (1987) 729.

[40] B. Andersson, G. Gustafson, C. Peterson, Z. Phys. C1 (1979) 105;
B. Andersson, G. Gustafson, G. Ingelman, T. Sjöstrand, Phys. Rept. 97 (1983) 31.

[41] A. Casher, H. Neuberger, S. Nussinov, Phys. Rev. D20 (1979) 179.

[42] C.D. Buchanan, S.B. Chun, Phys. Rev. Lett. 59 (1987) 1997;
C.D. Buchanan, S.B. Chun, Phys. Rept. 292 (1998) 239.

[43] B. Andersson, G. Gustafson, T. Sjöstrand, Z. Phys. C6 (1980) 235.

[44] M. Holder et al., Phys. Lett. B69 (1977) 377.

[45] J.D. Bjorken, Phys. Rev. D17 (1978) 171.

[46] C. Peterson et al., Phys. Rev. D27 (1983) 105.

[47] P.D.B. Collins, T.P. Spiller, J. Phys. G11 (1985) 1289.

[48] V.G. Kartvelishvili, A.K. Likhoded, V.A. Petrov, Phys. Lett. B78 (1978) 615.

[49] B. Andersson, G. Gustafson, B. Söderberg, Z. Phys. C20 (1983) 317.

[50] S.J. Brodsky, G.R. Farrar, Phys. Rev. Lett. 31 (1973) 1153;
D. Sivers, S.J. Brodsky, R. Blankenbecler, Phys. Rept. C23 (1976) 1.

[51] S.D. Drell, D.J. Levy, T.-M. Yan, Phys. Rev. D1 (1970) 1617;
V.N. Gribov, L.N. Lipatov, Sov. J. Nucl. Phys. 15 (1972) 675;
R. Gatto, P. Menotti, I. Vendramin, Phys. Rev. D7 (1973) 2524.

[52] P.D.B. Collins, T.P. Spiller, *A Model for Diffractive Heavy Flavour Production*,
Durham University DTP/84/22.

[53] I.G. Knowles, G.D. Lafferty, J. Phys. G23 (1997) 731.

[54] F. Ezawa, Nuovo Cim. A23 (1974) 271;
G.R. Farrar, J.D. Jackson, Phys. Rev. Lett. 35 (1975) 1416;
G.P. Lepage, S.J. Brodsky, Phys. Rev. D22 (1980) 2157.

[55] J. Kuti, V. Weisskopf, Phys. Rev. D4 (1971) 3418.

[56] P.V. Chliapnikov, V.G. Kartvelishvili, V.V. Kniazev, A.K. Likhoded,
Nucl. Phys. B148 (1979) 400.

[57] S. Filipponi, Y. Srivastava, Phys. Rev. D58 (1998) 016003.

[58] S. Drell, T.M. Yan, Phys. Rev. Lett. 24 (1970) 181;
G.B. West, Phys. Rev. Lett. 24 (1970) 1206.

[59] M.G. Bowler, Z. Phys. C22 (1984) 155.

[60] N. Isgur, M.B. Wise, Phys. Lett. B232 (1989) 113.

[61] E. Eichten, B. Hill, Phys. Lett. B234 (1990) 511.

[62] H. Georgi, Phys. Lett. B240 (1990) 447.

[63] M. Neubert, Phys. Rept. 245 (1994) 259;
T. Mannel, Rep. Prog. Phys. 60 (1997) 1113.

[64] D. Ebert, R.N. Faustov, V.O. Galkin, Phys. Rev. D57 (1998) 5663.

[65] CLEO Collaboration, S. Anderson et al., Nucl. Phys. A663–664 (2000) 647.

[66] DELPHI Collaboration, P. Abreu et al., Phys. Lett. B426 (1998) 231.

[67] R. Kokoski, N. Isgur, Phys. Rev. D35 (1987) 907; as quoted in [66].

[68] P.W. Higgs, Phys. Lett. 12 (1964) 132;
P.W. Higgs, Phys. Rev. Lett. 13 (1964) 508;
P.W. Higgs, Phys. Rev. 145 (1966) 1156;
F. Englert, R. Brout, Phys. Rev. Lett. 13 (1964) 321;
G.S. Guralnik, C.R. Hagen, T.W.B. Kibble, Phys. Rev. Lett. 13 (1964) 585;
T.W.B. Kibble, Phys. Rev. 155 (1967) 1554.

[69] ALEPH, DELPHI, L3, OPAL, and SLD Collaborations, *A Combination of Preliminary Electroweak Measurements and Constraints on the Standard Model*, hep-ex/0112021.

[70] ALEPH, DELPHI, L3, and OPAL Collaborations, *Search for the Standard Model Higgs Boson at LEP*, hep-ex/0107029 (EPSHEP 2001, Budapest).

[71] P. Schmüser, *Feynman-Graphen und Eichtheorien für Experimentalphysiker*, 2nd edition, Springer 1995.

[72] U. Amaldi, W. de Boer, H. Fürstenau, Phys. Lett. B260 (1991) 447.

[73] H.P. Nilles, Phys. Rept. 110 (1984) 1;
H.E. Haber, G.L. Kane, Phys. Rept. 117 (1985) 75.

[74] J. Ellis, *Supersymmetry for Alp Hikers*, hep-ph/0203114.

[75] R.D. Heuer, D. Miller, F. Richard, P.M. Zerwas (Editors), *TESLA Technical Design Report, Part III: Physics at an e^+e^- Linear Collider*, DESY-2001-011, ECFA-2001-209.

[76] OPAL Collaboration, K. Ahmet et al., Nucl. Instr. Meth. A305 (1991) 275;
OPAL Collaboration, P.P. Allport et al., Nucl. Instr. Meth. A324 (1993) 34;
OPAL Collaboration, P.P. Allport et al., Nucl. Instr. Meth. A346 (1994) 476;
M. Hauschild et al., Nucl. Instr. Meth. A314 (1992) 74;
O. Biebel et al., Nucl. Instr. Meth. A323 (1992) 169.

[77] J. Allison et al., Nucl. Instr. Meth. A317 (1991) 47.

[78] OPAL Collaboration, G. Abbiendi et al., Eur. Phys. J. C23 (2002) 437.

[79] OPAL Collaboration, G. Alexander et al., Z. Phys. C52 (1991) 175.

[80] ALEPH, CDF, DELPHI, L3, OPAL, and SLD Collaborations, *Combined Results on b-Hadron Production Rates and Decay Properties*, hep-ex/0112028.

[81] DELPHI Collaboration, P. Abreu et al., Phys. Lett. B345 (1995) 598;
ALEPH Collaboration, R. Barate et al., Phys. Lett. B425 (1998) 215;
L3 Collaboration, M. Acciarri et al., Phys. Lett. B465 (1999) 323.

[82] OPAL Collaboration, G. Alexander et al., Z. Phys. C66 (1995) 19.

[83] LEP/SLD Heavy Flavour Working Group, *Final Input Parameters for the LEP/SLD Heavy Flavour Analyses*, LEPHF/2001-01.

[84] OPAL Collaboration, G. Abbiendi et al., Eur. Phys. J. C18 (2001) 447.

[85] OPAL Collaboration, K. Ackerstaff et al., Z. Phys. C74 (1997) 413.

[86] N. Brown, W.J. Stirling, Phys. Lett. B252 (1990) 657;
S. Bethke, Z. Kunszt, D. Soper, W.J. Stirling, Nucl. Phys. B370 (1992) 310;
S. Catani et al., Phys. Lett. B269 (1991) 432;
N. Brown, W.J. Stirling, Z. Phys. C53 (1992) 629.

[87] OPAL Collaboration, K. Ackerstaff et al., Eur. Phys. J. C2 (1998) 213.

[88] OPAL Collaboration, G. Abbiendi et al., Eur. Phys. J. C7 (1999) 407.

[89] OPAL Collaboration, G. Abbiendi et al., Eur. Phys. J. C23 (2002) 397.

[90] OPAL Collaboration, R. Akers et al., Z. Phys. C63 (1994) 197.

[91] S. Yamashita, I. Nakamura, *LB160: Upgraded B-tagging for LEP2*, OPAL TN578, 1998.

[92] The neural networks were trained using JETNET 3:
C. Peterson, T. Rögnvaldsson and L. Lönnblad, Comp. Phys. Comm. 81 (1994) 185.

[93] OPAL Collaboration, G. Abbiendi et al., Eur. Phys. J. C8 (1999) 217.

[94] J. King, A. Martin, *A Study of b Quark Fragmentation into B^0 and B^+ Mesons*, OPAL TN288, 1995.

[95] T. Sjöstrand, *PYTHIA 5.7 and JETSET 7.4 Physics and Manual*, hep-ph/9508391.

[96] OPAL Collaboration, G. Alexander et al., Phys. Lett. B364 (1995) 93.

[97] OPAL Collaboration, M.Z. Akrawy et al., Z. Phys. C47 (1990) 505.

[98] SLD Collaboration, K. Abe et al., *Measurement of the b Quark Fragmentation Function in Z^0 Decays*, hep-ex/0202031, accepted by Phys. Rev. D.

[99] ALEPH Collaboration, A. Heister et al., Phys. Lett. B512 (2001) 30.

[100] V. Blobel, *The RUN Manual — Regularized Unfolding for High-Energy Physics Experiments*, DESY 84-118, OPAL TN361, 1996.

[101] A. Hocker, V. Kartvelishvili, Nucl. Instr. Meth. A372 (1996) 469.

[102] OPAL Collaboration, K. Ackerstaff et al., Eur. Phys. J. C1 (1998) 439.

[103] LEP Energy Working Group, R. Assmann et al., Phys. Lett. B307 (1993) 187;
LEP Energy Working Group, R. Assmann et al., Eur. Phys. J. C6 (1999) 187;
LEP Energy Working Group, R. Assmann et al., *Preliminary LEP Energy Calibration for 1997 Data*, CERN 1998;
LEP Energy Working Group, R. Assmann et al., *Evaluation of the LEP Centre-of-Mass Energy for Data Taken in 2000*, CERN 2001.

[104] OPAL Collaboration, G. Abbiendi et al., Eur. Phys. J. C13 (2000) 225.

[105] ALEPH Collaboration, D. Pallin, *Production of D_1 and D_2^* Mesons in Hadronic Z Decays*, ALEPH 98-047 CONF 98-021 (ICHEP 1998, Vancouver).

[106] DELPHI Collaboration, D. Bloch, R. Strub, *Narrow D^{**} Production in c and b Jets*, DELPHI 98-128 CONF 189 (ICHEP 1998, Vancouver).

[107] OPAL Collaboration, K. Ackerstaff et al., Z. Phys. C76 (1997) 425.

[108] D. Melikhov, O. Péne, Phys. Lett. B446 (1999) 336.

[109] P.R. Page, Phys. Rev. D60 (1999) 057501.

[110] K. Harder, *A Search for the First Radial Excitation of the $D^{*\pm}$*, Diploma thesis, University of Hamburg, 1998.

[111] OPAL Collaboration, K. Harder, J. Steuerer, *A Search for the Radial Excitation of the $D^{*\pm}$*, OPAL PN352, 1998 (ICHEP 1998, Vancouver).

[112] OPAL Collaboration, G. Abbiendi et al., Eur. Phys. J. C20 (2001) 445.

[113] OPAL Collaboration, R. Akers et al., Z. Phys. C65 (1995) 17.

[114] ALEPH, DELPHI, L3, and OPAL Collaborations, Nucl. Instr. Meth. A378 (1996) 101.

[115] OPAL Collaboration, G.Abbiendi et al., Eur. Phys. J. C13 (2000) 1.

[116] CLEO Collaboration, J.L. Rodriguez, *Hadronic Decays of Beauty and Charm from CLEO*, hep-ex/9901008 (Heavy Quarks at Fixed Target 1998, Batavia).

[117] ZEUS Collaboration, *Production of P-Wave Charm Mesons at HERA*, Abstract 854 (ICHEP 2000, Osaka).

[118] UA1 Collaboration, Phys. Lett. B122 (1983) 103;
UA2 Collaboration, Phys. Lett. B122 (1983) 476;
UA1 Collaboration, Phys. Lett. B126 (1983) 398.

[119] Planning Group of the CERN Directorate Service Unit, *LEP Energy Cost Estimates at 100 GeV*, DSU-SPU Technical Note TN3-97 S6.

[120] S. Geer, *Neutrino Factory and Muon Collider R&D*, hep-ex/0111016.

[121] C. Adolphsen et al., *Zeroth-Order Design Report for the Next Linear Collider*, SLAC-474, 1996.

[122] N. Akasaka et al., *JLC Design Study*, KEK-REPORT-97-1.

[123] G. Guignard (Editor), *A 3 TeV e^+e^- Linear Collider Based on CLIC Technology*, CERN-2000-008.

[124] R. Brinkmann, K. Flöttman, J. Rossbach, P. Schmüser, N. Walker, H. Weise (Editors), *TESLA Technical Design Report, Part II: The Accelerator*, DESY-2001-011, ECFA-2001-209.

[125] T. Behnke, S. Bertolucci, R.D. Heuer, R. Settles (Editors), *TESLA Technical Design Report, Part IV: A Detector for TESLA*, DESY-2001-011, ECFA-2001-209.

[126] Linear Collider notes, available at `http://www.desy.de/~lcnotes`.

[127] American Linear Collider Working Group, T. Abe et al., *Linear Collider Physics Resource Book for Snowmass 2001*, hep-ex/0106055, hep-ex/0106056, hep-ex/0106057, hep-ex/0106058.

[128] M. Beneke et al., *Top Quark Physics*, in: hep-ph/0003033.

[129] G.W. Wilson, *Precision Measurement of the W Mass with a Polarised Threshold Scan at a Linear Collider*, LC-PHSM-2001-009.

[130] T. Behnke, G.A. Blair et al., *BRAHMS: A Monte Carlo for a Detector at a 500/800 GeV Linear Collider*, LC-TOOL-2001-005.

[131] H.J. Schreiber, *SIMDET V4.01*, available at
`http://www-zeuthen.desy.de/lc_repository/detector_simulation/dev/SIMDET`

[132] G. Deptuch et al., *Design and Testing of Monolithic Active Pixel Sensors for Charged Particle Tracking*, LC-DET-2001-017.

[133] M. Schumacher, *Pad Readout Geometries for a TPC with GEM Readout for the TESLA Linear Collider*, LC-DET-2001-014.

[134] M. Gruwé, *Studies of dE/dx Capabilities of a TPC for the Future Linear Collider TESLA*, LC-DET-2001-043.

[135] C.J.S. Damerell, *A CCD-based Vertex Detector for TESLA*, LC-DET-2001-023.

[136] H. Bauke, *Performance Studies for the TESLA Forward Tracking System with Different Layouts*, LC-DET-2001-078.

[137] T. Behnke et al., *Performance Study of the Proposed TESLA Detector Using a Realistic Track Reconstruction Package*, LC-DET-2001-029.

[138] R.J. Hawkings, *Vertex Detector and Flavour Tagging Studies for the TESLA Linear Collider*, LC-PHSM-2000-021.

[139] R. Frühwirth, Nucl. Instr. Meth. A262 (1987) 444;
P. Billoir, Nucl. Instr. Meth. A225 (1984) 352.

[140] M. Elsing, Nucl. Instr. Meth. A447 (2000) 76.

[141] D. Wicke, *A New Algorithm for Solving Tracking Ambiguities*, LC-TOOL-1999-007.

[142] H. Vogt, *Event Display for TESLA*, available at
`http://www-zeuthen.desy.de/lc_repository/detector_simulation/dev/EVENT_DISPLAY`

[143] S.M.-Xella-Hansen et al., *Flavour Tagging Studies for the TESLA Linear Collider*, LC-PHSM-2001-024.

[144] T. Ohl, Comp. Phys. Comm. 101 (1997) 269.

[145] D.J. Jackson, Nucl. Instr. Meth. A388 (1997) 247.

[146] D. Dong, *Measurement of the b Quark Fragmentation Function in Z^0 Decays*, PhD Thesis, SLAC-R-550, 1999.

[147] P. Gagnon, Int. J. Mod. Phys. A17 (2002) 145.

Danksagung

In der Folge möchte ich einige der Personen nennen, die mich bei der Erlangung des Doktorgrades des Fachbereichs Physik der Universität Hamburg unterstützt haben — sei es direkt oder indirekt, wissentlich oder unwissentlich.

Höchster Dank gebührt meinen Eltern, die in vielerlei Hinsicht die Grundlage dieser Arbeit gelegt haben. Auch meine Schwester hat im nicht ganz so harten Geschwisterkampf dazu beigetragen, mich auf den (hoffentlich) richtigen Kurs zu setzen.

Von größter Bedeutung war und ist Katrin, die mich nicht nur mit unglaublicher Ausdauer in den Zeiten mit besonders großer Arbeitsbelastung (also im wesentlichen während der gesamten Dauer der Anfertigung dieser Arbeit) unterstützt hat, sondern der es auch gelungen ist, mich im richtigen Moment mal durch Abhalten von der Arbeit weiterzubringen.

Dem Forschungszentrum DESY als Financier dieser Arbeit verdanke ich "Brot und Spiele". Danke auch für das Gluon - es hat mich sehr beschäftigt. Im Zusammenhang mit letzterem sind besonders Dr. Ties Behnke, Dr. Klaus Desch, Prof. Dr. Rolf-Dieter Heuer und Prof. Dr. Albrecht Wagner zu nennen, die mich bei der Anfertigung dieser Arbeit betreut haben. Das erfolgreiche Ende steht zudem in engem Zusammenhang mit Prof. Dr. Beate Naroska, Prof. Dr. Walter Schmidt-Parzefall und Dr. Eckhard Fretwurst, denen ich für die Anfertigung von Gutachten beziehungsweise für die Leitung der Disputation danke.

Eine sehr angenehme und freundschaftliche Atmosphäre herrscht in der DESY-Gruppe FLC, bei deren Mitgliedern ich mich dafür ebenfalls bedanken möchte — allen voran bei Petra als moralischer Stütze und Organisationszentrum. Danke vor allem auch für geduldiges Ertragen zahlloser Probevorträge mit Überlänge!

Der OPAL-Kollaboration fühle ich mich sehr verbunden, aufgrund ihrer ausgesprochen freundschaftlichen und von Hilfsbereitschaft geprägten Umgebung — an mich herangetragen durch Dr. Pauline Gagnon, Dr. Richard Hawkings, Dr. Stefan Söldner-Rembold, Dr. Michael Thiergen, Mette Stuwe, Dawn Hudson und viele andere. Prof. Dr. Volker Blobel, Dr. Matthew Jones und Dr. Michael Thiergen danke ich für die Zurverfügungstellung ihrer Software, inclusive diesbezüglicher Beratung.

Sehr dankbar bin ich des weiteren für die anregenden Kaffeepausen und gelegentliche Blickwinkel und Unternehmungen außerhalb der Physik mit Katja, Jan, Marcel und Thomas.

Zur Dankbarkeit gehört auch Hoffnung — Hoffnung vor allem, dass ich im Gegensatz zu dem einen oder anderen früheren Fall in dieser Danksagung nicht die wichtigsten Personen vergessen habe. Eventuelle Opfer haben Anspruch auf Entschädigung in SCCU (Standard CERN Coffee Units).